Studies on Aero-Thermal Performances of Leakage Flows Injection from the Endwall Slot in Linear Cascade of High-Pressure Turbine

Wan Aizon W Ghopa

A dissertation submitted in partial fulfillment
of the requirements for the degree of

Doctoral of Philosophy

Mechanical System Engineering
Iwate University
2013

Dissertation Committee;

Professor Ken-ichi FUNAZAKI
Professor Hideki YANAOKA
Professor Kazuyuki UENO

Abstract

Present studies focus on thermal and aerodynamics investigations of leakage flow injection through a slot which is located at upstream of blade leading edge. In the real gas turbine, this slot is actually the gap between the combustor and turbine endwall as for the maintenance works consideration. However, the slot induced to the leakage phenomenon caused by the bypassed air that coming from the compressor side for turbine cooling purposes. Gas turbine manufactures intended to minimize these kinds of leakages in maintaining the aerodynamics performance of the turbine cascade. However, previous researchers found that the leakages could be used to protect the endwall surfaces from the hot gas since it could not be completely prevented. Thus, present study investigated the potential of leakage flows as a function of film cooling. Chapter 1 gives some introduction on present works about the need of film cooling to protect the wall surfaces. Several related studies by previous researchers are also explained. Chapter 2 explained the details of methodologies used in present studies. A leakage flow with 90° of injection angle was considered as for the baseline configuration. Liquid crystal was used for the time-varying endwall temperature measurement. The transient method was applied to determine the film cooling effectiveness, η and the heat transfer coefficient, h for the thermal performance evaluations. The details of the aerodynamics performances was revealed by conducting 5-holes Pitot tube measurement at blade downstream plane ($1.25C_{ax}$) and the total pressure loss coefficient, C_{pt} as well as the flow vorticity, ζ contours were plotted. Furthermore, the effects of the leakage flow with the mainstream consist of complex secondary flows structures also have been revealed by numerical investigation. In present study, the flow is analyzed by using the three-dimensional, steady Reynolds-averaged Navier-Stokes (RANS) equations by conducting Shear Stress Transport, SST turbulence model. The leakage was injected with a various amount (which is described by mass flow ratio, MFR) to observe the η performance at different injection cases. Chapter 3 provided details discussions on the aero and thermal performances of the leakage injection. Both experimental and numerical presented the performance of η increased when the injection amount increases. SST turbulence model captured the presence of the separation flow that caused the lower h region which also captured by the experimental. As for the aerodynamics performance, C_{pt} was increased after the introduction of leakage injection and indicated the increase trend when the MFR was being increased. Leakage flows were

prevented to be injected into high pressure region thus they tended to move towards lower pressure region which is between two stagnation regions. As a result, a newly generated vortex core was predicted. This accumulated vortex core (AFV) is considered to contribute to the additional losses at blade downstream. Chapter 4 presents the numerical investigation on the modification of slot configurations such as positions and orientations. The leakages flow by shallower injection angle, β towards mainstream was predicted to reduce the strength of the passage vortex thus increase the aerodynamics performance particularly at higher injection cases. Additionally, η also obviously increased by the slot orientation. To move away the slot from the blade LE was predicted to increase both aero and thermal performance. The leakage flow could laterally be penetrated to the mainstream and stayed closer on endwall surfaces. This is due to the fewer blockages influenced by the stagnation region since the slot located far away from the blade LE. In contrast, move the slot closer towards blade LE just increased the $C_{pt.}$ Furthermore, locate the slot closer to blade LE could not increase the protection layer except the level of η. Finally, Chapter 5 highlights the important points to be concluded based on present investigations. The potential of the leakage flows to protect the endwall surfaces has been proven and they were highly influenced by the secondary flows behavior on the endwall region. However, to increase the performance of cooling by increasing the injection amounts unfortunately reduces the aerodynamics performance due to the increase strength of the secondary flow vortices. The leakage flow with a shallow injection angle towards mainstream are predicted to provide a positive trends of cooling performance with a lower aerodynamic losses especially at higher leakage flow injection cases.

Keywords: Turbomachinery, secondary flow, endwall film cooling, leakage flow, purge flow, heat transfer, high-pressure turbine, liquid crystal, transient method, pressure loss, slot orientation, slot position.

ACKNOWLEDGMENTS

Firstly, I would like to express my sincere appreciation to my advisor, Professor Ken-ichi Funazaki, for his valuable advices and guidance that he offered me throughout these years. His generous support and constant encouragement in my research activities made me never give up and always keeps me on moving forward.

Highly grateful to the Dissertation Committee, Professor Yasaoka and Professor Ueno who have kindly provided their suggestions and comments to improve the dissertation. Also appreciating to them for their time in evaluating this dissertation.

Thanks are also to the staff of the workshop center in Iwate University especially Mr. Mamoru Kikuchi who always produced work of unrivalled caliber. I am also grateful to Associate Professor Taniguchi and Dr. Kato for their many supports, discussions and ideas in experimental and numerical simulation works. Colleagues of the Aero-engine Laboratory have not only provided me a kind environment but also a valuable source of assistance and friendship. Many thanks also to Mr. Kawabata and former doctoral course candidate, Dr. Kamil Abdullah for their kind help and supports.

I am deeply indebted to my research partner, Mr. Miura Takemitsu, whose currently working at Hitachi and Mr. Ito Ken-ichi currently working in Tokyo and Mr. Suzuki Yuuya who will continues the research activities. I believed that they did their best in helping me especially in experimental works.

Thank you to Hitachi Ltd for their financial support in developing a new wind tunnel and etc. Great thanks also to my employer, National University of Malaysia (UKM) and Ministry of High Education, Malaysia (MOHE) for their funding during my study period.

Of course cannot be denied a very special acknowledgment must be given to my parent and siblings who always give me a moral support and continuously pray for my success.

Last but not the least very special mention to my family especially my lovely wife who always stands right beside me since I was in secondary school is actually one of the key of my success.

Table of Contents

List of Figures

List of Tables

NOMENCLATURE

Latin letters

A	Sectional area
c	Specific heat
C	Actual blade chord
C_{ax}	Axial blade chord
CR	Convergence ratio
C_{ps}	Static pressure loss coefficient
C_{pt}	Total pressure loss coefficient
$\overline{C_{pt}}$	Area-averaged total pressure loss coefficient
C_{SKE}	Secondary kinetic energy coefficient
D_{acc}	Accuracy of the device
h	Heat transfer coefficient
l	Distance of slot from blade leading edge
$\dot{m}$	Mass flow rate
MFR	Mass flow ratio
n	number of pitch
P_d	Dynamic pressure
P_s	Static pressure
P_t	Total pressure
Q	Volume flow rate
Re	Reynolds Number
SKE	Secondary kinetic energy
T	Temperature
t	Time
U	Absolute velocity
u	Axial velocity component
v	Pitch wise velocity component
V_{ax}	Axial flow velocity direction
w	Span wise velocity component

x/C_{ax}	Normalized-axial direction
y/p	Normalized-pitchwise direction
z/s	Normalized-spanwise direction

Greek letters

α	yaw angle
β	leakage flow injection angle
ρ	Density
ζ	Vorticity
δ	Boundary layer thickness
δ_D	Device accuracy uncertainty
σ	pitch angle
ε	Standard deviation
η	Film cooling effectiveness
$\bar{\eta}$	Area-averaged film cooling effectiveness

Subscripts

ave	Average
aw	Adiabatic wall
Max	Maximum
Min	Minimum
mid	Mid span
out	Outlet
∞	Mainstream at inlet
2	Secondary

Acronyms

CFD	Computational fluid dynamic
EFD	Experimental fluid dynamic
HSL	Hue, saturation and light
LE	Leading edge
PS	Pressure side
SS	Suction side
SST	Shear Stress Transport
RGB	Red, green and blue
TE	Trailing edge
TLC	*Thermo-cromic* liquid crystal

Chapter 1

Introduction

This chapter provides some introduction on the gas turbine technologies. Increasing gas turbine thermal efficiency is an approach to increase the performance which leads to increase of turbine inlet temperature. The need of film cooling to protect the material surfaces from the hot gases is also explained to show it's a very effective way to allow further increases of turbine inlet temperature. In addition, the literature study has been done to investigate the current achievement of the gas turbine cooling focusing on the endwall side. The research objective is also includes in this chapter.

Background

Gas turbines are used to power aircrafts, trains, ships and electrical generators. Figure 1 illustrates the gas turbine structure of HF120 Turbofan manufactured by General Electric and Honda whereas Figure 2 shows the diagram of modern gas turbine. Generally, gas turbine can be divided into three sections; compression, combustion and expansion. The air flows through a fan which then be compressed with multistage compressor to a higher pressure. Energy is then added by injecting fuel into the compressed air inside the combustion chamber and igniting it so a high temperatures flow is generated in this stage. This high-temperature and high pressure gas enters a turbine, where it expands down to the exhaust pressure, producing a shaft work or thrust output in the process. The turbine shaft work is used to drive the compressor and other devices such as an electric generator that coupled to the shaft. The energy that is not used for shaft work comes out in the exhaust gases, so these have either a high temperature or a high velocity. The HF120 Turbofan is a gas turbine used for the jet

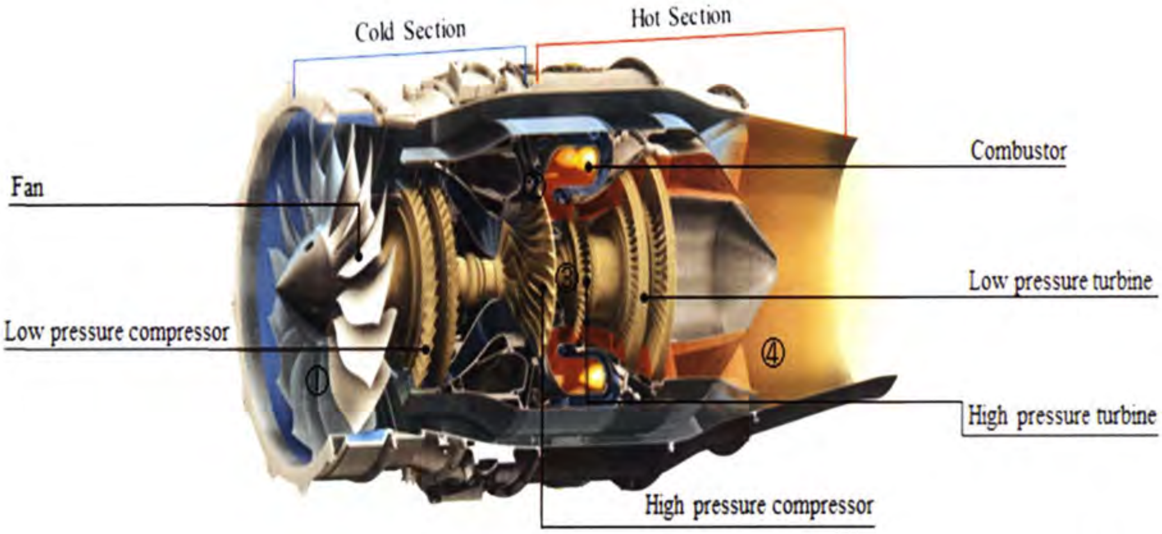

(Source: Adapted from GE Honda link [35])

Figure 1 Gas turbine structure- HF120 by GE Honda

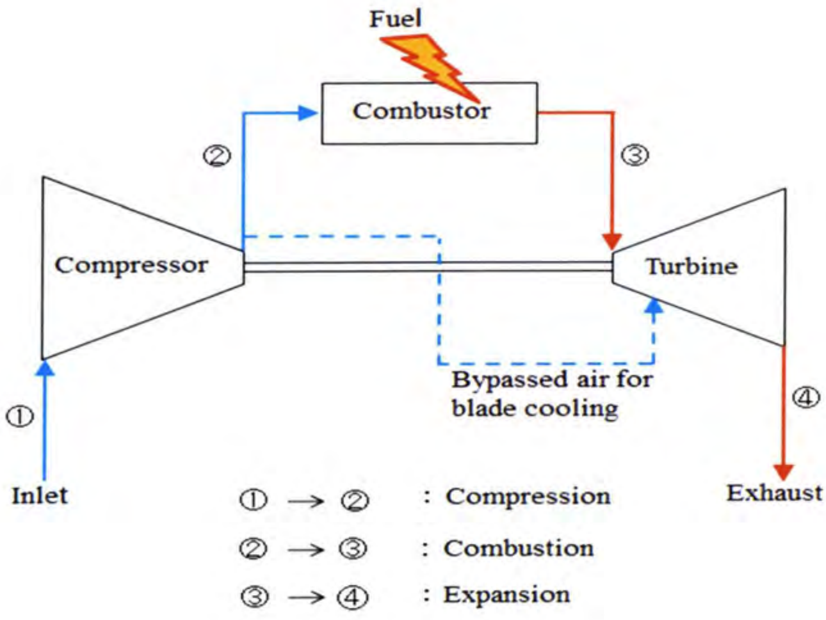

Figure 2 Diagram of modern gas turbine with cooling technology

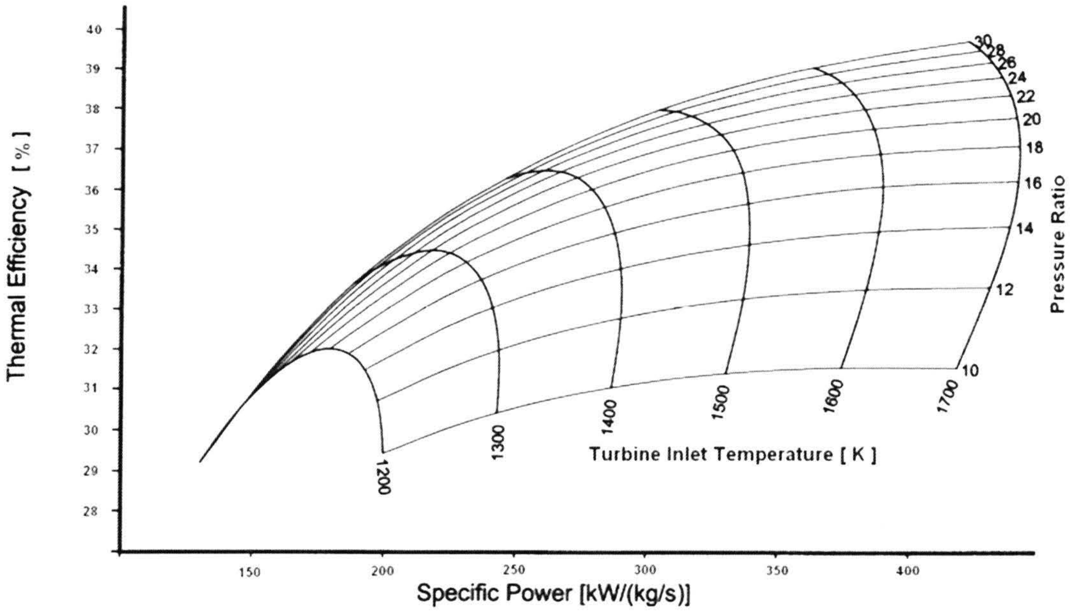

(Source: Genrup, 2005 [36])

Figure 3 Modern gas turbine performance chart

engines which are optimized to produce thrust from the exhaust gases, or from ducted fans connected to the gas turbines.

Now day's modern gas turbines have to fulfill the requirements of an increasing efficiency combined with very low emissions in a robust, cost-effective way. Indeed, a global warming due to the greenhouse effect is one of the most issue has been discussed and need to be prevented. Low emissions or reducing the fuel burning is considerable limited the amount of carbon dioxide gas released into the atmosphere. This can be realized by increasing the gas turbine thermal efficiency. Looking at the performance chart for the design of a modern gas turbine, see Figure 3, it is obviously that the need to achieve higher total gas turbine efficiency leads to an increase of the turbine inlet temperature. To take advantage of the higher turbine inlet temperature the turbine pressure ratio also has to be increased. The trend of increasing turbine inlet temperatures started in the 1940`s with the first jet engines proposed by Sir Frank Whittle and continues to modern gas turbines as shown in Figure 4. As it can be recognized from Figure 4, the increase in turbine inlet temperature has proceeded much faster than the progress in the development of more advanced vane and blade materials. Indeed turbine inlet temperature levels exceeded maximum tolerable material temperature by several hundred K starting in the 1960`s, and this trend has continued since ever. This

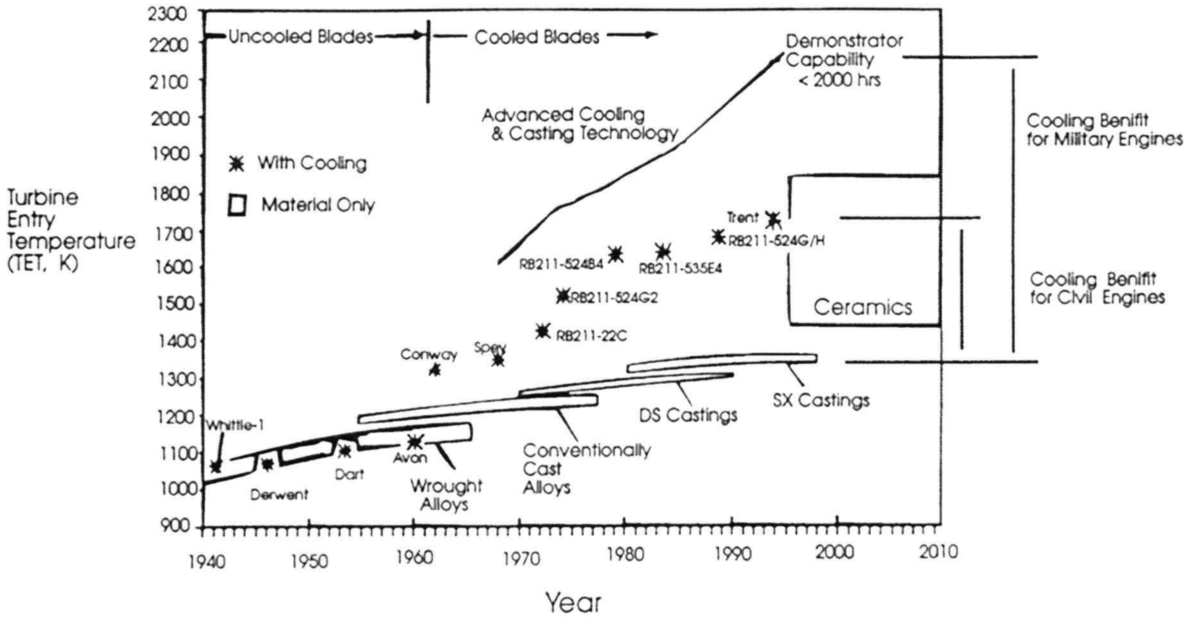

(Source: Royal Aeronautical Society/Aerospace, 1994)

Figure 4 Turbine inlet temperature based on advanced material and cooling technology

condition is realizable only through the application of advanced vane and blade cooling technology to keep the material temperature below the allowable, lifetime-limiting level. The extraction of the compressed cooling air bypassing the combustion chamber (as shown in Figure 2) leads to an additional increase of the already high turbine inlet temperature. These effects lead to a very high heat load of the nozzle guide vane hub and tip endwall of a modern gas turbine. This implicates that the endwall have to be provided with an advanced cooling technology to achieve the required lifetime-limiting material temperature.

Film cooling is an effective way to protect blade or endwall surfaces from the extremely high temperature gases. Figure 5 shows on how the ejected coolant into the mainstream produces the protection layer close to the endwall surfaces that mostly called film cooling. The coolant temperature, T_2 with a blue streamline is injected through holes or slot on endwall into the high temperature of the main flow, T_∞ indicated by the red streamline. Downstream of the hole or slot exit, the coolant will stay closer to the endwall surfaces and providing a layer which preventing the endwall surface not to be directly expose to the hot gas. Thus, the gas turbine can be operated at higher temperature exceeding its thermal stress limit since the material surfaces are protected by the film cooling. Film cooling effectiveness

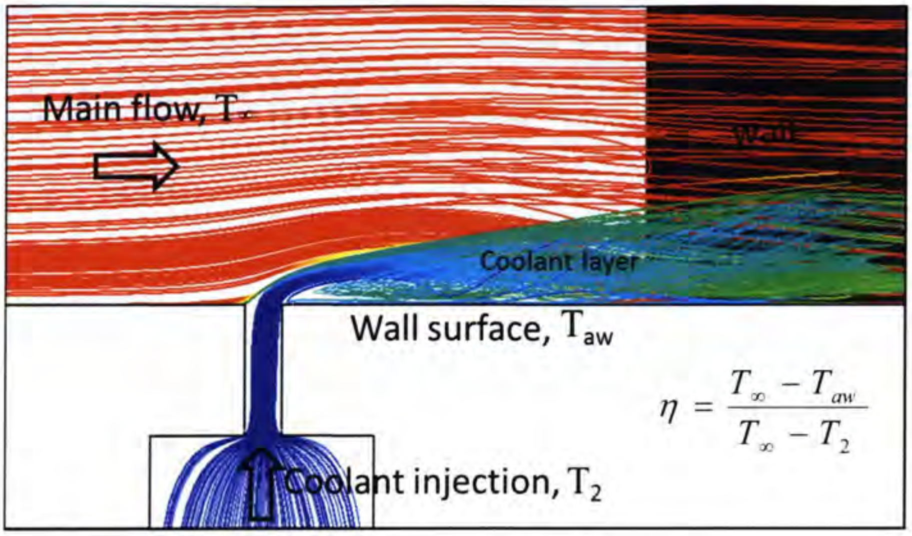

Figure 5 Film cooling concept

is a normalized temperature usually represented by η is a parameter used to evaluate the performance of film cooling. The high pressure turbine is just located downstream of the combustor chamber, thus the film cooling approaches are required at this stage. Figure 6 shows an example of the modern cooled gas turbine blade with film and internal blade cooling. As been discussed, the film cooling has not only been employed on the blade surface but also on the endwall of the turbine blade to provide necessary cooling protection for the component. As shown in the diagram from Figure 2, the extraction of the air from the high pressure compressor side unfortunately leads to the leakage phenomenon through the slots exist in high pressure turbine stage. Figure 7 shows the real high pressure turbine blade with cooling holes design on blade and endwall surfaces. According to the Figure 7, there are two locations of slots exist in high-pressure turbine stage. First slot is actually the gap between the combustor and turbine endwall located at upstream of blade leading edge while the second slot is the gap between the blade segments, respectively. The blade was split into several segments as for the maintenance works consideration. Gas turbine manufactures intended to minimize these kinds of leakages in maintaining the aerodynamics performance of the cascade. However, previous researchers found that the leakages through the upstream slot could be used as cooling air to protect the endwall surfaces from the hot gas since it could not be completely prevented. In addition, the high pressure from the leakage air also prevents the hot mainstream air ingestion into these gaps. For the cooling purpose, endwall side is considered more difficult than the blade surfaces due to the presence of the complex secondary flows structures which was believed to give a high impact on the heat transfer performance. Thus, the understanding of the endwall flow structures is highly important in this study in order to see their interaction with the coolant flow. The details of the secondary flows in the cascade are firstly explained in the next section.

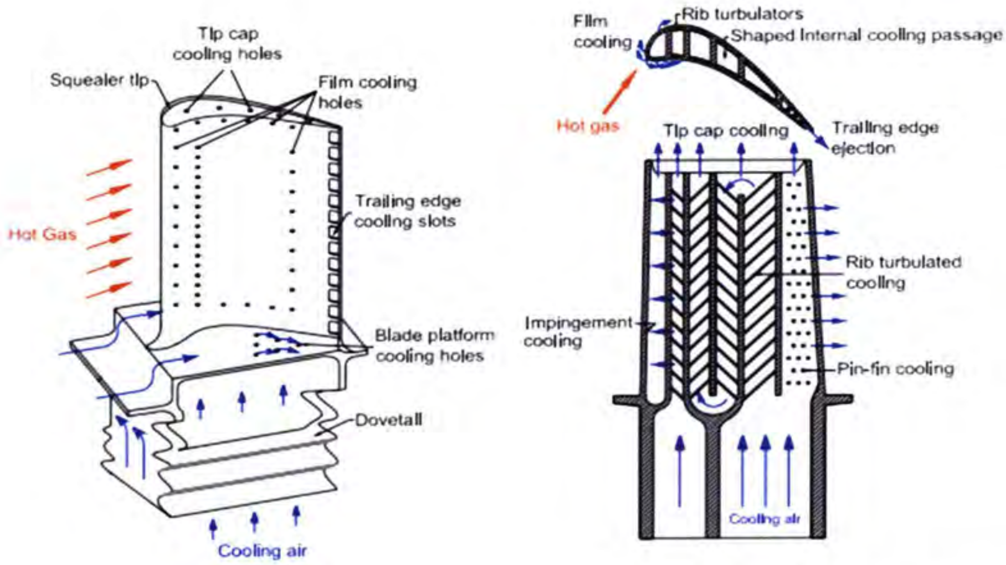

(Source: Adapted from Han et al. [37])

Figure 6 Modern cooled gas turbine blade

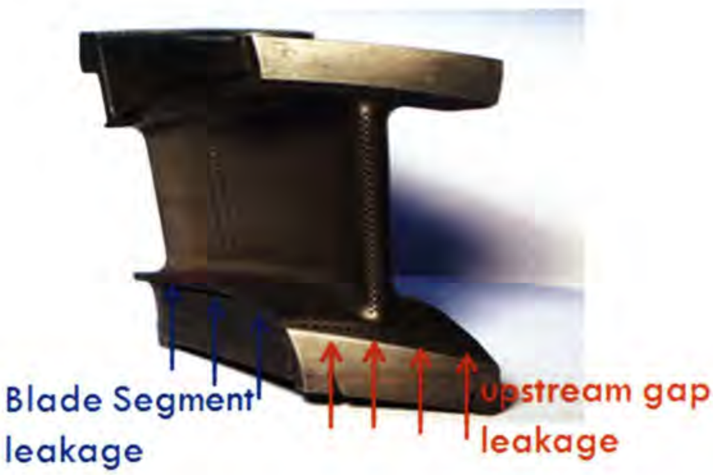

(Source: Adapted from Frank G. R., 2006 [38])

Figure 7 Leakage phenomenon influenced by bypassed cooling air in HPT

1.1 Secondary flows in the blade passage

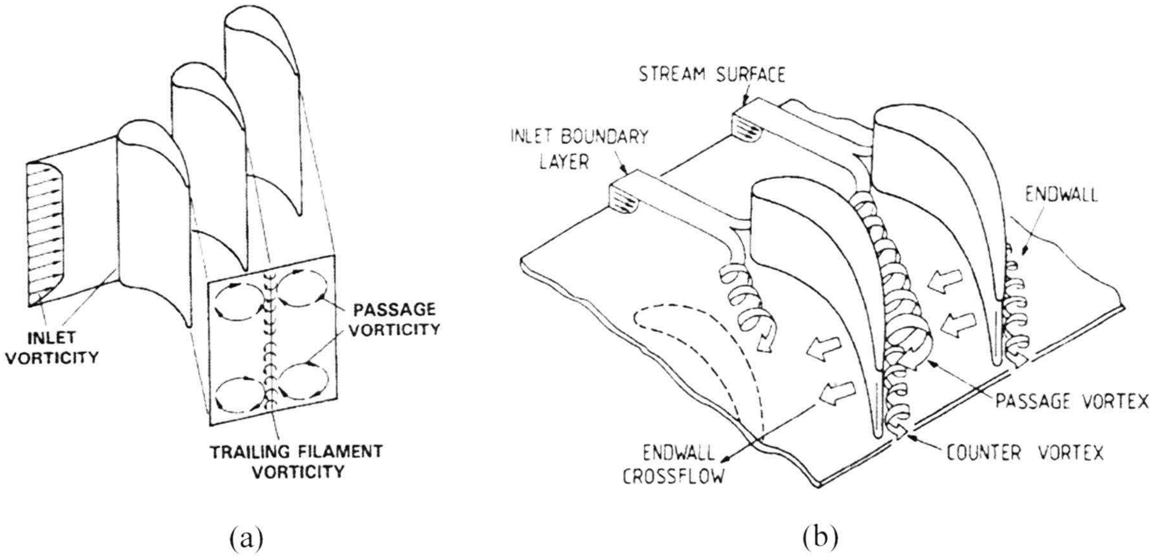

Figure 8 Secondary flow system; (a) Hawthorne, 1955, (b) Langston, 1977

Secondary flow structure generated in the blade row is the main factor that contributes to the endwall loss. Since the secondary flow is a result of viscous shear on the endwall, it is a large source of loss, contributing approximately one third of the total loss, Denton [1]. A common means of quantifying secondary flow is by its Secondary Kinetic Energy (SKE), which is normally defined as the kinetic energy associated with the velocity components perpendicular to the primary flow direction. In the classical secondary flow system, Hawthorne [2], the axis of vorticity is twisted as the flow passes through the blade passage. This axis is initially perpendicular to the flow direction, as it is caused by viscous effects in the boundary layer, but by the blade row exit two counter-rotating passage vortices have been formed, see Figure 8 (a). The vortex sheet also contains trailing filament vortices, which are caused by the radial change in blade circulation, Sieverding [3]. The inlet end wall boundary layer rolls up in front of the leading edge to form the horseshoe vortex, as first seen by Klein [4]. Measurements by Langston et al. [5], showed the evolution of the vortex through the blade row, Figure 8 (b): the pressure surface leg moving across the passage, due to the cross-passage pressure gradient, and merging with the passage vortex. The horseshoe vortex increases the SKE of the passage vortex by approximately 20 %, Georgiou et al. [6]. Sharma and Butler, [7], showed that the suction surface leg of the horseshoe vortex lifts up the blade surface where the separation line reaches the blade surface. It then orbits around, and is dissipated by, the passage vortex, although this type of interaction is dependent upon the particular cascade geometry and pressure ratio, Goldstein and Spores [8]. Any reduction or elimination of the leading edge horseshoe vortex is thought to have little effect on the shape and position of the passage vortex, Sieverding [3]. In addition to the horseshoe and passage vortices, several other vortices were found by Goldstein and Spores [8], see Figure 9. Sharma and Butler [9] also present a complex secondary flow models, shown in Figure 10. Wang et al. [10] also presented the flow field data within the vane stagnation plane illustrating the formation and dynamics of the leading edge horse-shoe vortex. The strongest is the corner vortex found in the suction surface end wall corner, which rotates in the opposite sense to the passage vortex. It is formed in a similar manner to the horseshoe vortex where the limiting streamline impinges on the suction surface near the position of maximum surface curvature, Sieverding [3], but is only formed when the blade loading is sufficiently high to give a strong interaction of the passage vortex with the blade surface. Its existence is shown by the radial angle distribution, which gives a reduction in overturning near the end wall, Gregory-Smith and Graves [11].

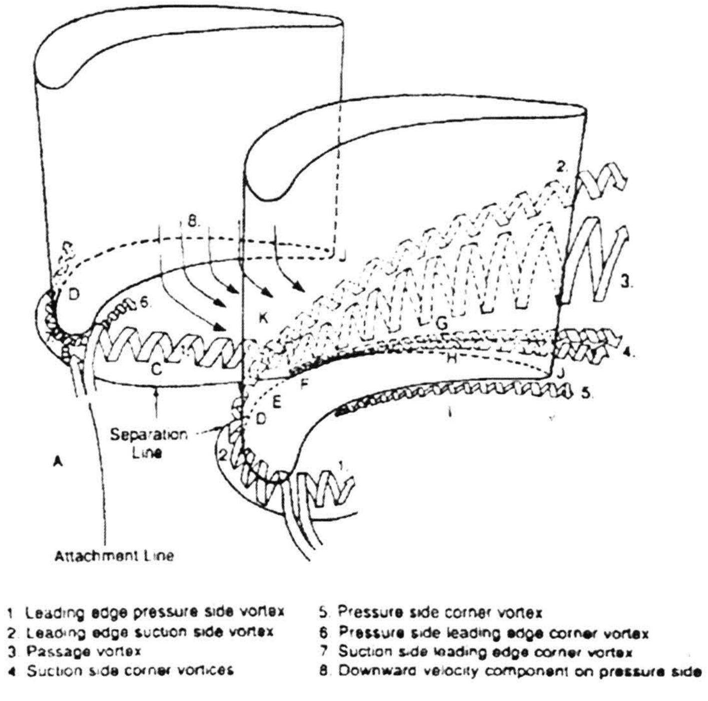

Figure 9 Endwall flow field, Goldstein and Spores, 1988

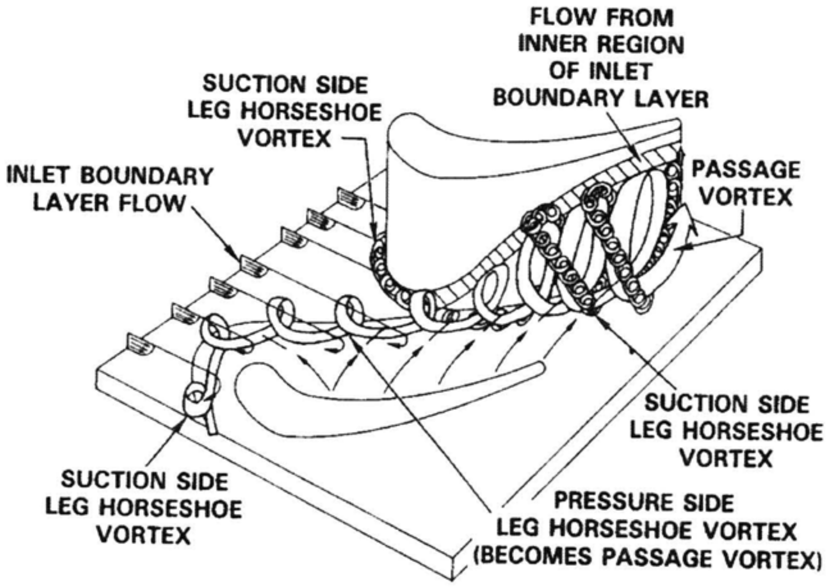

Figure 10 Cascade endwall flow structure by Sharma and Butler, 1996

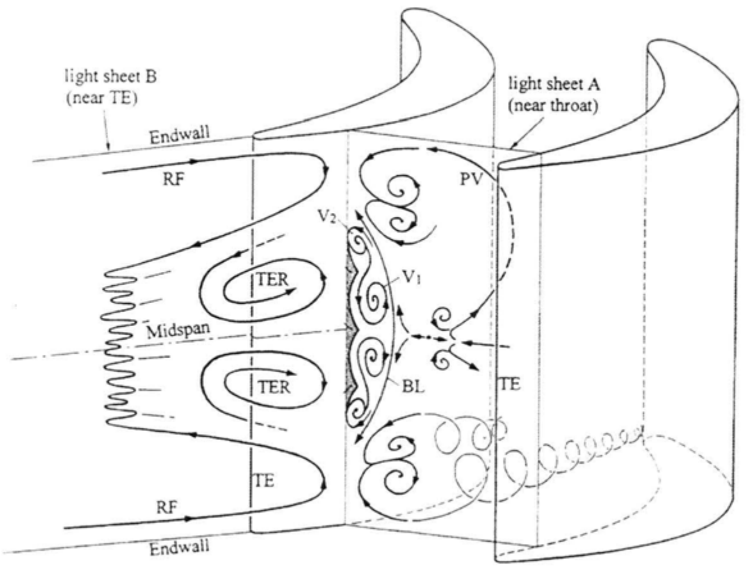

Figure 11 Detailed vortex system, Yamamoto et al., 1995

An investigation of the flow field downstream of the corner formed by a blade and a flat plate showed that the corner vortex dissipated quickly, disappearing by approximately 20 % chord length downstream, Abdulla-Altaii and Raj [12]. A pair of three-dimensional vortices, V_1 and

V_2, was also found inside the suction surface boundary layer, *BL*, near the trailing edge, *TE*, Yamamoto et al. [13], Figure 11: some of this low energy fluid is absorbed into the passage vortex, *PV*. Near the suction surface trailing edge, there are strong reverse flows towards the throat, *RF* and *TER*, and some of the vortices behave unsteadily due to the surrounding vortex movement. Having described the secondary flow structure, the corresponding losses can also be examined. There are three characteristic loss features at the trailing edge plane as well as the end wall boundary layer. Dependent upon the inlet boundary layer thickness and blade loading, these are more or less superimposed and as the loading increases they lift off from the end wall. The secondary flow strength is largely dependent upon the thickness of the upstream boundary layer and the amount of turning in the blade row, Sieverding [3]. Since dissipation within a vortex core is very high, the decay of the SKE yields an increase in entropy, Denton, [1]. Although some of the dissipation occurs within the blade row, most occurs after the trailing edge and it is often assumed that all the SKE is lost: although this exaggerates the loss, it partially accounts for other losses, such as the mixing losses, Sieverding [3]. The sum of the loss coefficient and the SKE was found to be approximately constant at any plane downstream of a two dimensional blade trailing edge, as was the mixed out loss, Moore and Adhye [14], implying that the decay in SKE closely matches the increase in entropy.

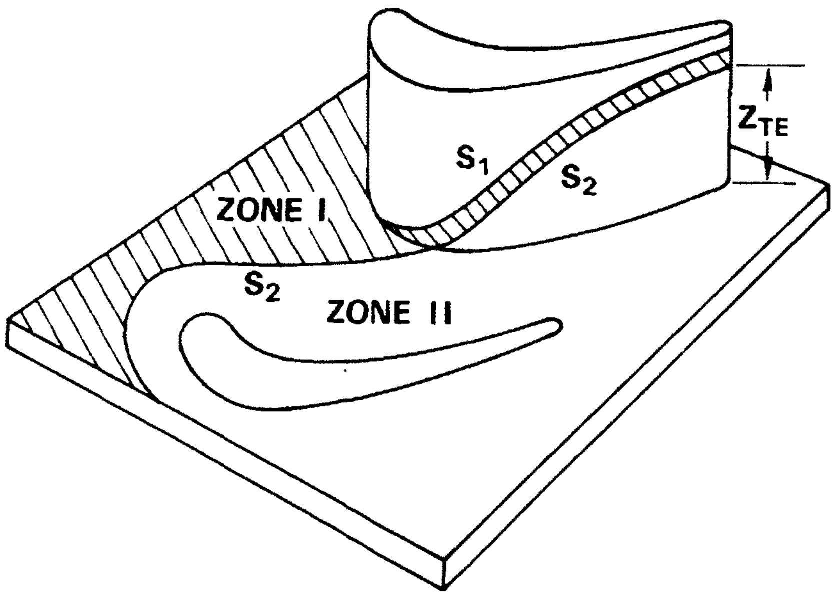

Figure 12 Endwall separation lines, Sharma and Butler, 1986

A method to estimate the endwall losses was developed by Gregory-Smith [15], showing a good agreement with experimental data: however, this was dependent upon the detailed blade design. It was later suggested that an indication of the strength of the endwall loss was the height of the separation line on the suction surface trailing edge, Sharma and Butler [7], see Figure 12, termed the penetration height, Z_{TE}. This correlation is only dependent upon the flow turning angle, α, the convergence ratio of the blade row, CR, and the ratio of the inlet boundary layer height, to the blade height, δ_1/h:

$$\frac{Z_{TE}}{C} = 0.15\frac{\alpha}{\sqrt{CR}} + 1.4\frac{\delta_1}{h} - 2.73\left(\frac{\delta_1}{h}\right)^2 + 1.77\left(\frac{\delta_1}{h}\right)^3 \tag{1}$$

1.2 Relevant studies by previous researchers

Previous section discusses on the existence of the secondary flows on the endwall region of the cascade without any disturbance from coolant air injection or by the effect of different inlet flow parameters. The study above clearly explained that the needs of the details investigation not only in the heat transfer behavior but also the interaction between complex secondary flows with the coolant air. These all information is required for the development of the modern gas turbine. This section will discuss about the related studies made by other researches for the endwall film cooling especially through the slot leakage air approach. Some other researcher defined as 'purge flow' if it is intended to inject the air from the slot for the cooling purpose. Studies by Kang et al. [16] and Radomsky and Thole [17] revealed the effect of inlet Reynolds number and turbulence level respectively on the formation of the horse-shoe vortex. Both studies were not included the purge flows. Using the same cascade of the previous study [16, 17], Sundaram and Thole [18] performed LDV measurements to reveals the effect of the purge flow on the endwall flow structure to enable direct comparison with the previous result [16, 17]. Rehder and Dannhauer [19], has carried out the experiments to reveal the effects of injection flow angle from the upstream clearance of linear cascade of LPT stator vanes. The observation shows that the leakage ejection perpendicular to the main flow direction amplifies the secondary flow, in particular the horse-shoe vortex and therefore

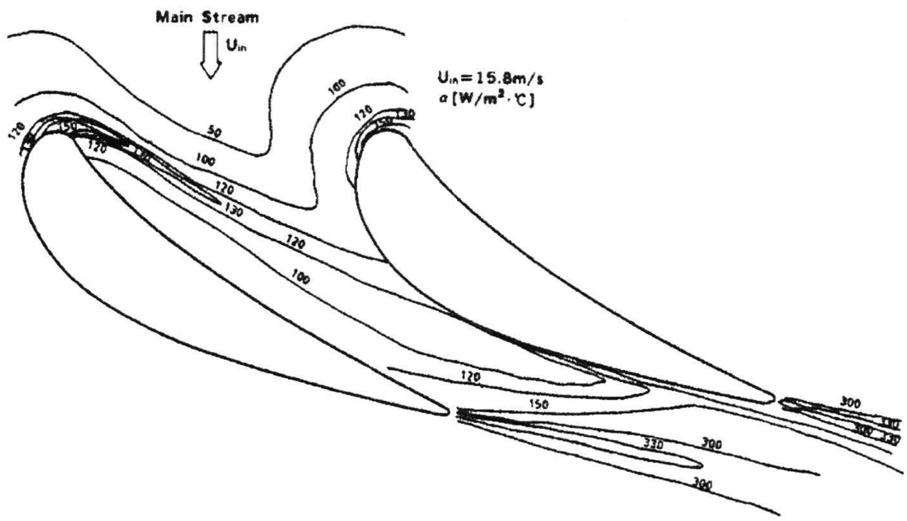

Figure 13 Endwall heat transfer distribution in cascade by Takeshi et al, 1990

increases the secondary losses near the endwall region, whereas tangential leakage ejection causes significant reduction of horse-shoe vortex and at the same time decreasing the secondary losses at the cascade exit. Recently, Thrift and Thole [20] investigated the effects of orientation and position of the purge flow. The observations show a dramatic difference in horse-shoe vortex formation at the stagnation plane which is directly influenced by the orientation and position of the purge flow. The earliest study that relates the endwall flow structure and film cooling has been made by Blair [21]. The work clarifies that, the horse-shoe vortex and passage vortex has a dominant impact on the heat transfer of film-cooled endwall. This also was proved by Takeshi et al. [22], as shown in Figure 13. They found that the heat transfer distribution on a vane passage endwall with the increased heat transfer in the leading edge region caused by the horse-shoe vortex. The heat transfer increased along the separation line and in the airfoil wake region. They also found a reduction of the endwall film cooling effectiveness near the blade leading edge due to the presence of the horse-shoe vortex. Blair [23] reported a slight increase of the heat transfer in the beginning of the flow passage with increasing Reynolds number due to earlier transition of the boundary layer. Further downstream, the heat transfer decreases at higher Reynolds numbers because of the thicker turbulent boundary layer. Again, higher heat transfer in the trailing edge wake region at the lower Reynolds number can be observed. Kost and Nicklas [24] presented aerodynamic measurement from a transonic cascade with an upstream normal leakage ejection located at $0.2C_{ax}$. They found that injection at this location promoted the separation and enhanced the horse-shoe vortex. Kost and Mullaert [25] continued the study by moved the slot location to $0.3C_{ax}$ upstream of the cascade. From the results obtained, they found that the slot flow stayed closer to the endwall and provided better film cooling than flow from the slot located at $0.2C_{ax}$ of cascade upstream. With 45 degree of leakage slot injection, Lynch and Thole [26] and Knost and Thole [27] performed adiabatic effectiveness experiments by a different slot location which was located at $0.96C_{ax}$ and $0.38C_{ax}$ upstream of the vane cascade respectively. It was noted that the coverage area of the leakage coolant was similar between the two locations. The effectiveness levels within the passage, however, were lower for the slot placed further upstream as the coolant had more distance to mix with the hot mainstream flow. The upstream leakage studies were also done by other researchers such as Piggush and Simon [28], measured heat transfer characteristic over the contoured endwall in the cascade of high-pressure turbine stators by the use of thermocouples on the endwall, emulating the leakage flows from the upstream clearance and the segment gap. The similar study also done by Lynch and Thole [26] using IR camera to determine the heat transfer and film cooling effectiveness distribution over the endwall with the emphasis on gap size. They observed that a narrower gap achieved a relatively uniform leakage flow along the circumferential direction, resulting in a wider coverage of the leakage flow on the endwall. The observations show a dramatic difference in horse-shoe vortex formation near the stagnation region which is directly influenced by the orientation and position of the purge flow. Studies on various test conditions are required to have detailed information on relevant studies. Based on above literatures, it is also clear that cooling air injection from upstream slot highly influenced the aerodynamics performance of turbine cascade. Furthermore, slot location and geometry as well as cooling air amount need to be carefully considered for the optimization purpose. In present works, a new model with slightly lower solidity and higher aspect ratio compared with previous test blade [29] has been designed. The slot location also was moved slightly away from the blade leading edge. The study focuses on both aero and thermodynamics effect of leakage flow on the endwall region of high-pressure turbine linear cascade. Aerodynamic measurements were performed by the use of pneumatic 5-hole pitot tube to measure a total pressure at blade downstream while the liquid crystal was used for the thermal investigation. The numerical simulation was also conducted for the validation and to predict the interaction of ejected leakage flow with the mainstream.

1.3 Research objectives

The objectives of the current study are to reveal the potential of leakage flows in providing the protection layer on the endwall surface in linear cascade of high-pressure turbine. In order to achieve present objectives, the studies concentrate on;

I. Investigation on the interaction between the leakage flow and the mainstream which influenced to the aerodynamics losses and cooling performance
II. Aero-thermal performance based on difference amount of leakage flow ejection
III. The performance of the numerical simulation in predicting the aero-thermal performance by the presence of secondary flow phenomenon on the endwall region
IV. The aero-thermal performance of leakage flow based on modification of slot orientation and position.

Chapter 2

Research Methodologies

This chapter presents the research methodologies implicated in present study. The experiments involve two main experimental procedures (aero and thermal measurement) which are conducted at Iwate University, Japan. Both of the measurements have been conducted in the same experimental setup which enable a directly investigation on the role of aerodynamics behavior onto thermal performance. Numerical simulation is also one of the approaches that were applied in this study in order to reveal the flow which cannot merely investigated by the experimental.

2.1 Test models

The test blade used in present study is shown in Figure 14. The blade design is merit to the first stage turbine which is operating in high pressure condition. The blade was designed by using 3-dimensional CAD (Computational Aided Design) software known as SolidWorks. Based on the 3D data obtained from the SolidWorks, the blade was manufactured by applying a rapid-prototyping method. In order to investigate the effect of the leakage phenomenon in high-pressure turbine cascade, 6 blades have been designed with 5 segments as shown in Figure 15. The two blades with hub endwall are expected to be a measurement region which consisted with a upstream leakage slot along the beginning of the endwall. Two segment leakage gaps also have been design where the first segment gap located between blade 2 and blade 3 while the second segment gap in between blade 4 and blade 5. Upstream slot was designed to have a merit to the gap between the first stage turbine endwall and combustor endwall while the gaps between the blades segments are merit to the

Figure 14 Test blade manufactured by rapid-prototyping method

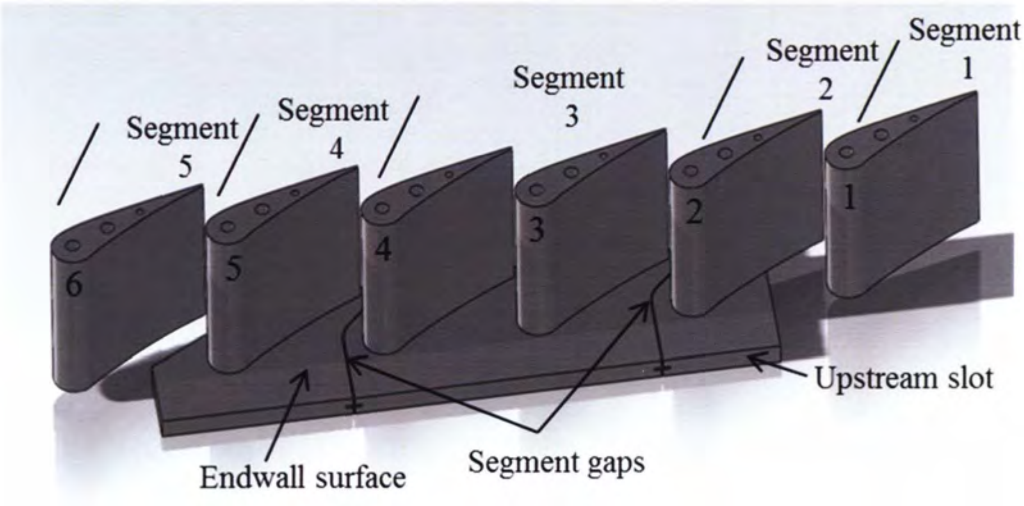

Figure 15 Test blade design-3D CAD image

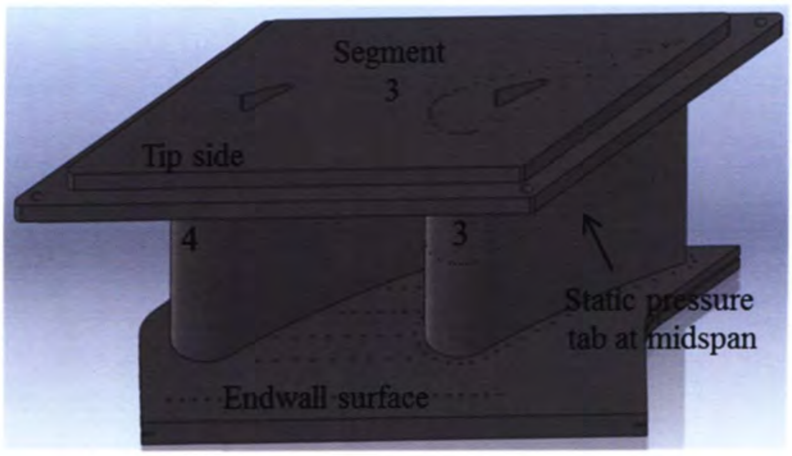

Figure 16 Blade segment 3 with static pressure tabs- 3D CAD image

Table 1 Blade profiles

Parameter	Profile
Span, h	117.68 [mm]
Pitch , t	115.91[mm]
Chord, C	120.23[mm]
Axial Chord, C_{ax}	62.34[mm]
Solidity, C/t	1.02
Aspect ratio, h/C	0.98
Inlet flow angle, β_1	0°
Outlet flow angle, β_2	72.3°
Fillet	No
Upstream gap width	4 [mm]
Segment gap width	1.25 [mm]

gap exist between the blades in the real gas turbine. In actual application, these gaps are designed in consideration of maintenance works where the hub/tip and blades has been split to several parts. However, present study will focuses on the leakage flow from the upstream slot. Figure 16 illustrates the blade model for static pressure measurement where the pressure tab was design on the endwall and mid span of blade PS and SS of blade segment 3. Thus, the test blade can easily be replaced for measurement purpose. The details of the test blade are shown in Table 1.

2.2 Test facility

The new test facility was designed for aerodynamic and endwall temperature measurements of a proposed test model. The experimental investigations were conducted in subsonic wind tunnel located in the Aerospace Laboratory at Iwate University. Figure 17 shows the test apparatus used in this study, indicating main blower, diffuser, settling chamber, contraction nozzle, transition duct and test duct. The main blower was used to drive the mainstream air into the test duct with maximum flow rate of 320 m^3/min at pressure of 3000 Pa. The diffuser is 1500mm long gradually-expanding passage following the test section with inlet size of 390 x 490mm up to 900 x 900mm at exit in which the flow speed decreases and the pressure rises. The flow kinetic energy coming from the main blower was converted to static pressure inside the settling chamber. The uniform flow structures are required to obtain more compatible results with numerical simulation. The modification of the mainstream flow structures was done by applying two screens and honeycomb inside the settling chamber to calm the flow and minimize the disturbances. The settling chamber's cross section dimension is 900 x 900mm and match up with the dimensions of the contraction nozzle. The contraction nozzle's purpose is to take a large volume of low velocity air and reduce it to a small volume of high velocity air without creating turbulence. The length the nozzle is 1100mm. The size of the large end, nearest the settling chamber was set at 900 x 900mm. The small end of the contraction nozzle was set at 580 x 178mm which fixed the size of transition nozzle (300mm length). The flow coming from the transition nozzle will be driven into the test section. The shape of the contraction nozzle was a cubic curve, and the curve was applied on those four surfaces. The secondary blower works to supply the secondary air into the mainstream. However, the secondary air will firstly go through the plenum chamber which is attached to the bottom side of the test duct parallel to slot position before it will be injected into the mainstream. To have the uniform flow to be injected, the screen is positioned inside the plenum chamber. A laminar flow meter was used to measure the mass flow rate of the secondary air.

Figure 18 illustrates the birdview of the test section. It consists of four parts: the inlet section, the blade section, secondary air inlet section for upstream leakage, and the outlet section. All components of the test section except the test cascade were made of acrylic-resin plate in order to keep visibility from outside. The inlet section is delimited by the hub endwall, the tip endwall and the two side walls. Beneath the both side endwall an adjustable boundary layer bleed is employed to secure a parallel approaching flow field with a new boundary layer. An L-type miniature pitot tube was placed upstream of the model leading edge for inlet flow velocity measurement. The inlet velocity was about 16-18 m/s to meet desired inlet Reynolds Number. The blade section is a linear cascade consisted of 6 blades which had four identical HP turbine nozzle blades, and two dummy blades at outer side. The profile of the blade is shown in Table 1. The top view of test section and geometry of the leakage slot are shown in Figure 19. The upstream leakage slot was located at $-0.63C_{ax}$ upstream of the blade leading edge. The slot extended about 4 pitches and the width was $0.064C_{ax}$ (4mm). In consideration for the baseline condition, normal injection into the main flow was applied in this study. Second slot; segment gaps were located between the blade segments with opening about 1.75 mm. This slot extended from $x/C_{ax} = -0.63$ until $x/C_{ax} = 1.25$ with a curve slot near the blade throat. Behind the cascade, exit velocities of 50-60 m/s were obtained (Mach number approximately 0.15). The air is expanded to atmospheric pressure. Both of tailboard angle at cascade downstream were adjusted with gradually expanding passage in order to obtain the uniformity of inlet flow structures. The coordinate system is also presented in Figure 19 where X-axis is parallel to axial flow direction, Y-axis is parallel to pitchwise direction and Z-axis is parallel to spanwise direction. Figure 20 indicates the 3D CAD of the plenum chamber used in present study.

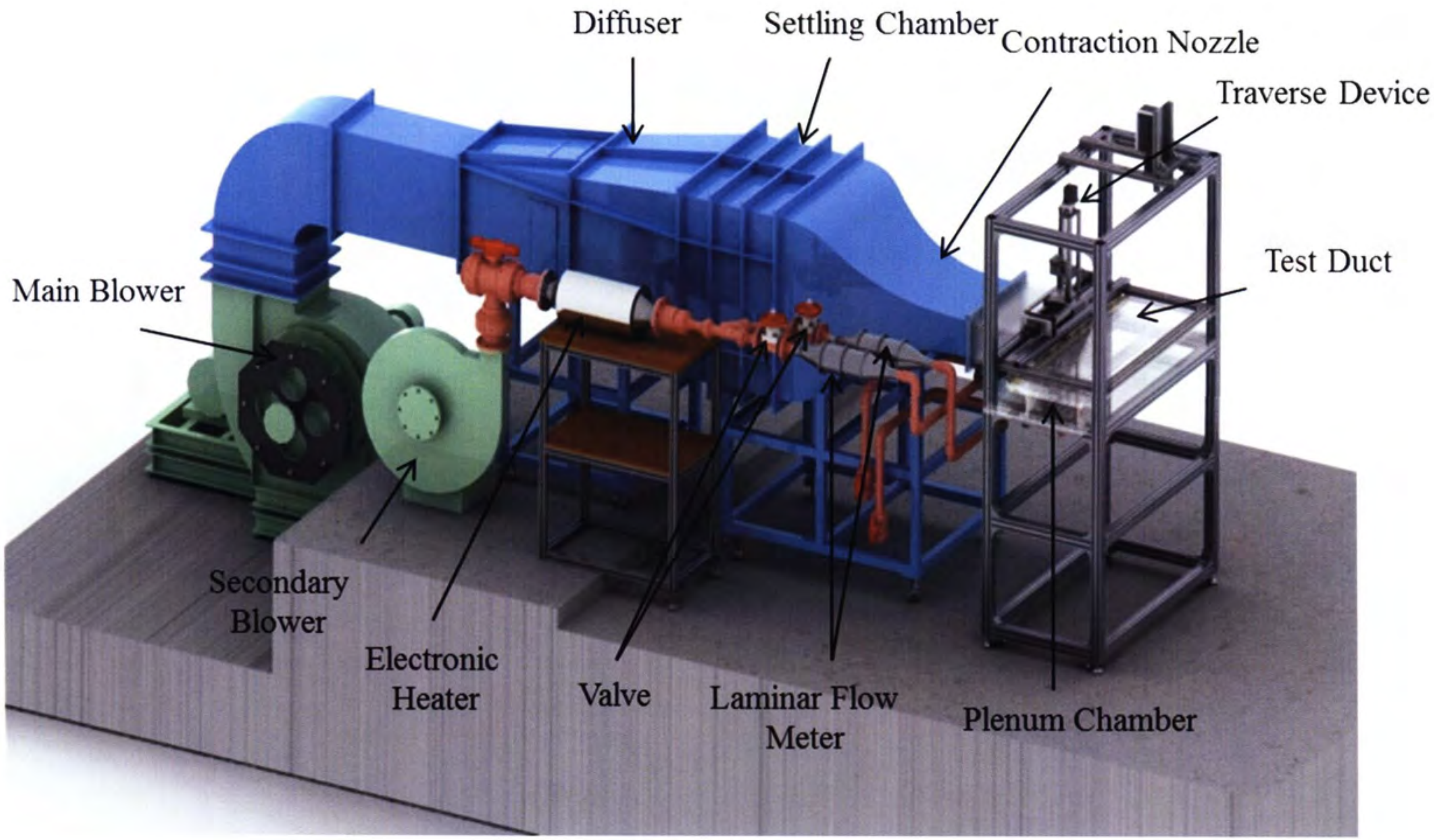

Figure 17 Schematic diagram of experimental facilities

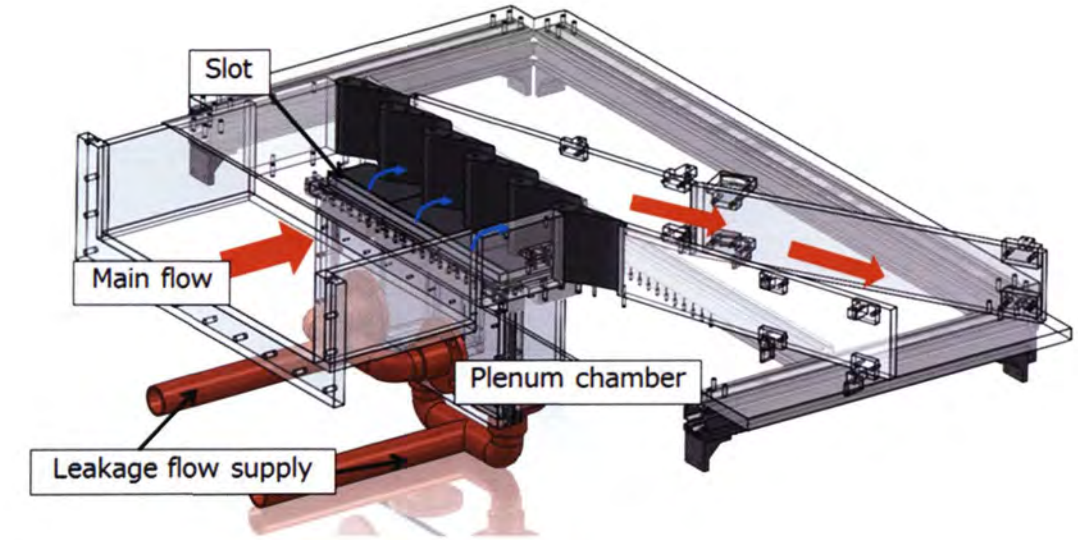

Figure 18 Birdview of the test duct

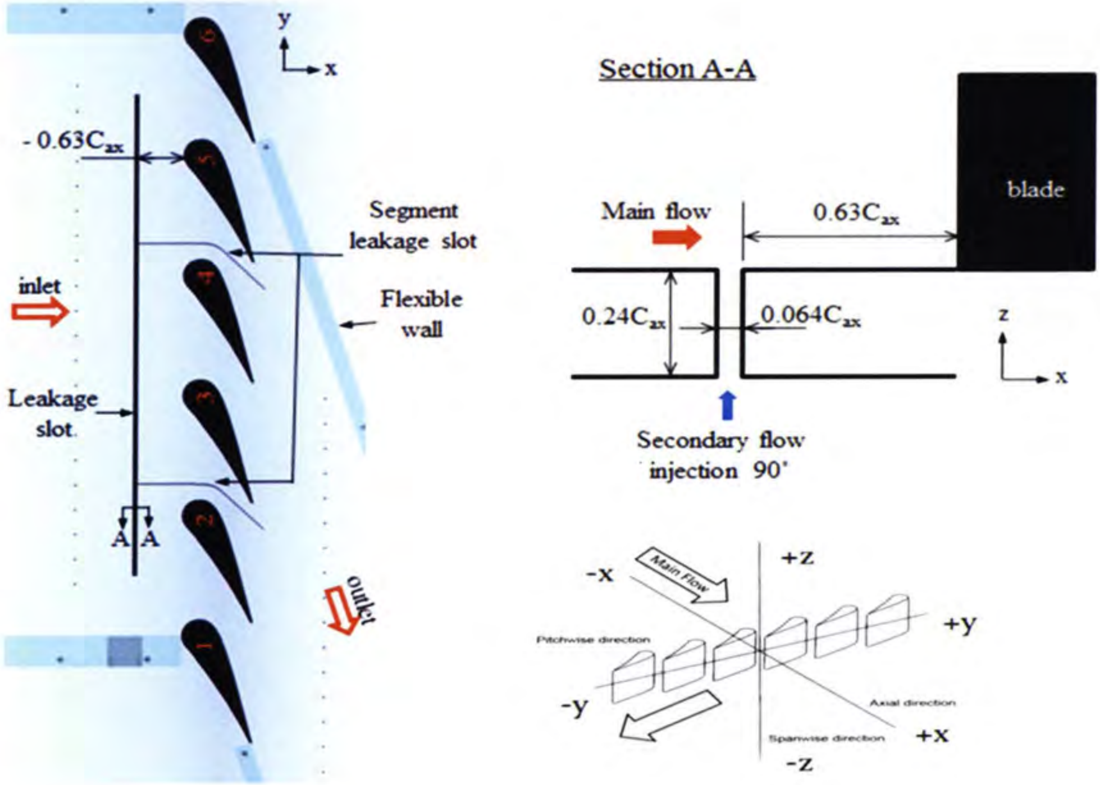

Figure 19 Overview of test duct

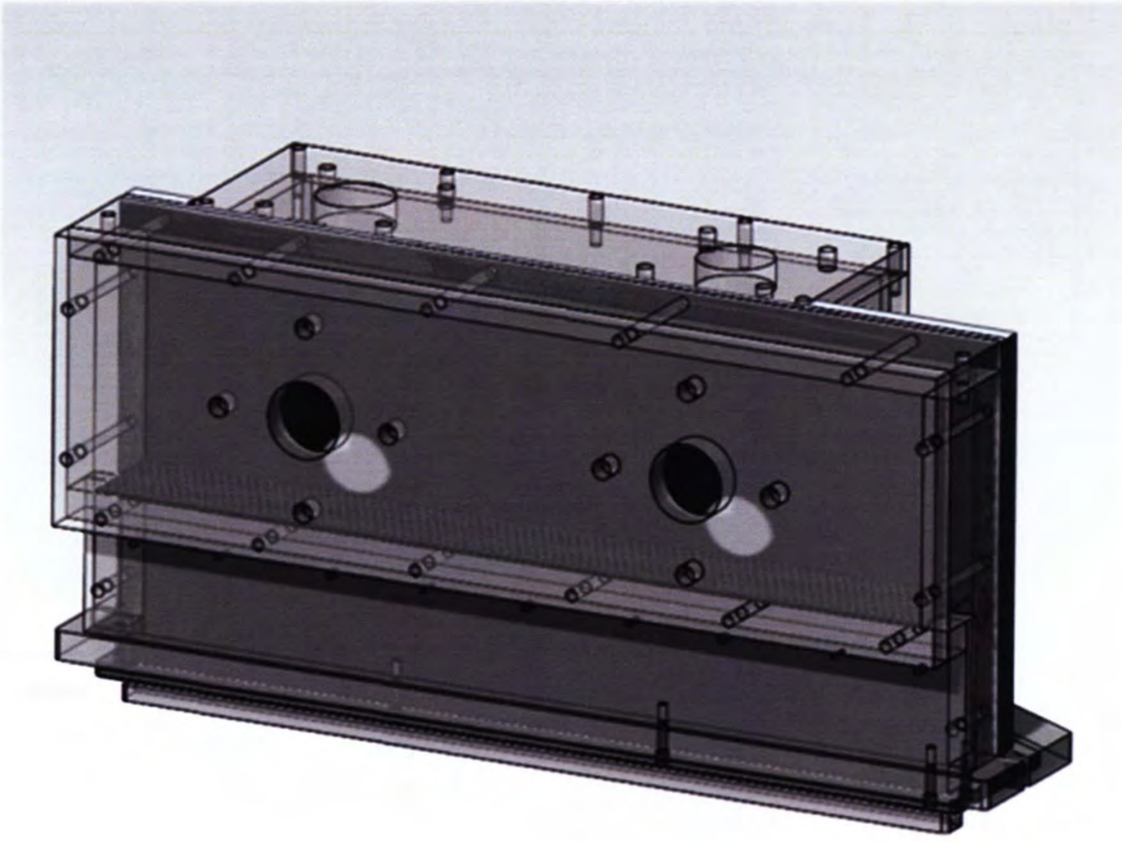

Figure 20 Plenum Chamber

2.3 Specification of measurement devices and laboratory equipment

The details of devices used are explained in the Table 2 below.

Table 2 Details of device and equipment

Device/equipment	Specifications
Main blower 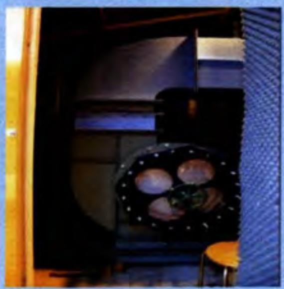	Manufacturer : MITSUYA FAN Model type : TVC No.4(Centrifugal type) Output : 18.5 kW Discharge flow rate : 320 m^3/min Discharge pressure : 200mmAq (20˚C) Rated speed : 2310rpm Outlet cross-sectional area : 400×500mm Rotation direction : clock-wise direction
Secondary blower 	Manufacturer : Okamoto Blower Model type : KO28-4 Output : 3.7 kW Discharge flow rate : 12 m^3/min Discharge pressure : 6.86 kPa (at 20℃) Speed : 2200 rpm
Laminar flow meter 	Manufacturer : Tsukasa Ken Measurement Model LFE-50B Rated flow 50 (l / s) F · S accurate to within ± 1.0% 0 ~ 80 (℃) use temperature range
Electric Heater 	Manufacturer: Kashima Co., Ltd. Model SR-9N Capacity: 13.5 (kW) Maximum wind speed 13.0 m^3/min

Pneumatic valve 	Manufacturer : CKD Co. Ltd Model type: AG31-01-2
Data logger (Aerodynamic measurement) 	Manufacturer : Nippon Electric Model : 7V14 Interface: RS232C
Data logger (Thermal measurement) 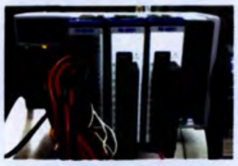	National Instrument Model: DAQ-9174
Pressure transducer 	Manufacturer : Setra System Co. Ltd Model : 265 Measurement range: 0~5000 Pa accuracy±0.25%(±12.5 Pa)
Thermocouple 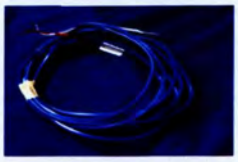	Manufacturer : Suzuki Seiki K type
Black paint	Manufacturer : Nippon Capsule Product Type: SSM-8
Digital Thermometer 	Manufacturer: AND Model: AD-5624 (Auto-detect max/min temperature)

Thermo-chromic liquid crystal (TLC) 	Manufacturer : Nippon Capsule Product Type: RW24~26
Miniature pitot tube 	Manufacturer : Tsukubari Kaseiki L-type Outer diameter: 4mm Length: 60mm
5-holes pitot tube 	Manufacturer: Suzuki Seiki Arrow type Head diameter: 2.1mm Outer diamater: 9.5mm Length: 648mm
Personal computer 	OS: Window 7, 64 bit Processor: i7-2600, 3.4GHz HD drive: 500GB Memory: 8GB
Digital video camera 	Manufacturer: Sony Model type: CCD camera HDR-FX1000
Traverse device 	2-dimensional axis Pitchwise direction: max 600mm Spanwise direction: max 300mm precision: 0.1mm Motion Controller: PCI-7210C Motor Unit: UMK268B

Voltage adjustor 	Volt slider Manufacturer : YAMABISHI Model: S3P-240-30
Lamp 	Manufacturer : Toshiba Co. Ltd Type : Halogen lamp JDR110V60W/K5F

2.4 Test condition

All measurements have been conducted at fixed inlet Reynolds number based on inlet midspan velocity and the actual blade chord length, Re_{in}=125000. The definition of the Reynolds is given by Eq. (2)

$$\mathrm{Re}_{\infty} = \frac{\rho_{\infty} U_{\infty} C}{\mu} \tag{2}$$

where;

ρ_{∞}, mainstream air density [kg.m^{-3}];

U_{∞}, mainstream inlet velocity [m.s^{-1}];

C, actual blade chord [m]; and,

μ , mainstream air viscosity [kg.m^{-1}.s^{-1}]

The Reynolds number involved in the real gas turbine is far exceeding the considered value in the present study. Due to the limitations of the experimental setup, only such Reynolds number can be considered in the present study. In order to investigate the effect of the different amount of the leakage into the mainstream, which represented by mass flow ratio, MFR given by Eq. 3,

$$MFR = \frac{\dot{m}_2}{\dot{m}_{\infty}} \times 100 \tag{3}$$

Here,

$$\dot{m}_2 = \rho_2 Q_2 = \rho_2 A_2 U_2 \tag{3.1}$$

$$\dot{m}_{\infty} = \rho_{\infty} Q_{\infty} = \rho_{\infty} A_{\infty} U_{\infty} \tag{3.2}$$

Thus,

$$\dot{m}_2 = (1.2839 \times 10^{-4}) MFR \rho_{\infty} U_{\infty} n \tag{4}$$

where;

$\dot{m}_2$, secondary air mass flow rate, [kg/s];

$\dot{m}_\infty$, mainstream air mass flow rate, [kg/s];

Q_∞, mainstream air volume flow rate, [m^3/s];

Q_2, secondary air volume flow rate, [m^3/s];

U_∞, mainstream inlet velocity, [$m.s^{-1}$];

ρ_2, secondary air density, [$kg.m^{-3}$];

ρ_∞, mainstream air density, [$kg.m^{-3}$];

A, cross-sectional area for 1 pitch at inlet, (=0.012839 [m^2]); and

n, pitch number, [$kg.m^{-3}$].

In present study, in order to investigate the effect of the leakage and its potential to become as one of the cooling configuration, four mass flow ratio have been considered at MFR = 0.75%, 1.25%, 1.75% and 2.25%. These MFR have been selected by consideration of low, intermediate, higher and extremely higher leakage injection, respectively. The consideration of higher mass flow ratio was made due to the promising thermal results that have presented by the previous researcher. Furthermore, the potential of the leakage flow ejection as a cooling can be investigated and discussed.

2.5 Aerodynamics investigation

As shown in Figure 21, the measurement system is constituted by pneumatic 5-holes Pitot tube, traverse device, pressure transducer and data logger which are connected to the computer for data collection. The RS232 cable was used as interface transferring the measurement data from logger into the computer. Two measurement planes have been traversed in present study;

I. Inlet flow verification at plane $-0.85C_{ax}$
II. Outlet flow investigation at plane $1.25C_{ax}$

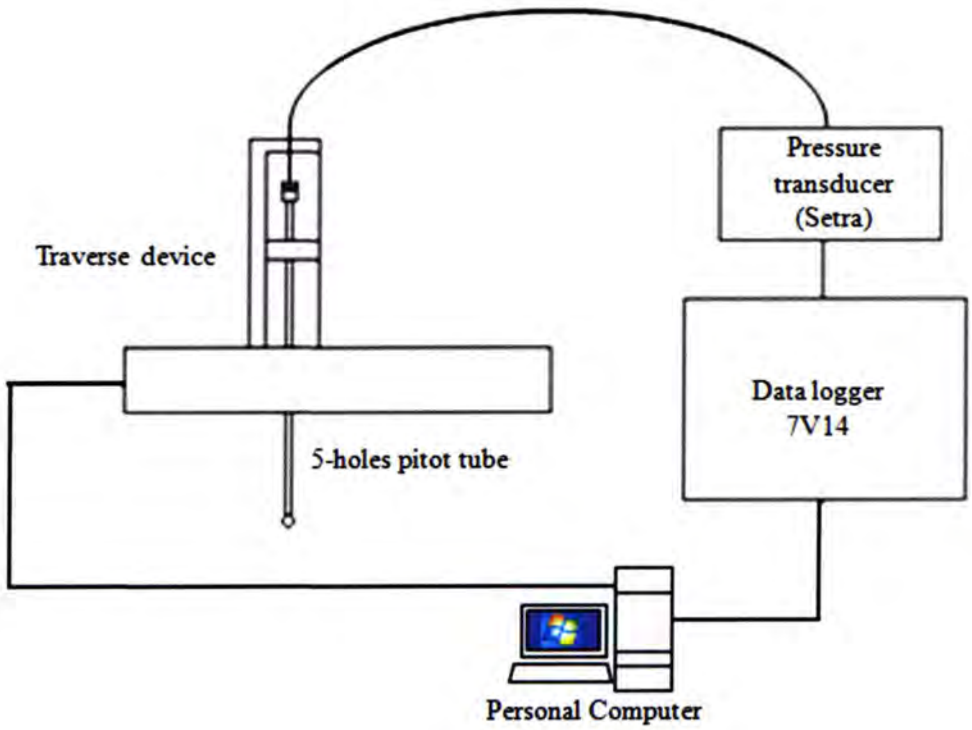

Figure 21 Data acquisition system

2.5.1 Inlet flow verification at plane $-0.85C_{ax}$

The locations of traverse planes are shown in Figure 22. The inlet flow field measurement has been conducted at the first in order to ensure uniform main flow structures entering the cascade. Pneumatic 5-holes Pitot tube measurements have been performed at $-0.85C_{ax}$ upstream of blade leading edge, indicated by red dot-line in Figure 22. To conduct the measurement with fewer disturbances, the probe has been traversed along the region of blade 3 till blade 5 where they are located almost at the middle of the cascade. 5-holes pitot tube was fixed at 0° to ensure its properly measure the incoming flow within calibration range of -36° to 36°. Since the head diameter of probe was 2.1 mm, thus the nearest distance of measurement from the endwall could be positioned approximately 2 mm which means about 2% of the span direction. Figure 23 illustrates the measurement grid for 2.4 pitch to investigate the flow uniformity and periodicity. As shown in Figure 23, the probe was traversed for 25 in pitchwise direction and 18 in spanwise direction to provide 450 measurement points. The main flows Reynolds number of 1.25×10^5 was fixed throughout all test cases. The inlet Re was determined by measuring inlet flow velocity using miniature Pitot tube located at -1.85Cax.

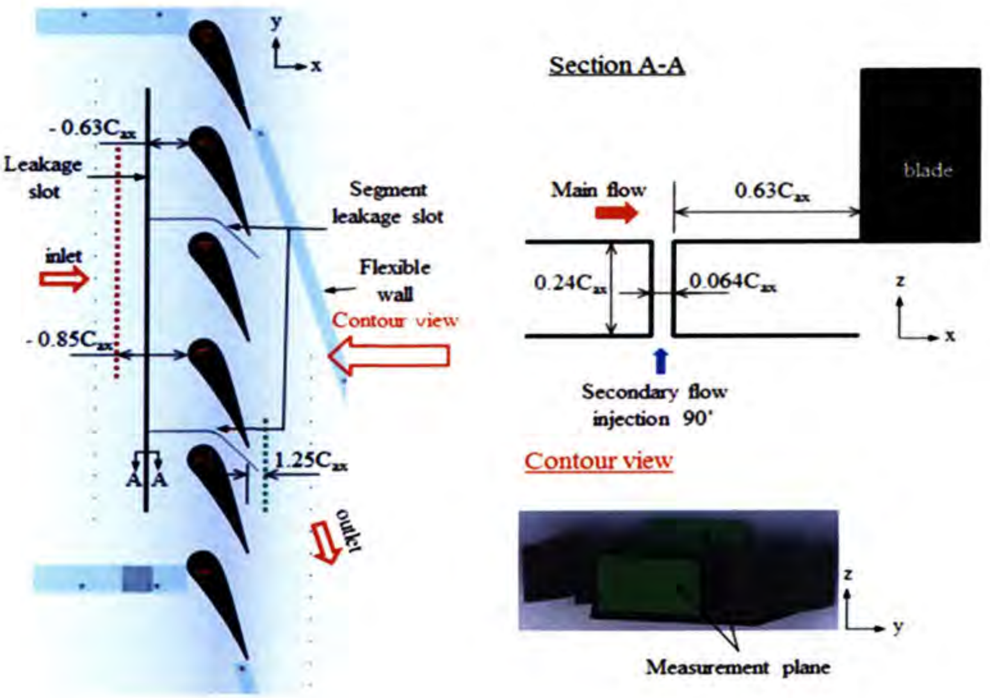

Figure 22 Aerodynamics measurement plane

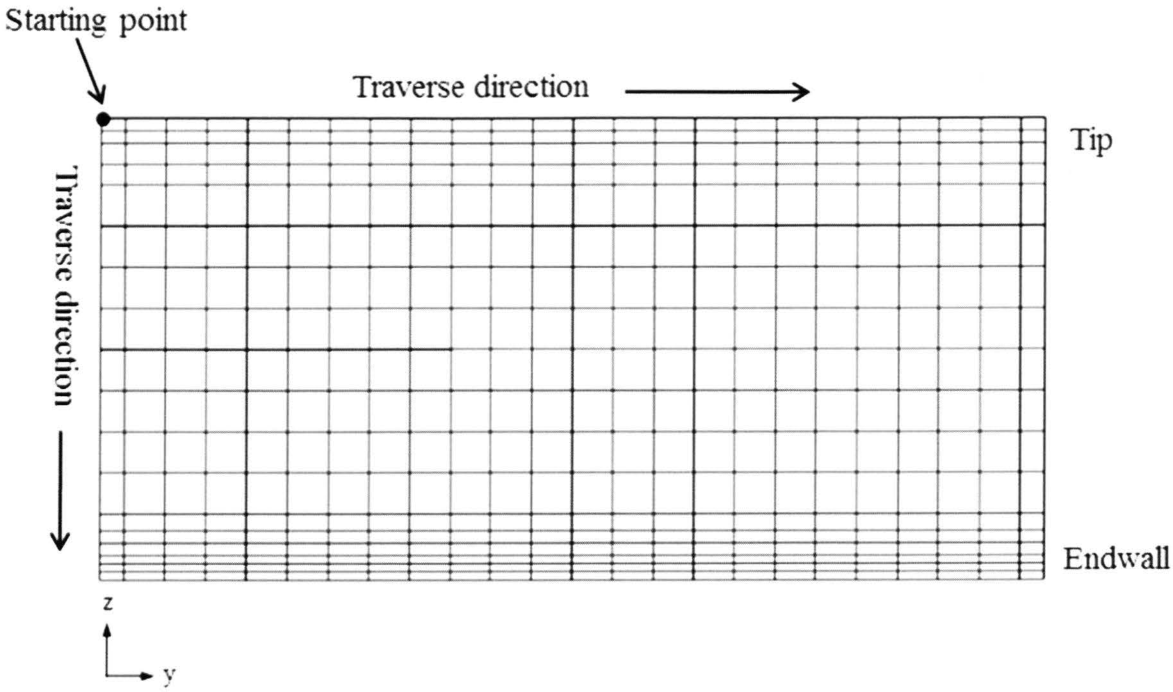

Figure 23 Measurement grid at inlet plane ($-0.85C_{ax}$)

2.5.2 Outlet flow investigation at plane $1.25C_{ax}$

The measurement was conducted at $1.25C_{ax}$ downstream of the blade LE which indicated by the green dot-line in Figure 22. In order to study the effect of the upstream leakage ejection included their injection amount, four MFR of 0.75%, 1.25%, 1.75% and 2.25% have been used in consideration on low, intermediate, high and extremely higher injection, respectively. The high and extremely high amount ejection were done in order to see the potential of the upstream leakage to work as cooling purpose thus their effect on the aerodynamics side also need to be revealed. However, the measurement without any leakage or secondary air injection was firstly carried out to observe a flow field of baseline condition at the same plane. This enables the direct comparison between baseline condition and leakage injection cases. For baseline condition case, a measurement was conducted without supplying a secondary air, therefore a flat endwall platform without slot was placed at the first to avoid a flow that coming from the high pressure mainstream moving into the slot which might be considered affecting the ongoing flow structures. The measurements at outlet plane were done by two phases where the first phase was to investigate a periodicity of flow at cascade outlet. 1600 points of measurement were started from the blade tip which traversing for 2 pitches and ended close to the endwall. On the other hand, second phase measurement were surveyed with a finer grid for only 1 pitch and a measurement started at midspan. The finest grid was 1 mm and coarsest was 10 mm with a 1148 points of measurement. Furthermore, the finer grid was adopted near the region where the blade wakes are expected. As shown in Figure 24, this plane has been surveyed by means of 28 traverses in the pitchwise direction, each of them constituted by 41 measuring points spaced with variable steps which have a finer grid near the endwall. For each measuring point 10 samples have been collected and the pressures were calculated as time-averaged components. However, results based on finer grid measurements only will be presented. As done for inlet measurement, the nearest distance of measurement from the endwall could be positioned approximately 2 mm which means the measurement range is approximately 2% to 50% of the span direction. Figure 22 indicates the viewpoint definition of all contours presented in this paper. Different case with inlet measurement, the probe was oriented to -72.3° of yaw angle for outlet flow measurement due to the flow turning at blade downstream. This angle was obtained based on the prediction using CFD simulation. The probe will not properly measure the total pressure at this plane by normal probe orientation as the flow deviation exceeding the maximum calibration range. Table 3 shows the flow conditions for each measurement.

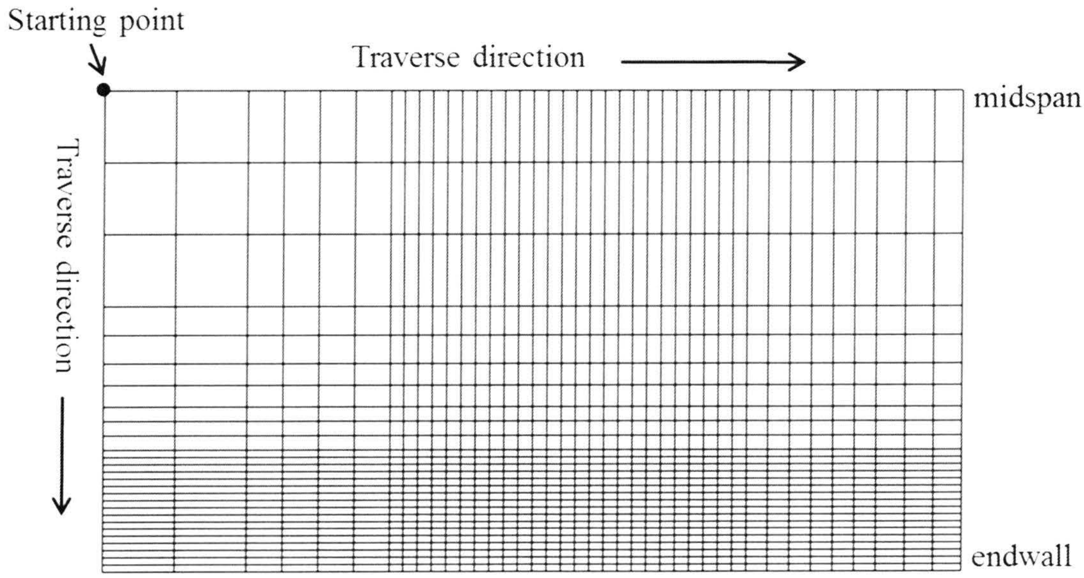

Figure 24 Measurement grid at outlet plane ($1.25C_{ax}$)

Table 3 Test flow condition

Parameter	MFR (%)				
	baseline	0.75	1.25	1.75	2.25
Re_∞	1.25×10^5				
$P_{t\infty}$[Pa]	1584	1749	1752	1662	1700
T_∞[°C]	33	36	37	34	40
T_2 [°C]		47	48	48	47
U_∞[m/s]	17.1	17.7	17.6	17.4	17.3

2.5.3 Data reduction

The flow measurement by conducting 5-holes pitot tubes enables the investigation of 3-dimensional flow structures at cascade downstream. Figure 25 illustrates the definition of the 5-holes Pitot tube to describe the yaw and pitch angle. The flow yaw angle, α and pitch angle, σ can be determined by applying 3 components of velocities measured by the 5-holes Pitot tube as shown in Eq. 5 and Eq. 6

Yaw angle : $$\alpha = \frac{180}{\pi} \times \tan^{-1}\left(\frac{v}{u}\right) \tag{5}$$

Pitch angle : $$\sigma = \frac{180}{\pi} \times \tan^{-1}\left(\frac{w}{u}\right) \tag{6}$$

where,

u, pitchwise direction velocity component [m/s]

v, spanwise direction velocity component [m/s]

w, axial direction velocity component [m/s]

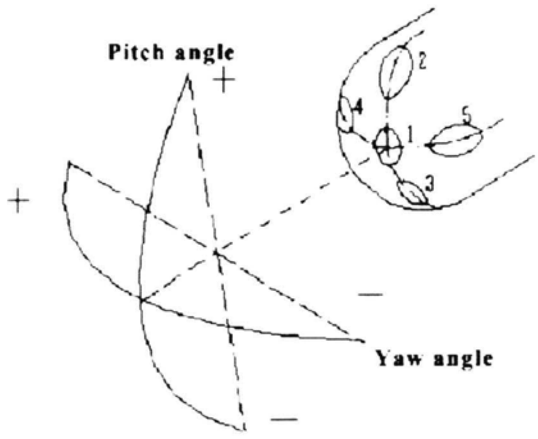

Figure 25 5-holes Pitot tube definition

The local total pressure obtained from the measurement along the plane also has been use to describe the aerodynamics performance of the test cascade by determine the total pressure loss coefficient, C_{pt} as presented in Eq. 7. Total pressure loss also can be defined as Eq. 8.

$$C_{pt,1} = \frac{P_{t,\infty} - P_{t,out}}{\frac{1}{2}\rho U_{\infty}^{2}} \tag{7}$$

$$C_{pt,2} = \frac{P_{t,ref} - P_{t,out}}{\frac{1}{2}\rho U_{\infty}^{2}} \tag{8}$$

Here,

$$P_{t,ref} = \frac{\dot{m}_2}{\dot{m}_2 + \dot{m}_{\infty}} P_{t,2} + \frac{\dot{m}_{\infty}}{\dot{m}_2 + \dot{m}_{\infty}} P_{t,\infty} \tag{8.1}$$

Note that the effect of the secondary air from the plenum chamber is neglected in Eq. 7 while it is taken into account in Eq. 8 by considering the total pressure inside the plenum chamber.

However, Eq. 7 has been used in present study due to the difficulty to measure the total pressure inside the plenum chamber within a very limited space. However, prediction presented that the different between these two equations was less than 1% and could be neglected. The vorticity, ζ as a rate of flow rotation in 2-dimensional plane (axis y and z) has been determined in order to reveal the flow behavior at those planes as defined by Eq. 9.

$$\zeta = \frac{\partial w}{\partial y} - \frac{\partial v}{\partial z} \tag{9}$$

Both C_{pt} and ζ contours presented by the experimental will be compared with the numerical simulation for validation which enables the more accurate prediction of flow structures in the blade passage. Finally, secondary kinetic energy coefficient, C_{SKE} as been shown in Eq. 10 was also determined for a details discussion on the flow behavior.

$$C_{SKE} = \frac{SKE}{\frac{1}{2}\rho U^2_{out,mid}} \tag{10}$$

Here,

$$SKE = \frac{1}{2}(V^2_{\sec} + W^2_{\sec}) \tag{10.1}$$

$$V^2_{\sec} = \left(u\sin(\alpha_{out,mid}) - v\cos(\alpha_{out,mid})\right)^2 \tag{10.2}$$

$$W^2_{\sec} = w^2 \tag{10.3}$$

In the mean endwall flow field, the rotational energy at the endwall is typically quantified by the magnitude of SKE. Using averaged exit flow angle at midspan as the primary reference direction, SKE is defined as half the sum of squared mean velocity component normal to the primary reference. SKE then be normalized with the dynamics pressure to determine the C_{SKE}.

2.6 Thermal investigation

2.6.1 *Thermo-chromic* liquid crystal (TLC)

The development of *thermo-chromic* liquid crystal (TLC) based thermography over the past 30 years has provided thermal engineers with a relatively in expensive technique for visualizing and measuring surface temperature. TLC is temperature indicators that modify incident white light and display color whose wavelength is proportional to temperature. *Thermo* is refers to temperature while *chromic* refers to color. They can be painted on a surface or suspended in the fluid and used to make visible the distribution of temperature. The displayed color is red at the low temperature margin and blue at the high end. The color changes smoothly from red to blue as a function of temperature. The chemical makeup of TLC material fixes its color-temperature response at the time of manufacture. A simple, two color/temperature design at or typically describes this response and can be useful in qualitative applications and for properly selecting a TLC formulation for a particular application. Engineers and scientist have successfully used TLC thermography to investigate various thermal phenomena in wide variety of applications. These applications include gas turbine heat transfer. In present study, RW24-26 of TLC has been used to describe that the color changes occurs at temperature range of 24°C to 26°C. In order to observe the color change due to the temperature different, the mainstream temperature must be below 24°C while the secondary air temperature should be higher than this range.

2.6.2 Temperature measurement by TLC

Thermal investigation was conducted by the same wind tunnel used for the aerodynamics investigation. However, some modifications on the test section have been done in order to obtain high accuracy of the measurement. As illustrates in Figure 26, the endwall side of the test section included the blades were black painted in order to reduce the light reflection towards camera during the measurement. To have a clear visualization on the endwall side from the top, the tip side wall of the cascade has been replaced with a flat and clean acrylic plate. Figure 26 also indicates the region of the temperature measurement which was focuses on the endwall region between blade 3 and blade 4. Figure 27 shows two configurations of TLC coating for the measurement. As shown in the figure 27, an acrylic plate was firstly painted by a black color then the TLC layer was coated for configuration A while the TLC layer was firstly coated then follows by the black panting. This configuration is actually depending on the camera position. In present study, configuration A was adopted since the temperature changes on the endwall was captured from the tip side of test section. This means the camera will be positioned from the top side of test section. Thus, the TLC layer must be coated on black painted acrylic plate in order to keep the visibility during the measurement. Figure 28 illustrates how the measurement was carried out, including camera and light positions. The color change of the TLC was recorded with a digital video camera, and recorded image data were captured by PC frame by frame, then converted from RGB images into HSL (Hue/Saturation/Lightness) images using a software (GraphicsConverter)(Hachiya, 2004). The accuracy of the measurement techniques was based on Funazaki [30].

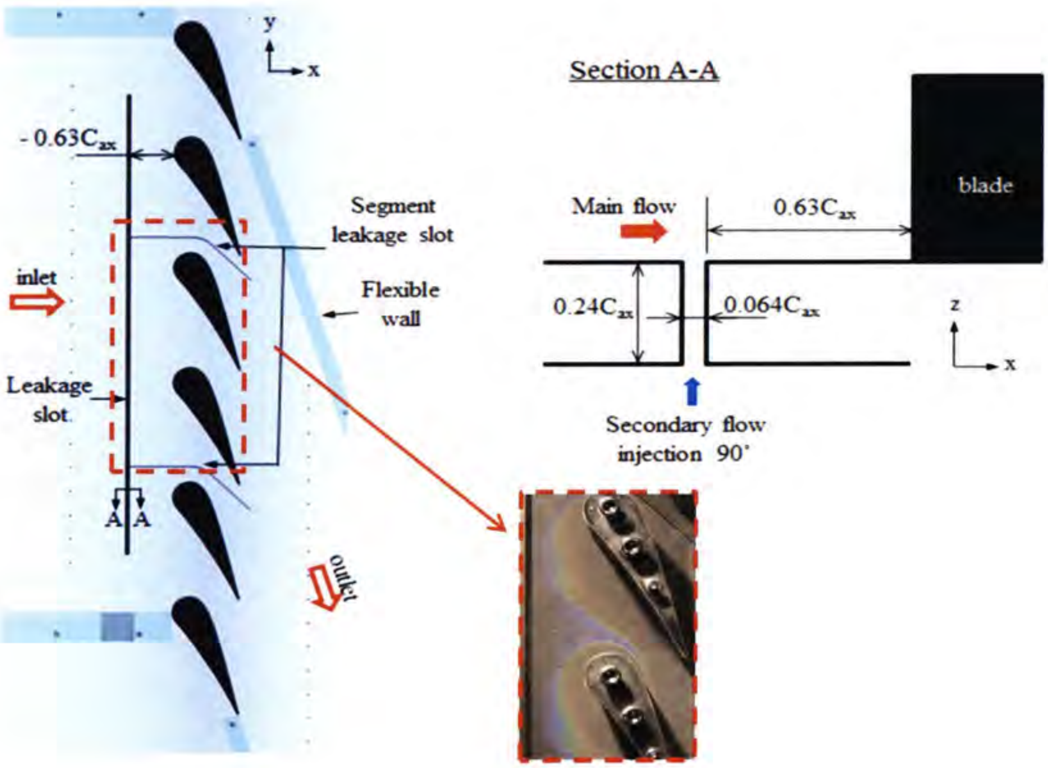

Figure 26 Temperature measurement region

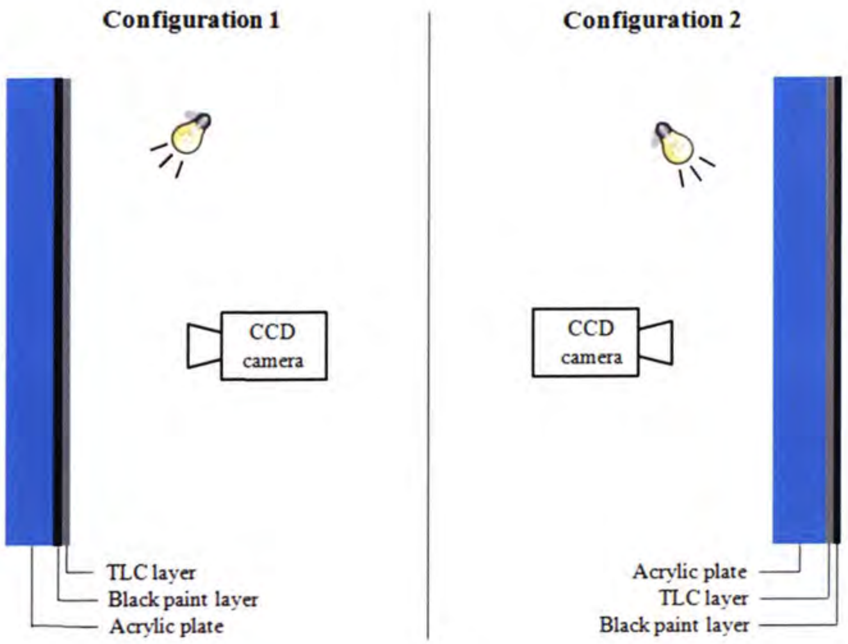

Figure 27 TLC coating configurations

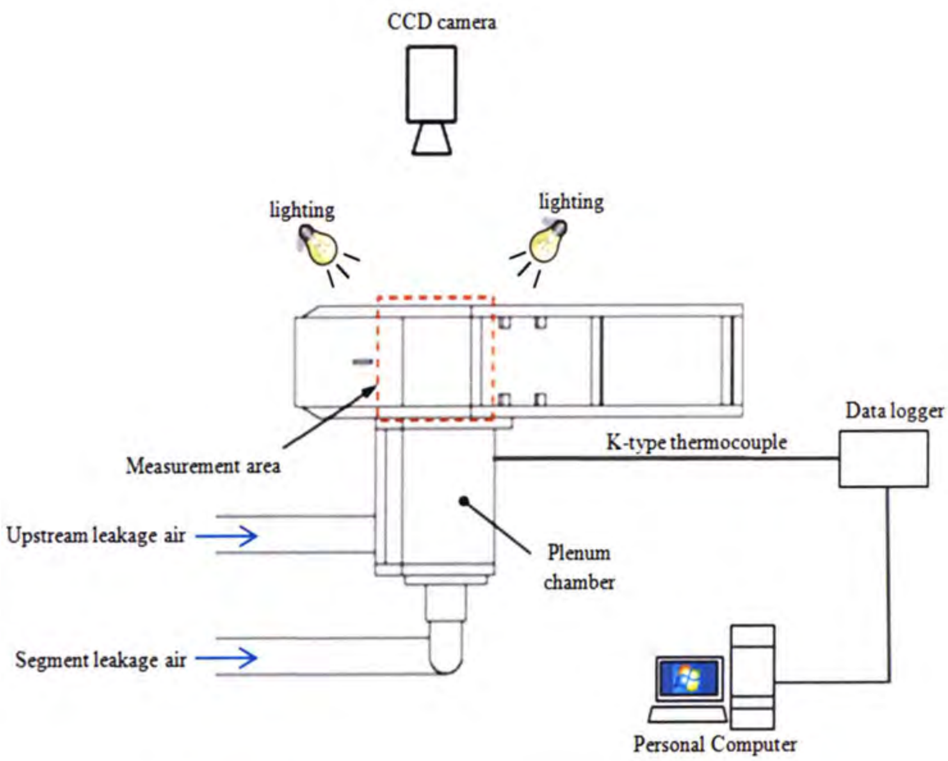

Figure 28 Temperature measurement system

2.6.3 TLC calibration

The relationship between the temperature and measured Hue of the reflected light defines the calibration curve for the TLC. Figure 29 shows the calibration device that was used where the stainless sheet was attached on the acrylic plate with two cooper electrodes were fixed at the end. The TLC was coated onto the stainless sheet surface by configuration A to have a similar condition with the measurement. The voltage was applied through the electrodes and the color changes due the temperature different on the calibration plate were captured by the same camera used in the measurement. At the same time, the temperature distribution was measured by sixteen K-type thermocouples which were attached on the bottom side of the plate. In order to reduce the uncertainties, the calibration test was conducted in place in the wind tunnel with the same lighting level and viewing angle used during the data acquisition phase of the measurement as shown in Figure 30. The RGB images captured during the calibration test which was converted to HSL images is shown in Figure 31. Then, Eq. 11 was used to obtain the relationship between temperature and Hue

$$\frac{T_s - T_L}{P_s - P_L} \times (P - P_L) + T_L \tag{11}$$

where,

P, Hue value at specified pixel position;

P_S, Pixel position of the low-temperature side thermocouple;

P_L, Pixel position of the high-temperature side thermocouple;

T_S, low side temperature measured at P_S; and

T_L, high side temperature measured at P_L.

Finally, the curve can be plotted as shown in Figure 32. Based on the Figure 32, the Hue range of 30~170 illustrating the most accurate characteristic has been selected for the data post-processing purpose.

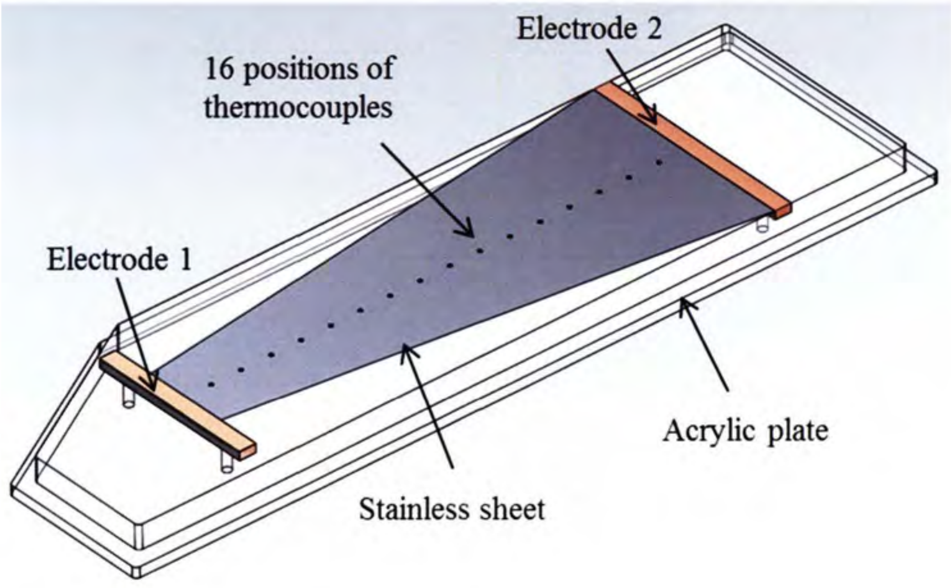

(a) Schematic view TLC calibration plate

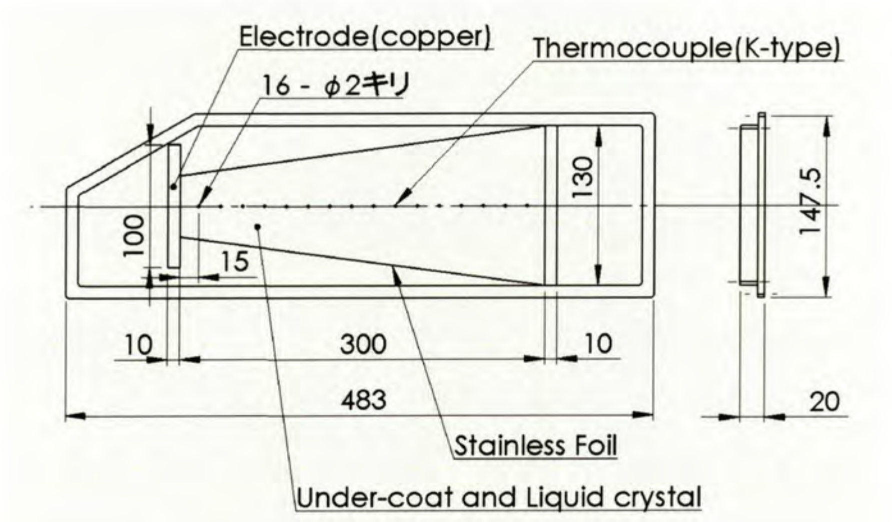

(b) TLC calibration plate with dimension

Figure 29 TLC calibration plate

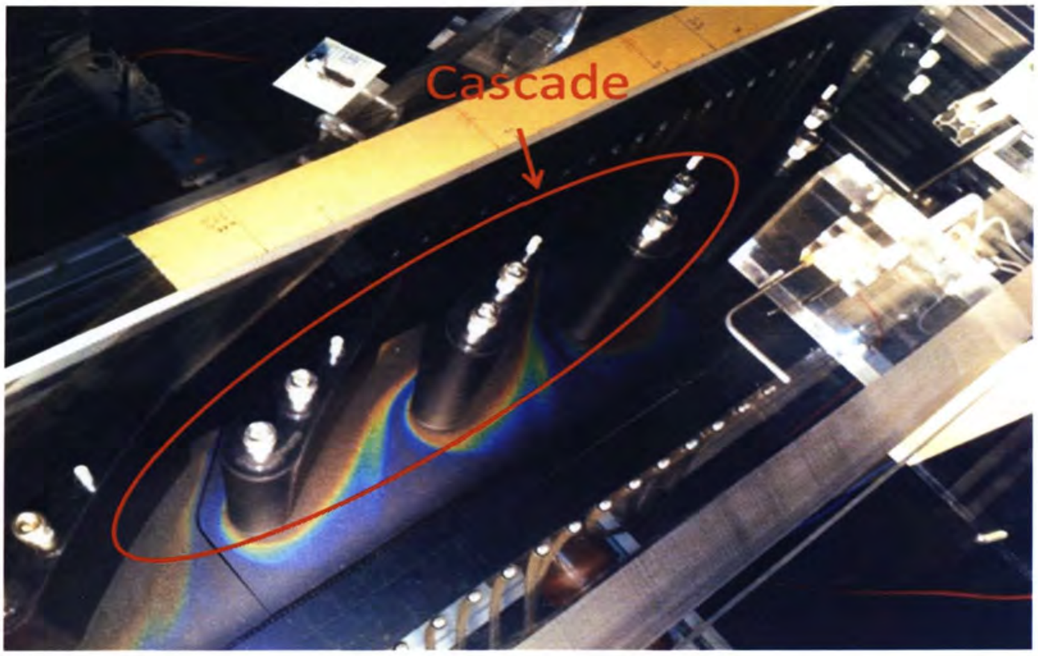

(a) Actual measurement

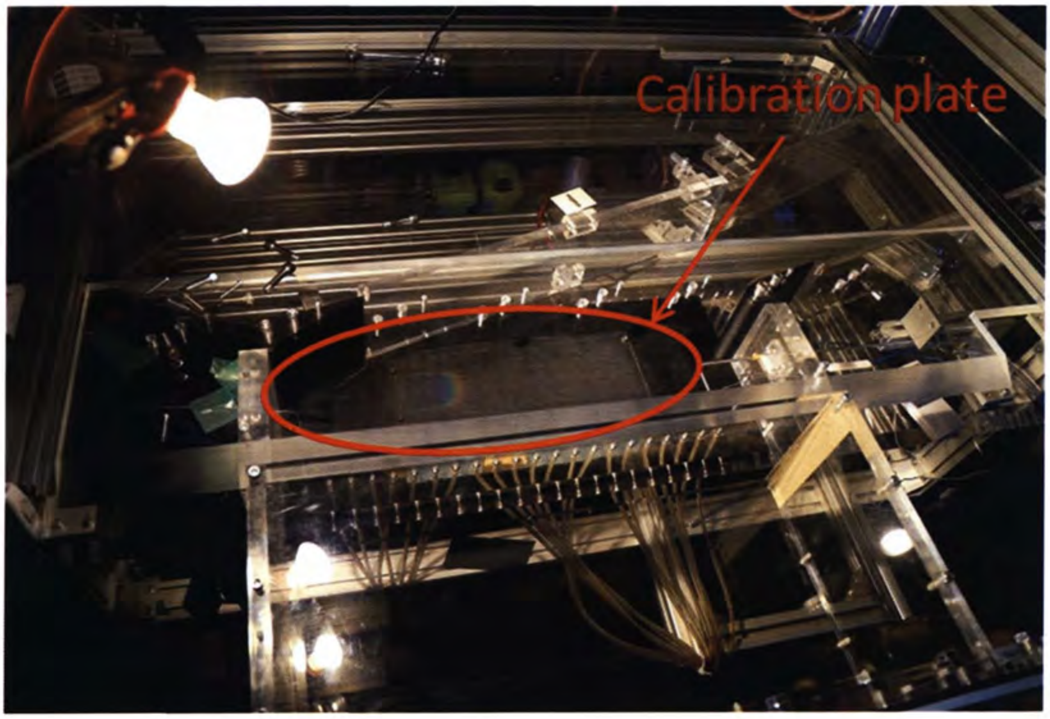

(b) Calibration test

Figure 30 Position of calibration plate during test

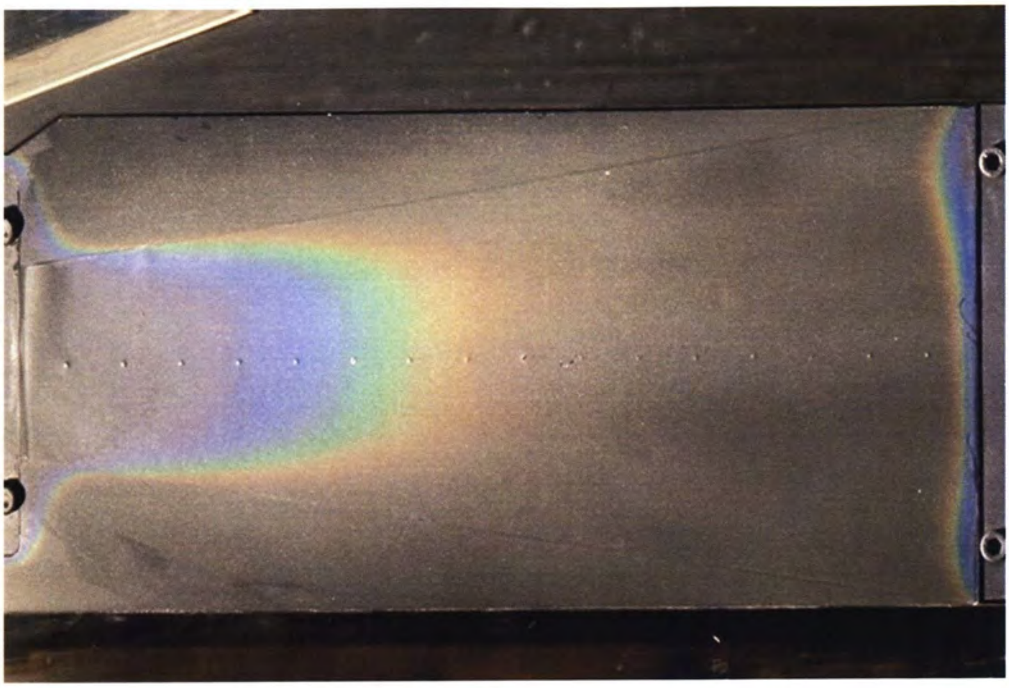

(a) RGB image

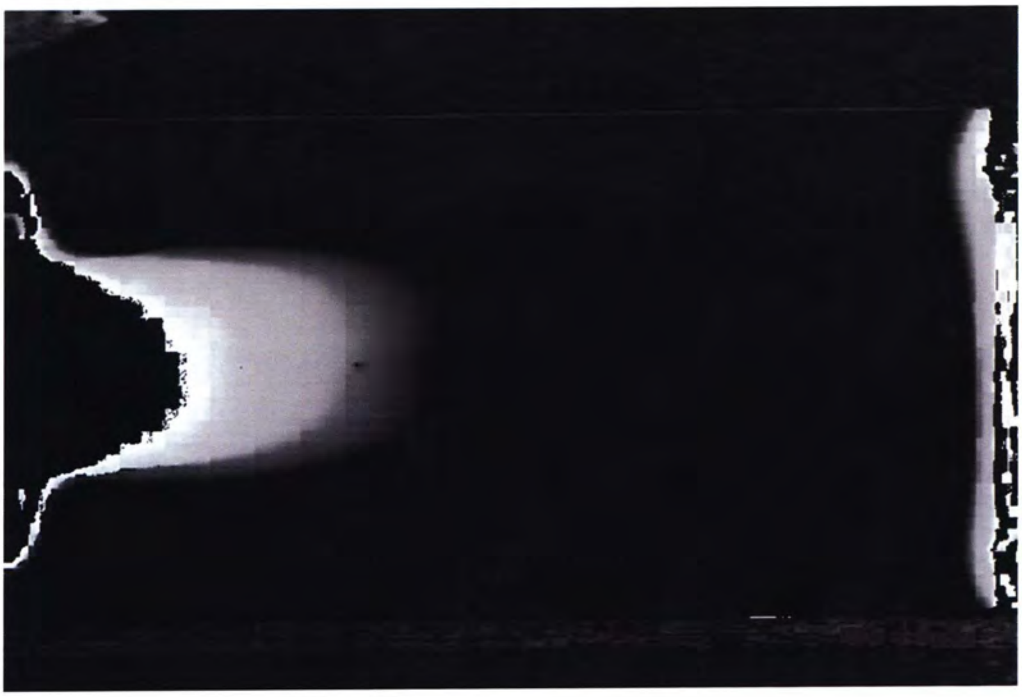

(b) Hue image

Figure 31 RGB image (a) converted to HUE image (b)

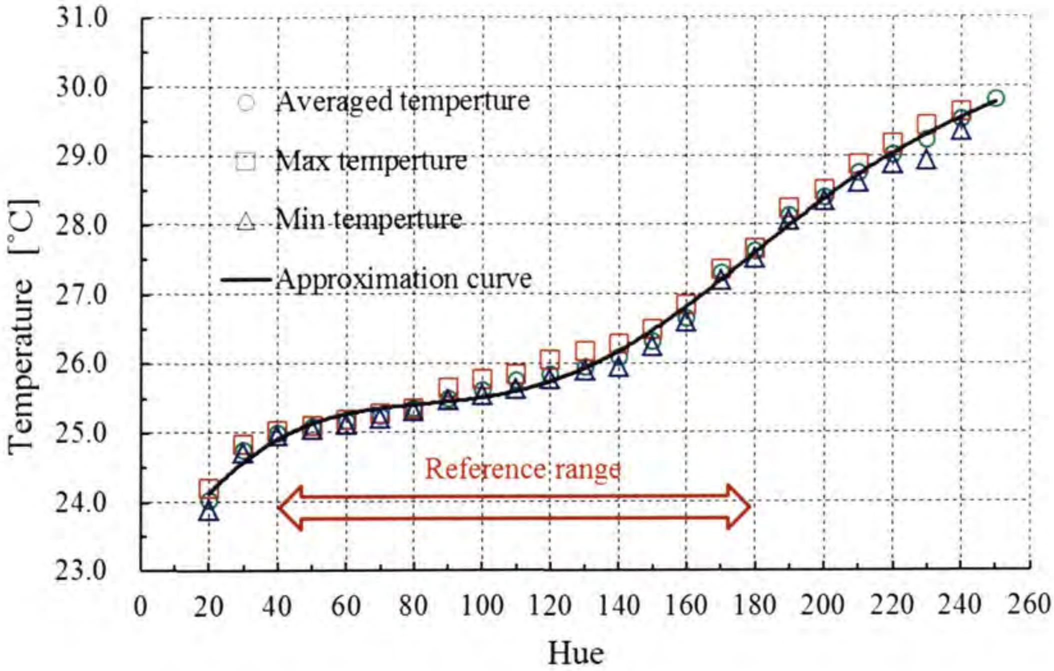

Figure 32 TLC calibration curve

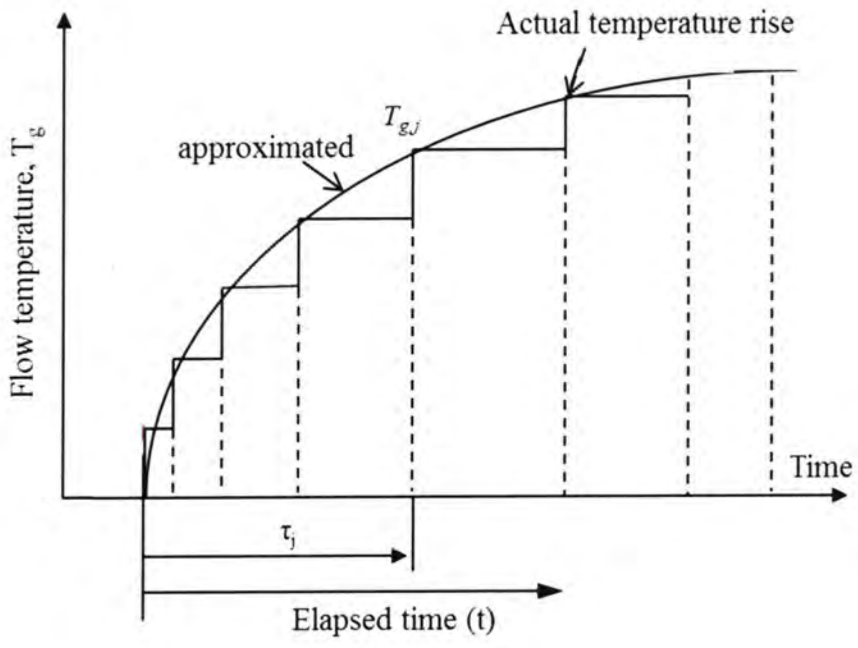

Figure 33 Temperature rise curve by step series of temperature gradual

2.6.4 Transient method

This study employed a transient method to determine heat transfer coefficient and film effectiveness from the time-varying temperature data of the surface. A brief description on the method is given in the following. Temporal change of the surface temperature on semi-infinite body T_w subjected to step-like temperature change of the flow over the body with constant heat transfer coefficient, h is provided from the solution of one-dimensional heat conduction equation as

$$\frac{T_w - T_i}{T_g - T_i} = 1 - \exp\left(\frac{h^2 t}{\rho c \lambda}\right) erfc\left(\frac{h\sqrt{t}}{\sqrt{\rho c \lambda}}\right). \tag{12}$$

Where,

T_i, initial temperature of the body;

T_g, flow temperature;

ρ, density;

c, specific heat; and

λ, thermal conductivity.

In a real situation, since it is almost impossible to obtain a step-like temperature rise of the flow, as shown in Figure 33, Duhamel's theory can be applied to cope with a gradual temperature rise. In this case the temperature rise is approximated by a series of steps with small temperature increase, which yields the expression for the time-varying wall temperature as

$$T_w(t) - T_i = \sum_{j=1}^{N} U(t - \tau_j)(T_{g.j} - T_{g.j-1}) \tag{13}$$

Here,

$$U(t - \tau_j) = 1 - \exp\left\{\frac{h^2(t - \tau_j)}{\rho c \lambda}\right\} erfc\left\{\frac{h\sqrt{t - \tau_j}}{\sqrt{\rho c \lambda}}\right\} \tag{13.1}$$

When applying the above-mentioned relationship to film cooling situation, the flow temperature T_g in Eq. 13 should be replaced by adiabatic wall temperature, T_{aw}. Since film cooling effectiveness η is defined as,

$$\eta = \frac{T_{aw} - T_\infty}{T_2 - T_\infty} \tag{14}$$

where T_∞ and T_2 are main and secondary flow temperatures. The adiabatic wall temperature can be written by

$$T_{aw} = \eta T_2 + (1-\eta)T_\infty \tag{15}$$

Suppose that the film effectiveness remains constant even when the temperature rise of the secondary flow is approximated by a series of step-like temperature change, the following expression can be used for T_{aw}

$$T_{aw,j} = \eta T_{2,j} + (1-\eta)T_\infty \tag{16}$$

Therefore, Eq. (13) can be rewritten by substituting Eq. (17) into $T_{g,j}$

$$T_w(t) - T_i = \eta \sum_{j=1}^{N} U(t-\tau_j)t_{2,j} - \tau_{2,j-1}) \tag{17}$$

Eq. 17 can be regarded as a non-linear equation with respect to two variables, i.e., film effectiveness, η and heat transfer coefficient h. Combination of two different wall temperatures for two different elapsed times t_a and t_b given by Eq. 17 yield

$$\frac{T_w(t_a) - T_i}{T_w(t_b) - T_i} = \frac{\sum_{j=1}^{N} U(t_a - \tau_j)(T_{2,j} - T_{2,j-1})}{\sum_{j=1}^{N} U(t_b - \tau_j)(T_{2,j} - T_{2,j-1})} \tag{18}$$

This is an equation only with respect to h, from which h can be determined by solving Eq. 18 numerically. Then, film effectiveness can be given as follows,

$$\eta = \frac{T_w(t_a) - T_i}{\sum_{j=1}^{N} U(t_a - \tau_j)(T_{2,j} - T_{2,j-1})} \tag{19}$$

However, there are required several procedures before the h and η can be properly calculated by this method. Figure 34 illustrates the procedures of overall data post processing.

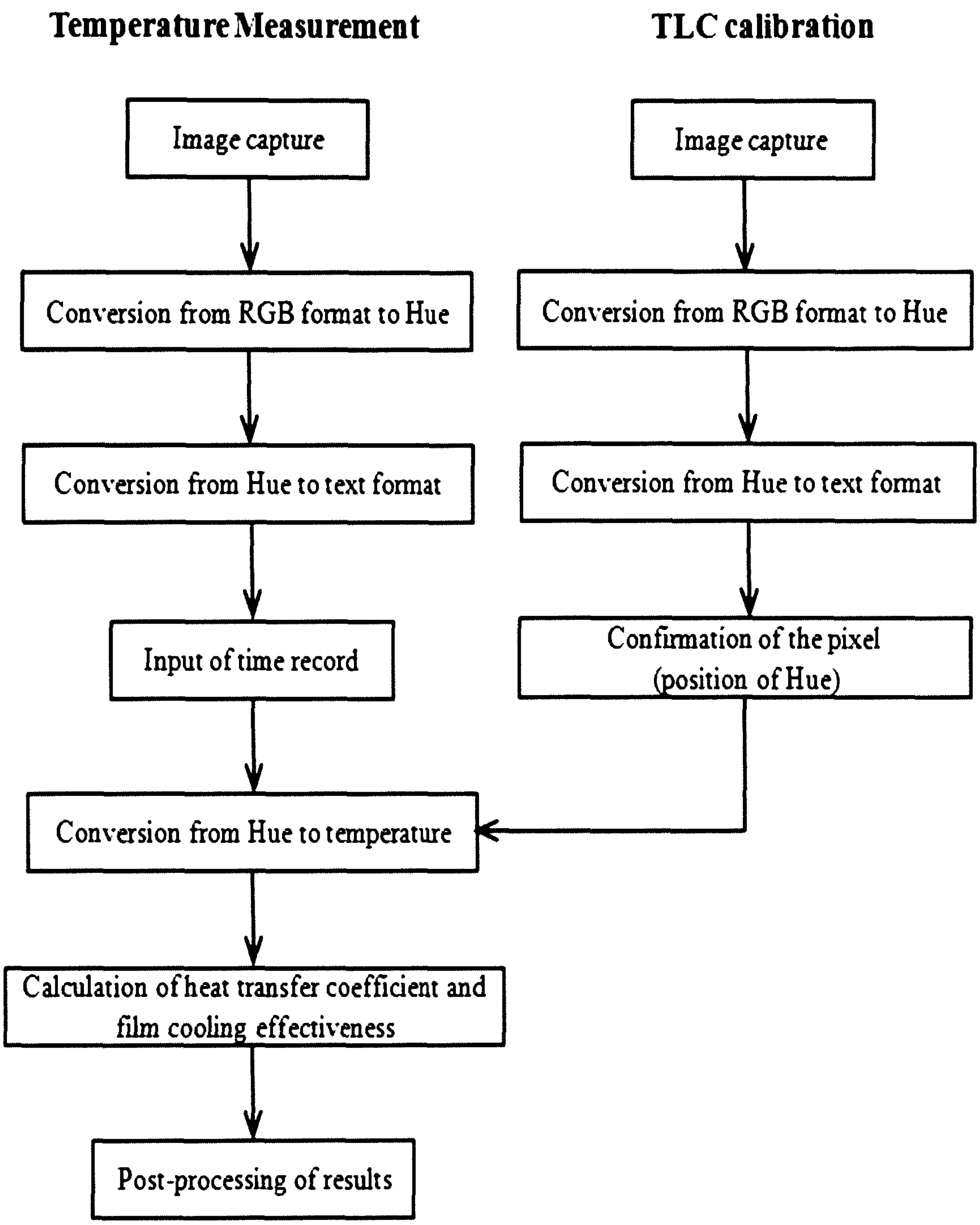

Figure 34 Data post processing procedures

2.7 Experimental uncertainty

2.7.1 Uncertainty definition

Experimental uncertainty analysis is important to evaluate the level of confidence in the results. Uncertainty analysis is a powerful tool for improving the value of experimental work, and can be applied during all phases of an experimental program. The greatest value of uncertainty analysis is almost certainly obtained when it is used during the planning of an experiment, Kline [31]. The general case of an experimental result, R, computed from j measured variables $X_{1...j}$, the data reduction equation is:

$$R = f(X_1, X_2, X_3.....X_j) \tag{20}$$

and the uncertainty in the experimental result is given by

$$\left(\frac{U_R(R)}{R}\right)^2 = \left(\frac{U_{X_1}(X_1)}{X_1}\right)^2 + \left(\frac{U_{X_2}(X_2)}{X_2}\right)^2 + \left(\frac{U_{X_3}(X_3)}{X_3}\right)^2 + ... + \left(\frac{U_{X_j}(X_j)}{X_j}\right)^2 \tag{21}$$

Here,

$$\left(\frac{U_{X_n}(X_n)}{X_n}\right) = \delta_D + \varepsilon \quad (\text{n} = 1, 2, 3, ...\text{j}) \tag{22}$$

Where,

U_R, uncertainty in the result,

U_{Xn}, uncertainty in the variable X_n

δ_D, device accuracy uncertainty

ε, standard deviation

This is the most general form of the uncertainty propagation equation, Coleman and Steele [32]. The uncertainty due to device accuracy, δ_D and the standard deviation, ε can be determined by Eq. 23 and Eq. 24, respectively.

$$\delta = \frac{D_{acc}}{\sqrt{3}} \tag{23}$$

$$\varepsilon = \frac{\dfrac{X_{n,Max} - X_{n,Min}}{2\sqrt{3}}}{X_{n,Average}} \tag{24}$$

Where,

D_{acc}, accuracy of the measurement device

$X_{n,Max}$, maximum value of X_n

$X_{n,Min}$, minimum value of X_n

$X_{n,Average}$, average of X_n

The overall experimental uncertainty can be calculated by determine the root square of Eq. 21. The details of the experimental uncertainties also presented by Moffat [33] and Alok [34].

2.7.2 Aerodynamic measurement uncertainties

In present study, the accuracy of the measurement device is also considered in the calculation. For instant, the uncertainty of the pressure transducer approximately ±1% (Setra 265: 0~5000Pa) is considered as one of the variable. The procedure to determine the uncertainty of the total pressure loss is explained below. Based on Eq. 7, C_{pt} is dependent on three variables; inlet total pressure, $P_{t,\infty}$, outlet total pressure, $P_{t,out}$ and dynamic pressure, P_d. By considering

$$P_{loss} = P_{t,\infty} - P_{t,out} \tag{25}$$

Thus, based on Eq. 21, the uncertainty of the total pressure loss can be determined by Eq. 26

$$\left(\frac{U(C_{pt})}{C_{pt}}\right)^2 = \left(\frac{U(P_{loss})}{P_{loss}}\right)^2 + \left(\frac{U(P_d)}{P_d}\right)^2 \tag{26}$$

Here,

$$\left(\frac{U(P_{loss})}{P_{loss}}\right)^2 = \left(\frac{U(P_{t,\infty})}{P_{t,\infty}}\right)^2 + \left(\frac{U(P_{t,out})}{P_{t,out}}\right)^2 \tag{26.1}$$

Based on Eq. 22, Eq. 23 and Eq. 24,

$$\left(\frac{U(P_{t,\infty})}{P_{t,\infty}}\right)=\frac{D_{acc,tran}}{\sqrt{3}}+\frac{\frac{P_{t,\infty,Max}-P_{t,\infty,Min}}{2\sqrt{3}}}{P_{t,\infty,Average}} \tag{26.2}$$

$$\left(\frac{U(P_{t,out})}{P_{t,out}}\right)=\frac{D_{acc,tran}}{\sqrt{3}}+\frac{\frac{P_{t,out,Max}-P_{t,out,Min}}{2\sqrt{3}}}{P_{t,out,Average}} \tag{26.3}$$

$$\left(\frac{U(P_{d})}{P_{d}}\right)=\frac{D_{acc,tran}}{\sqrt{3}}+\frac{\frac{P_{d,Max}-P_{d,Min}}{2\sqrt{3}}}{P_{d,Average}} \tag{26.4}$$

Where,

$D_{acc.tran.}$ accuracy of the pressure transducer (Setra 265)

$P_{t,\infty,Max}$, maximum value of inlet total pressure

$P_{t.out.Max}$, maximum value of outlet total pressure

$P_{d.Max}$, maximum value of inlet dynamic pressure

$P_{t,\infty,Max}$, minimum value of inlet total pressure

$P_{t.out.Max}$, minimum value of outlet total pressure

$P_{d.Max}$, minimum value of inlet dynamic pressure

$P_{t,\infty,Average}$, average of inlet total pressure

$P_{t.out.Average}$, average of outlet total pressure

$P_{d.Average}$, average of inlet dynamic pressure

Thus, the overall experimental uncertainty can be defined by Eq. 27 by substituting Eq. 26.1, Eq. 26.2, Eq. 26.3 and Eq. 26.4 into Eq. 26

$$\left(\frac{U(C_{pt})}{C_{pt}}\right)=\sqrt{\left(\frac{U(P_{loss})}{P_{loss}}\right)^2+\left(\frac{U(P_{d})}{P_{d}}\right)^2} \tag{27}$$

In present study, the uncertainty for the MFR was also determined by the same procedures. The uncertainties analysis results for C_{pt} and MFR is shown in Table 4. The dynamics pressure is the variable which was highly influenced the uncertainty during the measurement.

Table 4 Experimental uncertainties analysis for aerodynamics

Uncertainty	Baseline	MFR= 0.75%	MFR= 1.25%	MFR= 1.75%	MFR= 2.25%
C_{pt}(%)	±3.54	±3.34	±2.57	±2.96	±2.79
MFR	±2.54	±4.72	±4.55	±3.79	±3.12

2.7.3 Thermal measurement uncertainties

The thermal measurement was conducted based on the transient method by applying one-dimensional heat conduction equation as shown in Eq. 12. Based on the post processing procedures, the heat transfer coefficient, h was firstly determined follows by film cooling effectiveness, η. This means that η contour depends on h. Hence, the uncertainty of h will firstly determine then be included as one of the variable for η uncertainty analysis. From Eq. 12 and Eq. 21, the uncertainty for h is shown in Eq. 28.

$$\left(\frac{U(h)}{h}\right)^2 = \left(\frac{U(T_2 - T_\infty)}{T_2 - T_\infty}\right)^2 + \left(\frac{U(T_w - T_\infty)}{T_w - T_\infty}\right)^2 + \left(\frac{U(t)}{t}\right)^2 + \left(\frac{U(\lambda)}{\lambda}\right)^2 + \left(\frac{U(c)}{c}\right)^2 \qquad (28)$$

Since the same equation was used to determine η, thus its uncertainty can be defined as Eq. 29 where the h uncertainty is also included.

$$\left(\frac{U(\eta)}{\eta}\right)^2 = \left(\frac{U(h)}{h}\right)^2 + \left(\frac{U(T_2 - T_\infty)}{T_2 - T_\infty}\right)^2 + \left(\frac{U(T_w - T_\infty)}{T_w - T_\infty}\right)^2 + \left(\frac{U(t)}{t}\right)^2 + \left(\frac{U(\lambda)}{\lambda}\right)^2 + \left(\frac{U(c)}{c}\right)^2 \quad (29)$$

The thermocouple has been used for the plenum and mainstream temperature thus the device accuracy has been included to determine the uncertainty for $T_2 - T_\infty$ and $T_w - T_\infty$. At different elapsed time, t both uncertainties for h and η are highly influenced by the $T_2 - T_\infty$ and $T_w - T_\infty$ which mean a different uncertainty should be determined at different η. As the same procedures applied in aerodynamics uncertainties, the uncertainty for η=0.2 and η=0.5 are

$$\left(\frac{U(h)}{h}\right)_{\eta=0.2} = \pm 18.73\% \quad (30)$$

$$\left(\frac{U(\eta)}{\eta}\right)_{\eta=0.2} = \pm 25.49\% \quad (31)$$

$$\left(\frac{U(\eta)}{\eta}\right)_{\eta=0.5} = \pm 15.49\% \quad (32)$$

2.8 Computational fluid dynamics investigation

2.8.1 Upstream leakage flow modeling

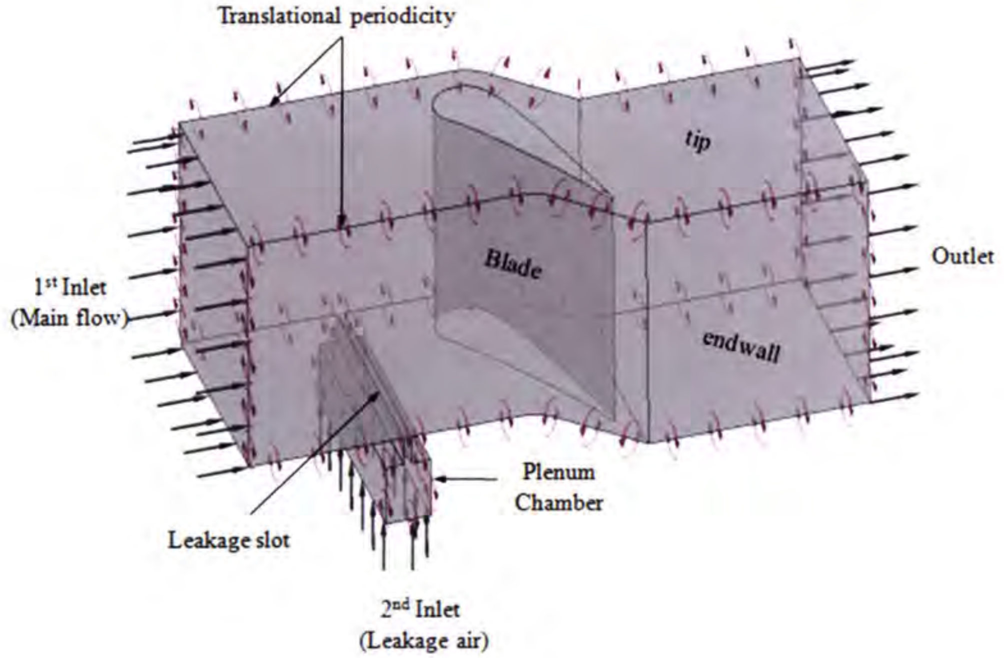

Figure 35 Computational Domain Details

As illustrates in Figure 35, the computational domain for the study of the three dimensional upstream leakage flows in linear cascade flow consisted of the plenum chamber, one pitch endwall domain with a single blade periodicity channel designed by slot located upstream the vane. The computational mesh system was created using Gridgen (Pointwise) to generate a fully structured meshes, see Figure 36. This is a multi-blocks meshing method which consisted of 14 fully structured blocks. The density of mesh cells is increased in the vicinity of the bottom, the top and the blade surfaces but also at injection location. The height of wall-adjacent cells in these regions is 0.02 mm with the objective to obtain y^+ value close to 1 along the walls. The entire computational domain comprises a total of 7.1 million of hexahedral cells. To evaluate the grid independence of the solution, meshes have been tested with a coarser, 5.3 million, and finest of 14.5 million of elements. Domain extended from $2.0C_{ax}$ upstream of the leading edge to $2.0C_{ax}$ downstream of the trailing edge.

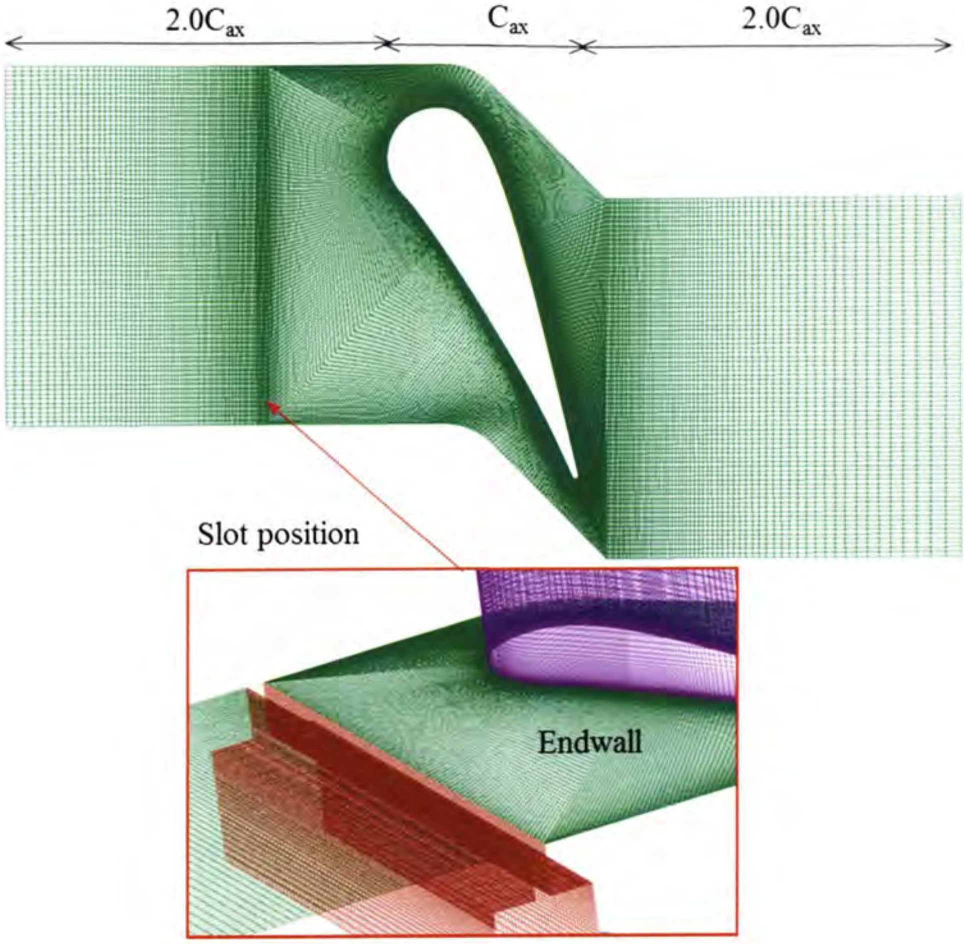

Figure 36 Mesh structures by Gridgen

The boundary conditions are defined in accordance with the measurement conditions for each case. Translational periodic boundary condition was applied on the pitchwise direction. Uniform distributions of measured total pressure and static temperature were specified on the main inlet boundary. As for the leakage flow, the measured mass flow rate and static temperature were specified on the entry plane of the plenum chamber. All walls were treated as adiabatic, no slips walls. However, fixed temperature wall condition was applied for the heat transfer prediction purpose. The simulations were carried out by ANSYS CFX ver. 14 involving Reynolds Average Navier Stokes (RANS) analyses with the employment of shear stress transport (SST) turbulent model. Solution were considered converge when root mean square (RMS) residuals of each transport quantity (mass, momentum, turbulent kinetic energy and heat transfer) had decreased by at least four order of magnitude and remained approximately constants for at least 1000 iterations.

2.8.2 Grid dependency test

For CFD, by considering the cost and CPU time required, other factors which contribute to the uncertainties in the simulation has been neglected except for the grid number. Figure 37 indicates the spanwise direction of total pressure near the blade downstream to explain the grid number used (7.1 million elements) was quite enough for the flow prediction. The change of the total pressure almost cannot be seen compared to the finest grid with 14.5 million elements. The calculated relative error of the predicted total pressure loss coefficient based on grid number of 7.1 million and 14.5 million elements is approximately 1.6%.

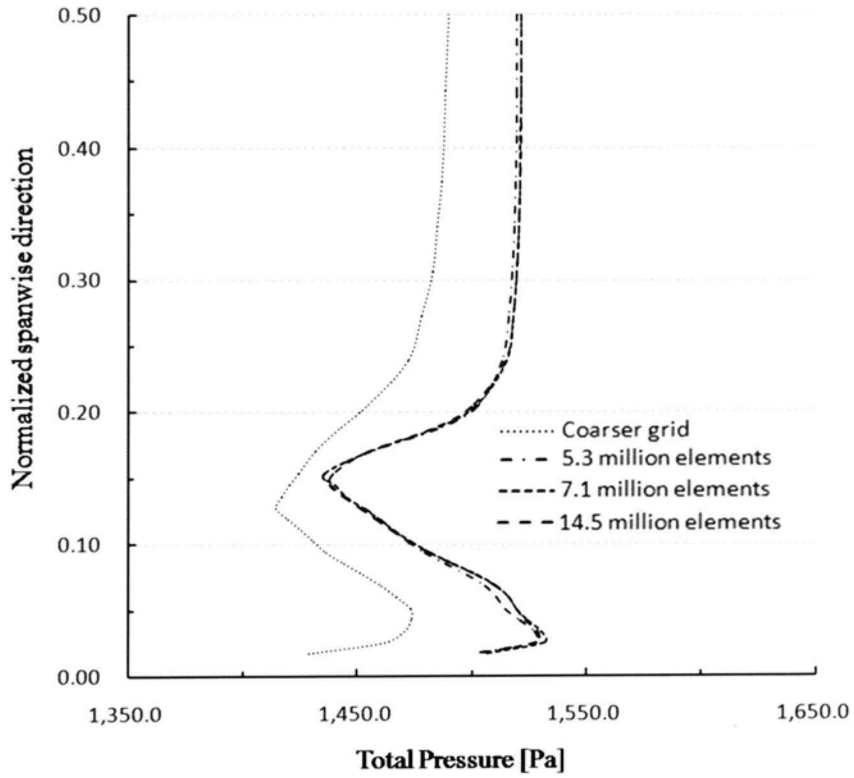

Figure 37 Grid dependency test

Chapter 3

Results and Discussions

This chapter presents the results and the discussion of the present study. The discussion involving the experimental works will includes the comparison with the numerical simulation. Both of aerodynamics and thermal behaviors will be included. Firstly, the details on the inlet flow behavior have been clarified included the blade profile investigation. The advantage of the CFD simulation enables the prediction of flow structures especially at the region where could not be obtained by the experimental.

3.1 Blade profile verification

The blade profile was verified by determined the static pressure loss on blade PS and blade SS as shown in Figure 38. The loss profile based on the EFD is compared to the CFD for the validation. The loss pick on the blade SS is parallel to the position of blade throat. Predicted loss profile almost in good agreement with the EFD except near the blade TE on blade PS. The difficulty in providing a measurement holes at this small area only allowed a few data can be taken. Furthermore, complexity of the flow due to the wake profile near the blade TE also the reason could be considered.

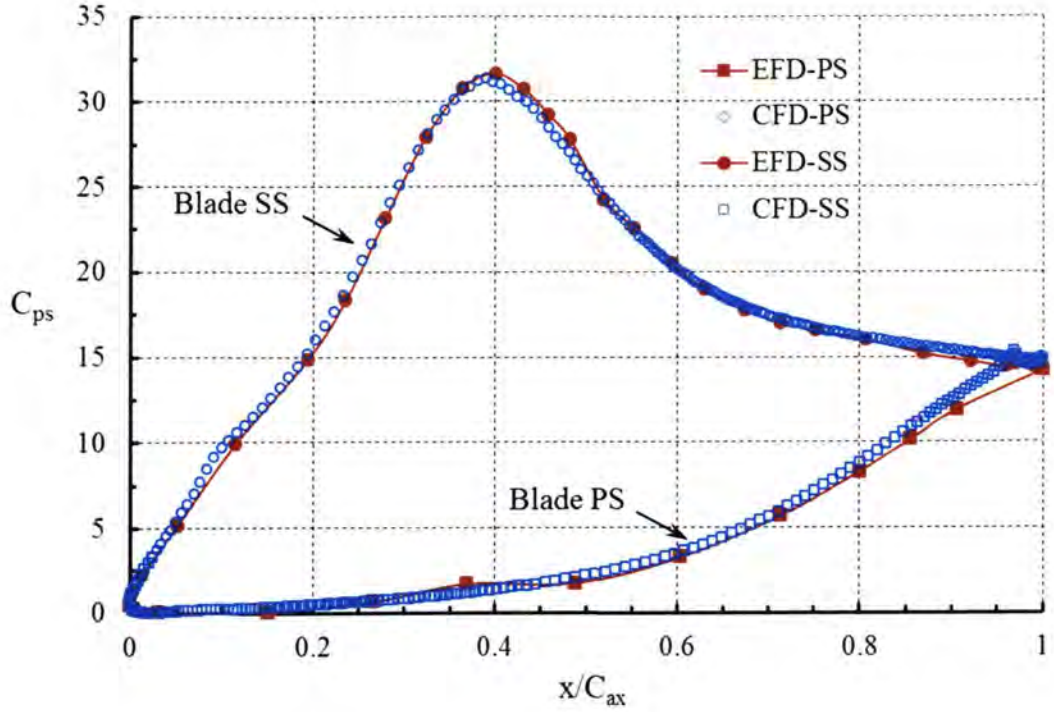

Figure 38 Static pressure loss coefficient on blade midspan

3.2 Inlet flow behavior

A new wind tunnel has been developed to investigate the effect of the leakage. This section will discuss on the inlet flow behavior in order to ensure the uniform flow structure is entering the cascade. Figure 39 illustrates the inlet axial velocity contour for the region from the endwall towards midspan (presented by normalized-span height, z/s) while Figure 40 showing the flow deviation contours (yaw angle). The red vertical dashed-lines in both figures show the position of the blade LE. The figures also indicate the contours for 2.4 pitches duration where the probe was traversed through 3 blades LE in pitchwise direction. Due to the unavailability of the device, the closer region measured at endwall side is approximately, z/s=0.02. The presence of the cascade located to downstream of the measurement plane influenced the incoming V_{ax} as presented in Figure 39. The lower flow velocity was obtained at the region close to the blade LE due to the flow turning influenced by the blockage due to the higher pressure in stagnation region. The higher V_{ax} regions indicates by yellow located closer to the blade PS at y/p=0 ~ 0.3, 0.65~1.3 and 1.75~2.3. In contrast, the lower V_{ax} closer to the blade SS was due to the higher flow deviation as illustrates in Figure 39. The ununiformed of the flow in pitchwise direction was captured on the left side of Figure 40 at region y/p=0~0.3 with a slightly higher flow deviation was due to the closer distance from the sidewall of the test section which influenced to the flow disturbance. The normalized axial velocity distributions in pitchwise and spanwise direction are shown in Figure 41 and Figure 42, respectively. In addition, the inlet velocity was compared to the profile based on CFD in Figure 42. The thicker boundary layer thickness for EFD is approximately z/s=0.1 (10mm) compared to the CFD which is approximately z/s=0.03 (3.5mm).

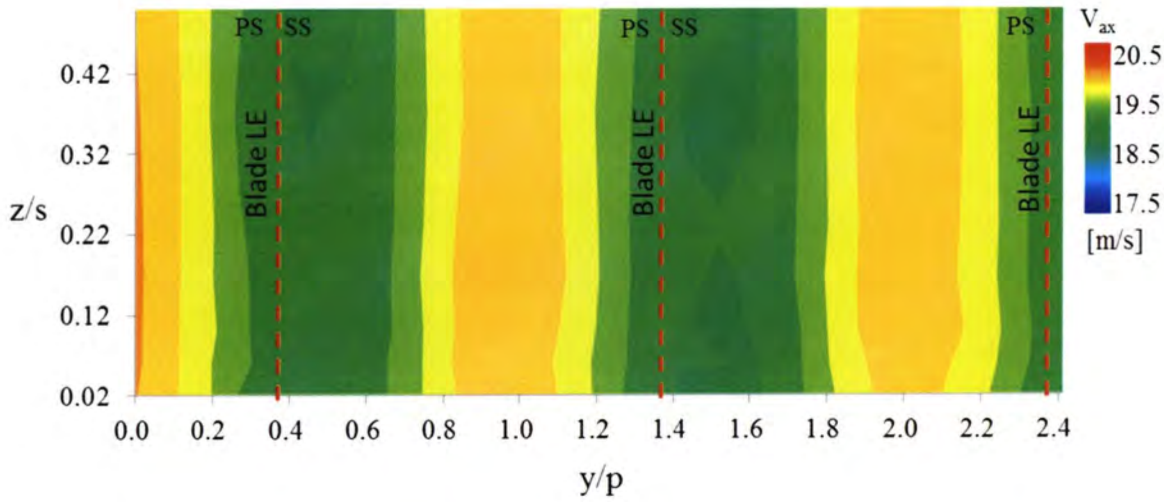

Figure 39 Inlet axial velocity

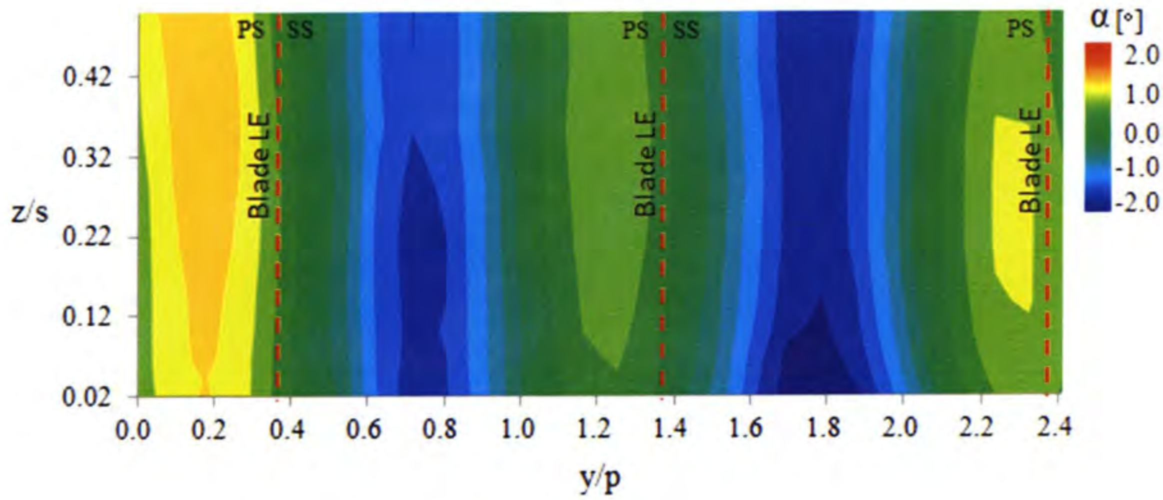

Figure 40 Inlet yaw angle, α

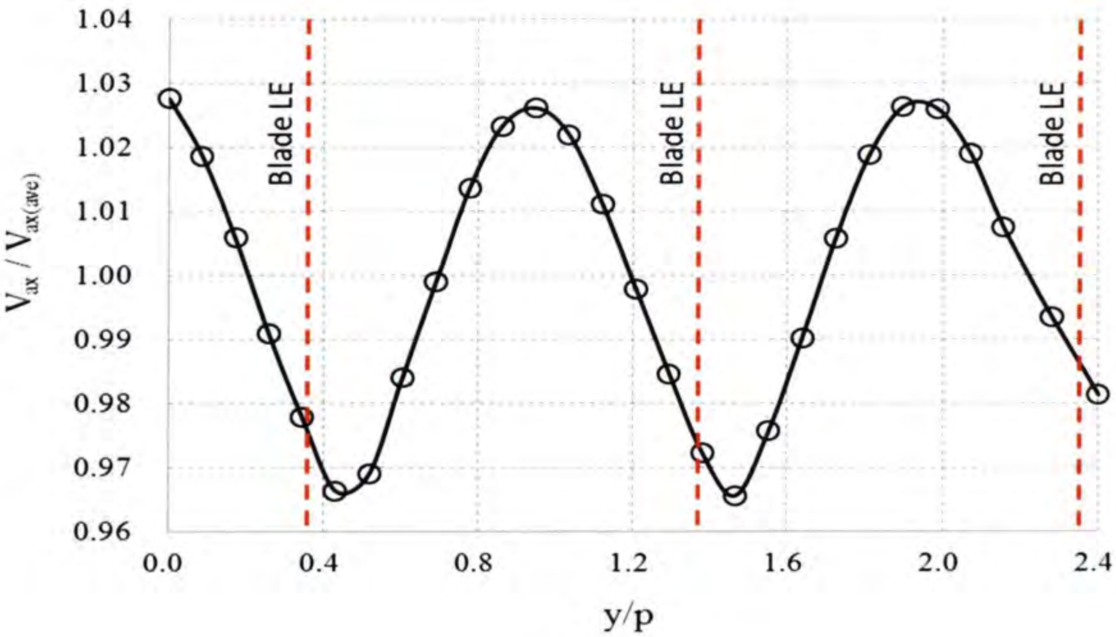

Figure 41 Pitchwise direction normalized inlet axial velocity (span –averaged)

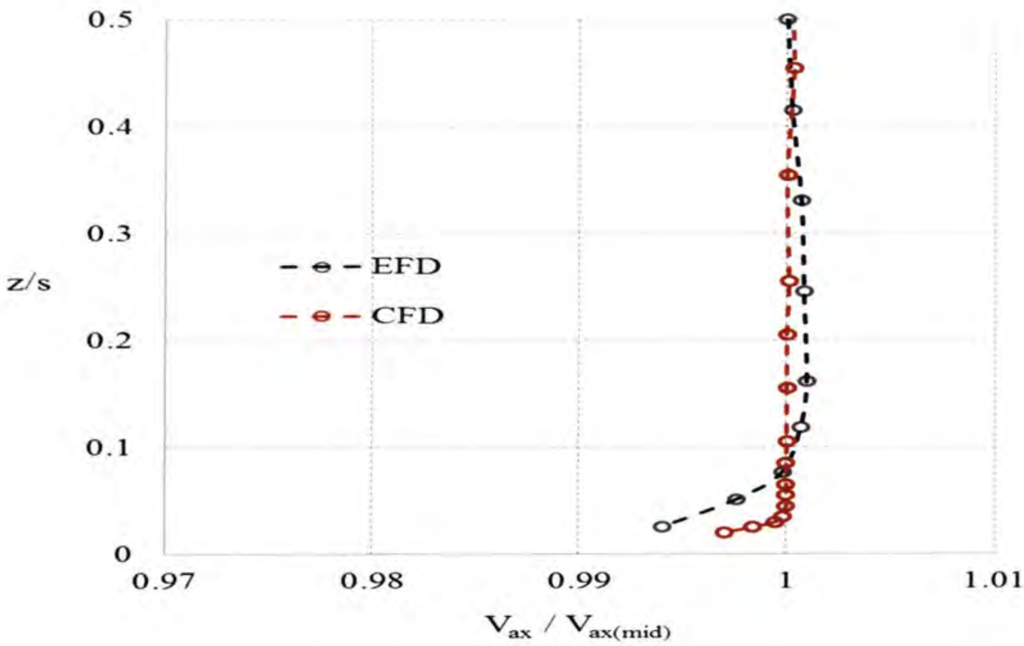

Figure 42 Spanwise direction normalized inlet axial velocity (pitch-averaged)

3.3 Aerodynamics performances at blade downstream

3.3.1 Baseline flow performance (without leakage flow)

The flow at plane $1.25C_{ax}$ has been revealed by conducting the 5-holes probe measurement which enables the three-dimensional flows measuring. The details on the baseline case need to be firstly discussed thus the flow behavior affected by the leakage flow injection could be clearly being observed and compared. Figure 43 presents the total pressure loss coefficients, C_{pt} with secondary velocity vector plotted, vorticity, ζ and secondary kinetic energy coefficient, C_{SKE}. in (a), (b) and (c) respectively, for the baseline case obtained by the EFD. The vertical axis of the contour represents the normalized spanwise direction while the horizontal axis is normalized pitchwise direction. The contour in spanwise direction starting from endwall, z/s=0.02 and ended at blade midspan, z/s=0.5. Noted that the nearest position of probe towards endwall is approximately 2 mm which means z/s=0.02. Figure 43 (a) shows the losses contributed by the wake profile which occurs along the spanwise direction in the region of y/p=0.35~0.5. In addition, the contours also characterized by the presence of the passage vortex represented by the first loss core centralized at y/p=0.48 and z/s=0.1. The second loss core also can be seen close to the endwall at y\p=0.38~0.42 which is considered associated with the interaction between boundary layer, wake profile and the corner vortex. The ζ contour plotted at the same plane in Figure 43 (b) explains the cause of the loss which is associated with the passage vortex consists of three ζ regions. The first region indicates in red located at y/p=0.4~0.6 and z/s=0.08~0.12 rotating in anti-clockwise direction. The second ζ region rotating in clockwise direction located at the bottom side of the first region. The flow direction due to these ζ is parallel with the secondary velocity vector plotted in Figure 43 (a). The third ζ region captured close to the endwall region could be considered as the corner vortex rotating in anti-clockwise direction. The magnitude of the rotational energy influenced by the secondary flows describes by C_{SKE} as presented in Figure 43 (c). The appearance of C_{SKE} region as captured in the figure is parallel to the position of the passage vortex which is presented in ζ contour in Figure 43 (b). Thus the contour explains the energy produces by the passage vortex for baseline case.

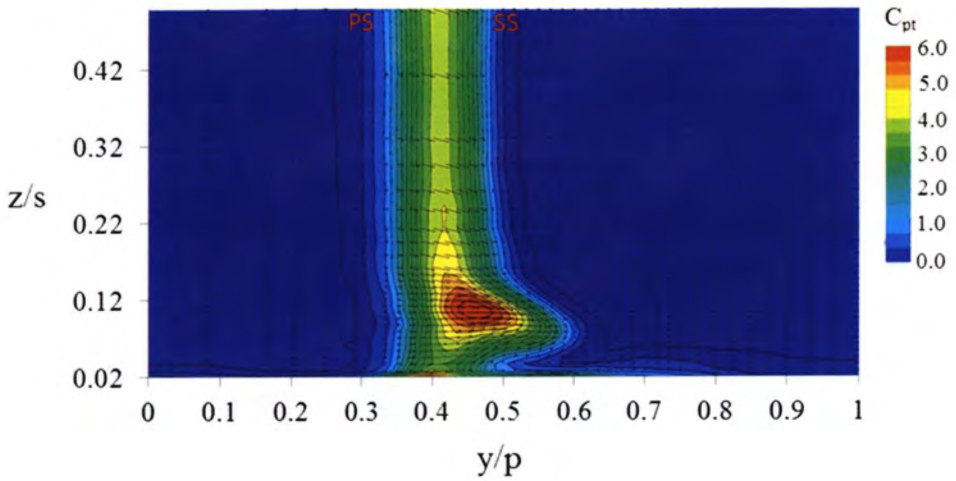

(a) C_{pt}

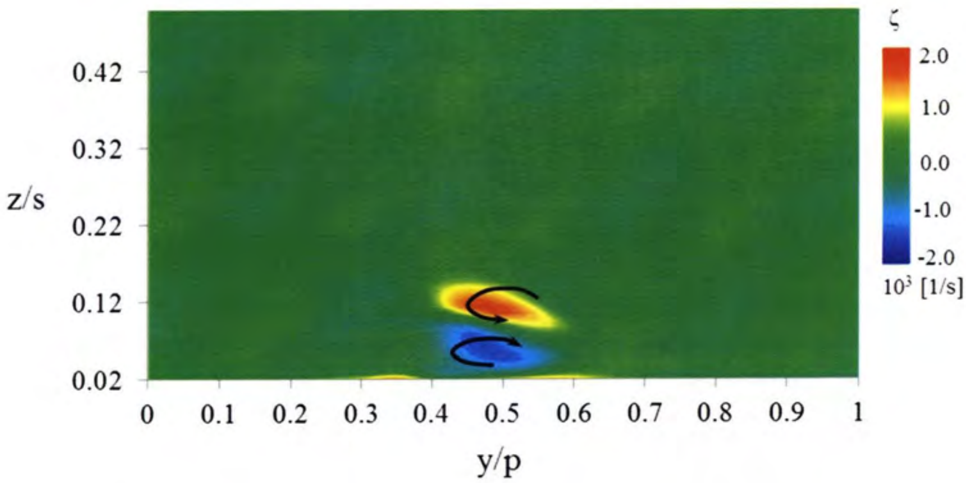

(b) ζ

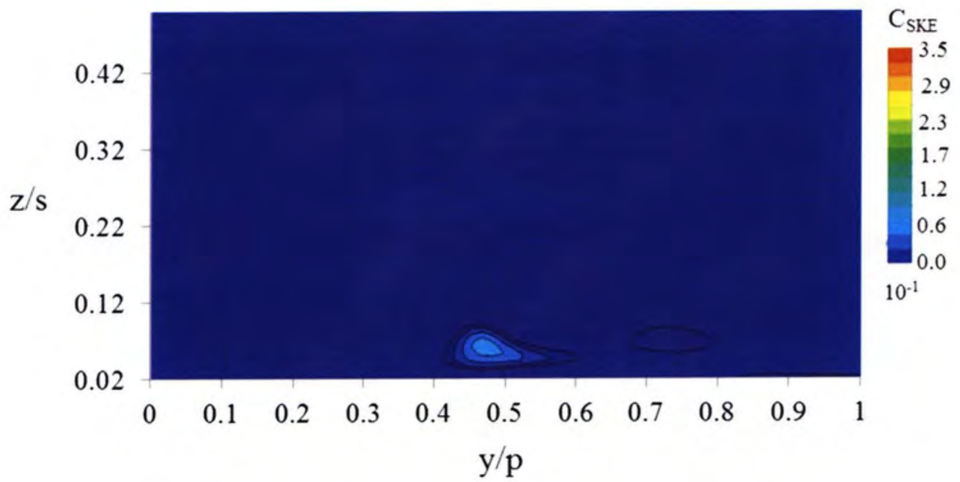

(c) C_{SKE}

Figure 43 Flow behavior at Plane $1.25C_{ax}$ -Baseline case

3.3.2 Leakage flow injection effects

The effects of the leakage flow from the slot which is located $-0.63C_{ax}$ upstream of the blade LE has been investigated by four different injection amounts. The leakage flow amount represented by MFR were ejected approximately 0.75% , 1.25%, 1.75% and 2.25% to describe the case for lower, intermediate, higher and extremely higher ejection. The same contours as discussed in previous section are plotted in Figure 44~Figure 47 for MFR =0.75%, 1.25%, 1.75% and 2.25%, respectively. According to those figures, there are three significant changes has been recognized compared to Figure 43 (a). Firstly, at a lower MFR of 0.75% presented in Figure 44 (a), the shape of the first loss core seems to be slightly changed. As shown in Figure 44 (b), the flow ζ indicated by the blue region which is rotating in clockwise direction increased its strength which might be one of the reasons of the change. However, the position of this core did not show any significant change. Secondly, the second loss core which is located at y/p=0.4 also slightly increased the region. However, the ζ contour as be shown in Figure 44 (b) did not show any significant change in term of the magnitude or region compared to the baseline case. The third change is the most significant effect could be observed when the leakage flow being injected even tough at lower MFR. The additional lost core region on the blade SS side located at y/p=0.55~0.87 and z/s=0.02~0.05 has been captured. Indeed, the additional loss region was likely occurred close to the endwall side. The secondary flow structure was being affected by the leakage flow ejection consequently contributes the additional loss near the blade downstream. This has been proved by the appearance of the newly vorticity contour near this region with a lower strength, see Figure 44 (b). The discussion above is mainly concentrates on the effect of leakage flow on lower injection case. The effects by the different amount of leakage injection was also been revealed.

Figures indicate that the upstream leakage ejection has a significant influence on the secondary flow structures across the MFR value. Increased the MFR from 0.75% to 1.25% did not give a significant effect on the first loss core in term of shape, see Figure 45 (a) but its position slightly shifted towards midspan. This phenomenon could clearly be seen when the MFR continuously be increased to 1.75% and 2.25%, see Figure 46 (a) and Figure 47 (a). The first loss core were shifted from z/s=0.10 to 0.13 for MFR=1.75% as shown in Figure 46 (a) and leakage injection with 2.25% presents the highest position among others approximately z/s=0.15, see Figure 47 (a). This might be considering that the leakage flow injection from the upstream of the blade LE caused the increase strength of the horse-shoe vortex (HSV) especially on the pressure-side leg horse-shoe vortex (PS-HSV). As a result, the PS-HSV had a higher fluid momentum compared to lower leakage injection or baseline cases to cross the mainstream flow from the blade PS to neighboring blade SS. Finally it developed as a passage vortex near blade TE. At the corner between blade SS and endwall, the passage vortex is expected to be lifted-off the blade surface with a higher position in spanwise direction by the higher fluid momentum thus presenting higher position of the loss core at blade downstream compared to a lower MFR injection. This is parallel to the suggestion made by Sharma and Butler [7]. In addition, not only the position, but also the shape of the loss core seems to be continuously changed. The transformation of the loss core shape can clearly observed at higher MFR of 1.75% and 2.25%. This core tends to change especially on the blade SS where it became oblongated towards pitchwise direction. For the second loss core, the region (red core) in Figure 47 (a) for 2.25% injection became wider in pitchwise direction and the region was expanded approximately from y/p=0.38~0.42 to y/p=0.38~0.55. The loss region became wider was due to the increase strength of the flow ζ near this region as shown by the ζ contours in Figure 44 (b) ~Figure 47 (b). As the MFR being increased, the strength of the corner vortex has been amplified which then contributed to the higher losses. This phenomenon could also influences to the blockage which might be considered to deflect the earlier flow direction slightly upwards. The higher position of first loss core at higher MFR also might be the result from this phenomenon.

The third loss core which was only be captured in the leakage ejection cases also continuously expended the region when the MFR increases. The third loss region which is localized on the blade SS side expanded almost half of the blade pitch for the extremely higher injection in Figure 47 (a). Furthermore, compared to lower injection case, this loss core likely to be lifted-up toward midspan as the same phenomenon has been captured on the first core. As discussed previously, the newly generated flow ζ at this region was being considered to responsible for the additional losses. Since the strength of the ζ in this region is increased when the MFR increases, see Figure 45 (b) ~ Figure 47 (b), the wider loss region was obtained. Additionally, higher strength flow ζ can easily penetrates into mainstream thus resulting higher position in spanwise direction. The increased strength of flow ζ near this region is also clearly be captured by the secondary velocity vector plotted which is centralized at y/p=0.76 and z/s=0.06, see Figure 47 (a). The formation of the vortical structure in this region explains a significant effects influenced by the leakage flow where the strength of the passage vortex was amplified. Based on Figure 44 (c) ~ Figure 47 (c), C_{SKE} contours are parallel with the above explanation where the increased strength of the passage vortex also can be seen by the increases of the secondary flow energy. As expected, MFR=2.25% provides the highest C_{SKE} magnitude compared to a lower MFR or baseline case. In this case, higher C_{SKE} consequently increase the passage loss associated by the secondary flows.

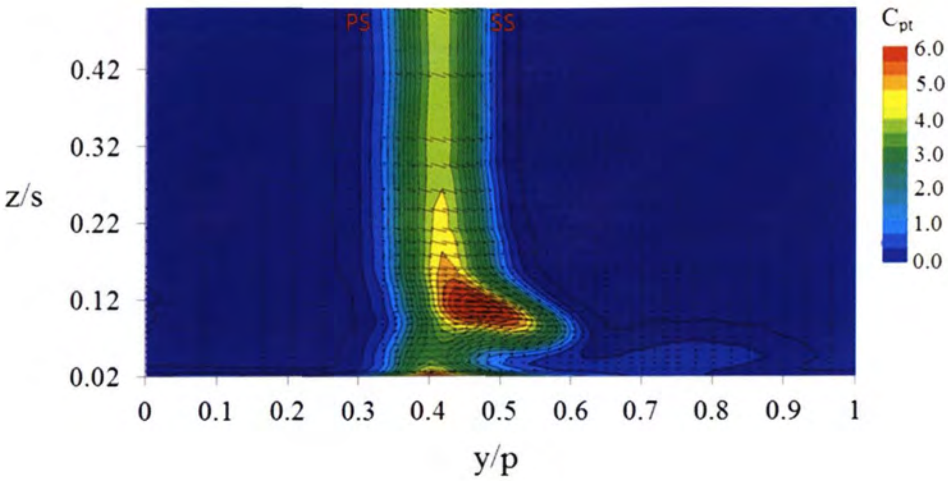

(a)C_{pt}

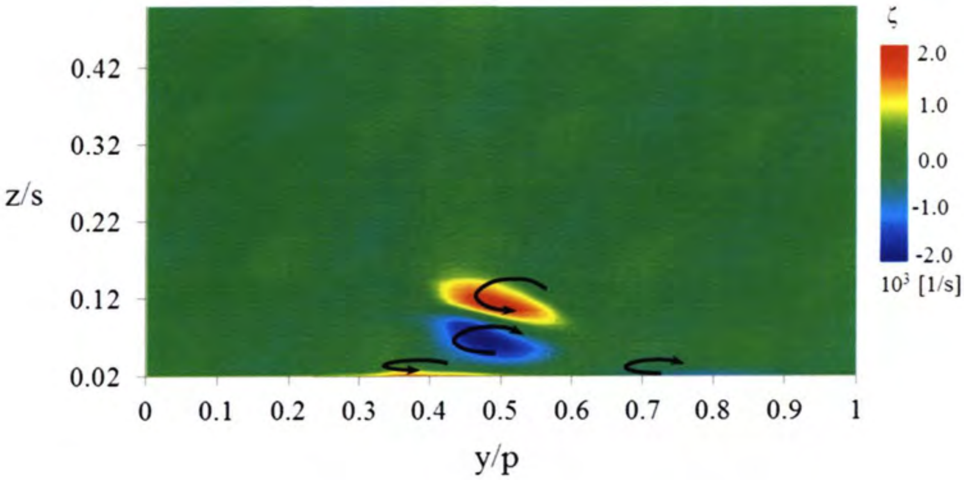

(b) ζ

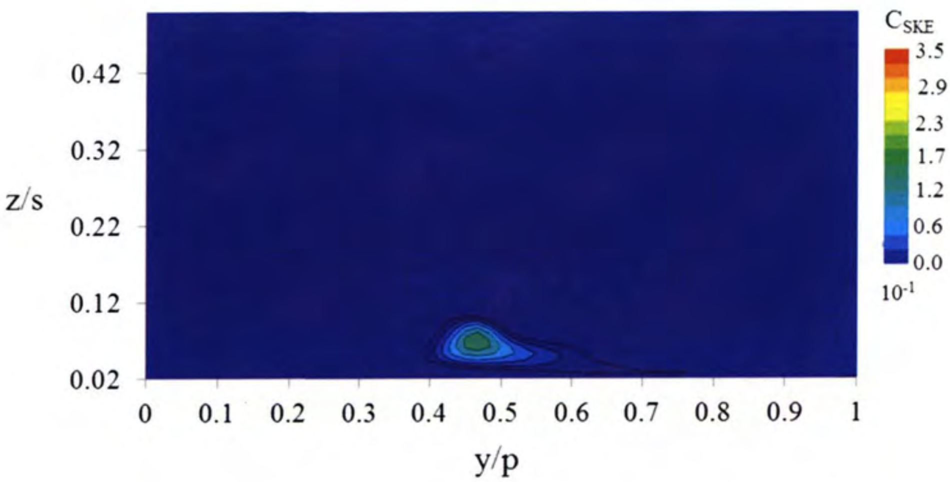

(c)C_{SKE}

Figure 44 Flow behaviour at Plane 1.25C_{ax}-MFR=0.75%

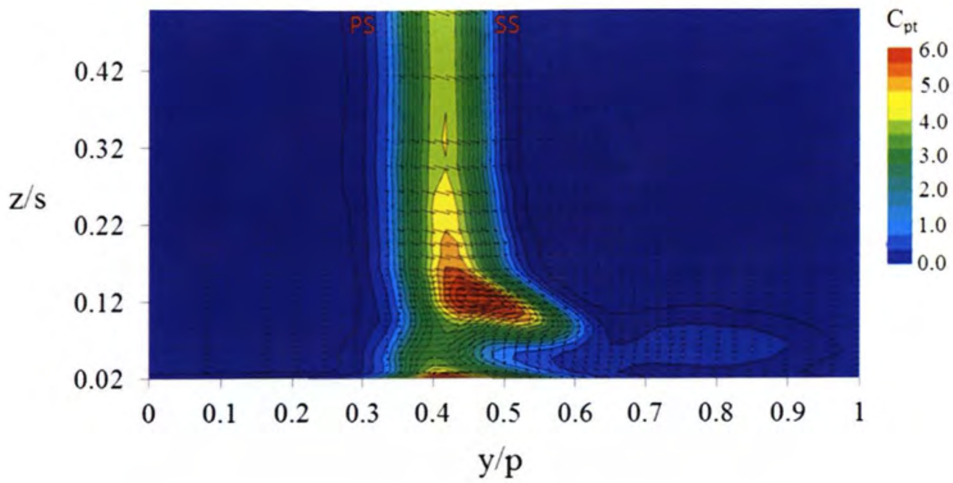

(a)C_{pt}

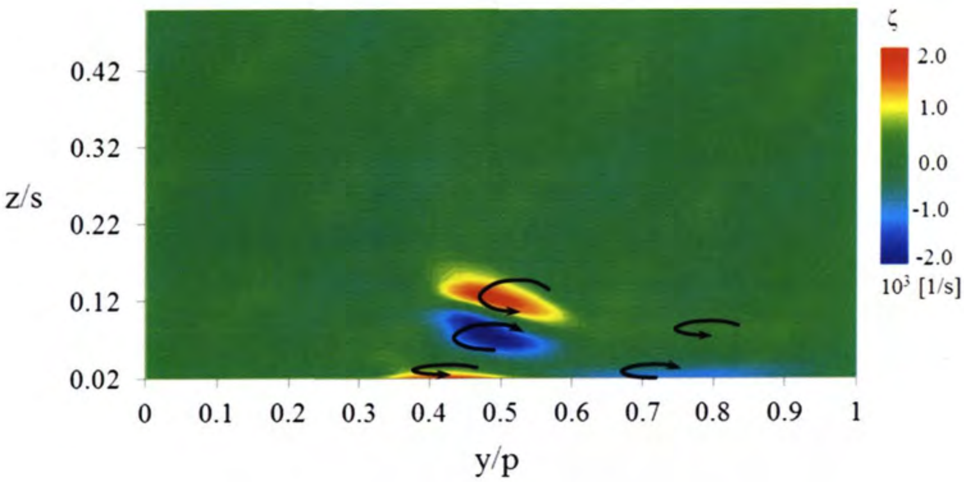

(b) ζ

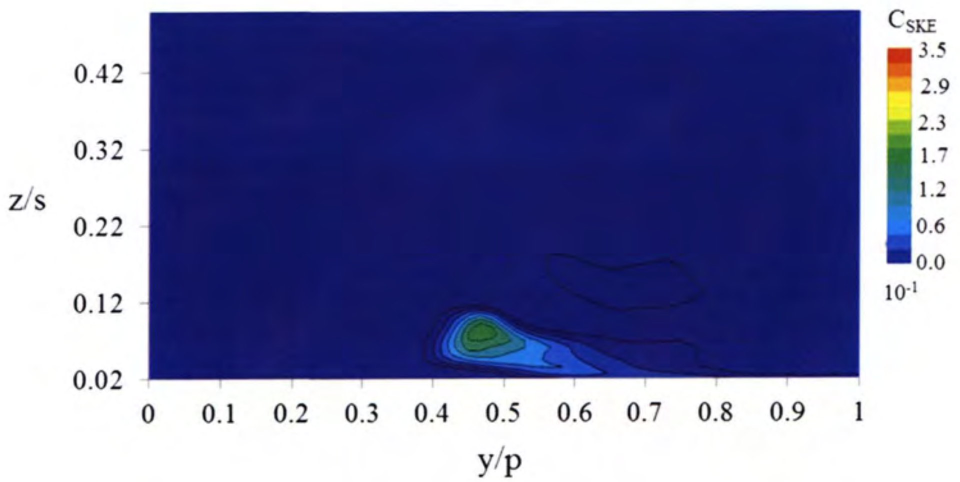

(c)C_{SKE}

Figure 45 Flow behaviour at Plane 1.25C_{ax}-MFR=1.25%

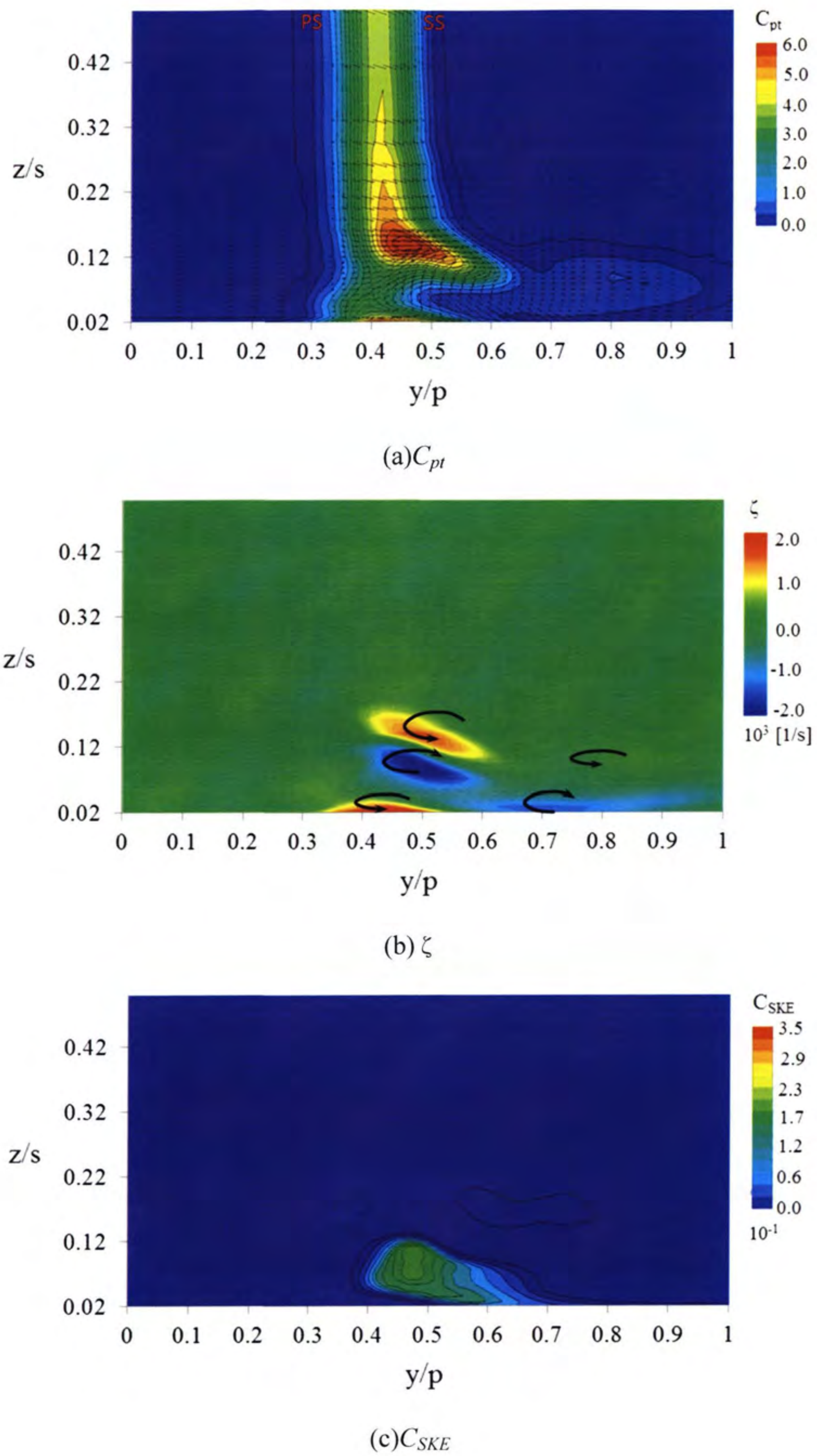

(a)C_{pt}

(b) ζ

(c)C_{SKE}

Figure 46 Flow behaviour at Plane $1.25C_{ax}$ -MFR=1.75%

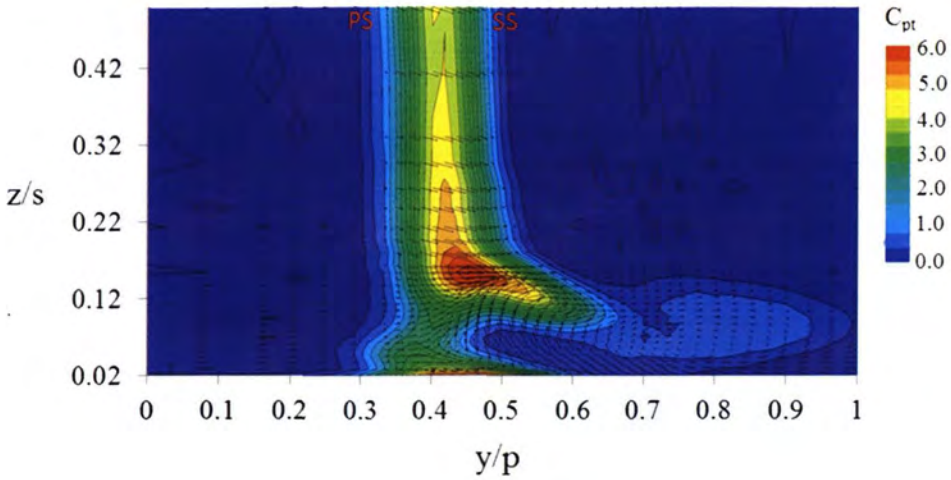

(a)C_{pt}

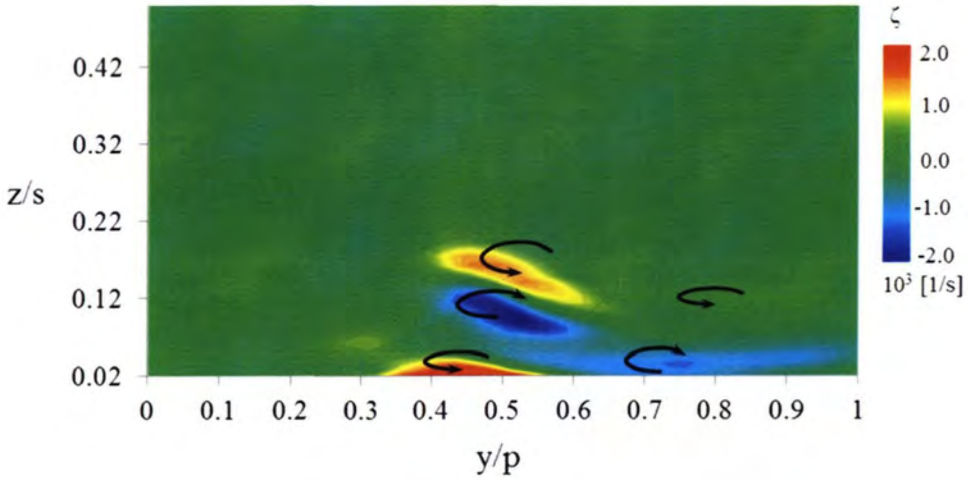

(b) ζ

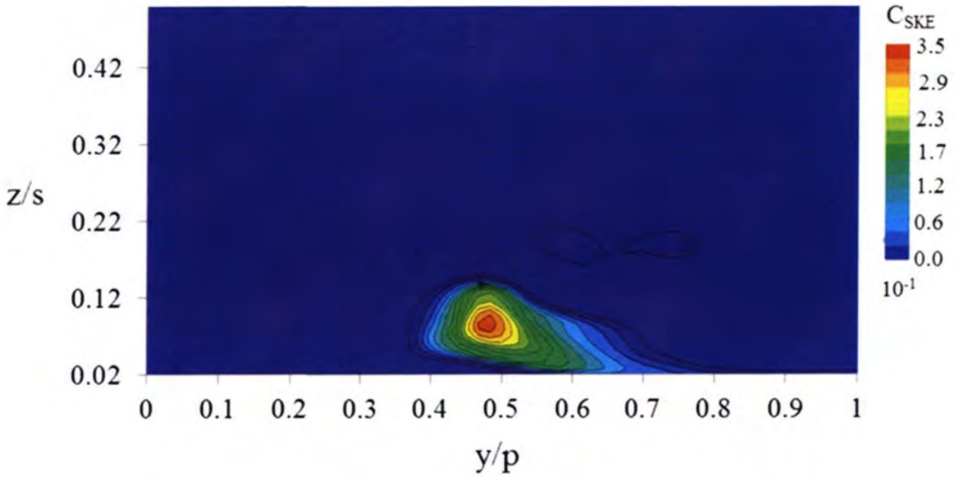

(c) C_{SKE}

Figure 47 Flow behaviour at Plane $1.25C_{ax}$ -MFR=2.25%

Normalized spanwise direction of $C_{pt}/C_{pt(mid)}$ and flow deviation at the same plane are plotted in Figure 48, by determining the average on pitchwise direction of each data. The graph illustrates the comparison between the leakage injections with the baseline case presented by the red line in (a) C_{pt} and (b) yaw angle, α. As be shown in Figure 48 (a), the $C_{pt}/C_{pt(mid)}$ =1 is actually belongs to the loss associated by the wake profile and for $C_{pt}/C_{pt(mid)}$ >1 can be considered as the loss associated by the secondary flows. For the baseline case, the loss influenced by the secondary flows can be observed from z/s=0.02 to z/s=0.3 with the maximum $C_{pt}/C_{pt(mid)}$ =1.33 located at z/s=0.08. The loss contributed by the secondary flows in spanwise direction spread slowly from z/s=0.3 to z/s=0.4 (indicates by $C_{pt}/C_{pt(mid)}$ >1)when the leakage flow are applied. The picth-averaged C_{pt} also presents the increases trend when the MFR increases. The maximum $C_{pt}/C_{pt(mid)}$ is approximately 1.39, 1.41, 1.5 and 1.58 for MFR = 0.75%, 1.25%,1.75% and 2.25% respectively. At the same time, as the MFR increases, the position of the pick slightly shifted toward midspan. This observation is in good agreement with the C_{pt} discussion made on Figure 43~Figure 47. The introduction of the leakage flow at upstream of the blade LE is considered to increase the strength of the PS-HSV which finally influenced to the higher flow blockage in the blade passages. As a result, a high flow deviation by the higher MFR was obtained as indicated in Figure 48 (b) thus resulting higher losses.

The aerodynamics performance of upstream leakage flows can be summarized by taking the mass-averaged C_{pt} for each case as shown in Figure 49. The approximate curve has been plotted thus the trend of aerodynamics performance can be observed. The contribution of the MFR towards the C_{pt} can directly specify from the graph. Measurement indicates the C_{pt} is linearly increases as the MFR increases. Based on the trend line obtained, applying the highest MFR=2.25%, resulting the $\overline{C_{pt}}$ =1.456 which means the loss was increased approximately 14.2%. In other words, in order to increase 1% of MFR, the loss is estimated to be increased about 6.3%. Another approach also can be used to describe the trend of loss with substituting the parameters into the linear function by taking the MFR parameter into account. As a result, Eq. 28 can be used to represent the loss trend for upstream leakage injection.

$$\overline{C_{pt}} = \gamma \mathrm{MFR} + \overline{C_{pt0}} \tag{33}$$

Where,

γ, loss increase rate (=0.080)

$\overline{C_{pt0}}$, baseline mass-averaged loss (=1.275)

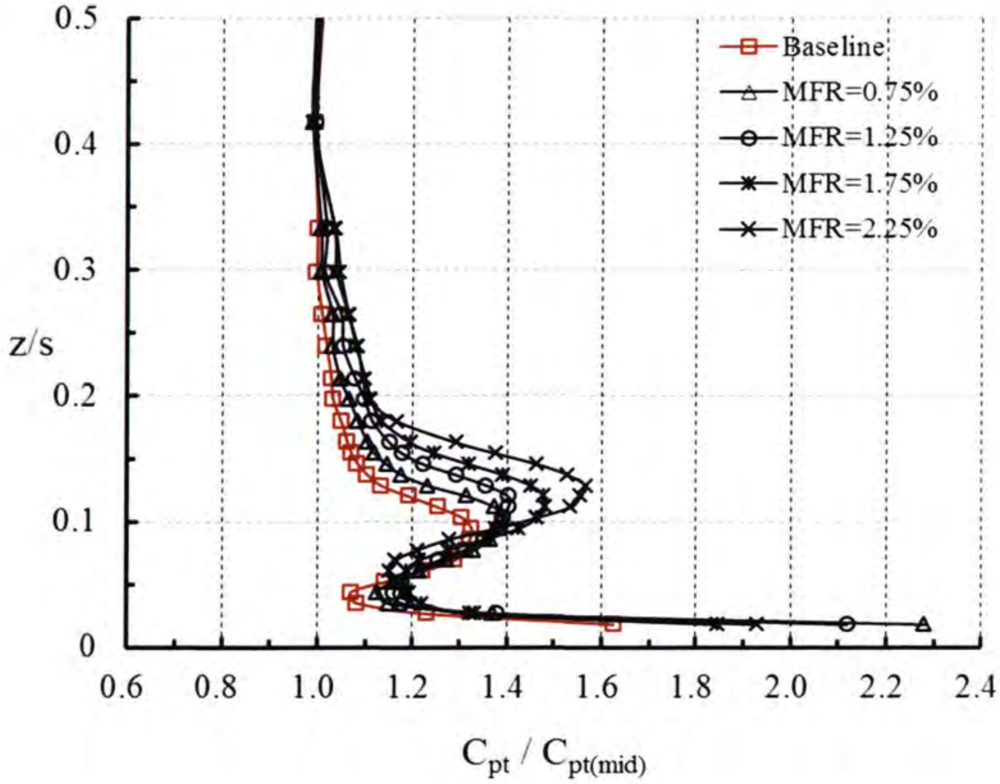

(a) Spanwise C_{pt}

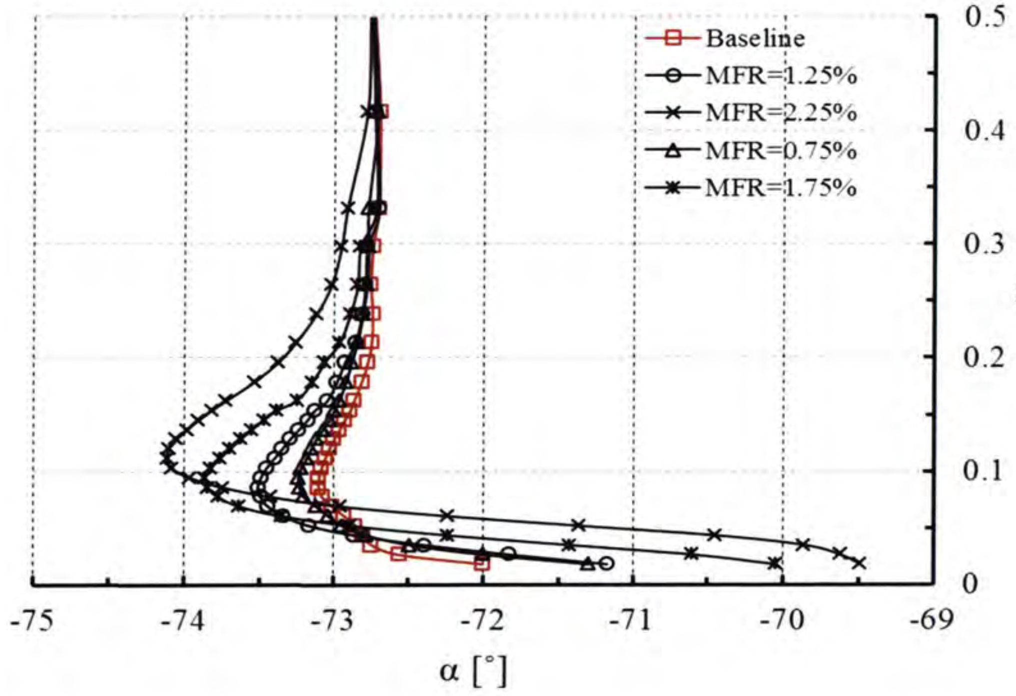

(b) Spanwise α

Figure 48 Pitch averaged C_{pt} (a) and yaw angle, α (b)

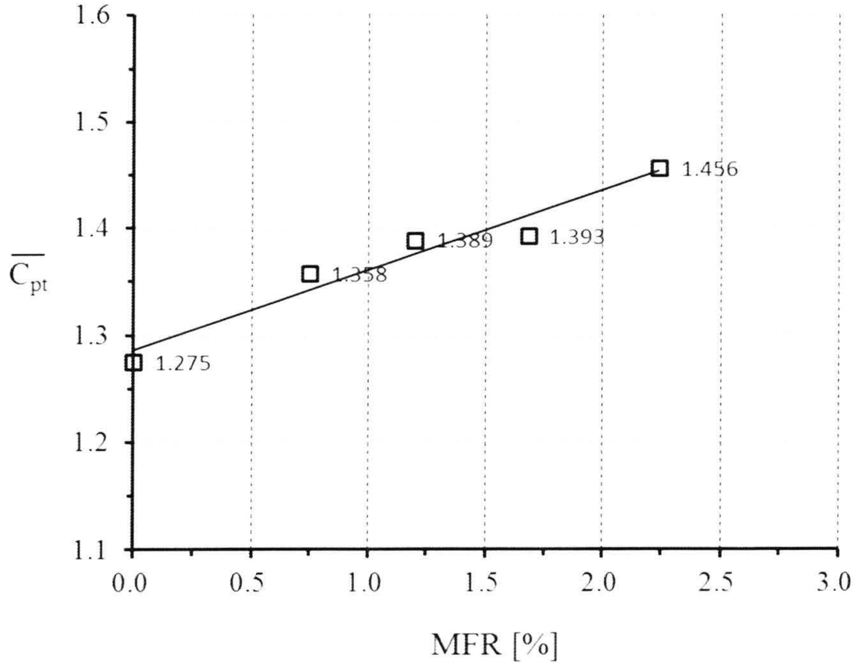

Figure 49 Trend line for mass-averaged total pressure loss at Plane 1.25C_{ax}

3.3.3 Predicted flow behaviour at Plane 1.25C_{ax}

The performance of numerical simulation in predicting the interaction between the leakage flow and the secondary flow on the endwall has been investigated by three cases. Firstly, the baseline case was predicted. Then it has been compared with another two injection cases: MFR=1.25% and 2.25% represent intermediate and extremely higher leakage injection. Figure 50 presents the C_{pt} contour (a), ζ (b) and C_{SKE} (c) for baseline case. The same figures are plotted for MFR=1.25% and 2.25% in Figure 51 and Figure 52. Without any leakage flow injection, Figure 50 (a) presents the loss contour for baseline case which was associated by the wake profile along the spanwise direction in the region y/p=0.3~0.5. The passage vortex was considered to be responsible to the loss core indicates with a higher loss region at y/p=0.43, z/s=0.10. As be shown in Figure 43 (a), this loss core was also be captured by the experimental. However, in comparison with the EFD, numerical simulation clearly predicted the existence of the loss core close to the endwall located at region y/p=0.35~0.5. The limitation of the measurement device to access this region caused the presence of loss core near this region was not clearly captured. In comparison to the baseline case, the loss core associated with the passage vortex can be observed to occur further away from the wall corresponding to the MFR values. At MFR = 1.25%, see Figure 51 (a), additional loss region can be observed to occur on the blade SS. Noted that, this new loss core was also presented by the experimental as shown in Figure 45 (a). As the MFR increases, the additional loss region also increases as shown by MFR= 2.25%, see Figure 52 (a). This additional loss region was also caused by the flow vorticity which is clearly captured on the blade SS. Additionally, in comparison with the measurement, CFD also clearly captured the presence of the vortical structure illustrates by the secondary velocity vector is centralized at y/p=0.75, z/s=0.11 to present the increased strength of the passage vortex in the cascade. Higher leakage flow ejection case causes deformation on the shape of the loss core characterized by the passage vortex. The CFD results show similar trends as the EFD. Similar to the EFD, the position of the loss core predicted by CFD seems to move away from the endwall as the MFR increases. Although the similar trend can be observed, the CFD results show a discrepancy in terms of the shape and location of the loss core. The discrepancy could be contributed by the different inlet flow profile used in the CFD which influence to the development of the passage vortex, see Figure 42. With regard to the loss region characterized by the corner vortex which has been observed earlier, see Figure 51, wider loss region can be observed at higher MFR indicating the increase of the corner vortex strength. The same trend of C_{SKE} is also presented by the CFD where the increases of the secondary flow energy can be observed after the leakage injection; see Figure 51 (c). Its continuously increase when the leakage flow changed to MFR=2.25%, see Figure 52 (c). However, CFD has predicted the higher secondary flow energy compared to EFD close to endwall side which been observed after the leakage injection. This higher flow energy might be sourced by the newly generated flow vorticity near this region. Figure 53 summarizes the predicted aerodynamics performance by determine the mass-averaged C_{pt} which is compared to EFD. A similar pattern can be observed between the EFD and CFD. Having the similar trends, the losses predicted by the CFD increased approximately 14.3% for MFR= 2.25%. Thus, it could be estimated that about 6.4% of loss increases when injecting a leakage flow by MFR=1%. The prediction is very close to the EFD with 6.3% of loss per MFR. In general, the graph shows that CFD is over predicted the losses in the range of 3%~5% in comparison to EFD. Based on Eq. 33, the loss predicted by CFD can be estimated by Eq. 34.

$$\overline{C_{pt}} = 0.085\text{MFR} + 1.331 \tag{34}$$

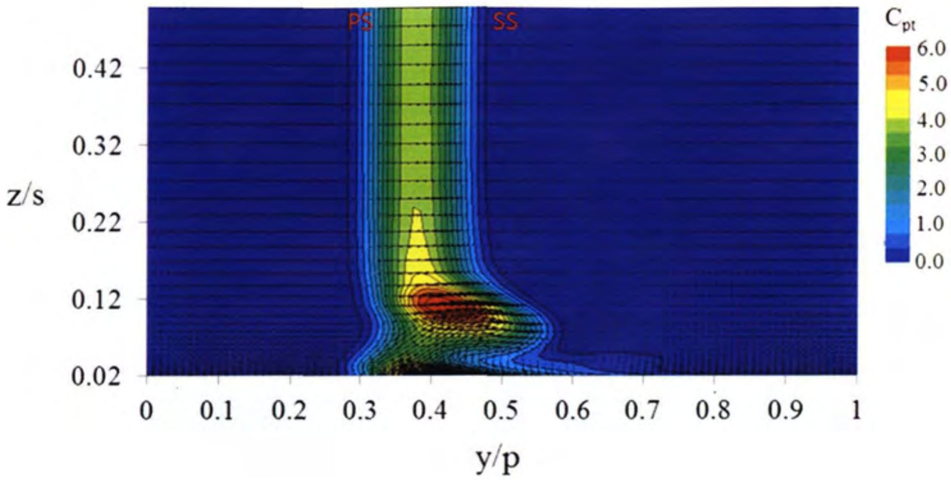

(a) C_{pt}

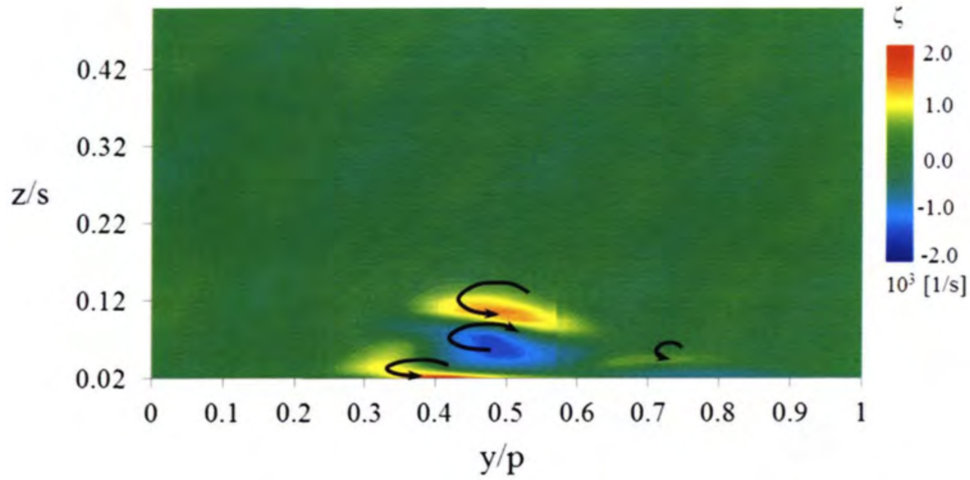

(b) ζ

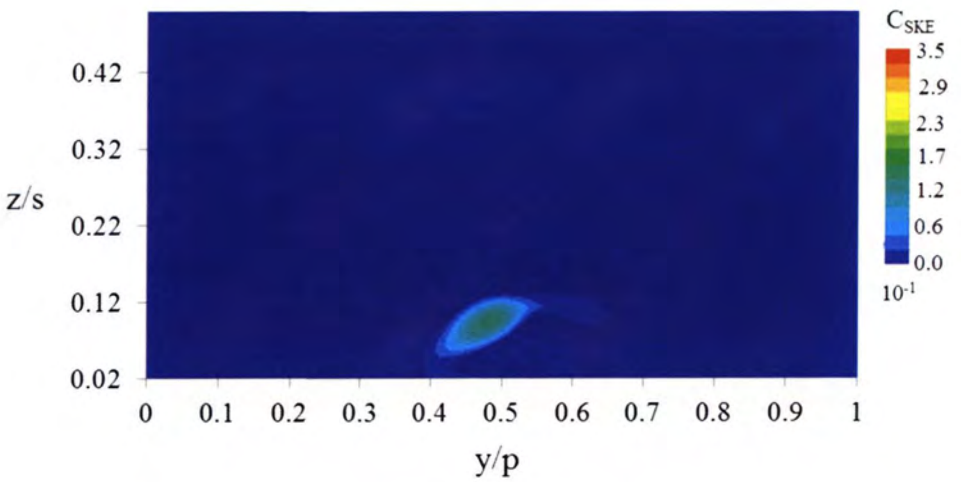

(c) C_{SKE}

Figure 50 Predicted flow behaviour- baseline case

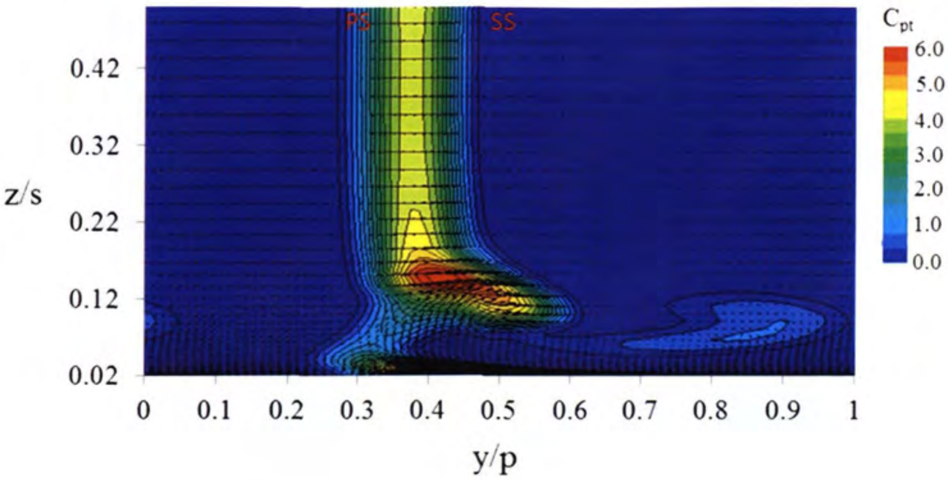

(a) C_{pt}

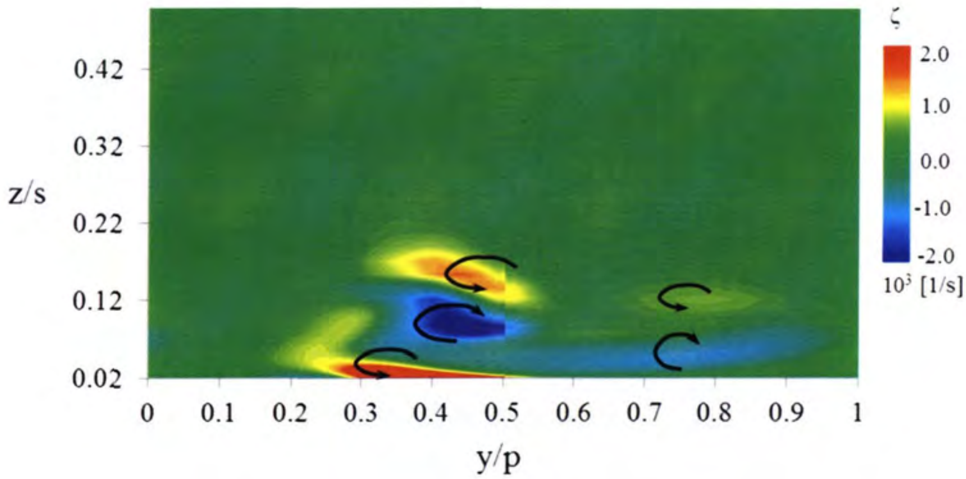

(b) ζ

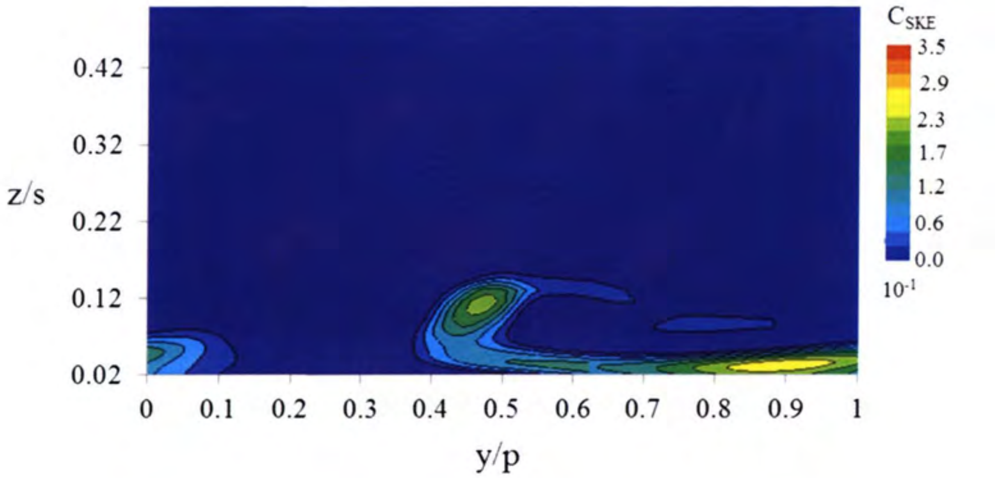

(c) C_{SKE}

Figure 51 Predicted flow behaviour-MFR = 1.25%

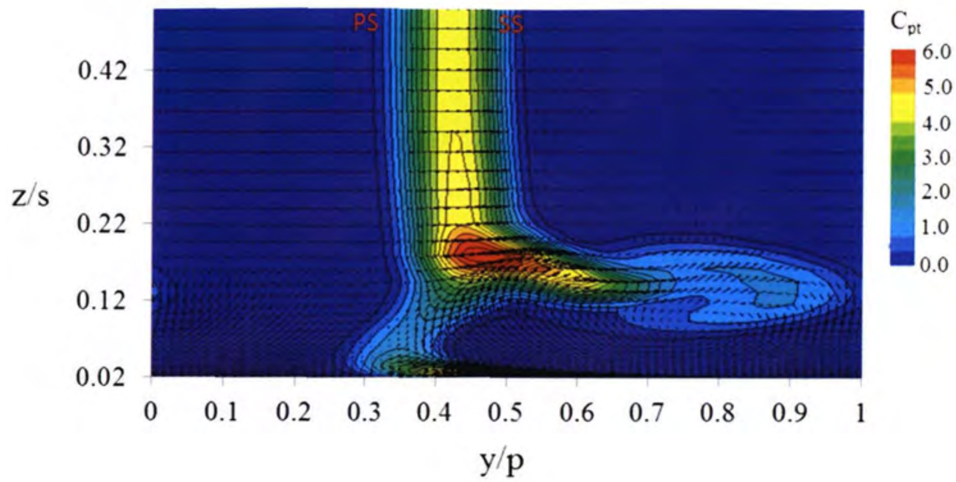

(a)C_{pt}

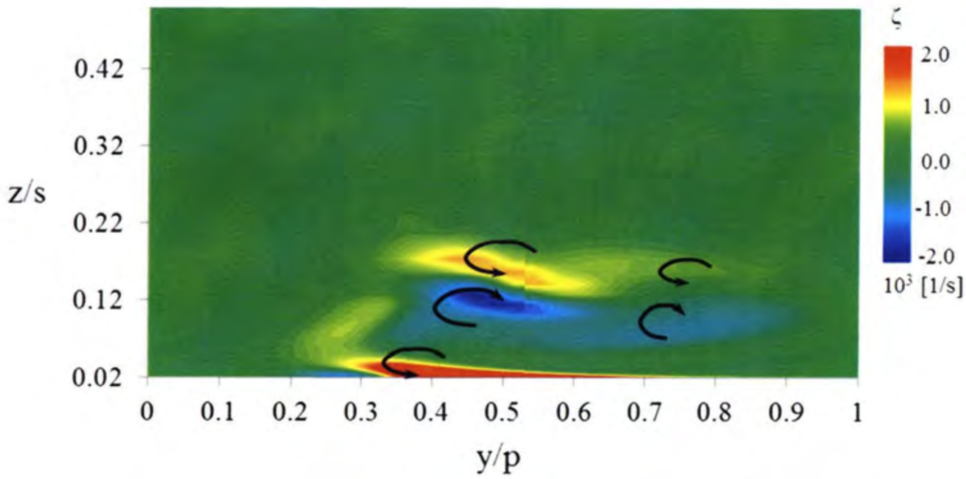

(b) ζ

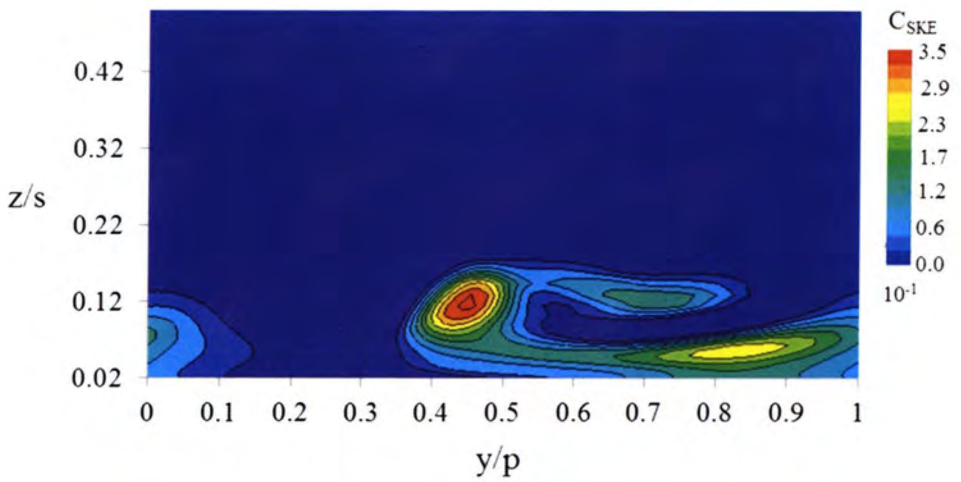

(c) C_{SKE}

Figure 52 Predicted flow behaviour-MFR=2.25%

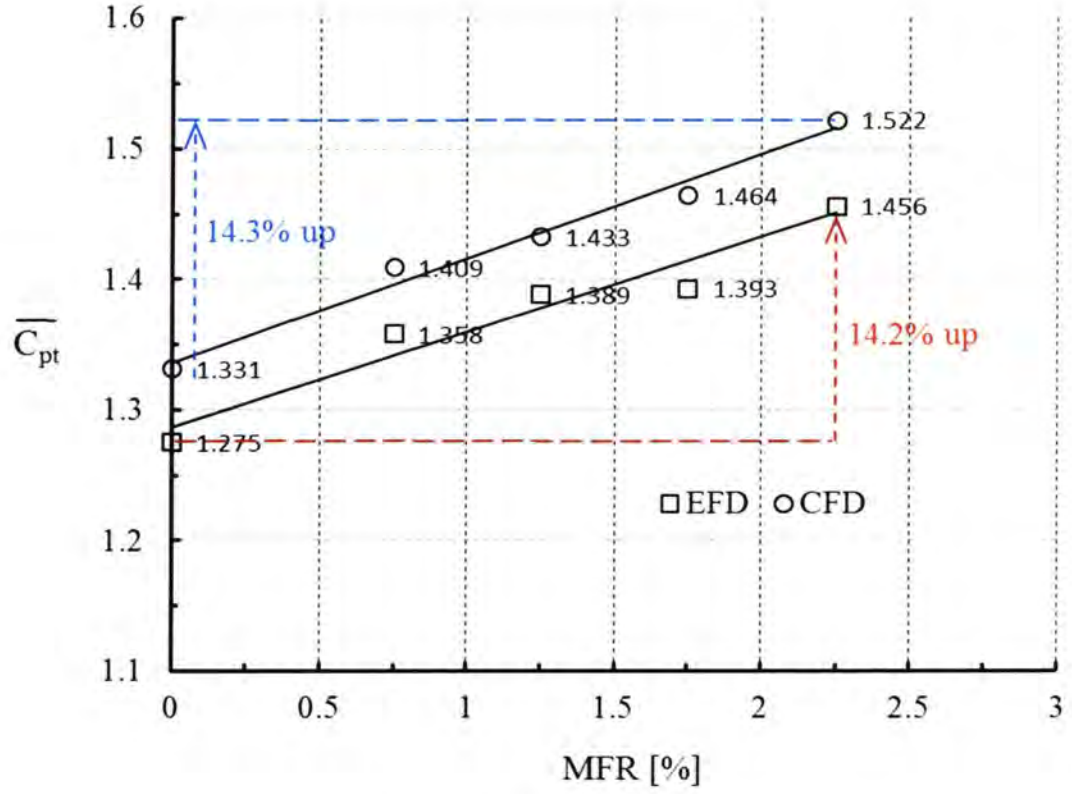

Figure 53 Loss trend in comparison between CFD and EFD

3.3.4 Predicted secondary flow structures

According to the discussion in the previous sections, even though the discrepancy in terms of position and shape of contours in comparison between CFD and EFD, they almost presented the similarity on the contour trend. For instant, the presence of the additional loss region which was due to the increased strength of the passage vortex has been captured in both studies. Thus, the advantage of the numerical simulation can be taken to predict the structures of the secondary flows before and after the leakage flow injection. Present section intended to provide details flow structures on the endwall region predicted by the CFD. The details will provide further understanding on the interaction between the leakage and the mainflow. Figure 54~Figure 56 show the vortex core generated at the swirling strength equal to 760 [s-1] for baseline case, MFR=1.25% and MFR=2.25%, respectively. The color of the vortex core is representing the vorticity, ζ valued within the range of 2000 [s-1] and –2000 [s-1]. In order to observe the formation of the vortical structures near the blade LE, a streamline is presented on stagnation plane on each figure where the line color represents the flow velocity. Furthermore, the ζ contour at Plane B which is located at approximately 60% from blade PS is also presented in each figure. These two planes enable the observation of the horse-shoe vortex (HSV) development in the cascade. Note that $x/C_{ax} = 0$ is parallel to the position of the blade LE.

In the baseline case as shown in Figure 54, CFD has predicted the formation of pressure side leg horse-shoe vortex (PS-HSV) and suction side leg horse-shoe vortex (SS-HSV) near the blade leading edge. PS-HSV travels from the blade PS to neighboring blade SS consequently meet the SS-HSV coming from adjacent blade LE. The presence of the leading edge corner vortex has also been predicted at both sides of blade leading edge with a smaller core compared to HSV. Based on the streamline, the HSV is centralized at $x/C_{ax} = -0.15$, z/s=0.02 and the higher ζ core captured on Plane B located at approximately $x/C_{ax} = 0.35$ illustrates the PS-HSV moving towards downstream of the blade passage. A modification of the existing secondary flow structures occurred when the leakage flow is injected, see Figure 55. The introduction of the leakage injection upstream of the blade LE unfortunately induced to the flow blockage just downstream of the slot (slot location, $x/C_{ax} = -0.63$). As a result, the strength of the HSV near the blade LE was amplified as indicates by the increases diameter of the swirling flow in Figure 55. Figure also clearly explained the increase of HSV strength with the higher swirling energy of the core compared to the baseline case. This resulting in increase of PS-HSV energy which will allow it to travel across from blade PS and lifted- off onto adjacent blade SS. At MFR=2.25%, ζ contour on Plane B in Figure 56 shows that the direction of the PS-HSV slightly shifted towards upstream. The PS-HSV seems to be merged with the adjacent flow ζ caused by the separation flow downstream of the slot. At MFR=1.25%, a newly generated vortex core can clearly be observed along the pitchwise direction just downstream of the slot. As shown in Figure 57, due to the high pressure near the blade stagnation region, ejected leakage flow tends to move towards centre of the blade passage and accumulated with the opposite flow direction of the leakage flow that coming from adjacent blade. This phenomenon has influenced to the formation of new vortex core (accumulated flow vortex, AFV) which then developed along the blade SS surface. As been shown in previous section, the presence of this vortex core is predicted to responsible to the additional loss which was generated after the leakage flow injection. As the MFR increases, the AFV strength is further increases. At MFR=2.25%, see Figure 56, ejected leakage flow has much higher momentum to penetrates into the main stream; particularly near the stagnation region compared to the lower MFR cases. Higher blockage consequently influenced to higher strength of the HSV. Noted that the higher energy of the PS HSV, the earlier the reattachment onto the adjacent blade SS occurs. The position of the PS-HSV shifted again toward upstream compared to the lower injection and baseline cases as shown in Plane B in each figure. This phenomenon consequently deflected the direction of the LE CV upwards. The explanation parallel to the position of first loss core which is shifted towards midspan at a higher MFR as shown in C_{pt} contours in EFD and CFD.

To obtain the full understanding on the vortex propagations, the vortex core generated near the blade trailing edge are also presented in Figure 58~Figure 60. Again, the ζ contour at Plane 1.25Cax is also shown in order to directly recognize the sources of the ζ from the vortex core. Further downstream of the blade leading edge, it can be observed that PS-HSV was deflected by the SS-HSV before attaching onto the adjacent blade SS surface, see Figure 58. This SS-HSV is actually coming from adjacent blade suction, losing its swirling energy when travels away from the blade leading edge. In contrast, the strength of the LE-CV increases near the blade throat and developed in the same direction with the PS-HSV to become a large passage vortex at blade downstream plane.

The first C_{pt} core which was presented in Figure 43 (a) and Fig. 50(a) are considered to be associated with this particular vortex core. Figure 58 also shows the origin of the counter vortex (CV) located just downstream of the blade throat. The CV rotating in anti-clockwise direction was also captured by the ζ contour shown in Figure 50 (b) ~ Figure 52 (b). Figure 59 and Figure 60 also clearly indicate the development of the AFV near the blade TE. Thus, the newly generated vortex core, AFV at upstream seems to be responsible to the additional losses. Since the ζ contours based on CFD is showing almost similar trend with the EFD, the predicted vortex core could explain the sources of the flow vorticity as shown in bottom side of Figure 58~Figure 60. Figure 61 shows the birdview of the flow streamline in comparison between baseline and injection cases.

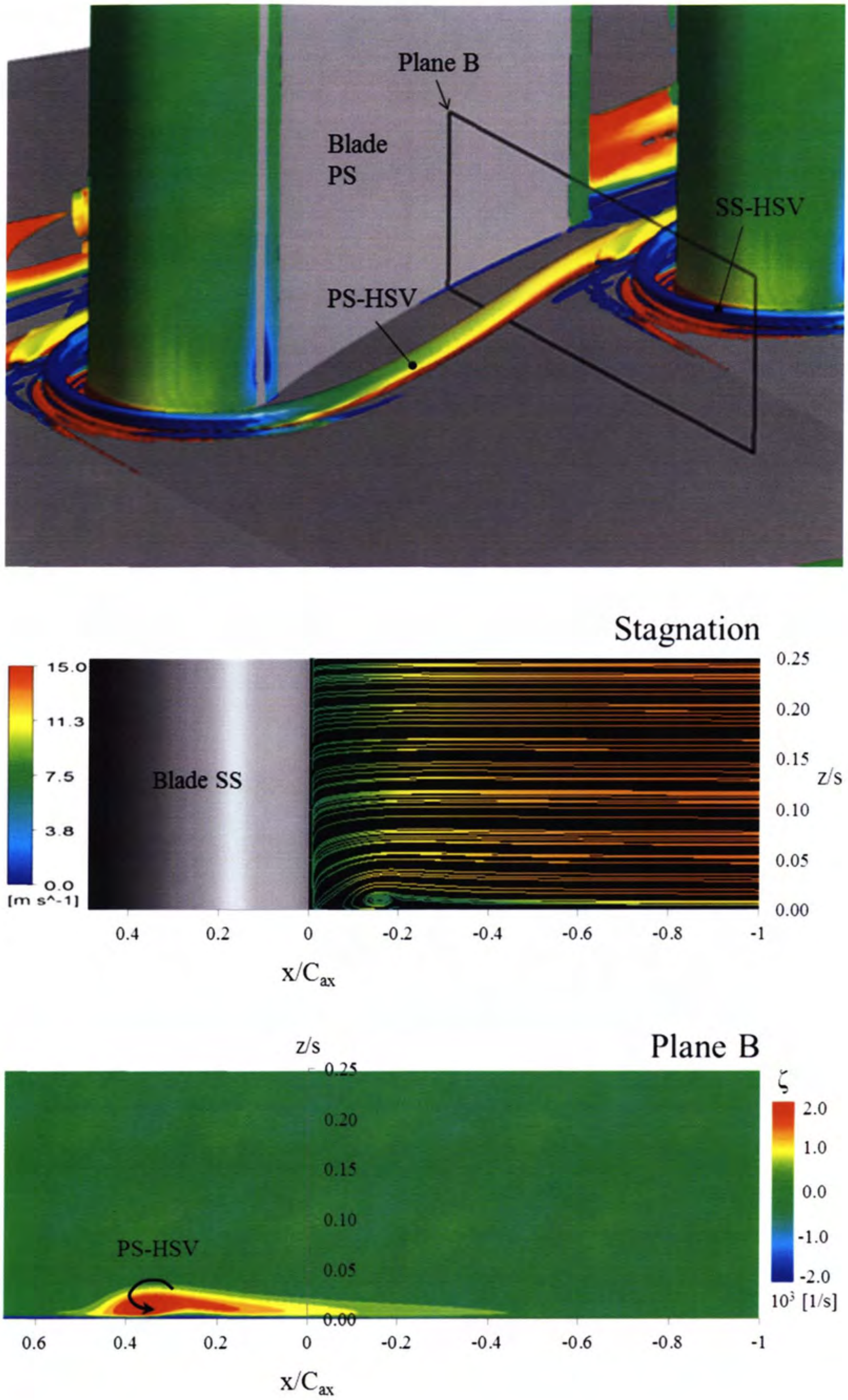

Figure 54 Predicted secondary flow structures at upstream for baseline case

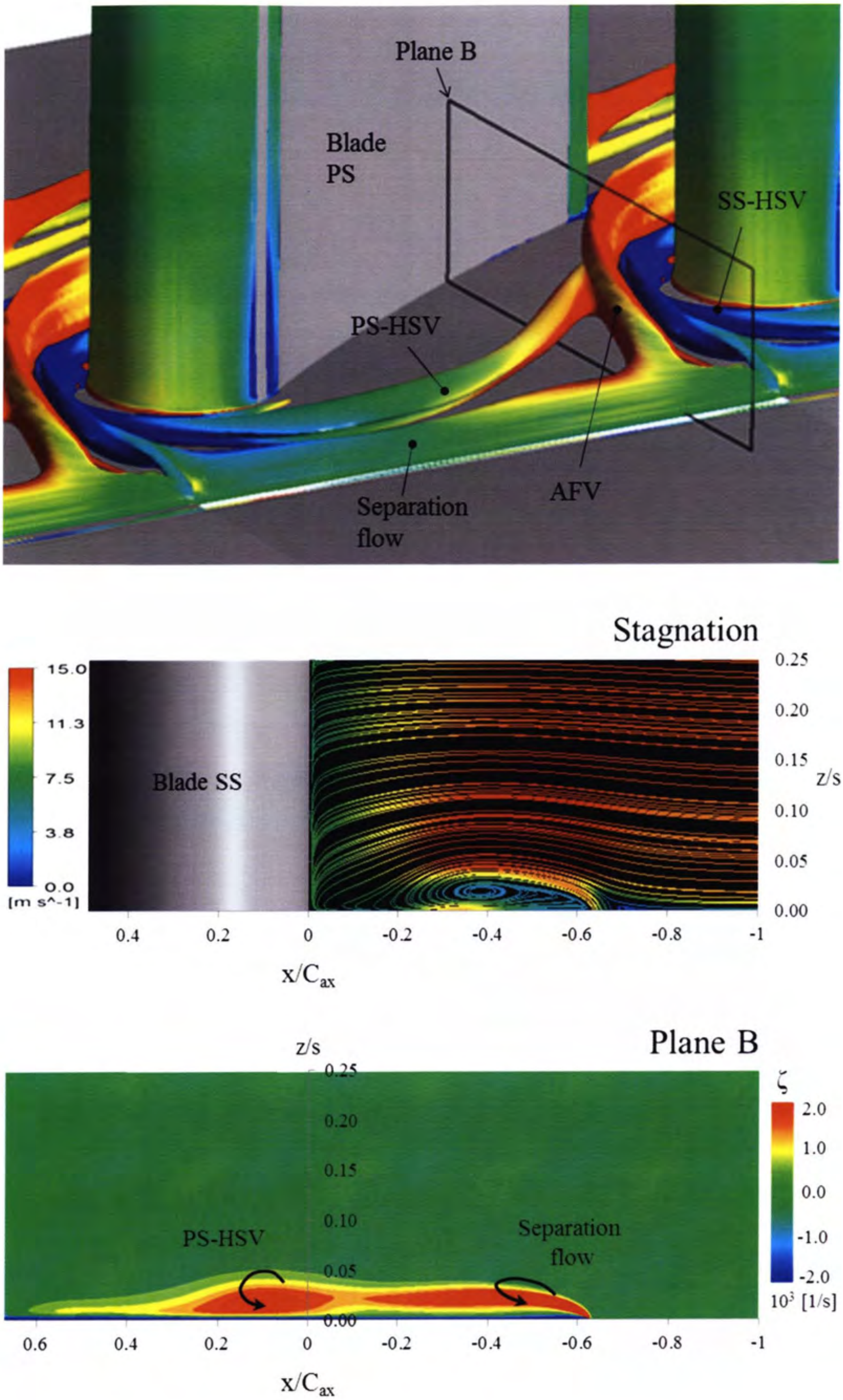

Figure 55 Predicted secondary flow structures at upstream for MFR=1.25%

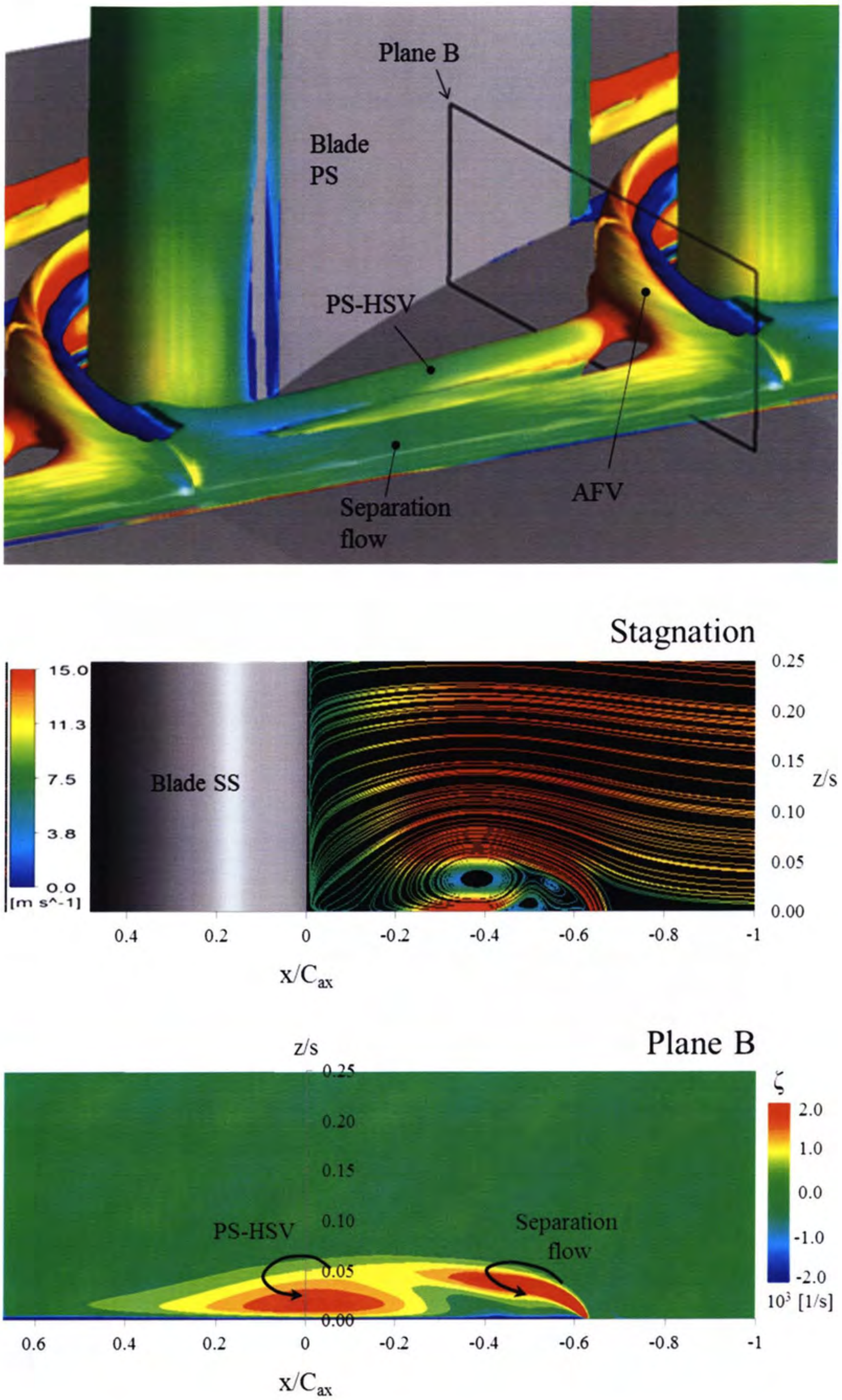

Figure 56 Predicted secondary flow structures at upstream for MFR=2.25%

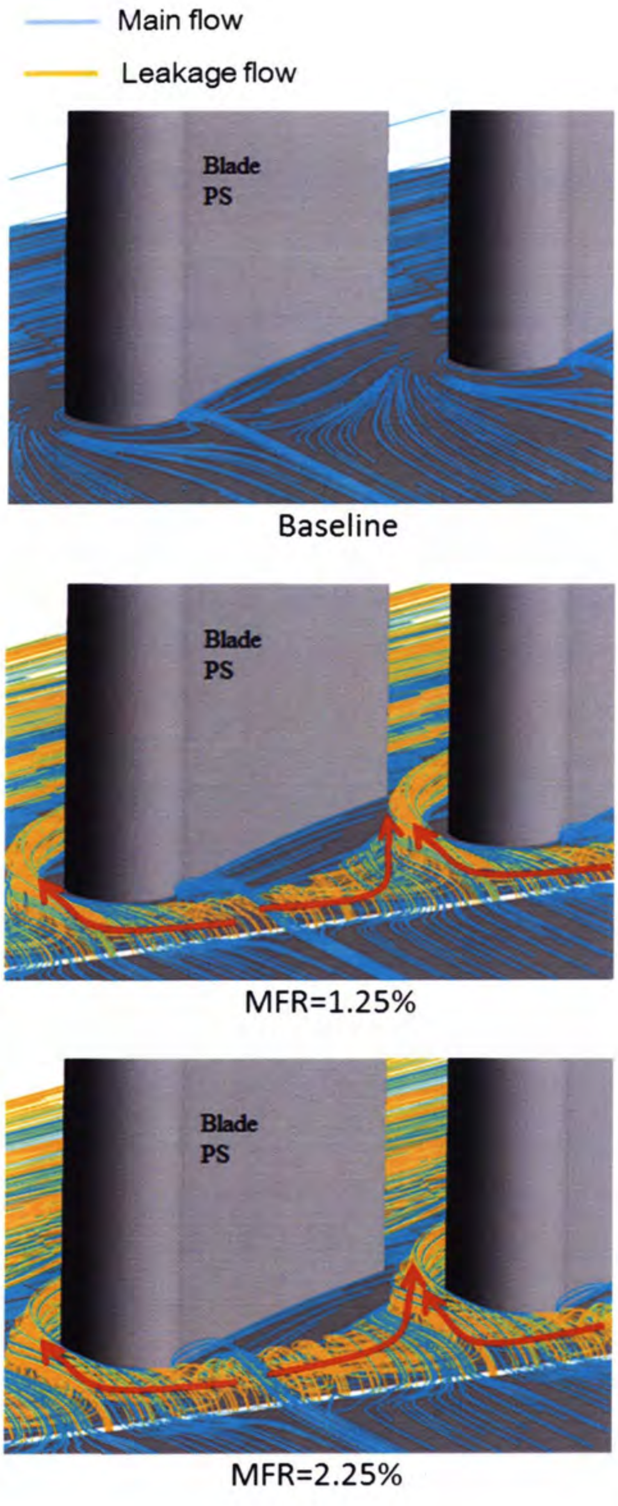

Figure 57 3D streamline on the endwall region for baseline (top), MFR=1.25% (middle) and MFR=2.25% (bottom)

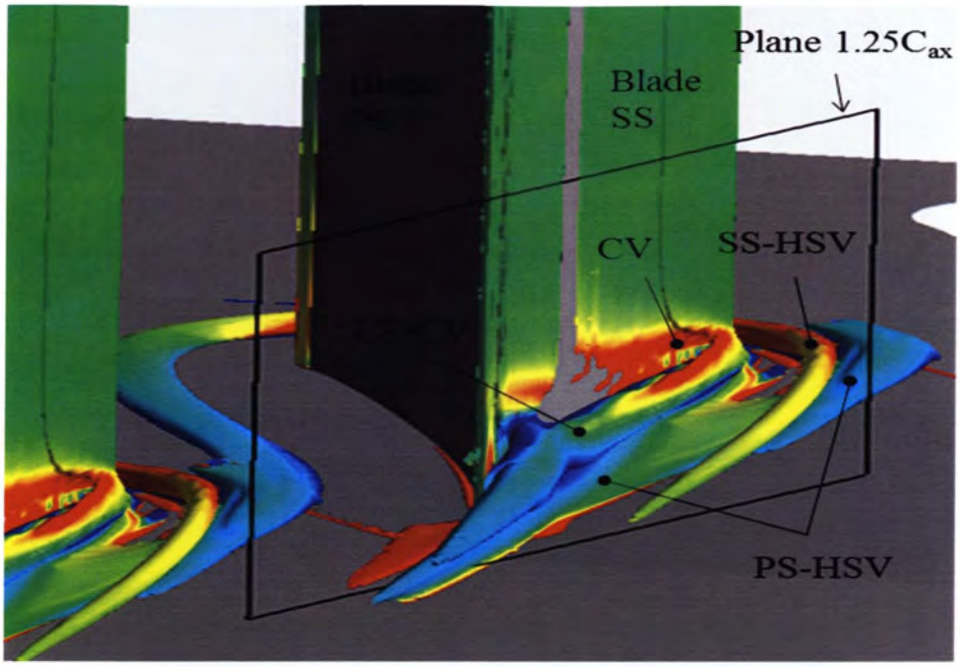

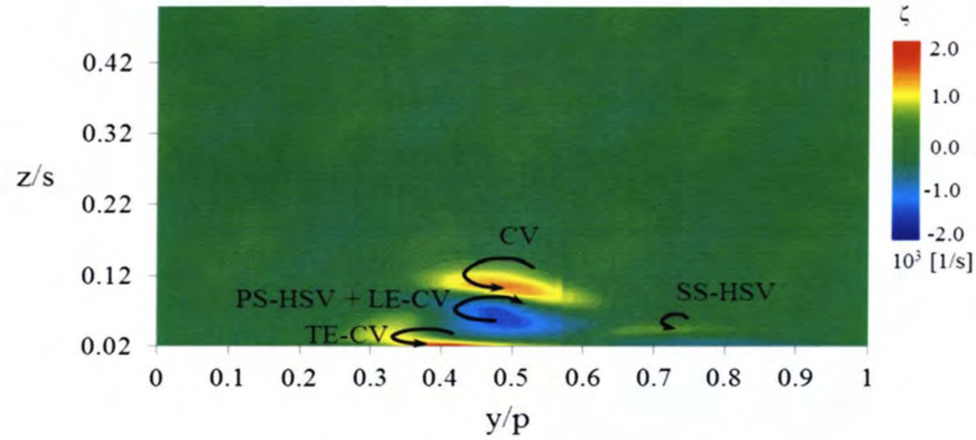

Plane 1.25C_{ax} vorticity-CFD

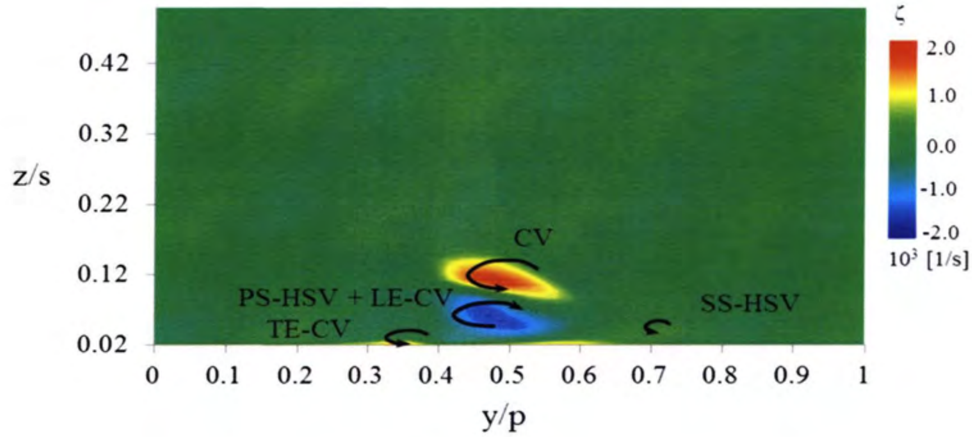

Plane 1.25C_{ax} vorticity-EFD

Figure 58 Predicted flow structures at downstream for baseline case

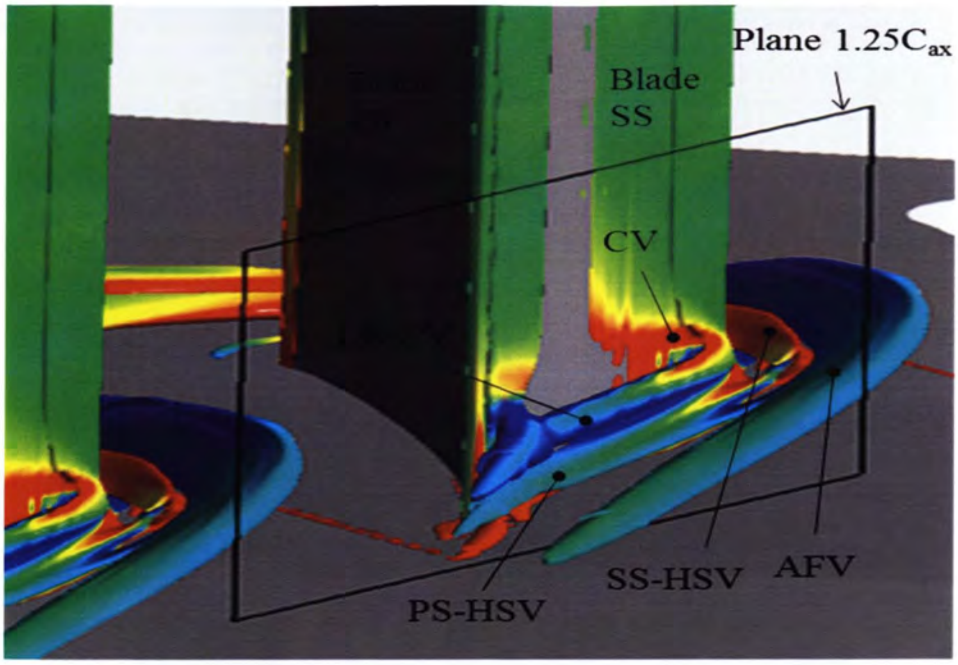

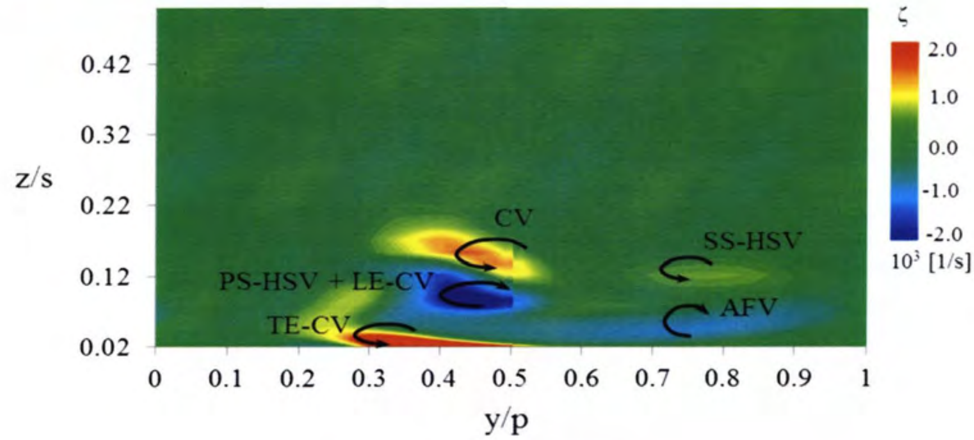

Plane 1.25C$_{ax}$ vorticity-CFD

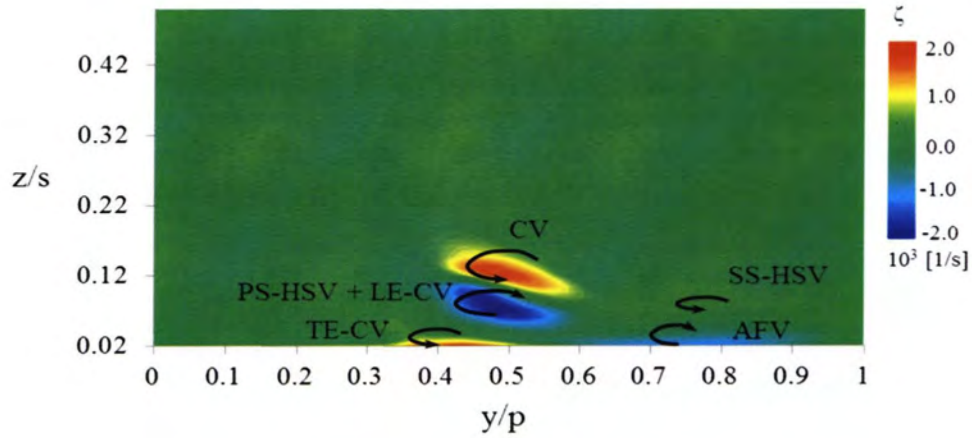

Plane 1.25C$_{ax}$ vorticity-EFD

Figure 59 Predicted flow structures at downstream for MFR=1.25%

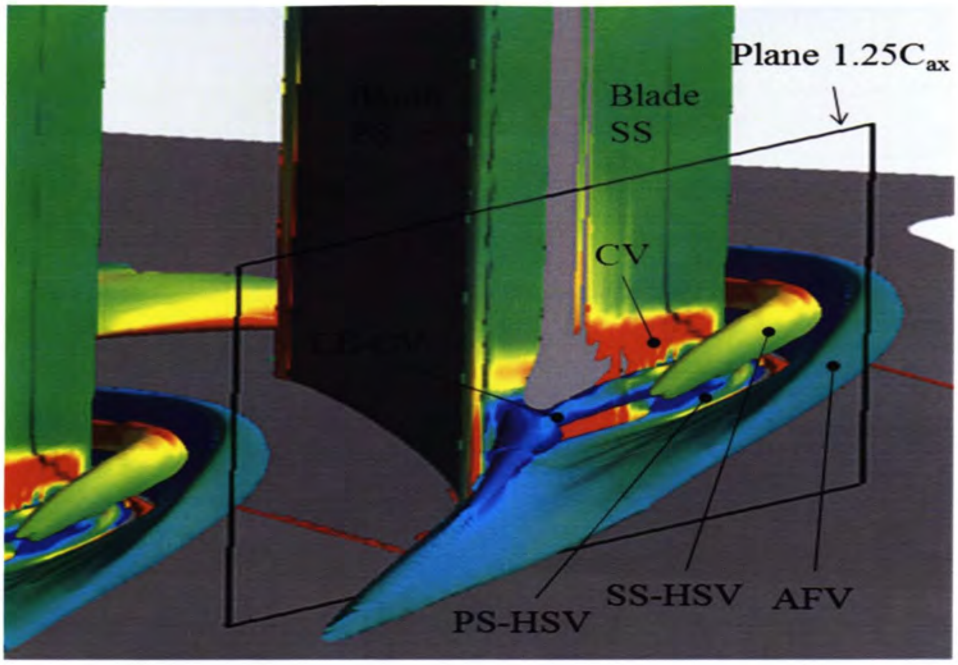

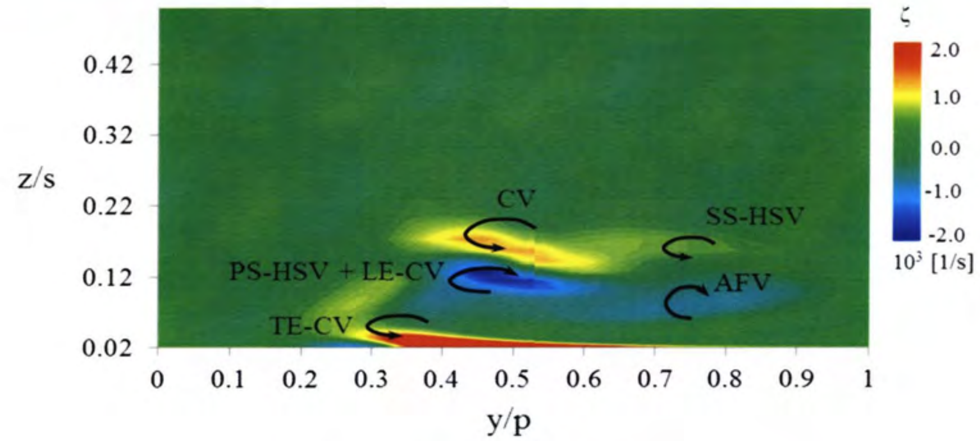

Plane 1.25C$_{ax}$ vorticity-CFD

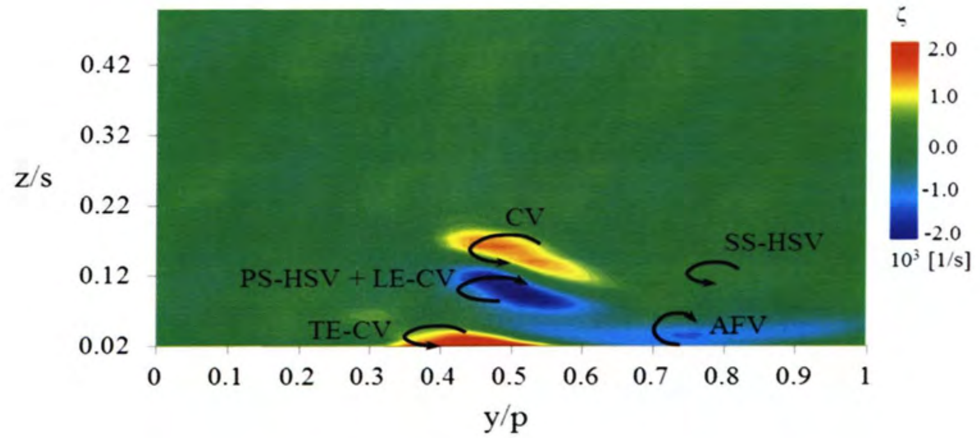

Plane 1.25C$_{ax}$ vorticity-EFD

Figure 60 Predicted flow structures at downstream for MFR=2.25%

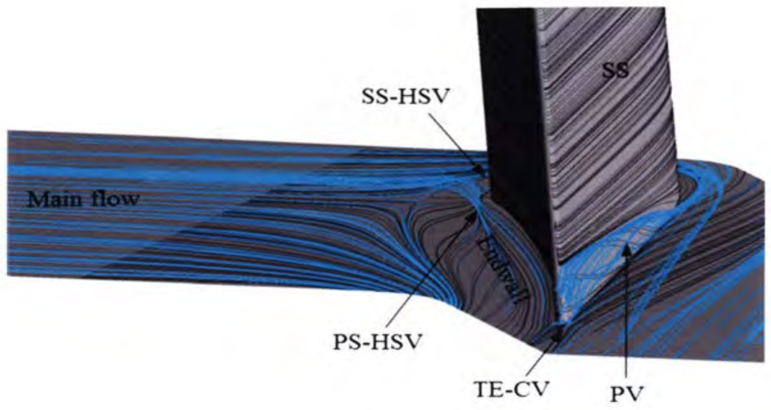

(a)Baseline case

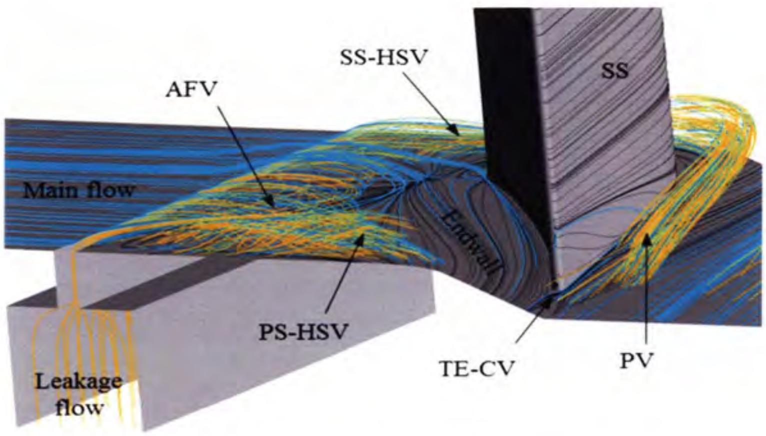

(b) MFR = 1.25%

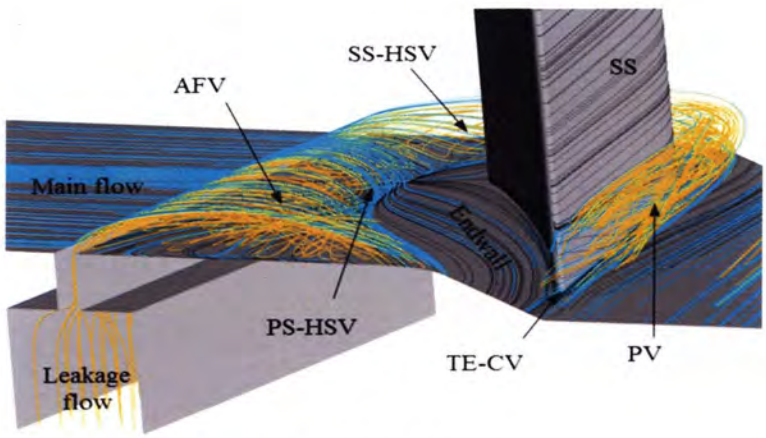

(c)MFR = 2.25%

Figure 61 Birdview of flow streamline for baseline, 1.25% and 2.25% injections

3.4 Effect of the secondary air behaviour on C_{pt} contours

3.4.1 CFD modelling

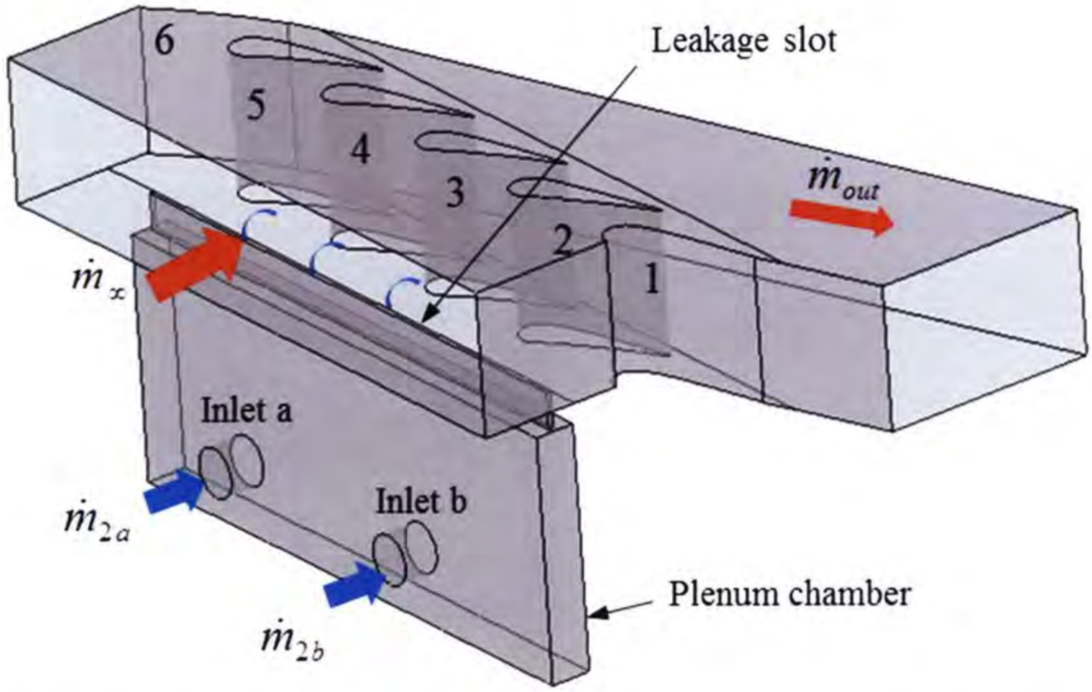

Figure 62 CFD modelling to predict the effect of secondary air profile on C_{pt}

The discrepancy in terms of shape and position of the loss contours between CFD and EFD shown in previous section especially for the leakage injection cases were considered due to the different secondary inlet profile. In CFD, the translational periodicity was applied on the interface between the pitch thus the uniform flow distribution were predicted along the slot exit. However, the secondary flow behaviour cannot be revealed in real situation due to the difficulty of measurement device to access in a very limited area inside the plenum chamber. Furthermore, it is very difficult to obtain a uniform flow distribution inside the plenum chamber. Thus, the mass flow rate, $\dot{m}_2$ has been applied on the secondary inlet boundary condition based on the experimental condition which was measured by laminar flow meter. From Figure 18, a secondary air coming from the laminar flow meter was split into two inlet pipes before entering the plenum chamber. In order to predict the flow with almost the same condition to the real situation, a new CFD model including the plenum chamber with two inlets (**a** and **b**) was also generated as shown in Figure 62. Plenum chamber extended for 4 pitches parallel to the slot length. Gridgen was applied to generate the mesh with 12.4 million elements with fully structured multi blocks. By considering the time and cost required, approximately 1.5 million of mesh element were generated for each blade pitch. The same grid topology was applied on each blade pitch thus the bias causes by the grid itself can be avoided. This model enables the studies on the secondary air behaviour on the C_{pt} contours. The same turbulence model used in previous flow prediction, SST was adopted. From Figure 62, the total mass flow rate at cascade downstream can be represented as

$$\dot{m}_{out} = \dot{m}_{\infty} + \dot{m}_2 \tag{35}$$

Since the secondary air inlet was split into two pipes (inlet **a** and inlet **b**), here $\dot{m}_2$ can be represented as

$$\dot{m}_2 = \dot{m}_{2a} + \dot{m}_{2b} \tag{36}$$

Thus,

$$\dot{m}_{out} = \dot{m}_{\infty} + \dot{m}_{2a} + \dot{m}_{2b} \tag{37}$$

In order to investigate the effect of the flow inside the plenum chamber, fixed $\dot{m}_2$ at MFR=2.25% was predicted with several cases by different $\dot{m}_{2a}$ and $\dot{m}_{2b}$. Five cases were predicted in this study.

Case 1

$$\boxed{\dot{m}_{2a} = \dot{m}_{2b} = \frac{1}{2}\dot{m}_2}$$

Case 2

$$\boxed{\dot{m}_{2a} = \frac{2}{3}\dot{m}_2} \qquad \boxed{\dot{m}_{2b} = \frac{1}{3}\dot{m}_2}$$

Case 3

$$\boxed{\dot{m}_{2a} = \frac{3}{4}\dot{m}_2} \quad \boxed{\dot{m}_{2b} = \frac{1}{4}\dot{m}_2}$$

Case 4

$$\boxed{\dot{m}_{2a} = \frac{1}{3}\dot{m}_\infty} \quad \boxed{\dot{m}_{2b} = \frac{2}{3}\dot{m}_\infty}$$

Case 5

$$\boxed{\dot{m}_{2a} = \frac{1}{4}\dot{m}_\infty} \quad \boxed{\dot{m}_{2b} = \frac{3}{4}\dot{m}_\infty}$$

The same mass flow rate was applied to $\dot{m}_{2a}$ and $\dot{m}_{2b}$ in Case 1, $\dot{m}_{2a} > \dot{m}_{2b}$ in Case 2 and Case 3 while $\dot{m}_{2a} < \dot{m}_{2b}$ in Case 4 and Case 5. These all cases were applied into two secondary inlets and the different flow behaviour inside plenum chamber were expected. Since the measurement grid of the total pressure was located at downstream of the Blade 3, see Figure 22, thus the same position of the C_{pt} contour will be observed to see the changes of the flow behaviour by each cases.

3.4.2 Results and discussion

Predicted flow streamline inside the plenum chamber by different mass flow rate from inlet **a** ($\dot{m}_{2a}$) and inlet **b** ($\dot{m}_{2b}$) at fixed $\dot{m}_2$ is presented in Figure 63. There are three different colours of streamline; blue represents the main flow, yellow represents a leakage flow coming from inlet **a** while red represents a leakage flow coming from inlet **b**. All cases illustrate that the leakage flow from both inlets were deflected by the plenum chamber wall which just located close to the air inlet. Thus they tend to move towards side and bottom wall and finally penetrated into the mainstream. This phenomenon influenced to the high turbulence flow inside the chamber. It clearly shows that the flow inside the plenum chamber is ununiformed before entering the mainstream through the slot. Furthermore, the flow structures inside the chamber is significantly depends on the amount of flow from inlet **a** and inlet **b**. Case 1 in Figure 63 (a) presents that the penetration of the flow toward each other from both inlet almost the same since the same mass flow was applied. For the Case 2 and Case 3 where $\dot{m}_{2a} > \dot{m}_{2b}$, see Figure 63 (b) and (c), the flow inside the chamber is highly influenced by the yellow streamline ($\dot{m}_{2a}$) and consequently changed the flow structure. On the other hand, Case 3 and Case 4 for $\dot{m}_{2a} < \dot{m}_{2b}$, see Figure 63 (d) and (e), the flow is highly influenced by red streamline ($\dot{m}_{2b}$) instead of yellow. Figure 64 (a)~(d) presents the endwall streamline which illustrates the direction of the leakage flow coming from the plenum chamber based on Case 1~Case 5, respectively. The concentration of flow observation will be made on the flow structures between Blade 3 and Blade 4 where its parallel to the position of the traverse grid at blade downstream. As being discussed in previous section, the leakage flow coming from the slot tends to move towards center of the blade passage due to the high pressure close the blade stagnation region. Then it accumulated with the opposite flow direction coming from adjacent blade stagnation region to generate a newly vortex core, AFV (as shown in Figure 56). The shape and position of the C_{pt} contours presented in previous section for the leakage injection cases are considered to highly influenced by the formation of AFV.

As shown by Case 1 in Figure 64 (a), AFV is actually generated by the accumulation of flow coming from inlet **a** and inlet **b** (illustrates by the arrow **a** and **b**). However, red streamline coming from inlet b mostly influences the AFV. In Case 2 when $\dot{m}_{2a}$ was increased, see Figure 64 (b), red streamline seems to be reduced and its almost the same with the yellow streamline coming from inlet a to generate AFV. However, when the $\dot{m}_{2a}$ continuously increases as Case 3 in Figure 64 (c), AFV mostly influenced by the yellow streamline. In contrast, AFV was mostly generated by the red streamline when $\dot{m}_{2b}$ being increases and yellow streamline was eliminated at this region, see Figure 64 (d) and (e). The changes of flow phenomenon presented by Case 1~Case 5 is considered at least to change the characteristic of the AFV consequently effected to the shape and position of the C_{pt} contours at blade downstream. C_{pt} contours downstream of Blade 3 for Case 1~Case 5 are presented in Figure 65 (a)~(e). The range of contours are the same with the C_{pt} contours shown in Figure 47 (a) and Figure 52 (a) thus direct comparison can be made towards EFD and the periodicity applied CFD modelling. Periodicity applied CFD model was presented in Figure 35 and Figure 36 in Chapter 2. The first loss core in Figure 65 slightly changed among the cases. Even though this core was actually associated by the PS-HSV and also LE-CV, the change of the AFV characteristics is predicted to give some effect on the development of PS-HSV since it was deflected by the AFV near the blade SS (as shown in Figure 56). As a result, slightly different shape of first core was presented by each cases. Furthermore, the different flow structure inside the chamber gives a significant change on the third loss core. The different leakage fluid momentum from both sides (**a** and **b**) is considered might be changed the direction and strength of the AFV which thus resulting different C_{pt} contour at downstream. In comparison with the EFD in Figure 47 (a), Case 3 illustrates almost the similar shape of third core among the cases. Additionally, the shape is also significantly different in comparison with periodicity model (earlier model) in Figure 52 (a). However, it is difficult to investigate the actual condition by the measurement in order to have a similar condition in CFD simulation due to the accessibility of the measurement device in such region.

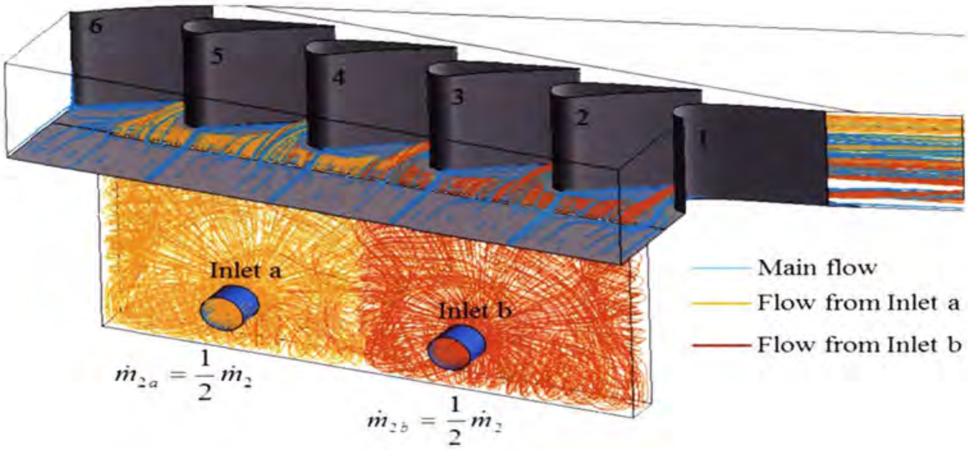

(a) Case 1

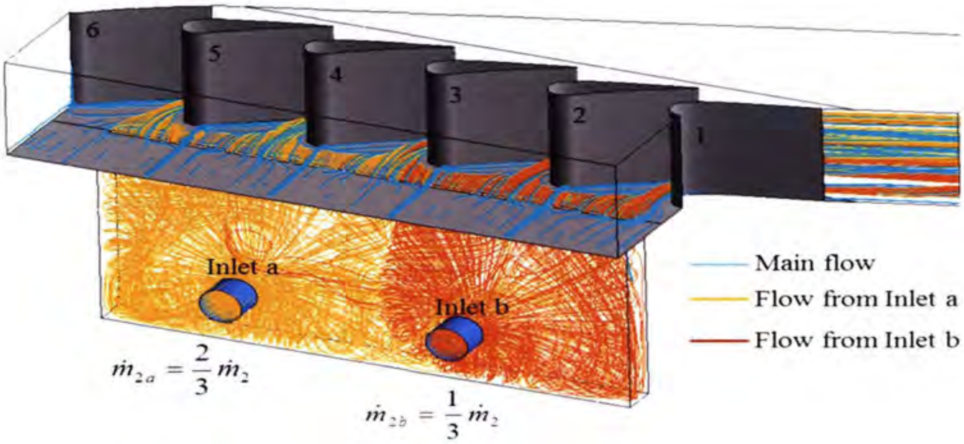

(b) Case 2

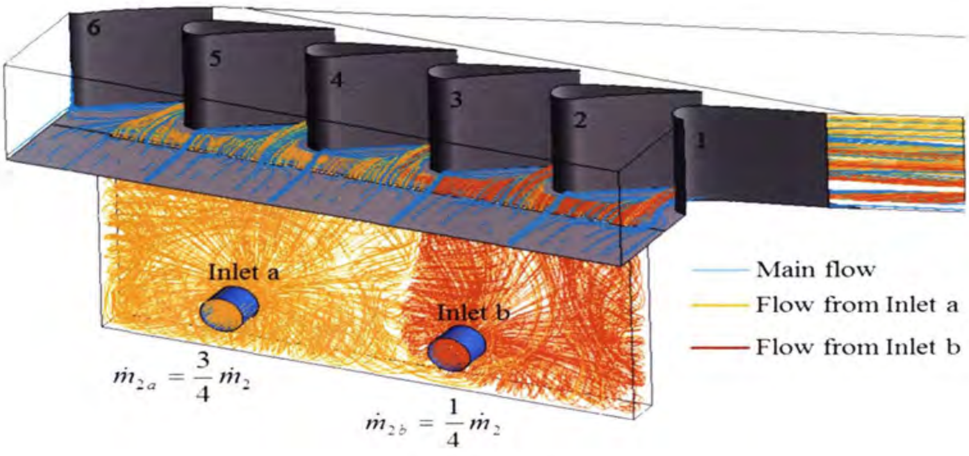

(c) Case 3

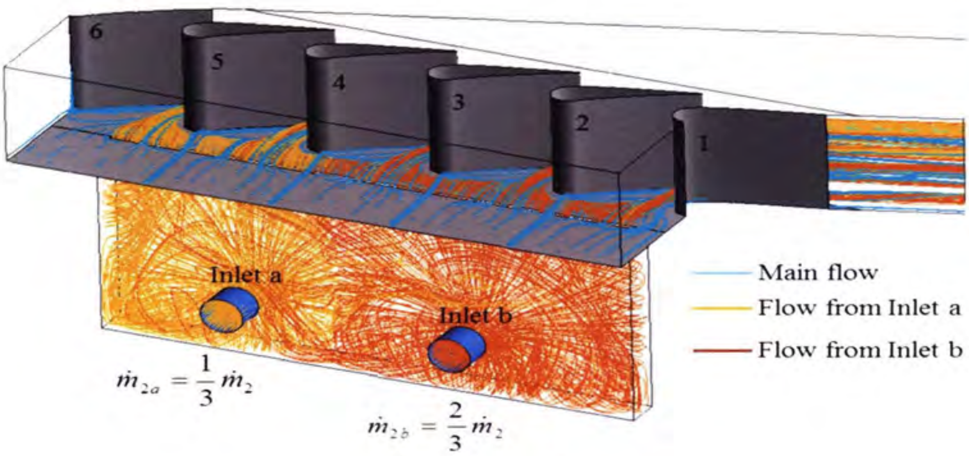

(d) Case 4

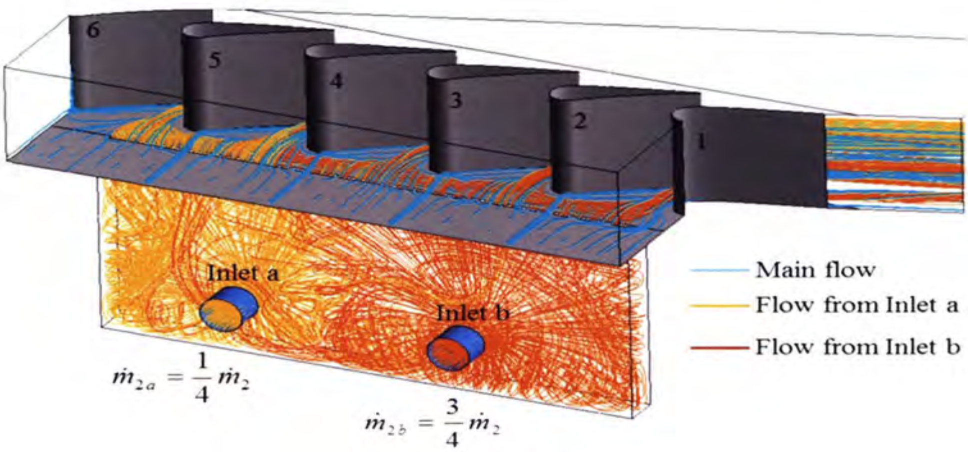

(e) Case 5

Figure 63 Plenum chamber flow streamline for each case

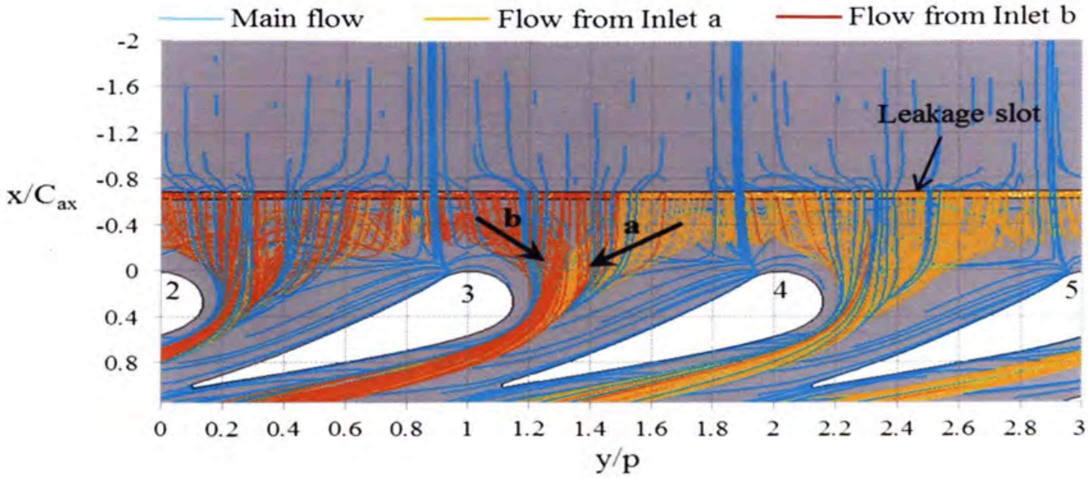

(a) Case 1

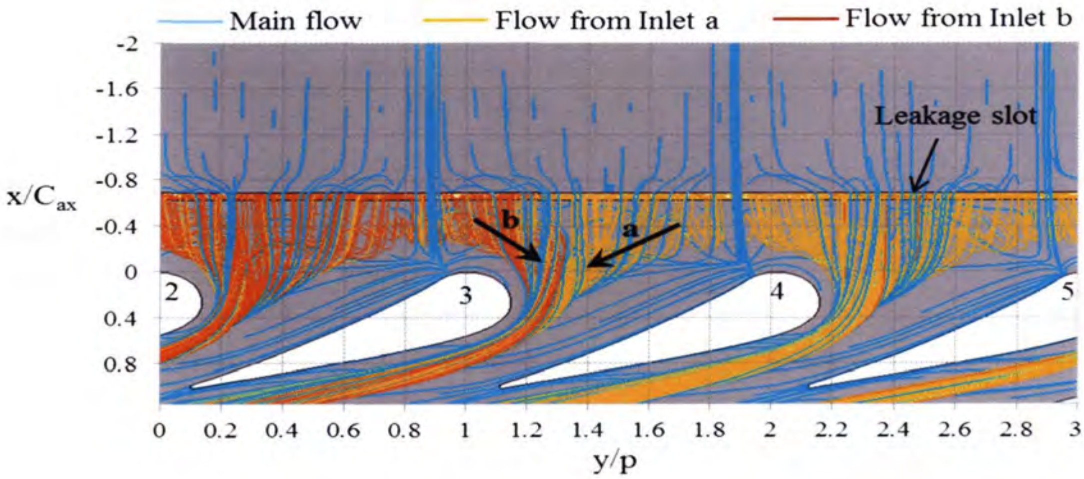

(b) Case 2

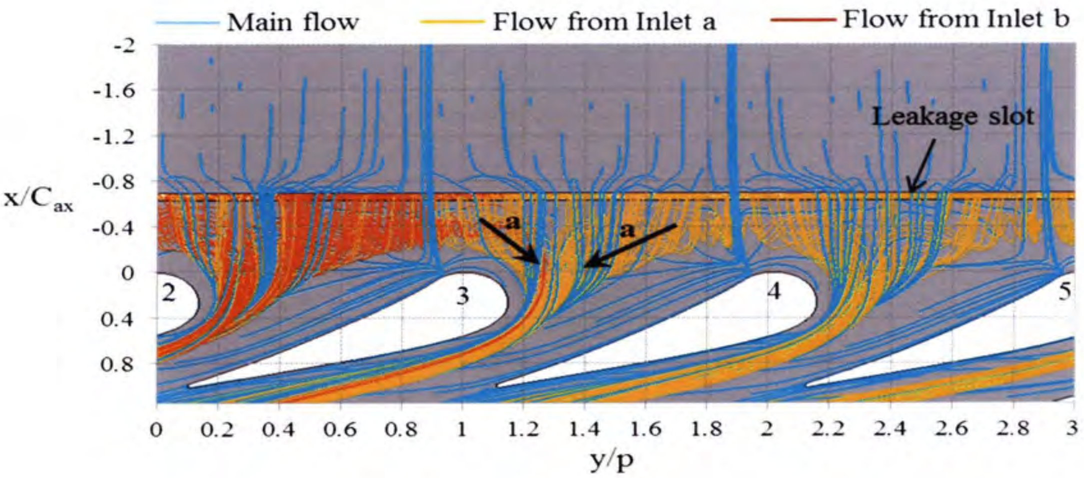

(c) Case 3

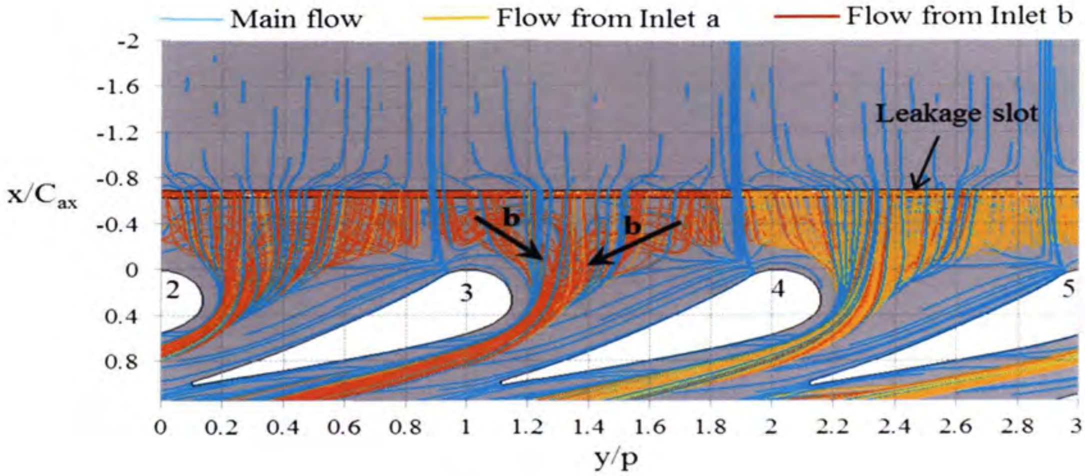

(d) Case 4

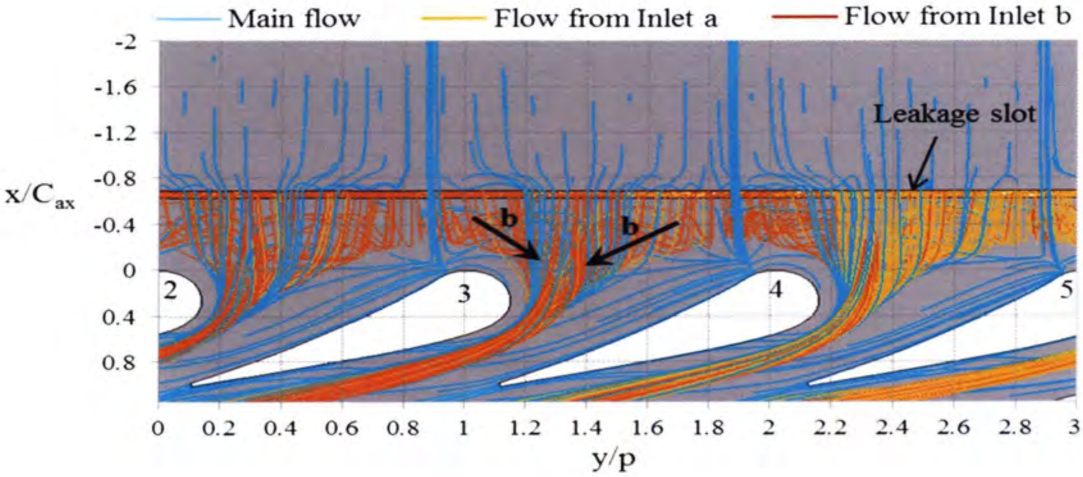

(e) Case 5

Figure 64 Endwall streamline for each case

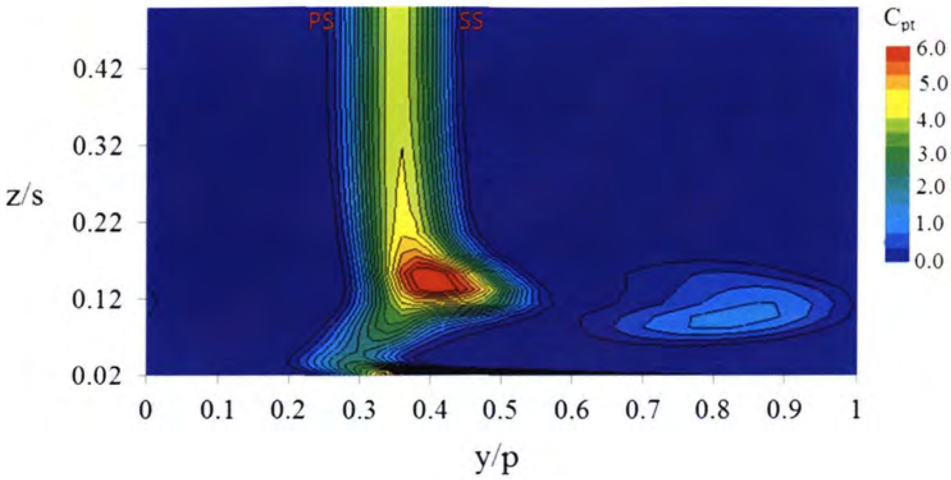

(a) Case 1

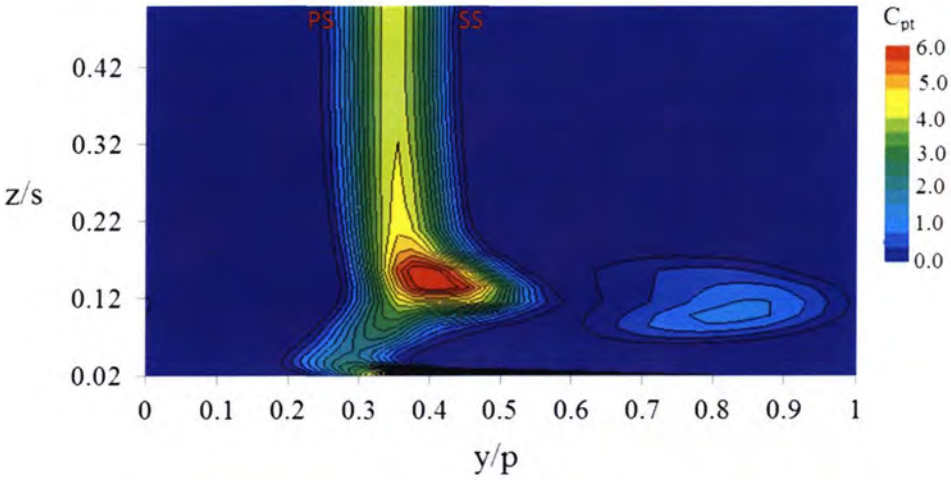

(b) Case 2

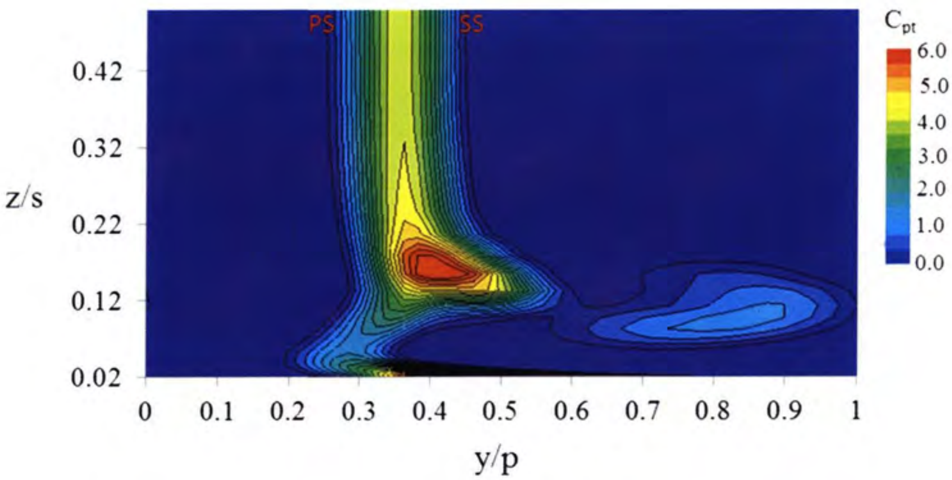

(c) Case 3

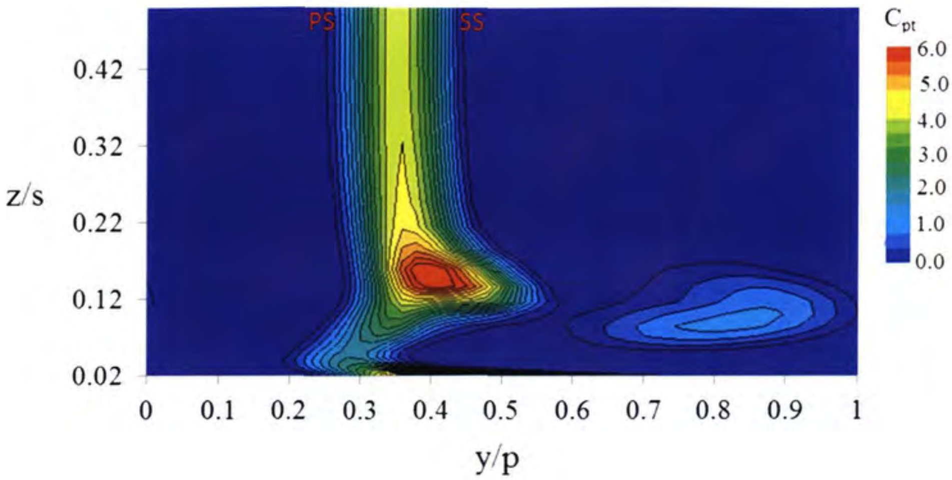

(d) Case 4

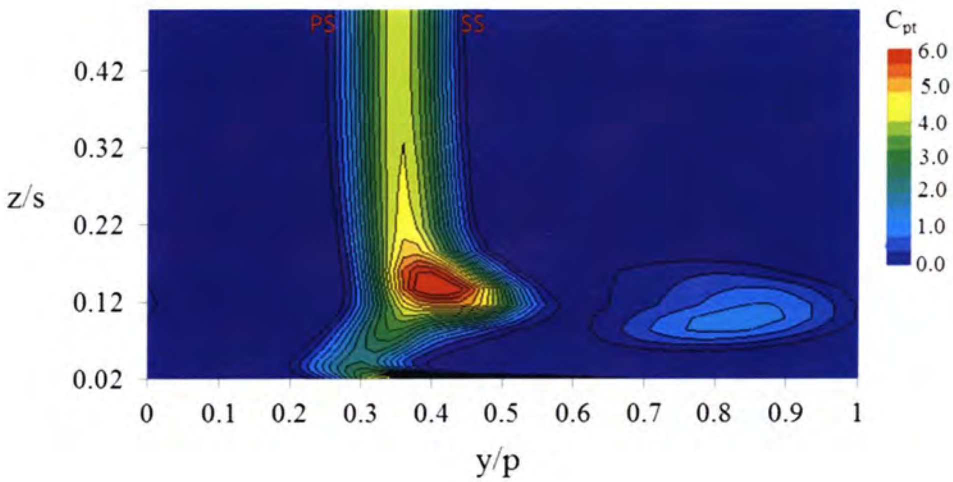

(e) Case 5

Figure 65 C_{pt} contour at Plane $1.25C_{ax}$ for each case

3.5 Thermal performances

3.5.1 Experimental based performances

The potential of the leakage flow injection to protect the endwall surfaces has been revealed by conducting liquid crystal for surface temperature measurement. Based on the temperature data, non-dimensional temperature which is represented by film cooling effectiveness, η is used to describe the cooling performance of leakage flow. The blue contour illustrates the lower η while the red one illustrates the higher η. Figure 66 (a) ~Figure 69 (a) indicate the η contours for MFR=0.75%, 1.25%, 1.75% and 2.25%, respectively. In order to have details information about the thermal performance, the heat transfer coefficient, h and the RGB propagation illustrated by the liquid crystal are also included in each figure. Figures illustrate the contour from the position of the leakage slot (x/C_{ax}= -0.63) till downstream of the blade TE for two pitches (y/p = 0~2). View of the two blades also included and that is the actual camera angle during measurement. Noted that the axis showing by the gridlines is only referring to the endwall surfaces and invalid for the blade tip region. This is because the camera was slightly inclined in order to capture the most important region in the measurement. At lower injection of 0.75%, see Figure 66 (a), the unprotected region in pitchwise direction is observed from y/p=0.2~0.8 and y/p=1.4~1.9. This is because the leakage flow was unable to be injected near the stagnation region due to the higher pressure. This influenced them to be injected into the mainstream at the lowest pressure region located between the two blades at approximately y/p=0.8~1.3. Since the leakage flow only be penetrated near this region, high level of η contours was obtained. However, when the leakage flow increased to 1.25%, see Figure 67, the protection region became wider not only in pitchwise direction but also in axial direction. Unlikely the case for 0.75%, the leakage flow provides a protection layer along the cascade pitch even though at a lower level η. Upstream of the blade LE, leakage flow provided the protection layer from x/C_{ax}=-0.63 to x/C_{ax}=-0.43 which approximately 35% of the endwall surfaces towards blade LE. This might be considered that the leakage flow had enough momentum to be penetrated into the higher pressure mainstream especially close to the stagnation region. At y/p=0.8~1.2, the contour also seems to expand from x/C_{ax}=-0.03 to x/C_{ax}=0.57 and the contour shape at this region are highly influenced by the secondary flow behavior. They likely influenced by the flow which is moving towards blade SS. Further increases the MFR to 1.75%, see Figure 68, the wider η

contour is presented. Approximately 50% of the endwall surfaces on upstream region are protected. However, at region y/p=0.8~1.2, no significant change on the protection layer can be observed in axial direction except in pitchwise direction. As expected, MFR=2.25%, see Figure 69, presented the greatest cooling performance compared to other cases where approximately 90% of protection layer is provided on the endwall surfaces close to the blade LE. The penetration of the leakage flow further downstream of the blade approximately x/C_{ax}=0.7 also can be observed at y/p=0.6~1.2. However, overall η contours illustrate the low η region just downstream of the leakage slot especially at higher MFR. As discussed in previous section, the normal injection of the leakage flow towards mainstream direction influenced to blockage which introduced to the separation flow. As a result, the leakage flow could not stay closer to the endwall resulting lower η at this region. Figure 70 presents the laterally averaged η starting from the slot position, x/C_{ax}=-0.63 and ended at blade TE, x/C_{ax}=1.0. Most of the cases show that the η pick are located at approximately x/C_{ax}=-0.4. This is might be the position where the leakage flow reattached to the endwall surface after the flow separation phenomenon which is occurred just downstream of the slot. The reattachment point of the leakage flow on the endwall surface downstream of the slot is closer to the slot position due to the weaker flow separation by the MFR=0.75%. This was explains by the position of the pick of each cases in Figure 70. The reduce trend of cooling performance is presented towards blade downstream. The leakage flow mixed out with secondary flow which finally prevented most of the leakage flow to stay closer to the endwall surface. This is considered as the main reason of the reduce trend as indicated in the Figure 70. Due to the higher penetration of the leakage flow into the mainstream at higher MFR, the protection region is higher compared to lower cases in axial direction. The cooling performance indicates in Figure 70 is parallel with the η contours presented in Figure 66 (a) ~Figure 69 (a) where the higher performance of η showed by higher MFR. The cooling performance is summarized by determined the mass-averaged of η as shown in Figure 71. The performance can be increased by increasing the amount of the leakage flow. MFR=2.25% illustrates the highest performance among the cases. $\bar{\eta}$ seems to be linearly increased as the MFR increases which approximately 6.7% for every 1% of MFR. Thus, the relationship between $\bar{\eta}$ and MFR can be represented by Eq. 38.

$$\bar{\eta} = 0.067\mathrm{MFR} \tag{38}$$

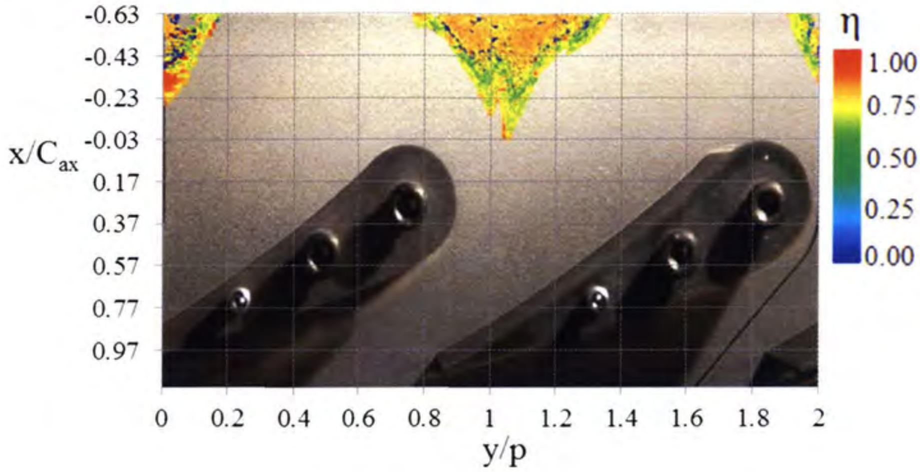

(a) Film cooling effectiveness

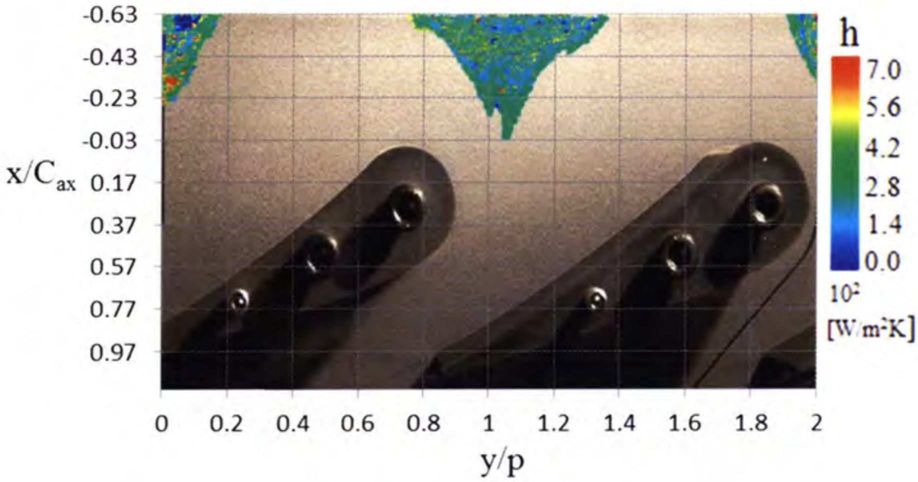

(b) Heat transfer coefficient

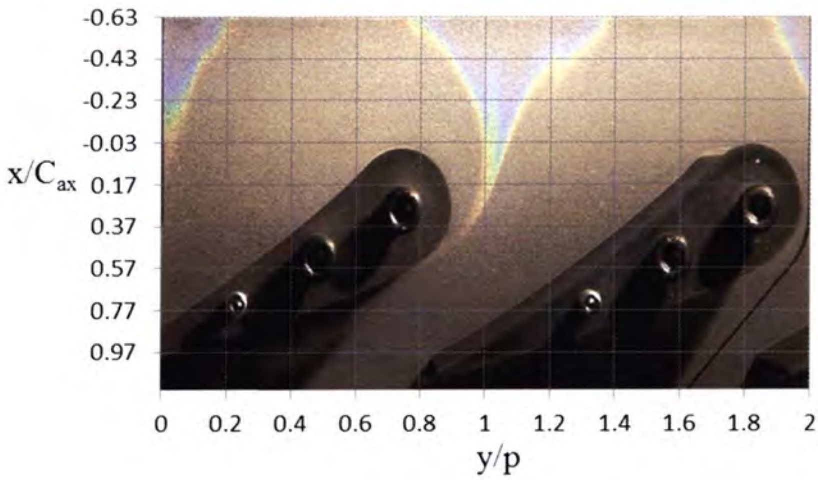

(c) Liquid crystal RGB propagation

Figure 66 Thermal performance for MFR = 0.75%

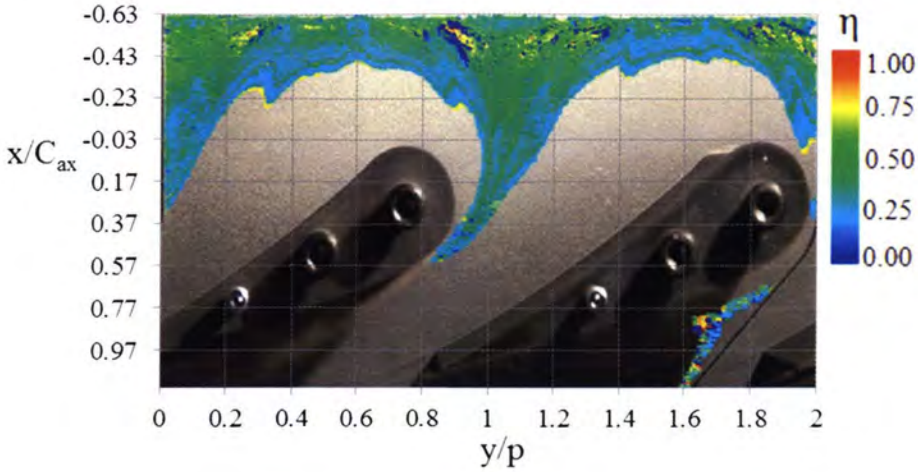

(a) Film cooling effectiveness

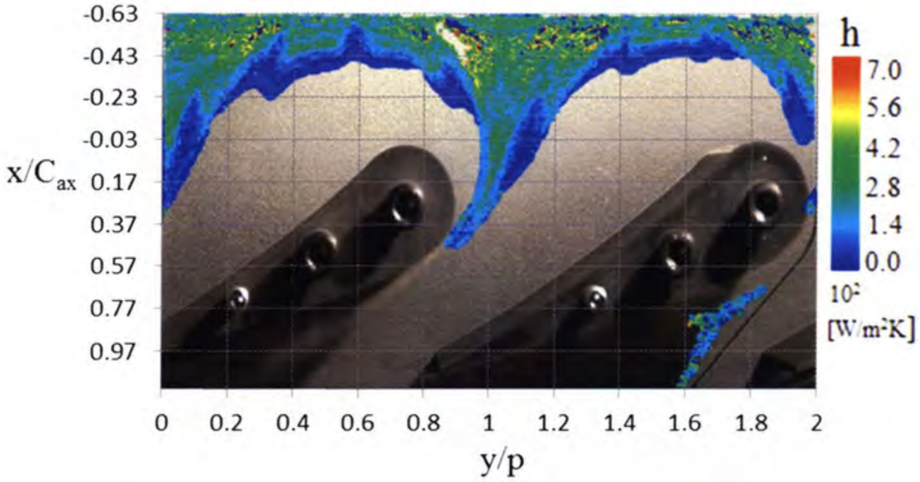

(b) Heat transfer coefficient

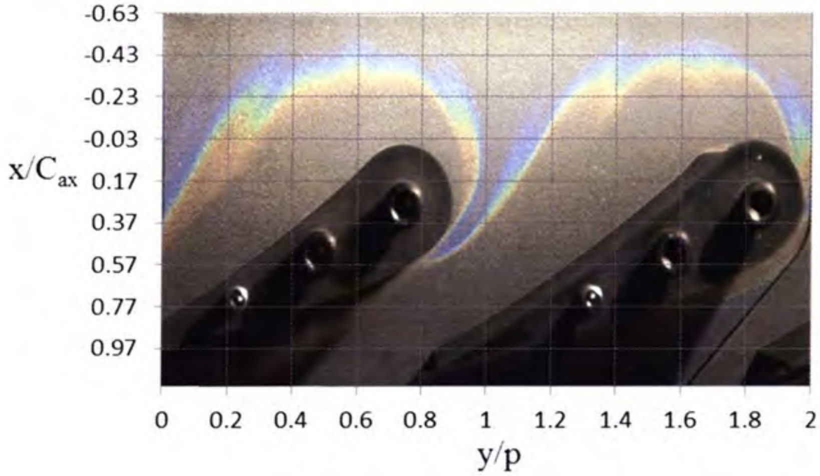

(c) Liquid crystal RGB propagation

Figure 67   Thermal performance for MFR = 1.25%

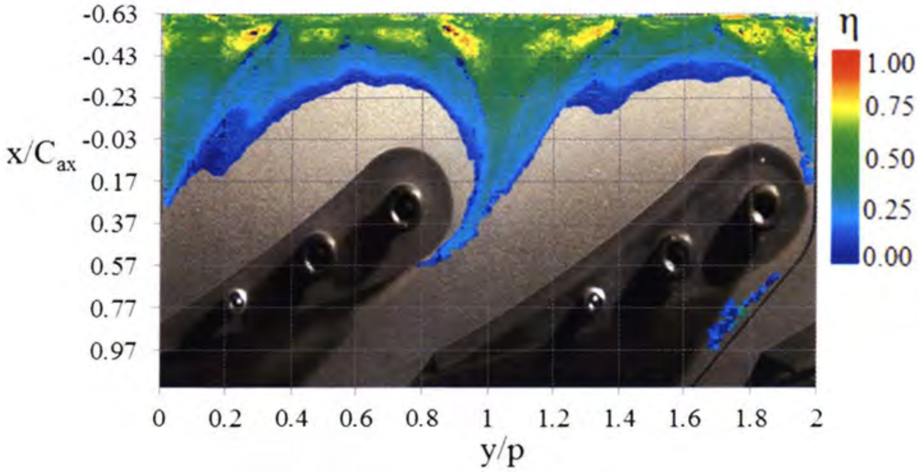

(a) Film cooling effectiveness

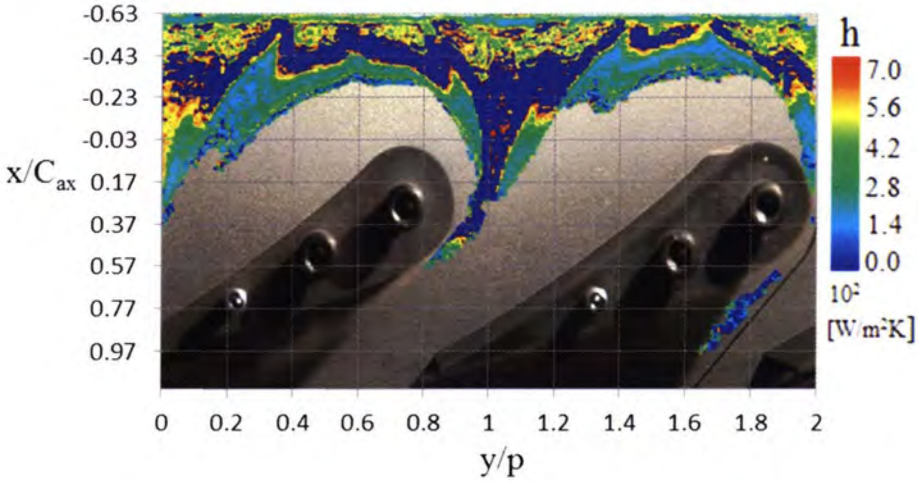

(b) Heat transfer coefficient

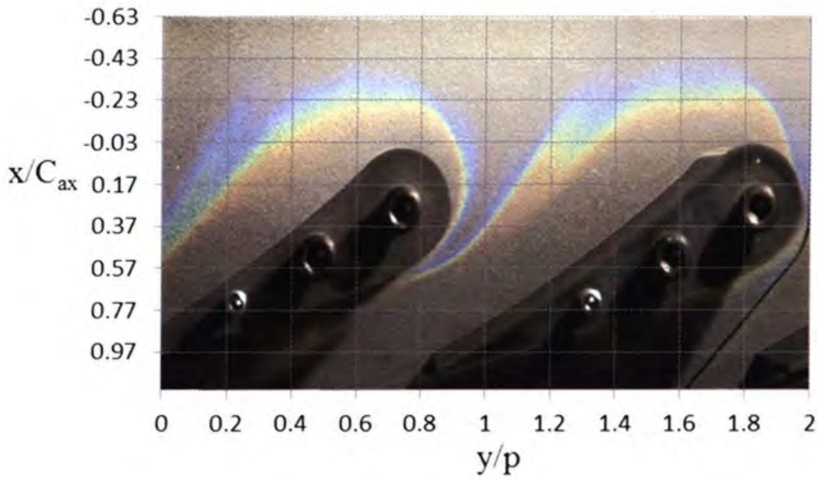

(c) Liquid crystal RGB propagation

Figure 68 Thermal performance for MFR = 1.75%

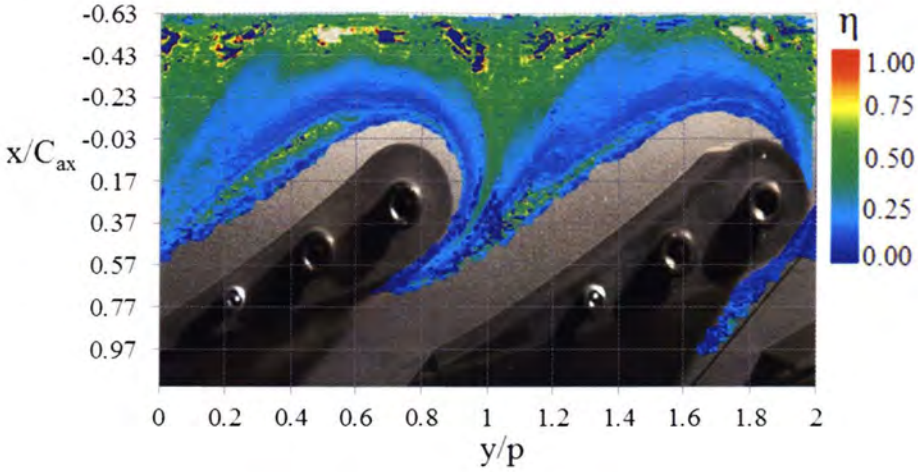

(a) Film cooling effectiveness

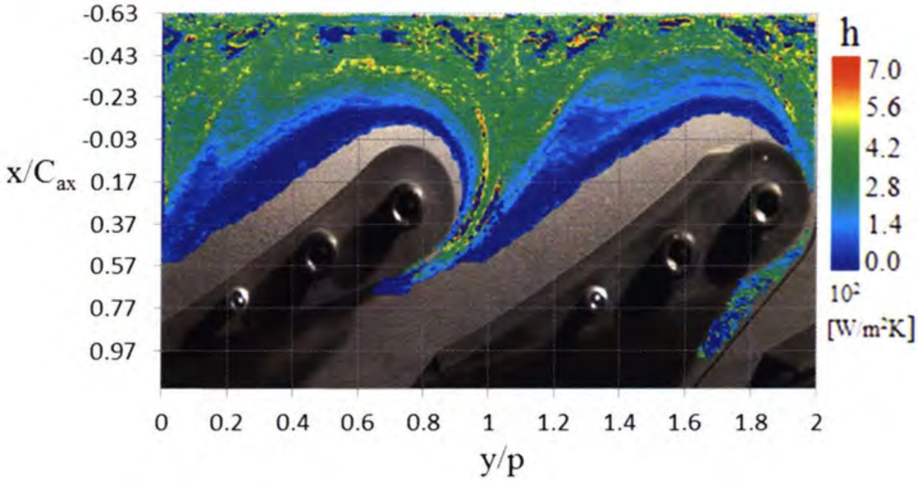

(b) Heat transfer coefficient

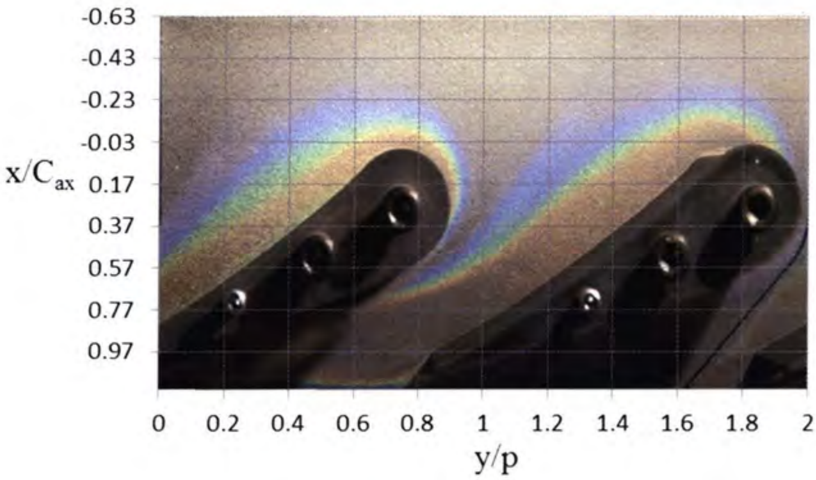

(c) Liquid crystal RGB propagation

Figure 69 Thermal performances for MFR = 2.25%

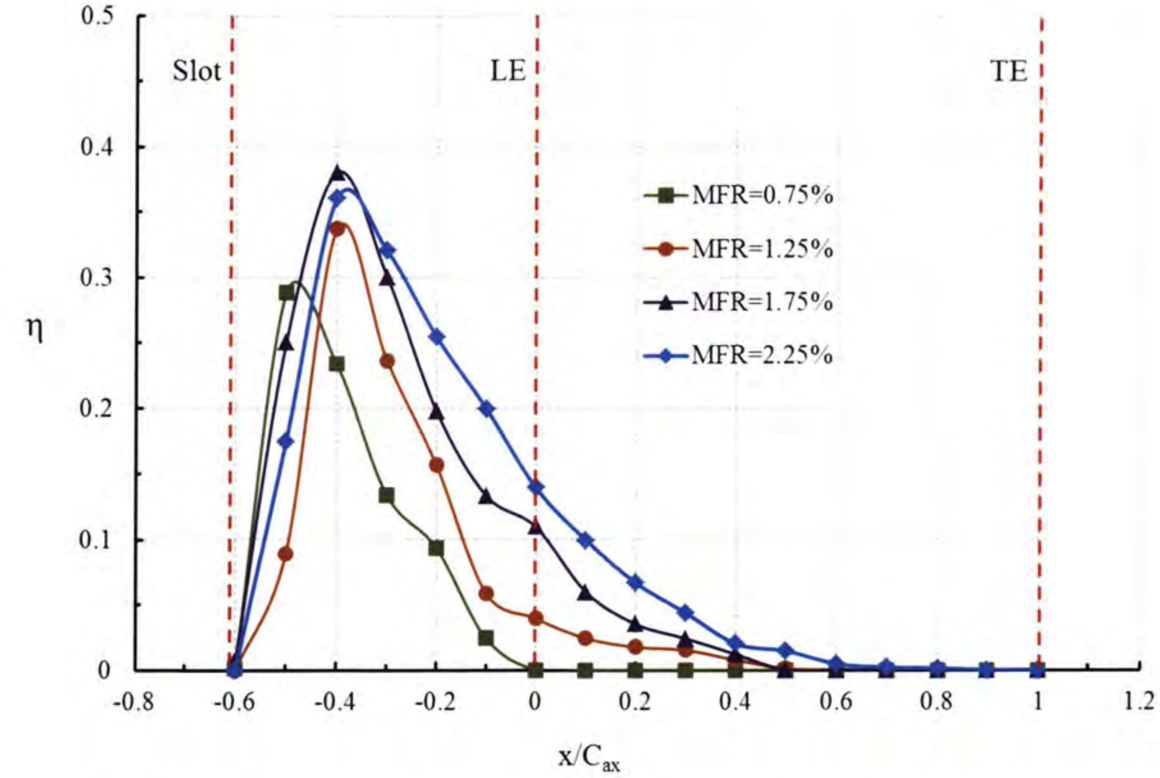

Figure 70 Laterally averaged film cooling effectiveness-EFD

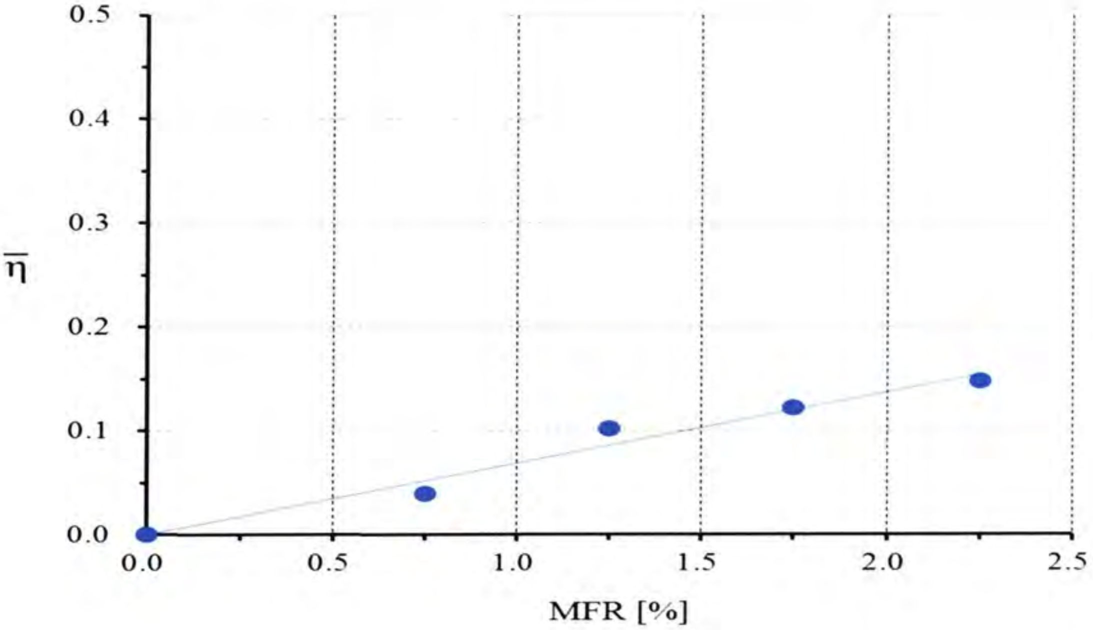

Figure 71 Mass-averaged film cooling effectiveness-EFD

3.5.2 Predicted thermal performances

The performance of the numerical simulation to predict the thermal behaviour under the influenced of the leakage flow has been investigated. As the same turbulence model applied in the aerodynamic prediction, SST was also being applied in this investigation. Figure 72~Figure 75 illustrate the predicted film cooling effectiveness (a) and the heat transfer coefficient (b) for MFR=0.75%, 1.25%, 1.75% and 2.25%, respectively. The region illustrates in the figure is the same which were presented in Figure 66~Figure 69 in order to enable the direct comparison between experimental and the prediction. At MFR=0.75% indicates in Figure 72 (a), the higher η is obtained at the region between y/p=0.8~1.4. Even though it is about 20% wider compared to the measured η, see Figure 66 (a), the prediction presents a similar behaviour of performance indicated by the measurement. CFD also predicted that the leakage flow tends to be penetrated near this region due to the higher pressure close to the stagnation region. As a result, the lower η is presented near the stagnation region with approximately 0.15~0.25 (light blue region). Noted that this protection layer was not be captured by the measurement at the same injection case. The difficulties to obtain almost the same leakage flow profile inside the plenum chamber and the heat loss during the measurement are considered as main reasons. Furthermore, the smaller range of the liquid crystal used to capture the endwall temperature changes also one of the reason. As the MFR increases, the η contour became wider in both axial and pitchwise direction. If the lower η indicates with light blue region is neglected, the similar contour is predicted at MFR=1.25% where it increased to x/C_{ax}=-0.43 and this can be observed along the slot in pitchwise direction. When the MFR increases, the increase trend of η can continuously observed in Figure 74 (a) and Figure 75 (a). However, unlikely the contour obtained by the measurement, no significant changes of the η contour (tail shape contour) showing at region x/C_{ax}=-0.03 towards downstream except the light blue layer. But this tail shape contour exist at the region between x/C_{ax}=0.57~0.67 in both measurement and prediction expect the MFR=0.75%. The heat transfer coefficient parallels to the η contour where they also increases as the MFR increases. The dark blue region illustrates the h with almost close to 0 were captures along y/p=1.0. Noted that this is the region where the leakage flow was accumulated and the formation of the AFV also occurred at this region. The dark blue region also can be seen along the pitchwise direction. This region shifted slightly downstream as the MFR increases. This might be due to the high strength of the separation flow at higher MFR.

At higher MFR of 1.75% and 2.25%, see Figure 74 (b) and Figure 75 (b), the apparent of the dark blue region became more significant at x/C_{ax}=-0.43 and MFR=2.25% illustrates the widest. This is the second separation flow exists between the separation flow vortex and the HSV near the blade LE. Separation flow prevented the leakage flow to stay closer to the endwall surfaces thus low *h* was obtained. The thermal performance between CFD and EFD is compared based on the mass-averaged η as shown in Figure 76. The red approximate line indicates the linear increase trend is also obtained by the prediction. The relationship between the η and the MFR is describes in Eq. 39.

$$\bar{\eta} = 0.127\text{MFR} \tag{39}$$

Based on Eq. 38 and Eq. 39, the predicted increase rate of η is higher about half of the measurement where the η increase approximately 12.7% for every 1% of MFR. As being explained, due to the different leakage profile, heat loss and the smaller range temperature measurement were the main reasons. In CFD, the adiabatic wall condition was applied to the plenum and endwall surfaces thus the heat loss could be considered as 0.

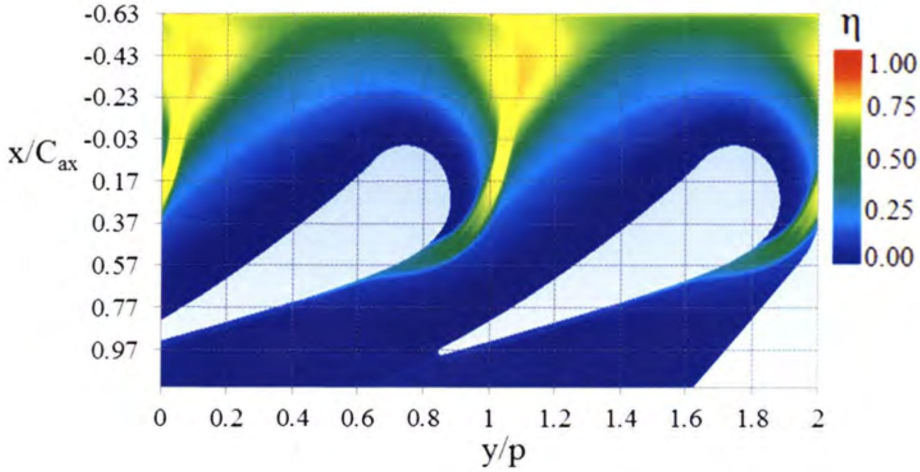

(a) Film cooling effectiveness

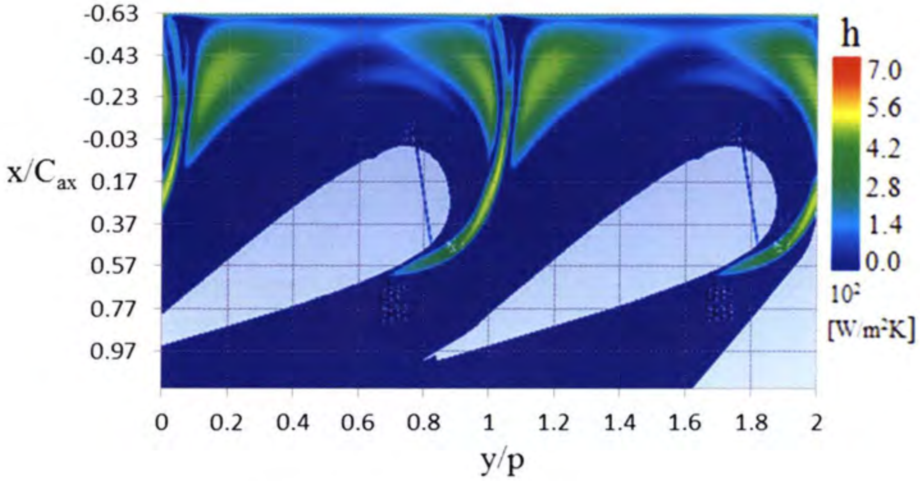

(b) Heat transfer coefficient

Figure 72 Predicted thermal performance for MFR = 0.75%

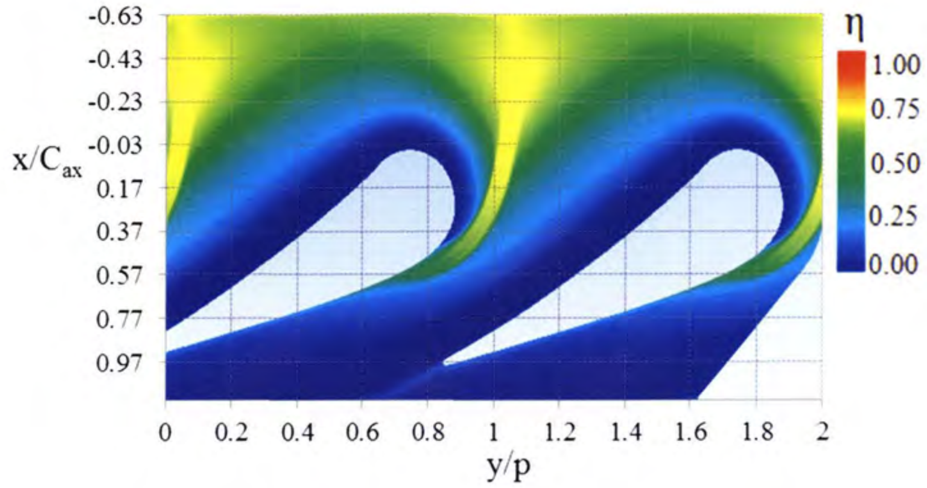

(a) Film cooling effectiveness

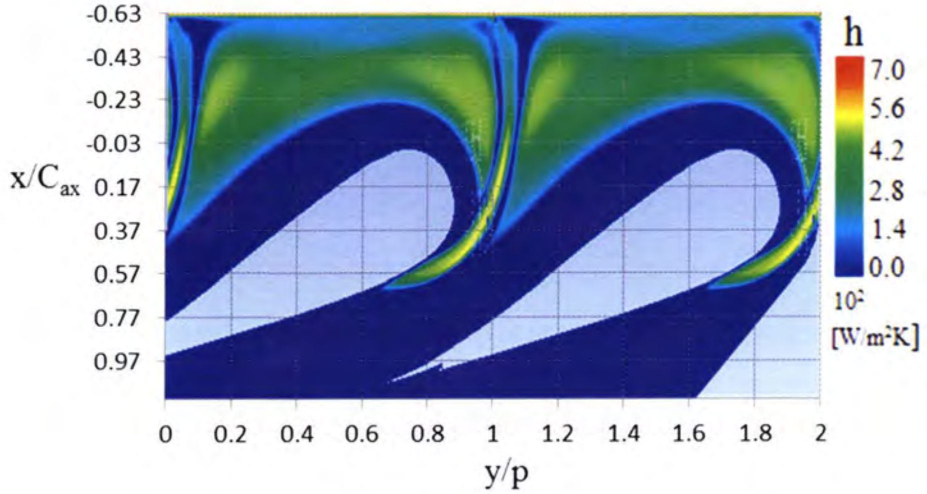

(b) Heat transfer coefficient

Figure 73 Predicted thermal performance for MFR = 1.25%

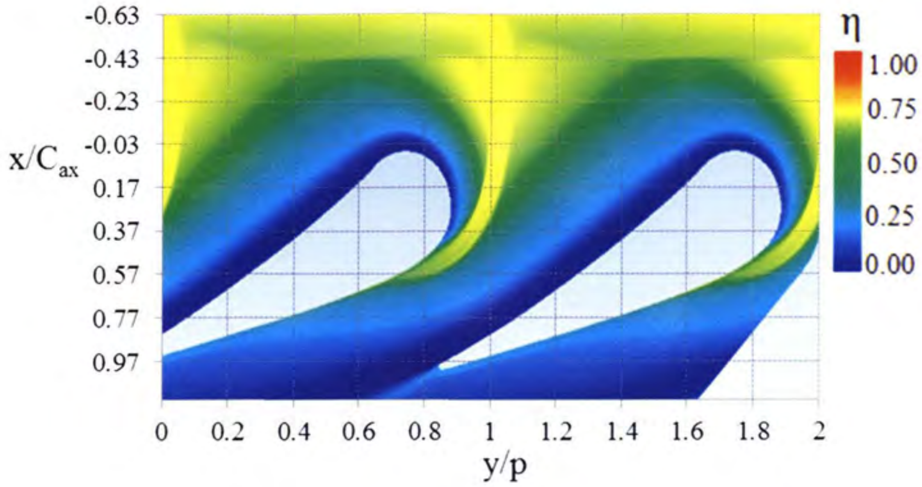

(a) Film cooling effectiveness

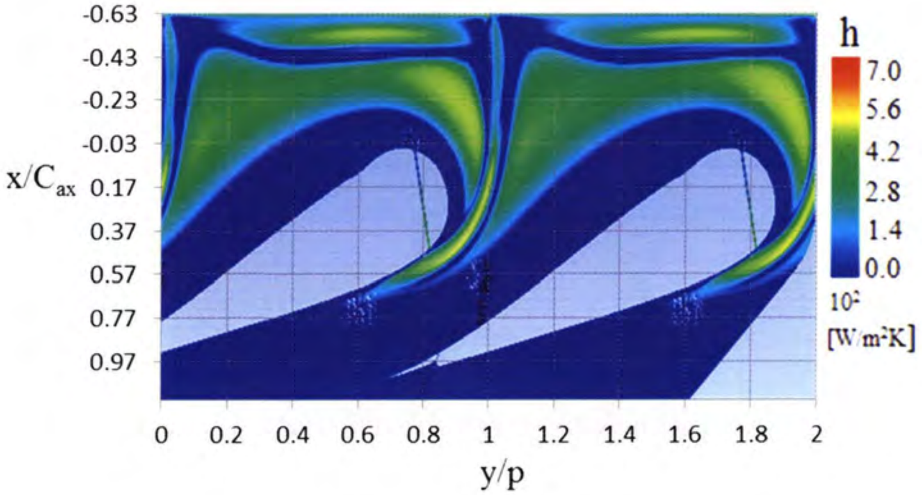

(b) Heat transfer coefficient

Figure 74 Predicted thermal performance for MFR=1.75%

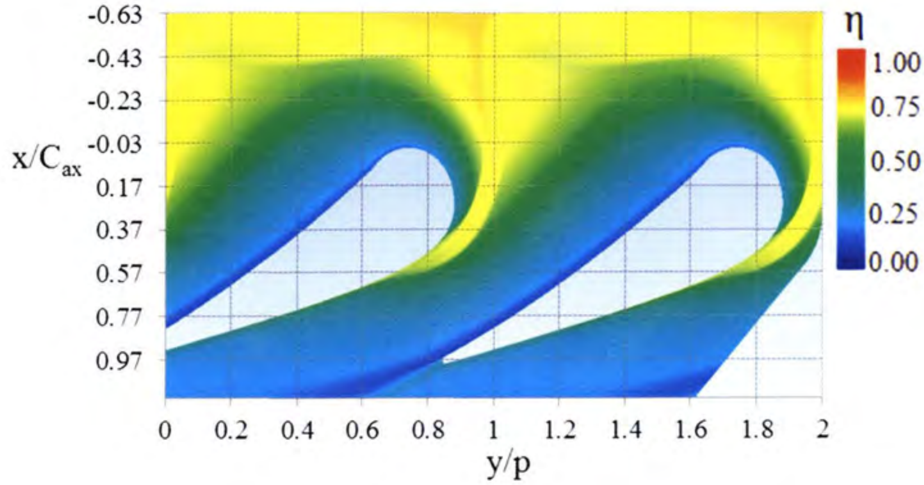

(a) Film cooling effectiveness

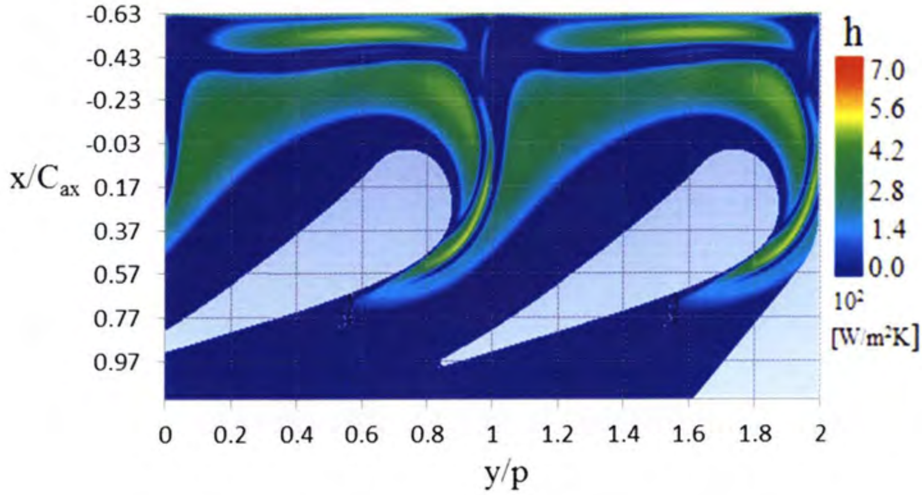

(b) Heat transfer coefficient

Figure 75 Predicted thermal performance for MFR=2.25%

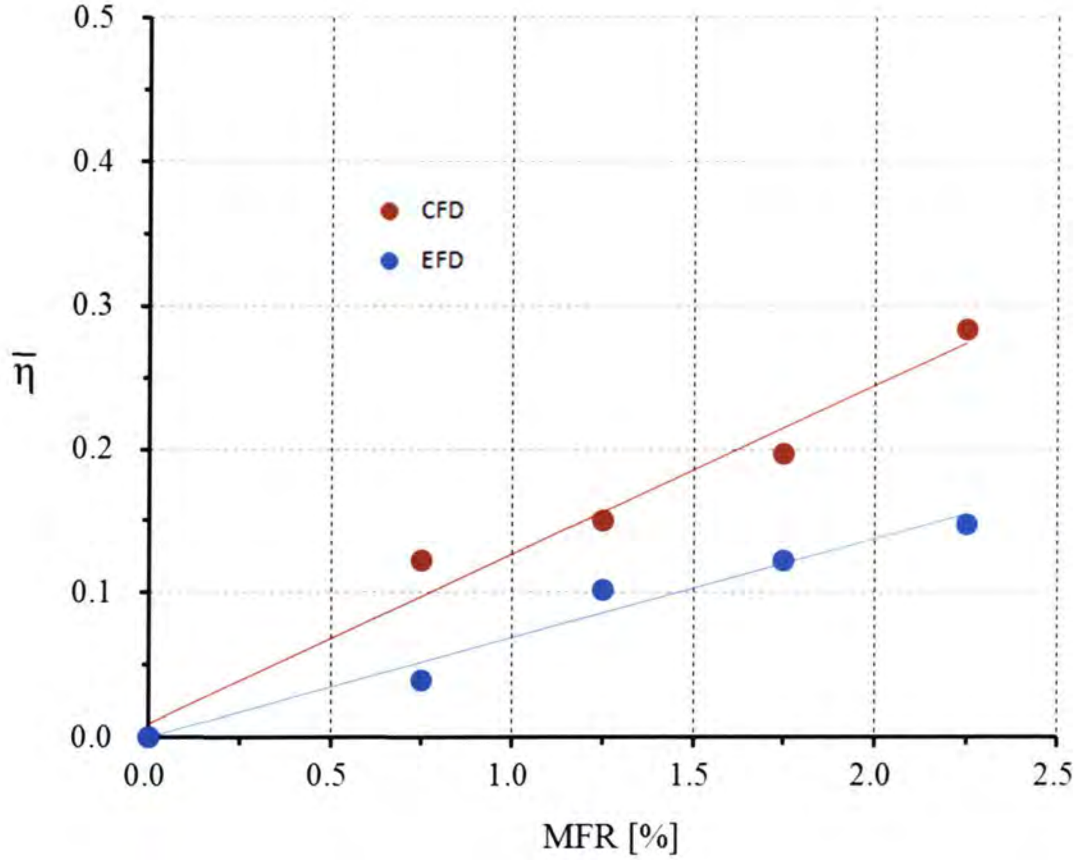

Figure 76 Mass-averaged film cooling effectiveness

3.6 Flow behaviour effects on thermal performances

Figure 77 shows the effect of the secondary flow structures on endwall η distribution in (a) and blade SS surface (b) at MFR=1.25% with the endwall streamline superimposed. Cooling layer provided by the leakage flow seems to be highly influenced by the secondary flows structures. The presence of the PS-HSV and SS-HSV near the blade leading edge leaves the area unprotected. These vortex prevented the leakage flow to go through this area which finally mixed out with the main stream moving towards adjacent blade SS. The contour shows that higher η was observed at the region where the leakage flow was accumulated. Furthermore, the cross flow and the development of the passage vortex (PV) from blade PS to neighbouring blade SS provide a wider cooling coverage on the endwall region near the blade SS instead of blade PS. The merging of PS-HSV and LE-CV to generate a larger PV along the blade SS surface enable the coolant to provide a lower η trail as shown on the right figure. The details of η on the blade SS surface explain in Figure 78 (a) and Figure 78 (b) for MFR=1.25 and MFR=2.25%, respectively. ζ contour at Plane B which were presented in Figure 55 and Figure 56 also shown on the right figure. As shown in Figure 78, the η strikes on the blade SS illustrates the reattachment position of PS-HSV which was coming from adjacent blade PS. The higher MFR cases with high fluid momentum enable to cross the mainstream with higher flow deviation thus could reached the neighbouring blade SS earlier. Furthermore, the wider η in spanwise direction ($Z_H > Z_L$) explains that higher MFR injection lifted off blade surface in higher position due to the higher C_{SKE}.

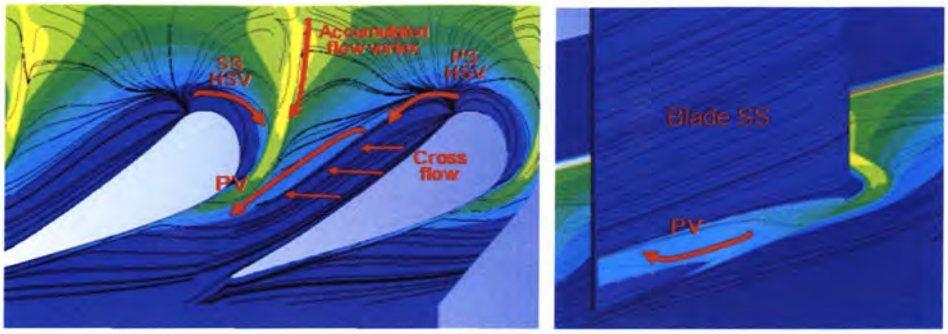

(a) Endwall side (b) Blade SS side

Figure 77 η contours influenced by secondary flow behaviour

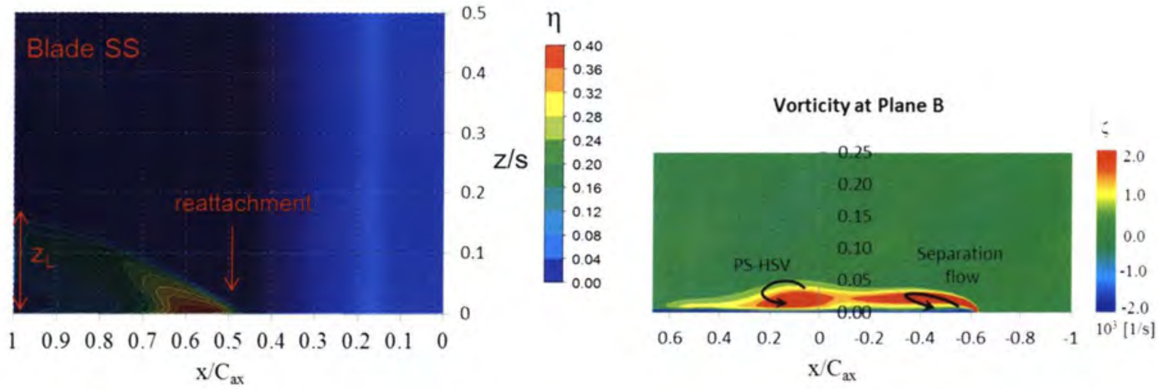

(a) η on blade SS (left) and ζ on Plane B (right) at MFR=1.25%

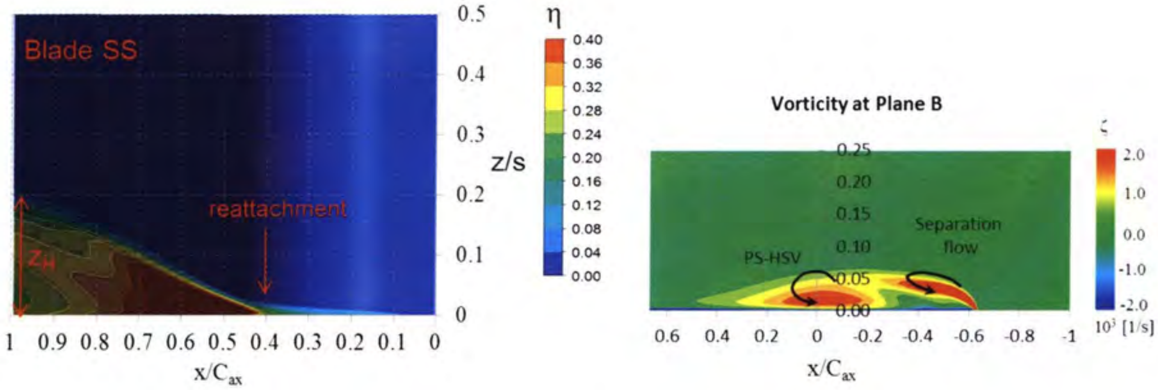

(b) η on blade SS (left) and ζ on Plane B (right) at MFR=2.25%

Figure 78 Effect of flow structures on blade SS film cooling effectiveness

3.7 Overall performances

Based on the discussion in previous sections, it is clearly explain that the leakage flow has a high potential to provide the protection layer on the endwall surfaces. However, the changed of the existing flow structures caused by leakage injection resulting the increases of the C_{pt}. This cannot be neglected since a significant change of C_{pt} contours were captured in both EFD and CFD. The relationship between the C_{pt} and η is presented in Figure 79. The approximated lines are also drawn and compared between EFD and CFD. Both EFD and CFD illustrate that the C_{pt} and η are proportional to the MFR where the higher the MFR, the wider the protection layer and the loss continuously increases. The relationship between C_{pt} and η can be represented in Eq. 40 and Eq. 41 for EFD and CFD, respectively.

$$\text{EFD: } C_{pt} = 1.21\,\bar{\eta} + 1.271 \tag{40}$$

$$\text{CFD: } C_{pt} = 0.68\,\bar{\eta} + 1.331 \tag{41}$$

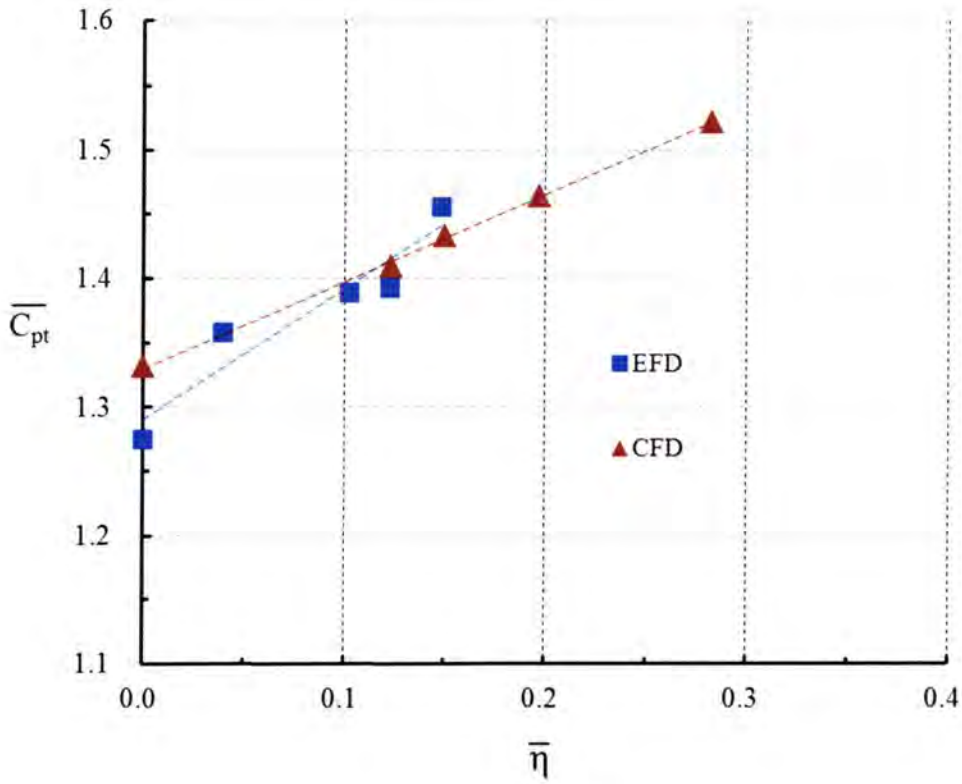

Figure 79 Aero-thermal performance of leakage flow

Chapter 4

Slot Modifications Effect by Prediction

This chapter provides details on the extended studies in order to improve current aero-thermal performance as discussed in Chapter 3. The modification of slots is expected to improve their performance. The numerical investigation on the slot configuration focuses on the slot orientation and its position from the blade LE. The leakage flow with various injection angles, β are compared to the baseline configuration with 90° injection. For the slot position studies, the slot with various position, l from the blade LE were compared to the baseline slot position which is located at $-0.63C_{ax}$ upstream from blade LE. This chapter provides the prediction results to show their effect on current aero-thermal performance. This investigation aims the improvement of the aero-thermal performance which could be considered in actual gas turbine application.

4.1 CFD modeling

Based on the good agreement that have been achieved between the EFD and CFD for baseline configuration as presented in Chapter 3, the present section intended to predict the performance of leakage flow injection with a different slot configuration. The modification of the slot in term of slot orientation and position were considered could provide some modification on the existing performance. In order to obtain a direct comparison with the predicted baseline configuration, the same mesh and grid topology was applied to the mainstream and the blade domain. The only change that was made is the slot configuration. The injection angle, $\beta=90^\circ$ and position, $l=x/C_{ax}=-0.63$ which was presented in the previous chapter is considered as the baseline slot configuration. As shown in Figure 80, the slot were oriented to three different injection angles, $\beta=60^\circ$, $45^\circ$and 30°. However, in order to see their effect only by the injection angle, all cases were fixed at slot position, l =-0.63 where it is the same position with the baseline slot configuration. Since the slot was inclined, the slot width, d_b = 4 [mm] is actually become shallower with d_β = 4.Sin(β) [mm]. The endwall thickness was fixed at $0.24C_{ax}$ for all cases. The effect by the slot position was predicted by another three slot positions. Since l =-0.63 is considered as baseline slot position, the slot was firstly shifted to l =-0.90 where it was move away from the blade LE. Due to the limitation of the slot distance in the real gas turbine, the slot was also move closer to the blade LE with two cases of l =-0.36 and -0.10. The thermal and aerodynamics performance by the slot modification will discuss in the next section.

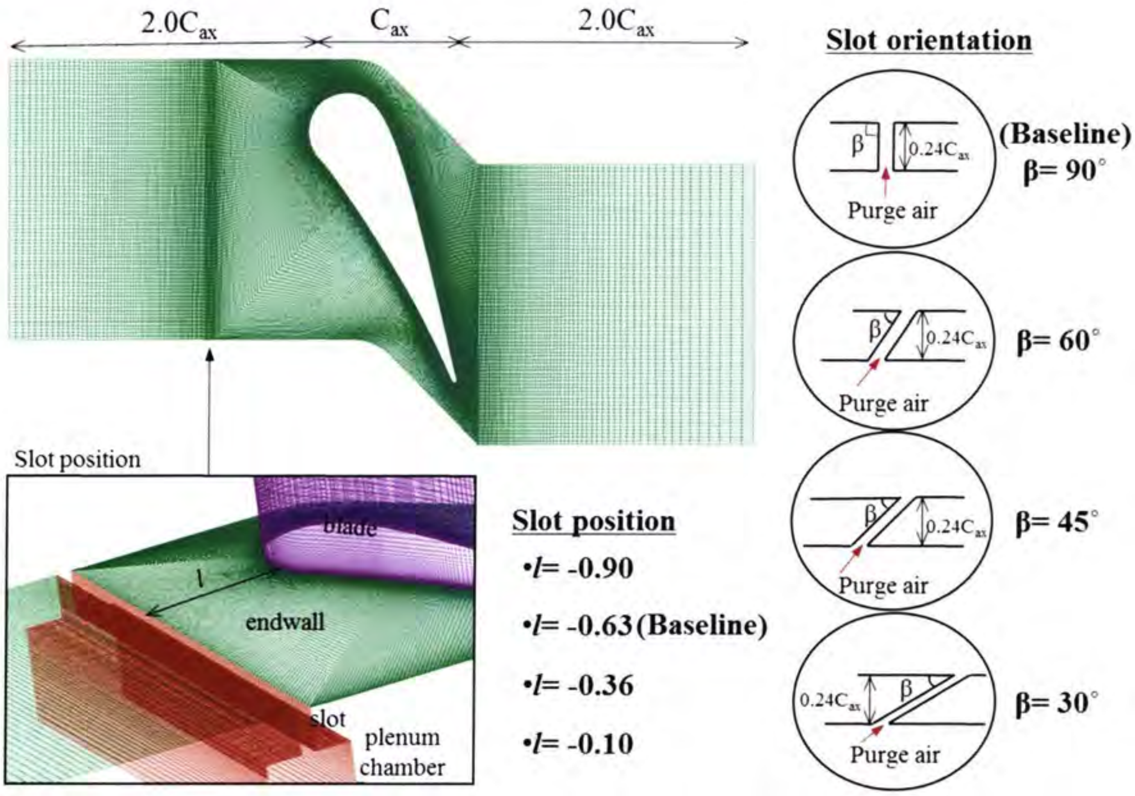

Figure 80 CFD modeling for slot orientation and position

4.2 Leakage flow performance influenced by slot orientation at l=-0.63

4.2.1 Aerodynamics performances

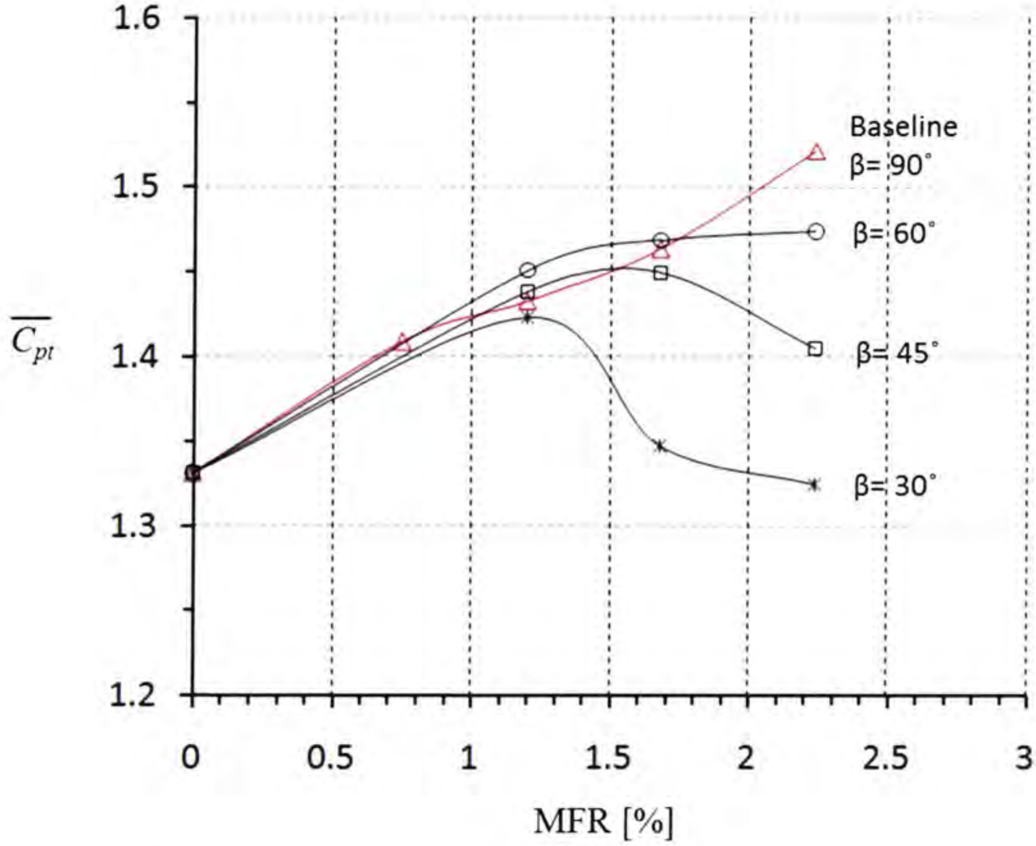

Figure 81 Mass averaged C_{pt} by the effect of β at l=-0.63

Five cases of MFR, 0.75%, 1.25%, 1.45%, 1.75% and 2.25% have been predicted for each configuration. Mass averaged C_{pt} was determined and plotted in Figure 81 to present the slot performance in comparison to baseline configuration indicated by the red line. Regardless the β, injecting a leakage flow up to MFR=1.25% is predicted to increase the loss. However, not the case for the higher MFR of 1.75% and 2.25% where the loss started to reduce slowly for β= 60˚cases. Continuously shallower the β to 45˚ and 30˚, the loss indicates the decrease trend as the MFR being increased. The $\bar{C}_{pt}$ not only lower than the baseline case but also in comparison with the lower MFR showing by the same slot configuration particularly at

MFR=2.25%. According to the trend shown in Figure 81, the shallower the injection angle, the $\bar{C}_{pt}$ will starts to reduce at lower level of MFR. Figure 82 and Figure 83 present the C_{pt} contours for MFR=1.25% and 2.25%, respectively in comparison with different β. At MFR=1.25%, the shape of first loss core significantly changed at β =60° (Figure 82 (a)) and C_{pt} seems became wider at the bottom side of the core. In the contrary, the third core slightly reduced and the region exists closer to the endwall side. Further reduce the β to 45° and 30° as shown in Figure 82 (b) and (c), both loss cores reduced especially at β =30°, the third core is very weak. At MFR=2.25%, a very interesting results is shown in Figure 83 because it's contradicting with C_{pt} contour shown by the baseline case (Figure 52 (a)) when the MFR being increases. Especially for β =30°, see Figure 83 (c), the loss drastically reduced where the second and third loss cores mostly eliminated by leakage flow injection. These explain that the strength of the TE-CV and AFV became weaken and the influences of these vortexes to loss almost cannot be seen. The reduce strength of the PS-HSV also being explained by the deformation of the first loss core in the same figure. This phenomenon is parallel to the loss distribution shown in Figure 82.

The details flow structures by each β in the blade passage are shown in Figure 84~Figure 86 for MFR=2.25% since a very interesting result has been shown by the case. All β cases captured the presence the PS-HSV but the secondary flow seems to be modified by this slot configurations. The modification of the secondary flow structures is predicted to improve the blade passage by the less strength of the vortex core shown in each figure. In comparison with the baseline slot configuration at similar MFR, see Figure 56, the changes of β to a shallower angles seem to reduce the strength of the HSV indicated by the flow streamline at stagnation plane. At MFR=2.25%, the leakage flow has enough momentum and can easily be penetrated into the mainstream includes the blade stagnation region. By normal injection, the penetration of the leakage flow influenced to the flow blockage and high flow separation occurred at downstream of the slot. However, the less flow blockage at this region was predicted by shallower injection consequently reduce the strength of HSV. The smaller diameter of vortical structure might explain the reduce strength of HSV. By β =30° as shown in Figure 86, the occurrences of the flow separation almost cannot be seen and the HSV with a small diameter shifted closer to the blade LE wall. The development of PS-HSV has been observed by the ζ plotted on Plane B. In comparison with baseline slot configuration (Plane B ζ in Figure 56), PS-HSV seems to slightly shifted towards downstream by β =60°and closer to blade PS by β =45° and β =30°, see Plane B in Figure 84~Figure 86. Noted that this phenomenon is contradicting with usual case where the PS-HSV is expected to cross the mainstream before lifted-off neighboring blade SS. Additionally, in comparison with the baseline case with no leakage flow injection, see Figure 54, the existing flow structures is actually being improved without PS-HSV crossing the mainstream thus less flow deviation occurs. This is due to the weaker PS-HSV with a low fluid momentum unable to cross the mainstream and it highly influenced by the higher momentum of leakage flow. This means that the formation of passage vortex near the blade SS occurs without the presence of PS-HSV and this might be the reason of the lower C_{pt} contour obtained by this case.

The most significant change on the secondary flows is the strength of the AFV reduced by β =45°and the formation of such vortex almost cannot be observed by β =30°. The endwall flow streamline illustrates in Figure 87 explains the formation of AFV by β =60° and the elimination of the AFV by shallower injection angle at β =30°. In usual case, the leakage flow tends to migrate toward blade center due to the high pressure region near the blade stagnation. However, as explained above, inclined slot toward this region could provide enough fluid momentum thus they can easily be penetrated and reached the blade PS wall before being deflected particularly by β =30°, see Figure 87 (c). Deflected leakage flow leaves a significant flow behavior indicated by the vortex core on the blade PS defined by DFV. The presence of DFV also can be observed in Plane B indicated by negative ζ rotating in clock wise direction. At β =30°, DFV seems to be appeared till the blade midspan.

The vortex core propagation near the blade TE by each β are presented in Figure 88~Figure 90. The ζ contour at Plane $1.25C_{ax}$ is also illustrates in the same figures. By β =60°, the influenced of the AFV which contributed to the third loss core (see Figure 83 (a)) is clearly shown by the negative ζ region in Figure 88 (a). However, the ζ is slightly lower in comparison with baseline slot configuration (see Figure 60) resulting lower losses. By β =45° and β =30° shown in Figure 89 and 90, the first loss core is predicted to be associated by the LE-CV alone without the combination with the PS-HSV. This illustrated by the lower ζ region parallel to the position of first loss core shown in Figure 83 (b) and (c). The reduced strength and elimination of the AFV by β =45° and β =30°, respectively is considered as the major change which contributed to the reduce loss where the appearance of the AFV in the ζ contour almost cannot be seen.

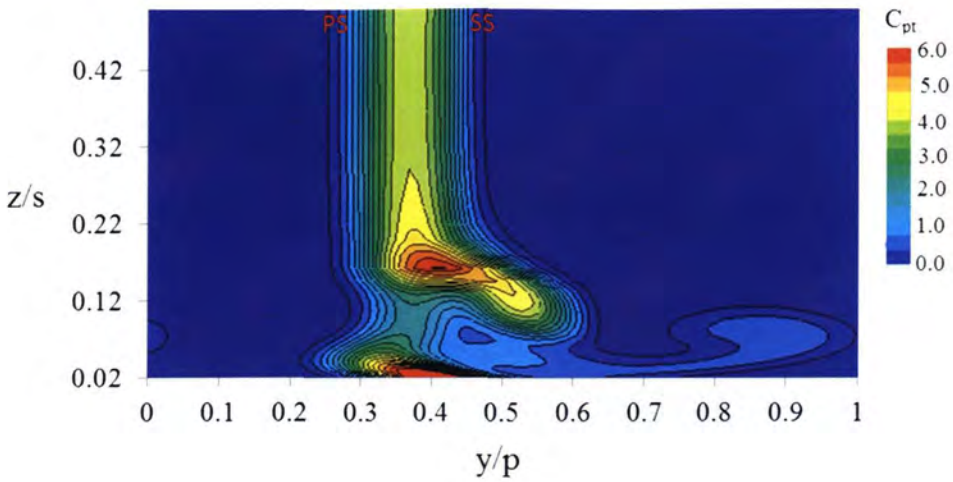

(a) β= 60°

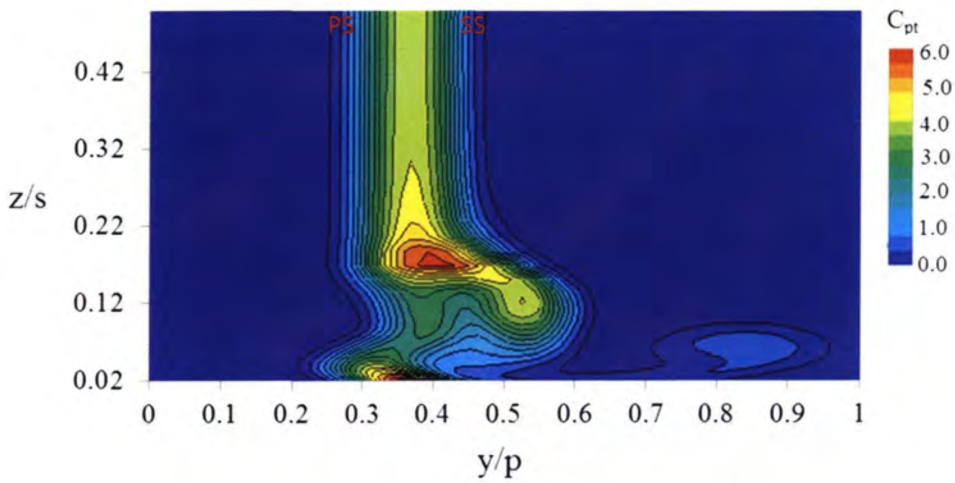

(b) β= 45°

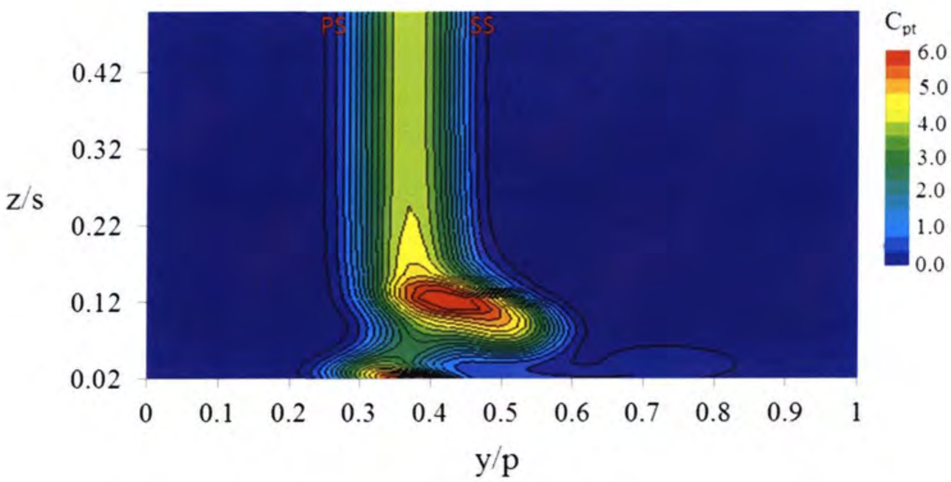

(c) β= 30°

Figure 82 Predicted C_{pt} contour at MFR-1.25% by three different β

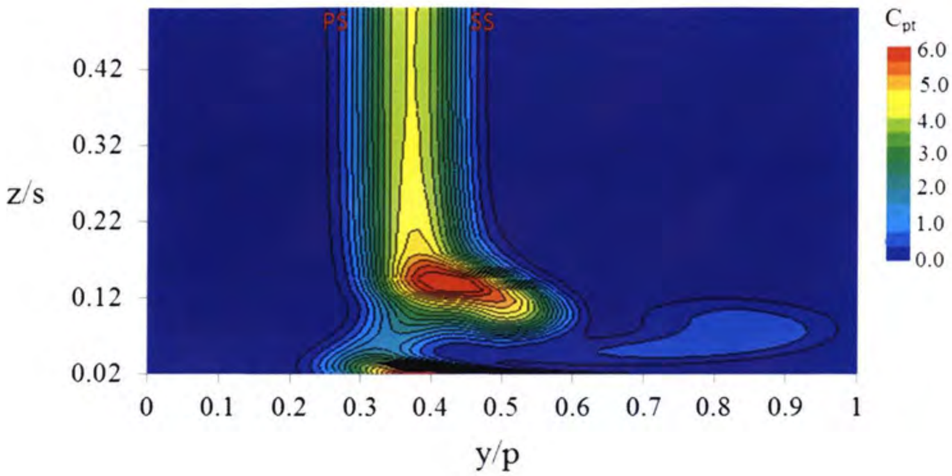

(a) β= 60°

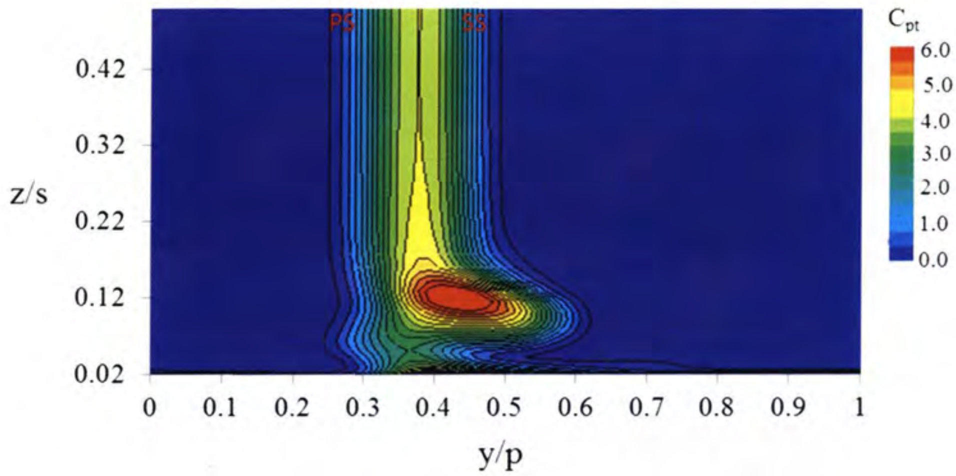

(b) β= 45°

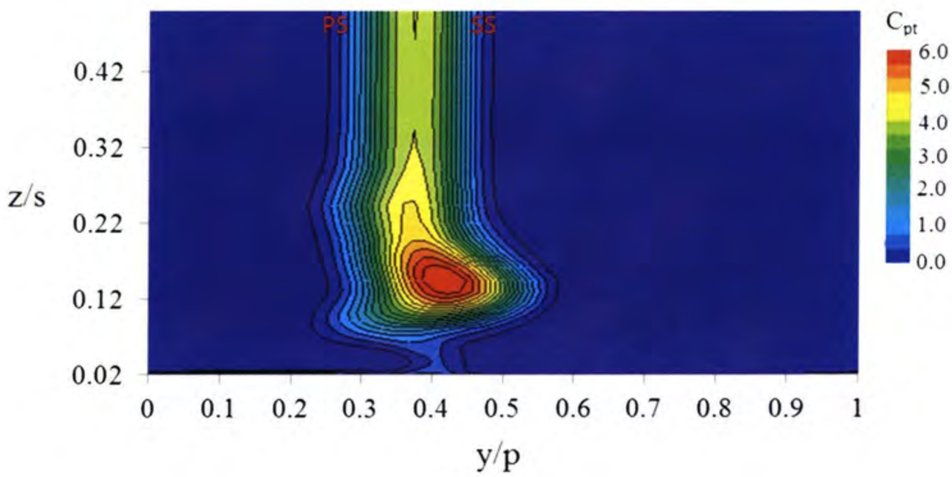

(c) β= 30°

Figure 83 Predicted C_{pt} contour at MFR-2.25% by three different β

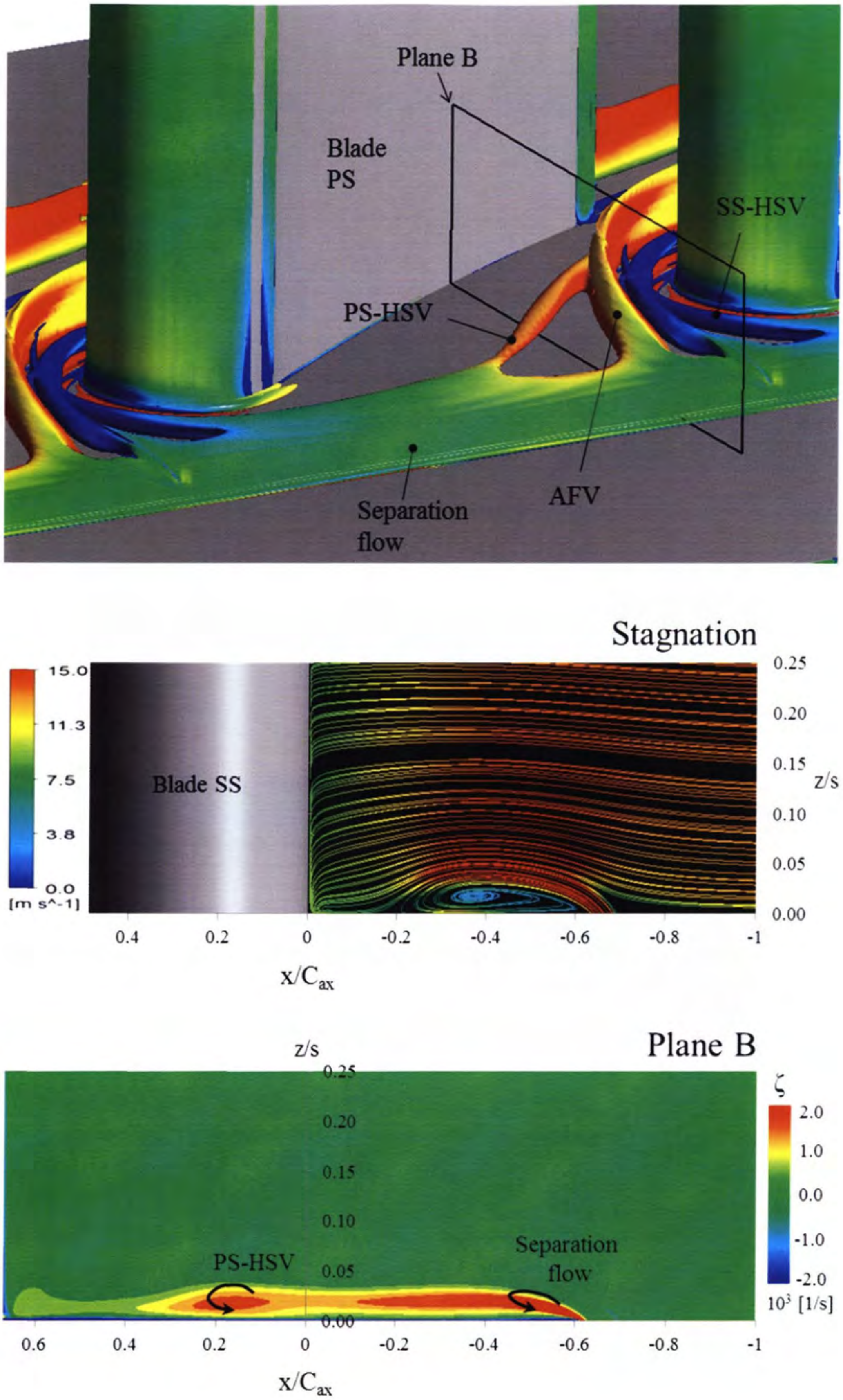

Figure 84 Predicted flow structures near blade LE at MFR=2.25% by β=60°

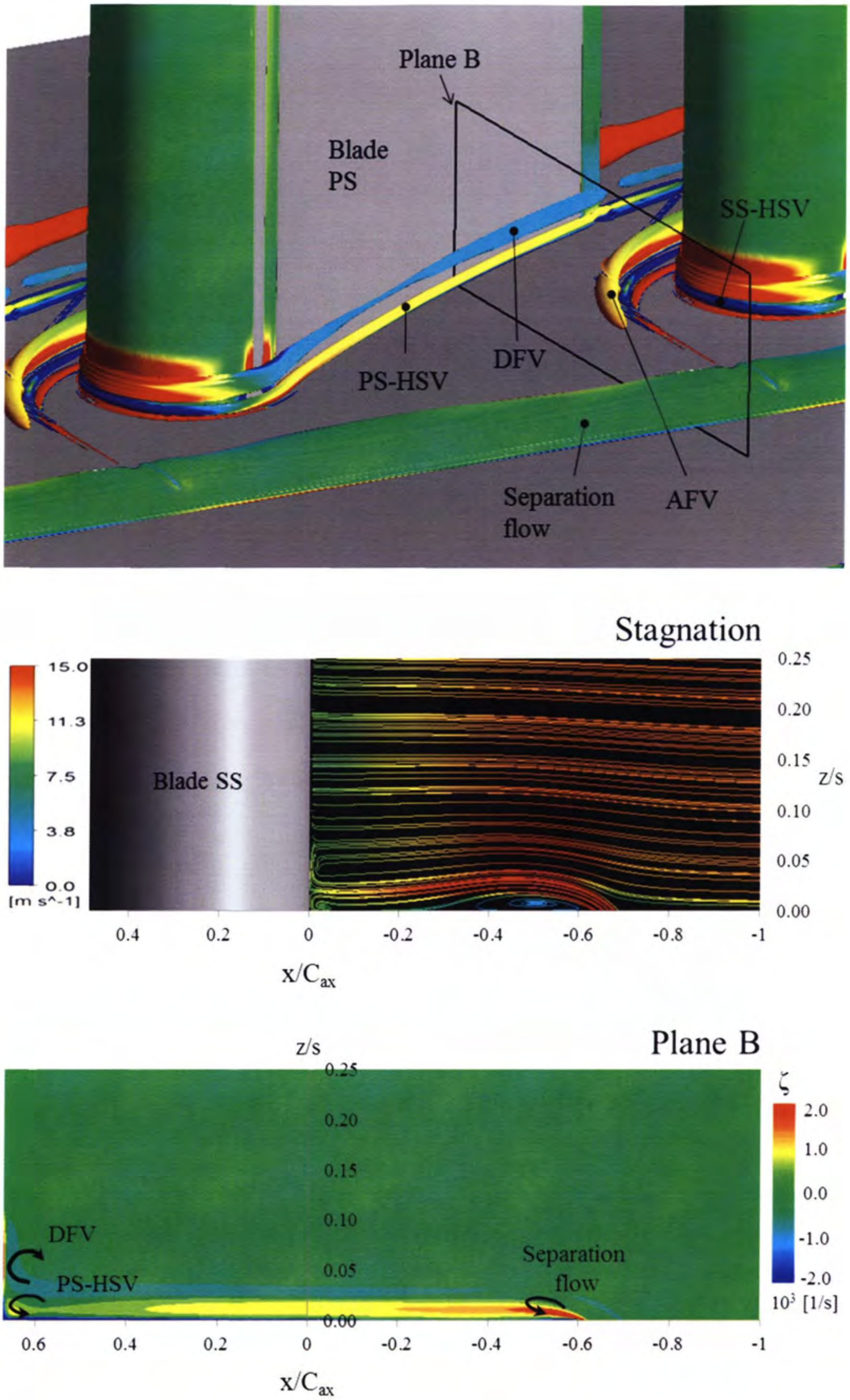

Figure 85 Predicted flow structures near blade LE at MFR=2.25% by β=45°

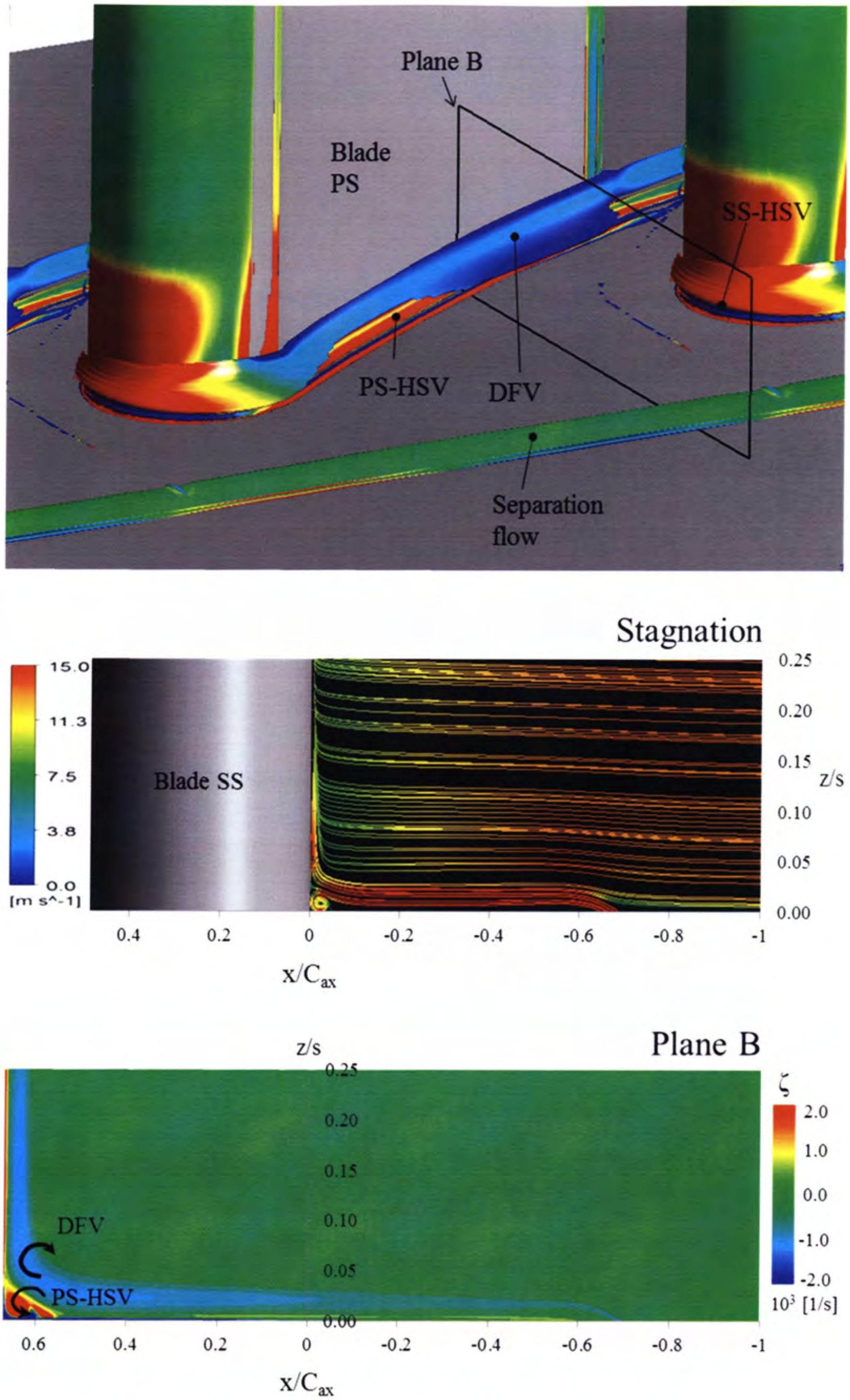

Figure 86 Predicted flow structures near blade LE at MFR=2.25% by β=30°

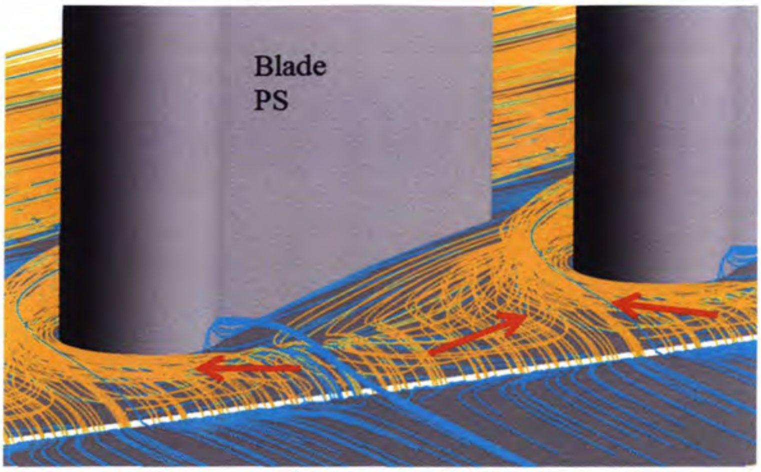

(a) Endwall streamline by β=60°

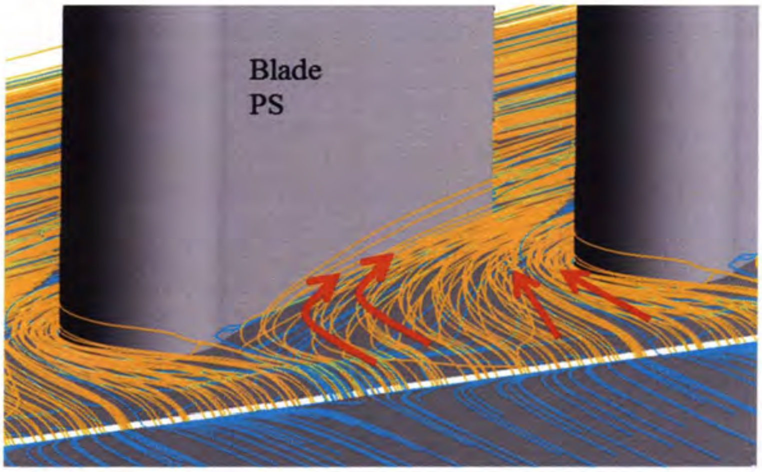

(b) Endwall streamline by β=45°

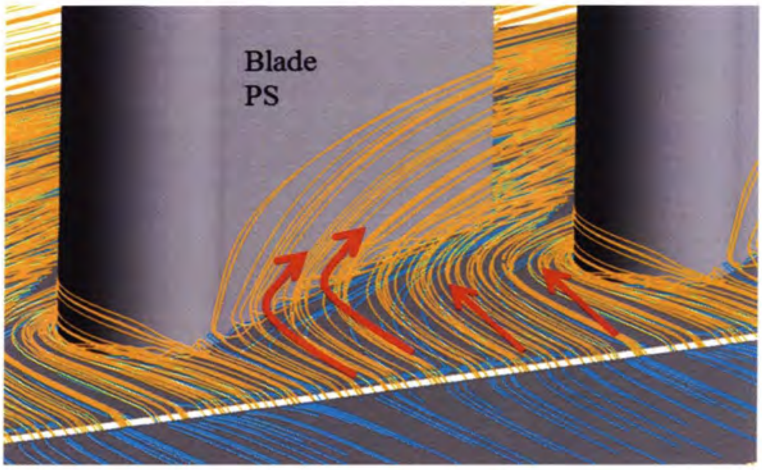

(c) Endwall streamline by β=30°

Figure 87 Predicted flow streamline on endwall region by slot orientation effect

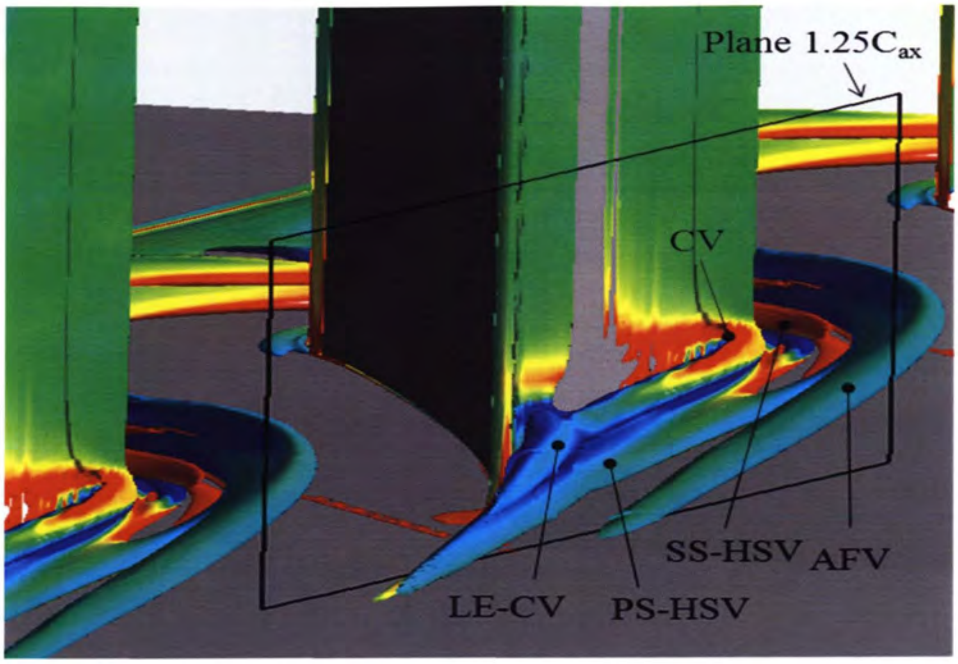

(a) Vortex core

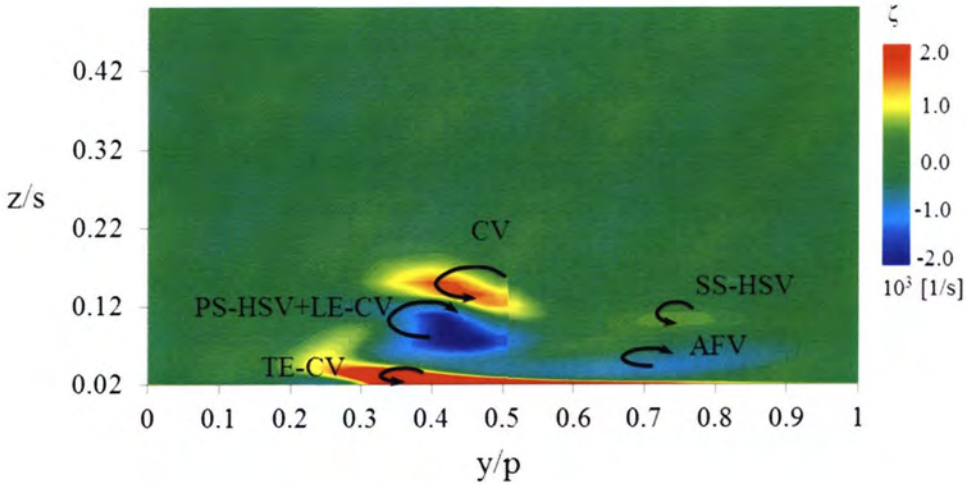

(b) Plane 1.25C$_{ax}$ vorticity

Figure 88 Predicted flow structures near blade TE at MFR=2.25% by β=60°

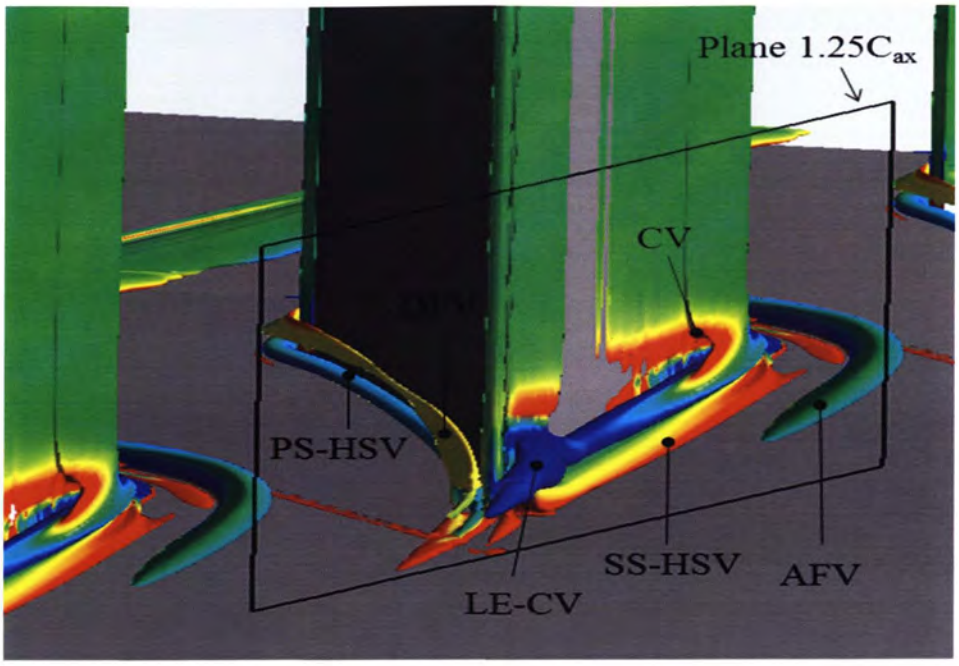

(a) Vortex core

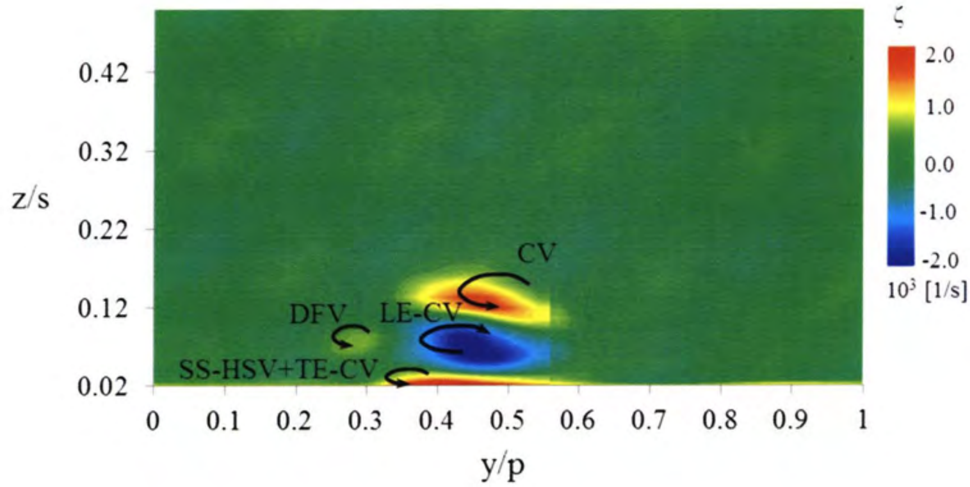

(b) Plane 1.25C$_{ax}$ vorticity

Figure 89 Predicted flow structures near blade TE at MFR=2.25% by β=45°

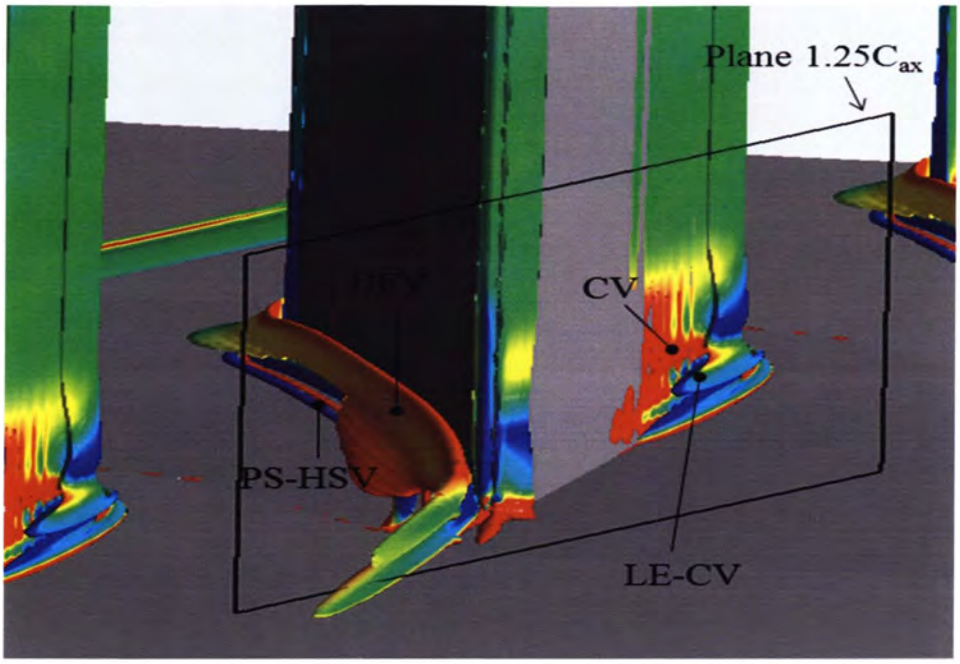

(a) Vortex core

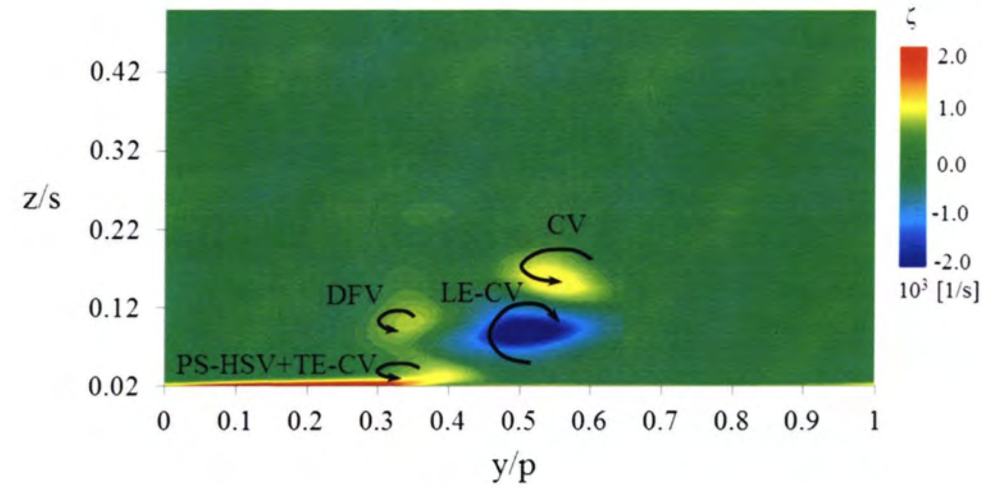

(b) Plane 1.25C$_{ax}$ vorticity

Figure 90 Predicted flow structures near blade TE at MFR=2.25% by β=30°

4.2.2 Thermal performances

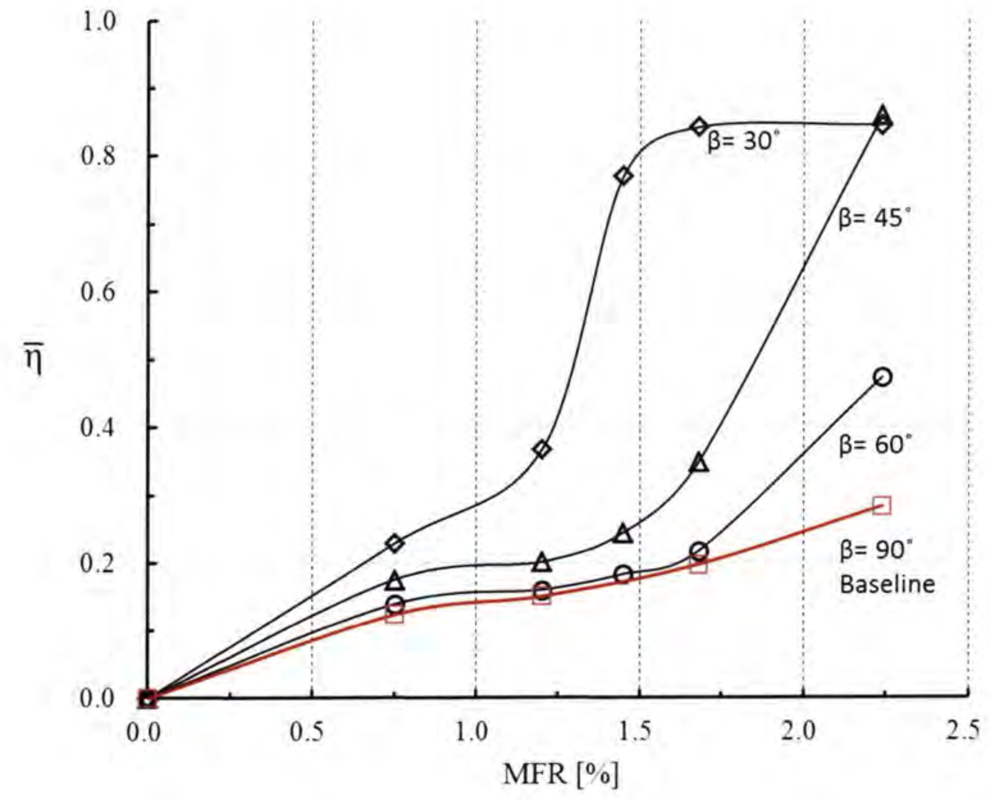

Figure 91 Thermal performance by different β at *l*=-0.63

Thermal performance of the slot based on β is presented in Figure 91 by determine mass-averaged η in comparison with the baseline slot configuration indicated by red line. By β= 60°, there are no significant improvement of η till the MFR was been raised up to 1.75%. At MFR=2.25%, the leakage flow by β= 60°increased the cooling performance approximately 70% relatively to baseline slot configuration. A positive performance trend is predicted when the β was inclined to 45° and 30°. A significant improvement can be observed even though at lower MFR of 0.75% especially approximately 90% of performance increased by β= 30°. At extremely higher injection by MFR=2.25%, slot with β= 30° seems to reach maximum line where the cooling performance is predicted almost the same with β= 45° at $\bar{\eta}$ =0.85. This means the cooling performance increases more than 100% in comparison with the baseline. Since the average has been determined based on fixed endwall area which is starting from x/C_{ax} =-0.63 and ended at x/C_{ax}=1.15 in axial direction, the cooling performance downstream of fixed area was not counted. Noted that the starting point is actually the position of the slot, l =-0.63. This might be the reason why injection by β= 30°is almost the same with β= 45° as shown in Figure 91.

Figure 92 and Figure 93 present the η contour based on the different β for MFR=1.25% and MFR=2.25%, respectively. The same figure which were presented by Figure 73(a) and 75(a) to illustrates 2 pitches of endwall starting from x/C_{ax} =-0.63 and ended at x/C_{ax}=1.15. Noted that the mass-averaged η presented in Figure 91 was determined based on this area. At MFR=1.25%, no significant increase of the protection layer provided by β= 60° and β= 45° in comparison with baseline injection except the increased level of the η. The leakage injection at this MFR still unable to eliminate or reduce the strength of the PS-HSV which preventing the leakage flow to protect the endwall close to the blade PS region. However, the leakage flow could stay closer to the endwall side due to the less flow separation in comparison with the normal injection case thus resulting higher level of η. By β= 30°, see Figure 92 (c), the level of η further increases and the protection layer has spread towards blade LE and also slightly closer towards blade PS region. This might be due to the reduced strength of the HSV or PS-HSV. As shown in Figure 84~Figure 86, further increases the MFR to 2.25% were predicted to significantly modified the secondary flow structures generated by baseline slot configuration at same MFR. The reduced strength of PS-HSV by β= 60° at MFR=2.25% influenced the leakage flow to further expand the η as shown in Figure 92 (c). Since the strength of PS-HSV has been drastically reduced by β= 45°and β= 30°, the leakage flow can easily reached the blade PS region and whole endwall surfaces was been protected. The higher penetration of leakage flow towards the blade PS by β= 30° compared to β= 45°(see Figure 87) provides slightly higher level of η near this region as shown in Figure 93 (c). Furthermore, higher penetration towards blade PS by β= 30° influenced the leakage flow to stayed closer to the blade PS surface and leave wider protection layer strike as shown in Figure 94. This is also a very interesting thermal performance shown by such slot configuration where this region usually unprotected by normal injection. This caused the endwall region close to the adjacent blade SS obtained lower level of η indicated by a green region since the leakage flow tend to move along the blade PS.

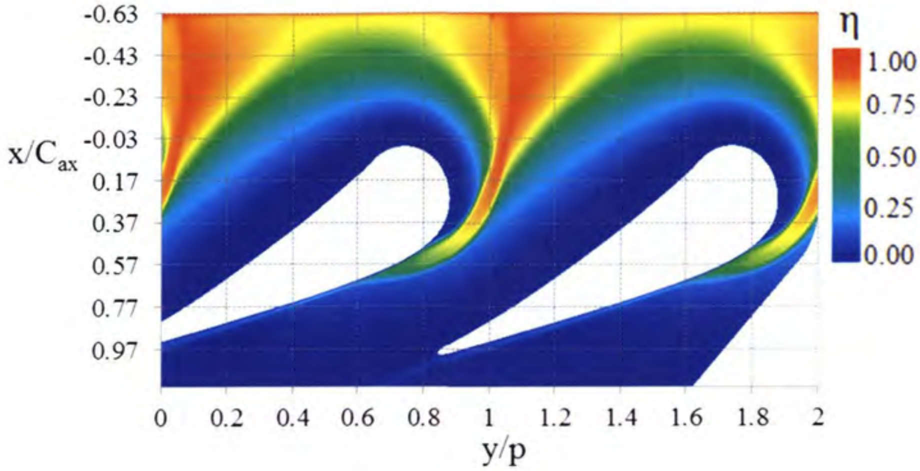

(a) β= 60°

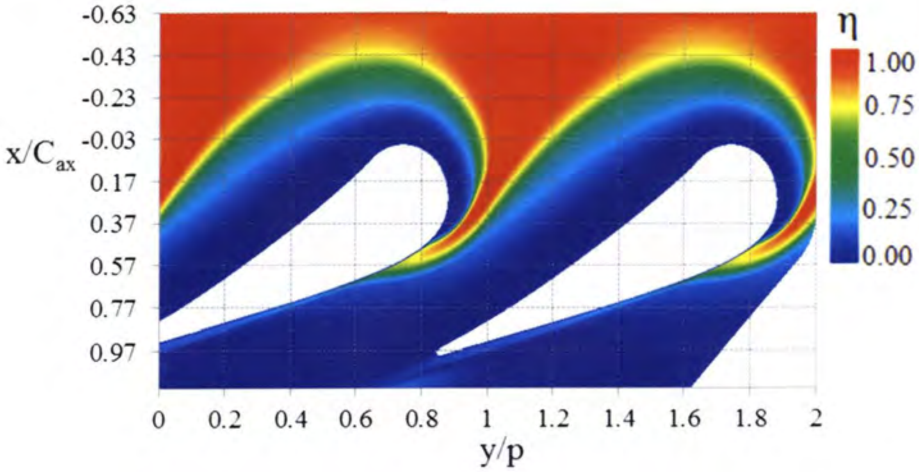

(b) β= 45°

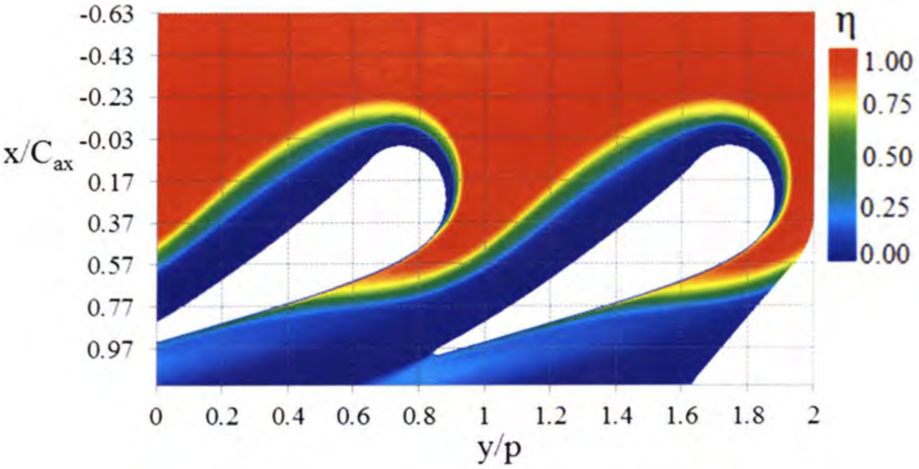

(c) β= 30°

Figure 92 Predicted η contour at MFR=1.25% by three different β

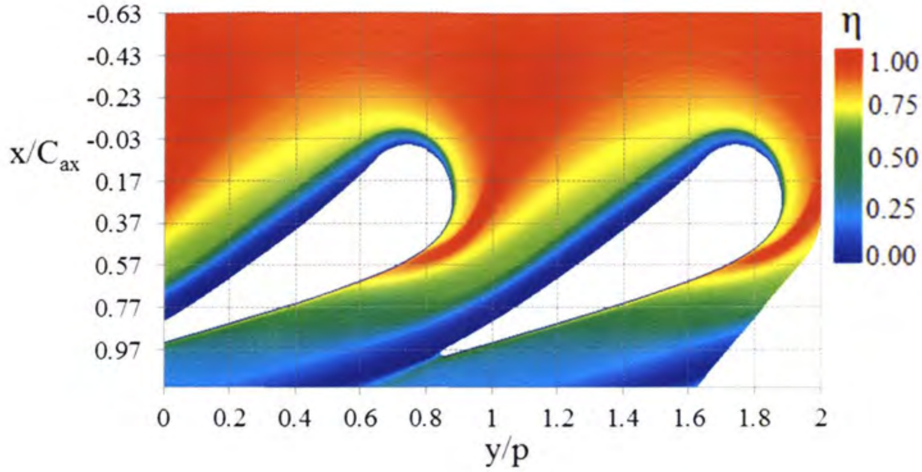

(a)β= 60°

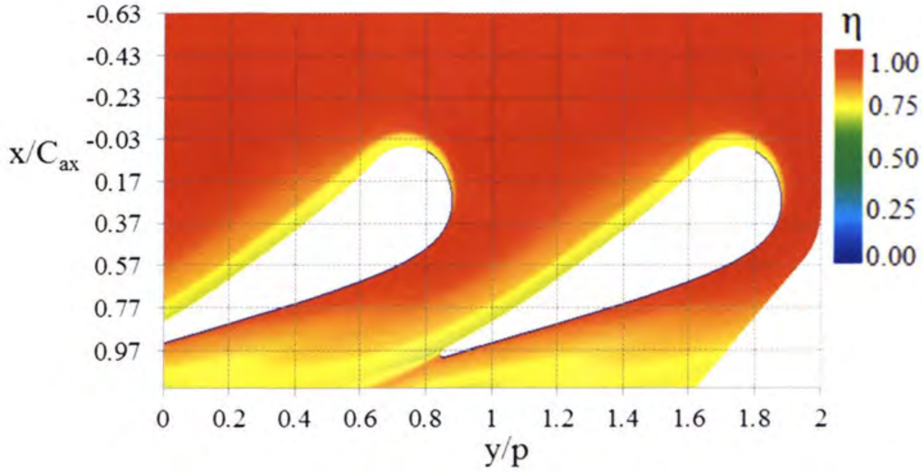

(b)β= 45°

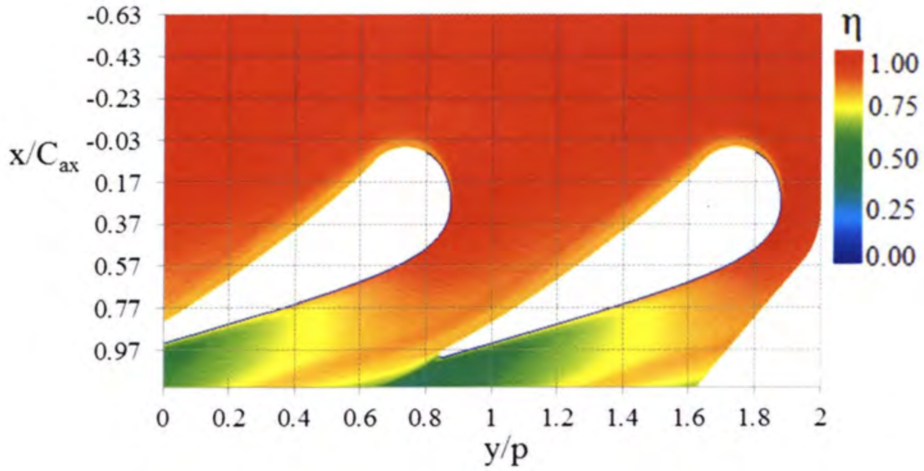

(c)β= 30°

Figure 93 Predicted η contour at MFR=2.25% by three different β

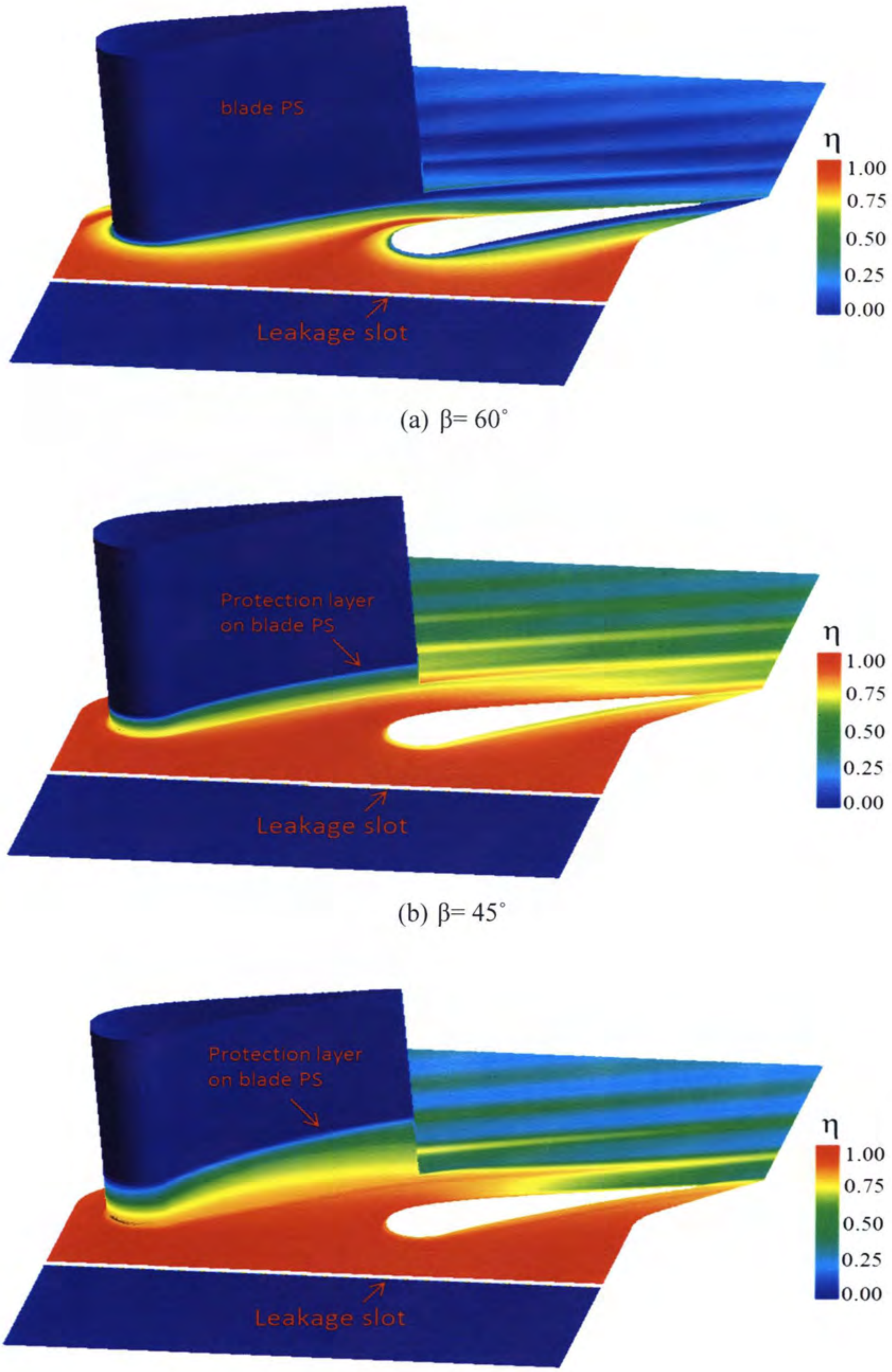

(a) β= 60°

(b) β= 45°

(c) β= 30°

Figure 94 η contour to illustrate the protection layer on the blade PS by different β

4.3 Leakage flow performance influenced by the slot position with $\beta = 90^{\circ}$

4.3.1 Aerodynamics performances

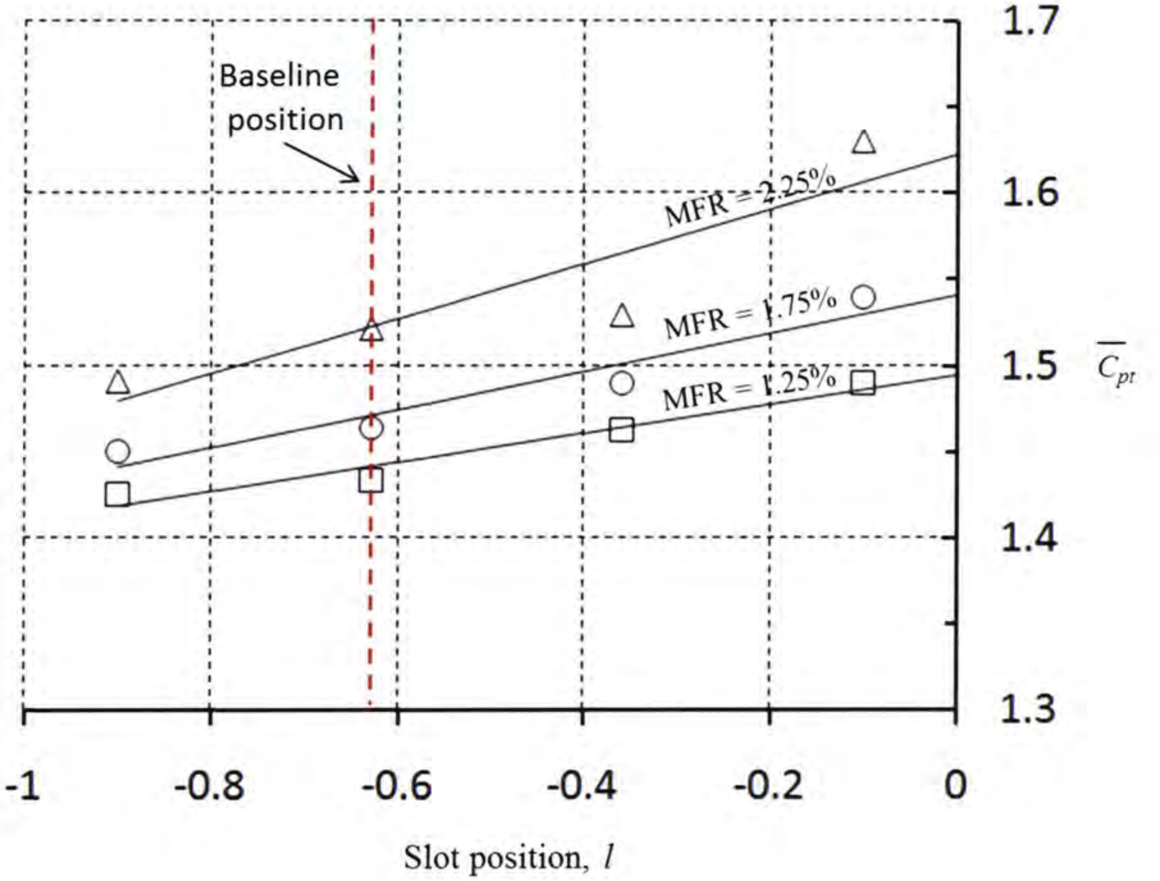

Figure 95 Mass average C_{pt} by the effect of slot location, l

Move the slot away from the blade leading edge had illustrated the increased of cooling performance where the coolant could stay closer to endwall surface thus provided better surface protection [25]. Present study intended to predict the performance of leakage flow injection with a different l from blade LE. l were translated to -0.90, -0.36 and -0.10. Three cases of MFR (1.25%, 1.75% and 2.25%) were predicted at each slot position. Figure 95 presents the loss trend by determined the mass averaged of C_{pt}. The red vertical line illustrates the position of the baseline slot located at l= -0.63. Regardless the l, MFR of 2.25% is always provides the highest loss among the cases. However, as l moved away from the blade LE, the prediction shows that the loss is linearly reduced. This phenomenon also follows by another two cases of MFR=1.75% and 1.25% where the lowest losses were obtained at l= -0.90. This means that l= -0.10 presents the highest loss among the case. The injection of leakage flow closer to the blade LE might be induced to the higher flow blockage which then amplifies the strength of HSV. As a result, the higher loss caused by the secondary flow structures was obtained. Figure 96 presents the C_{pt} contour based on MFR=1.25% in comparison of different l. When the slot moved closer to the blade LE at l= -0.36, the first and third loss cores seem to be increased. Further closer at l= -0.10, see Figure 96 (c), the third core merged with the first loss core resulting wider loss which associated by the PS-HSV. In contrary, in comparison with the baseline slot configuration, see Figure 51 (a), a significant change cannot be seen on the first and third loss cores except the level of C_{pt} slightly reduced.

The details of the secondary flow structure exist in the blade passage are explain by predicted vortex core as shown in Figure 97~Figure 99 for MFR=1.25% by the effect of l. At the same swirling strength level, the strength of the PS-HSV is predicted to be reduced when the slot moved away from the blade LE at l= -0.90 as been shown in Figure 97. In comparison with the baseline slot position, the vortical structures showing by the flow streamline at stagnation plane slightly weaken due to the less flow separation. The leakage flow can easily be penetrated into the mainstream since the slot is far enough from the higher pressure region. As a result, the leakage flow could stayed closer to the endwall surfaces . However, as shown in Figure 100 (a), the leakage flow tends to move towards center of the blade passage further downstream of the slot to generate AFV.

In case for l= -0.36 as shown in Figure 98, the injection near the high pressure region seems preventing the leakage flow to be reattached on the endwall surfaces thus high flow separation occurred just downstream of the slot. A very complicated flow structures has been predicted by the leakage injection at this slot position. To move the slot further downstream at l= -0.10 where the slot is actually located parallel to the higher pressure region at blade LE. Thus, the leakage injection with MFR=1.25% is predicted did not has enough momentum to be penetrated into the stagnation region as being shown by flow streamline at stagnation in

Figure 99. The leakage flow is totally prevented to be penetrated into the higher pressure region thus it tends to swirl inside the slot just upstream of slot exit. They tended to be penetrated near the blade center where the pressure is lower. The formation of the AFV by l= -0.36 and l= -0.10 cases are also observed in Figure 98 and Figure 99. The secondary flow structures near the blade TE are presented in Figure 101~Figure 103 with the ζ contour plotted on Plane 1.25C_{ax}. There are almost similar flow structure has been shown by the case at l= -0.90 and l= -0.36. However the different phenomenon has been shown by l=-0.10, the PS-HSV seems to be deflected by the AFV and develop along the passage before be attached on the adjacent blade SS near TE. This is a different phenomenon where in usual case the reattachment of PS-HSV occurs near the blade throat.

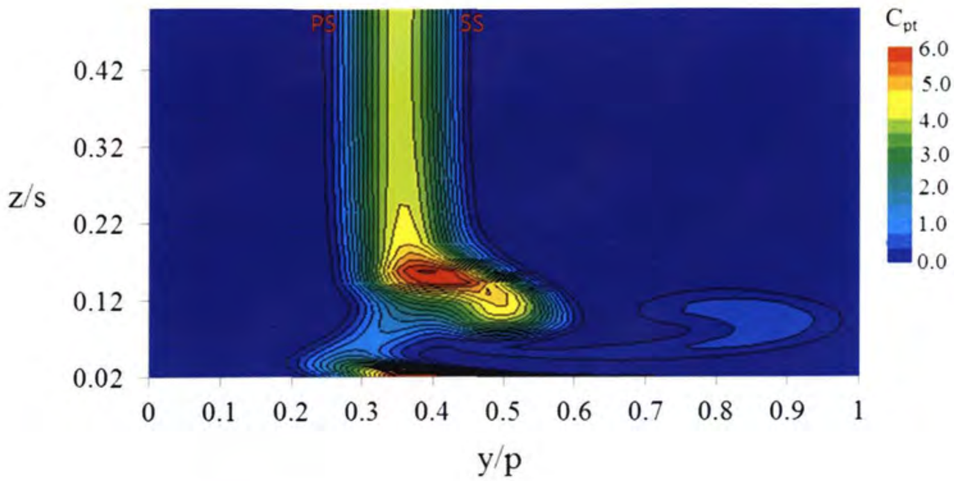

(a) l = -0.90

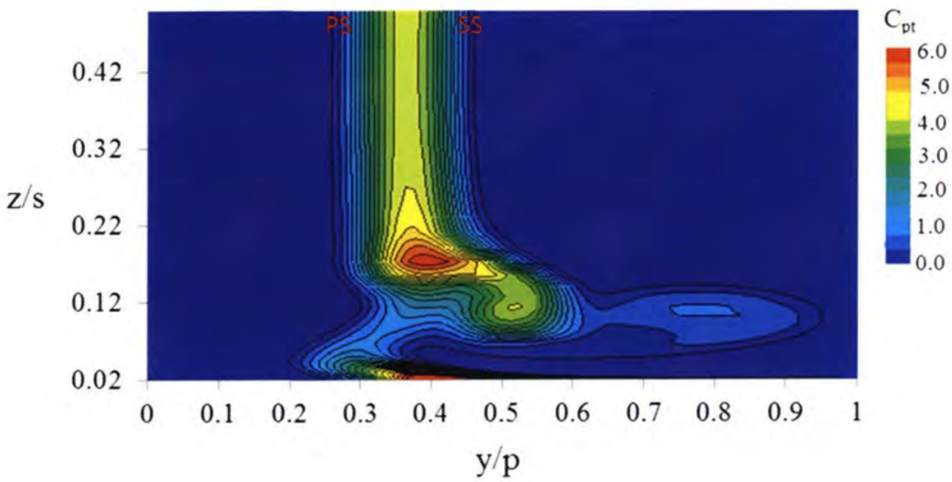

(b) l = -0.36

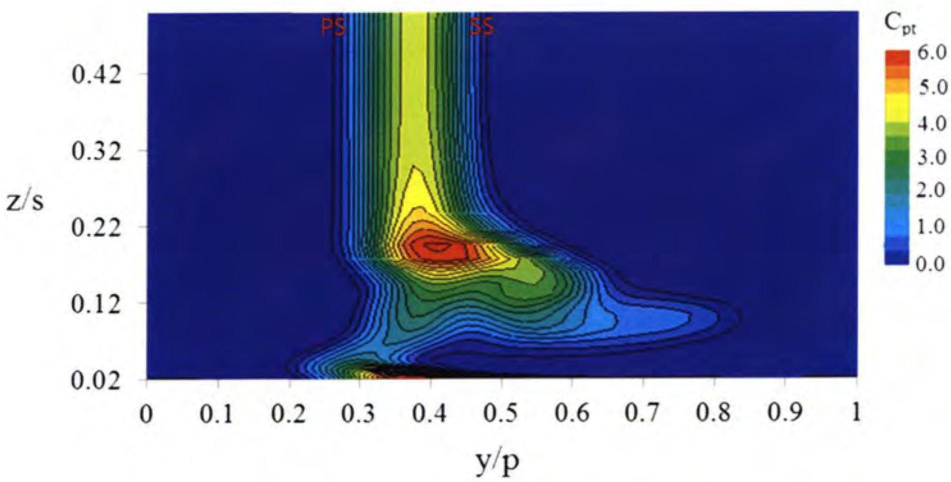

(c) l = -0.10

Figure 96 Predicted C_{pt} contour at MFR-1.25% by three different l

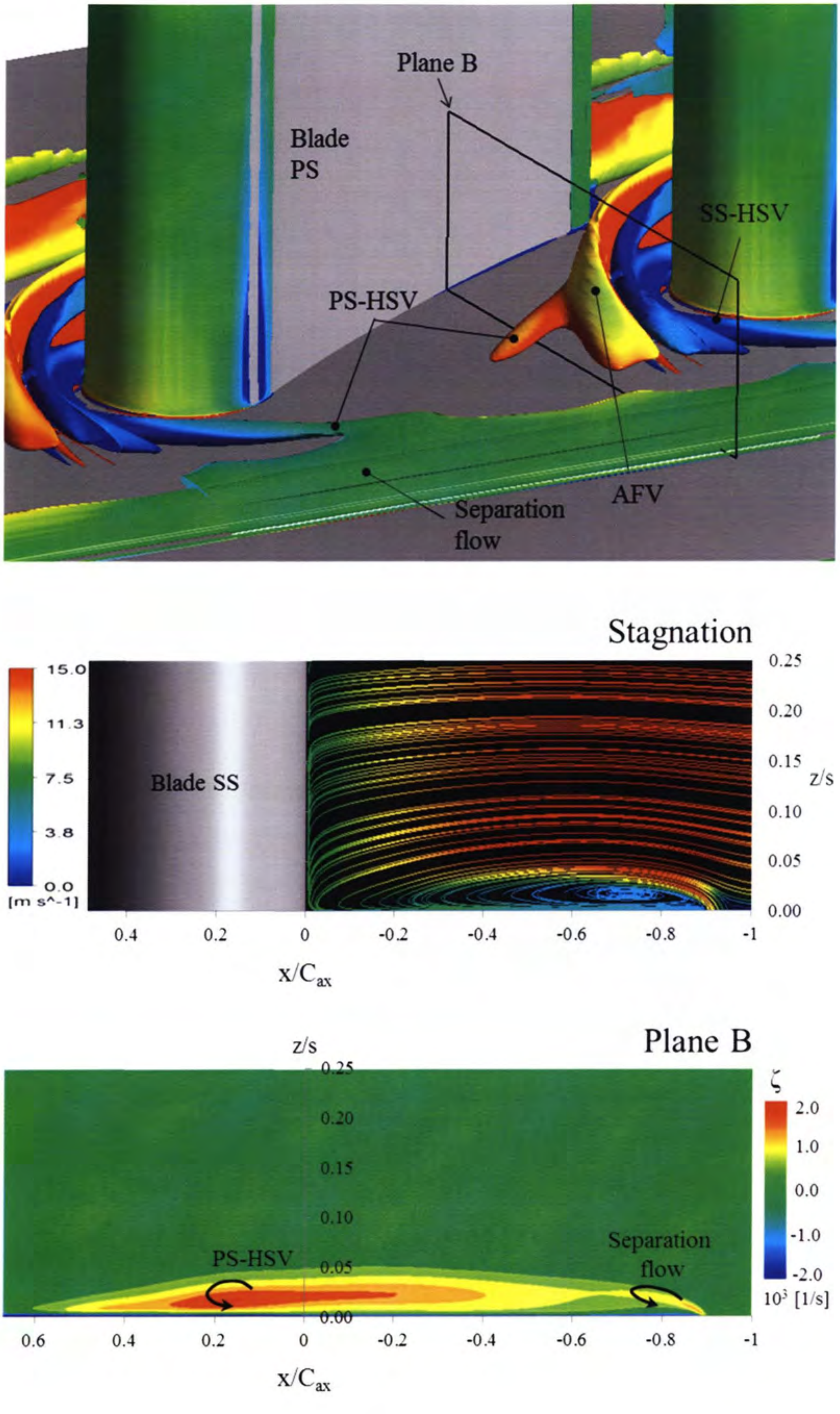

Figure 97 Predicted flow structures near blade LE at MFR=1.25% by l=-0.90

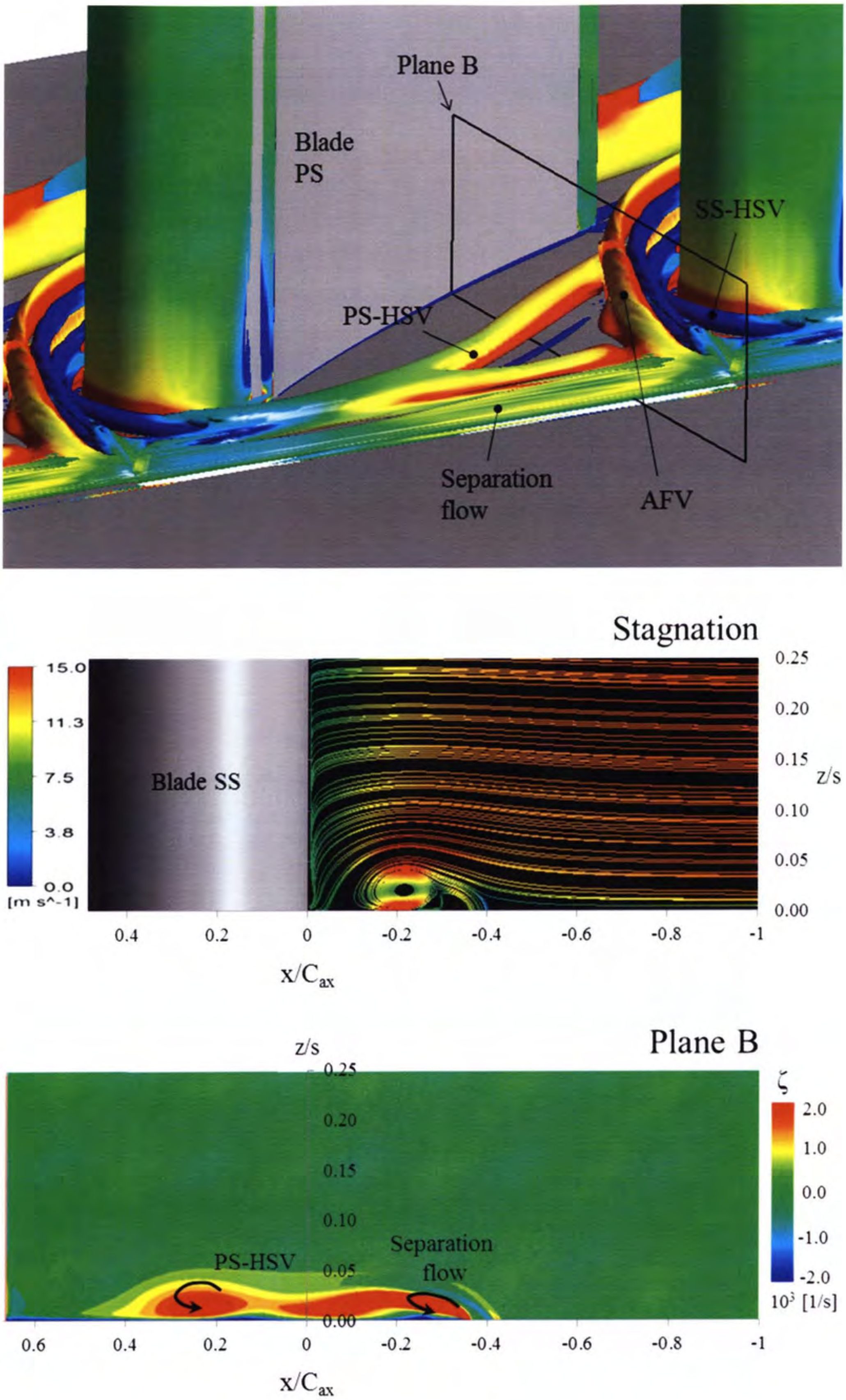

Figure 98 Predicted flow structures near blade LE at MFR=1.25% by l=-0.36

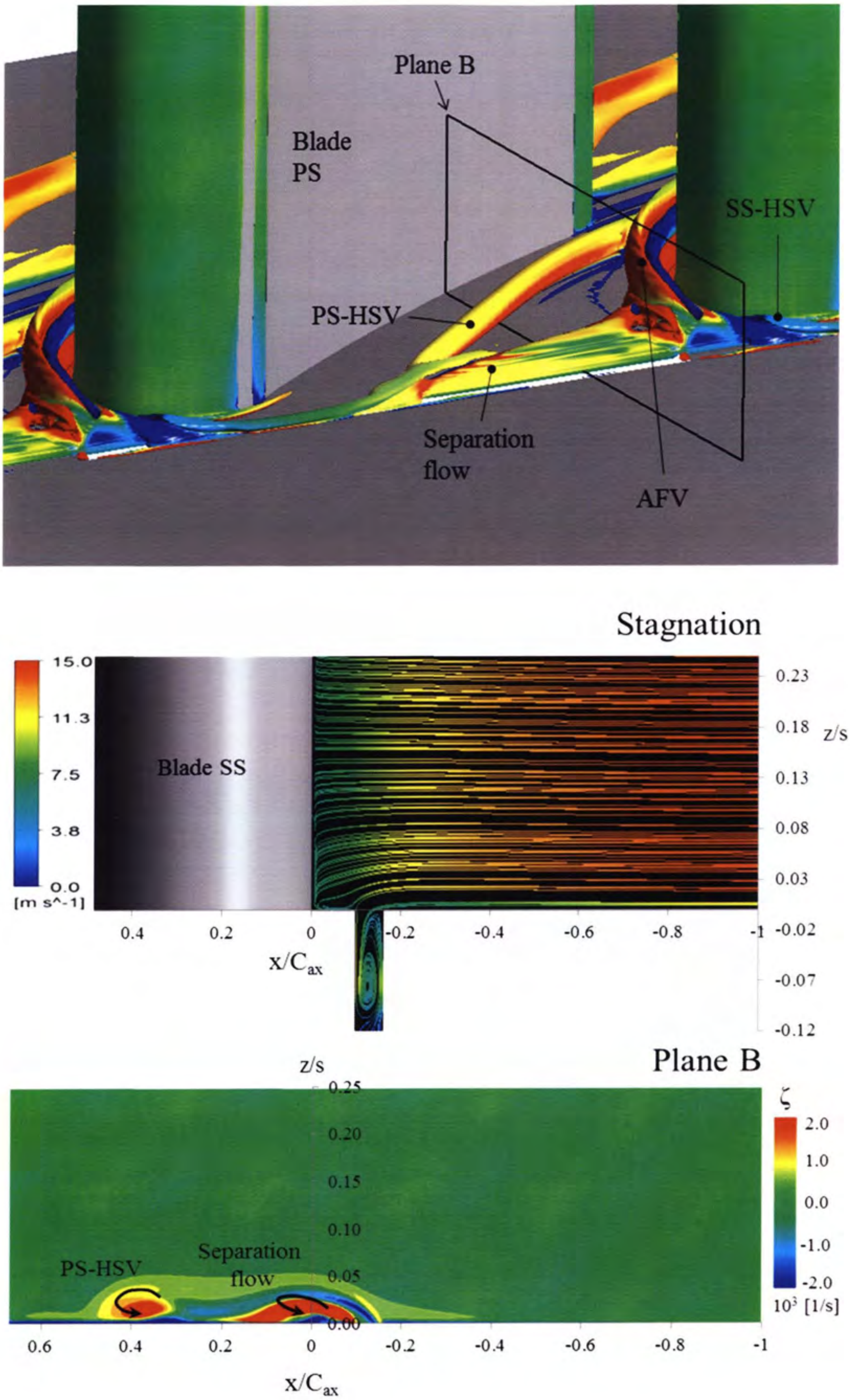

Figure 99 Predicted flow structures near blade LE at MFR=1.25% by l=-0.10

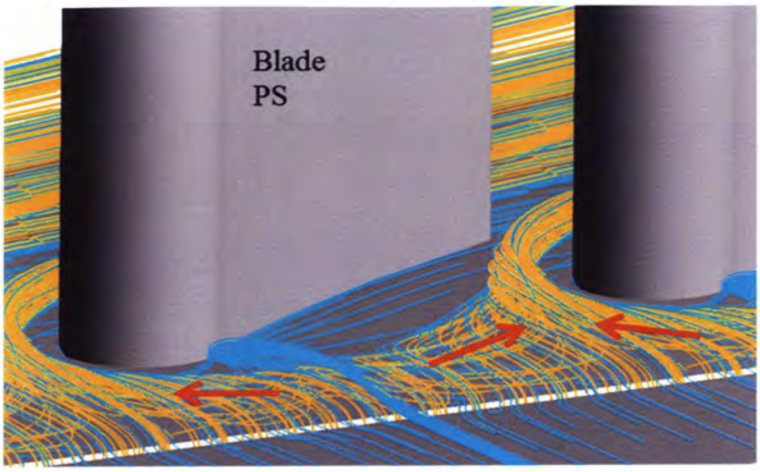

(a) Endwall streamline by l=-0.90

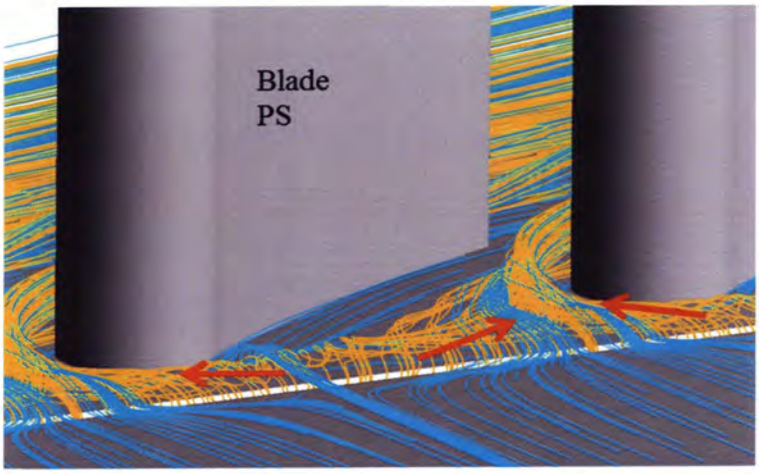

(b) Endwall streamline by l=-0.36

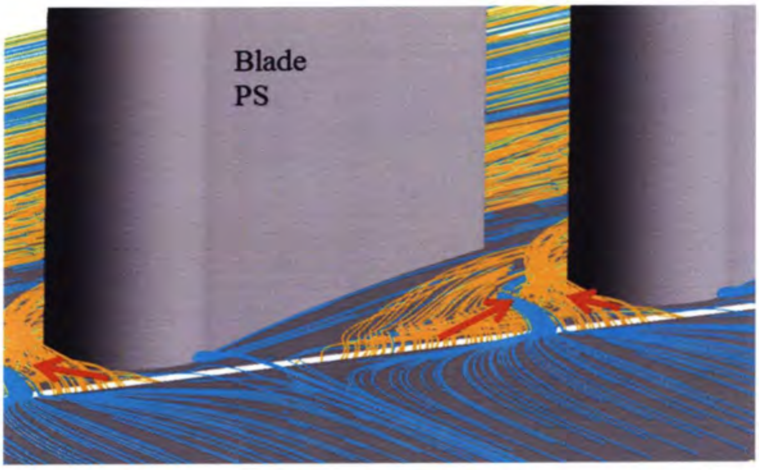

(c) Endwall streamline by l=-0.36

Figure 100 Predicted flow streamline on endwall region by slot position, *l* effect

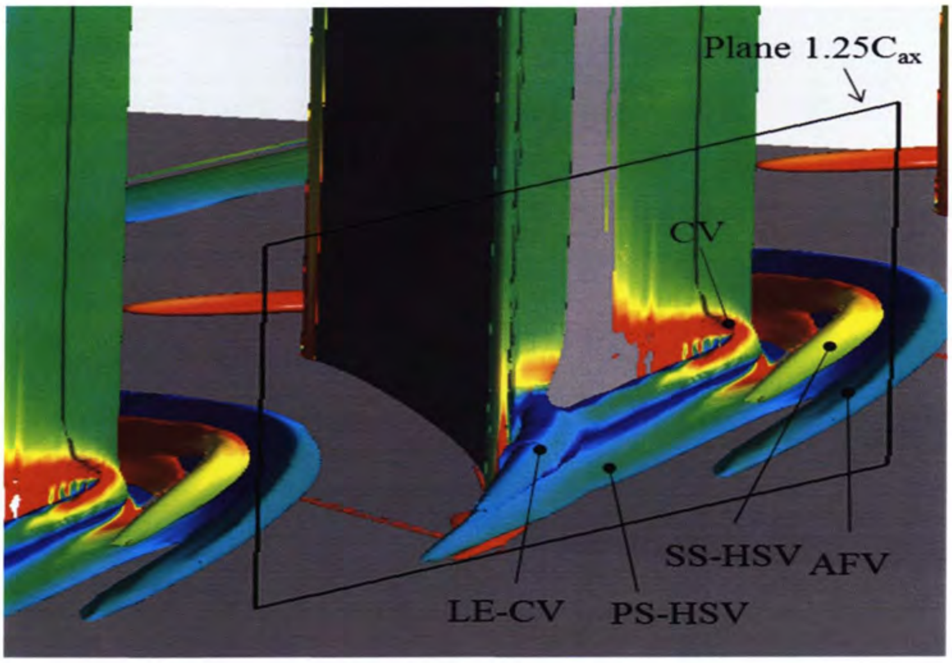

(a) Vortex core

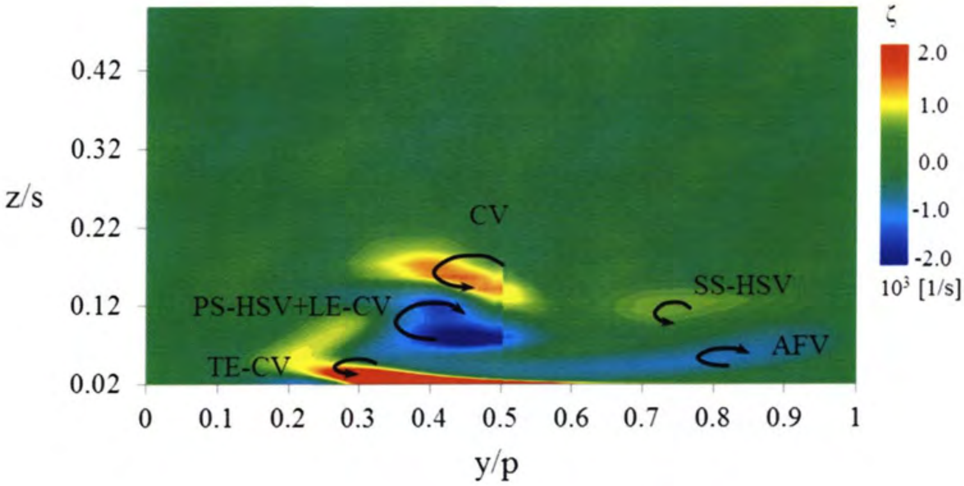

(b) Vorticity at Plane 1.25C$_{ax}$

Figure 101 Predicted flow structures near blade TE at MFR=1.25% by l=-0.90

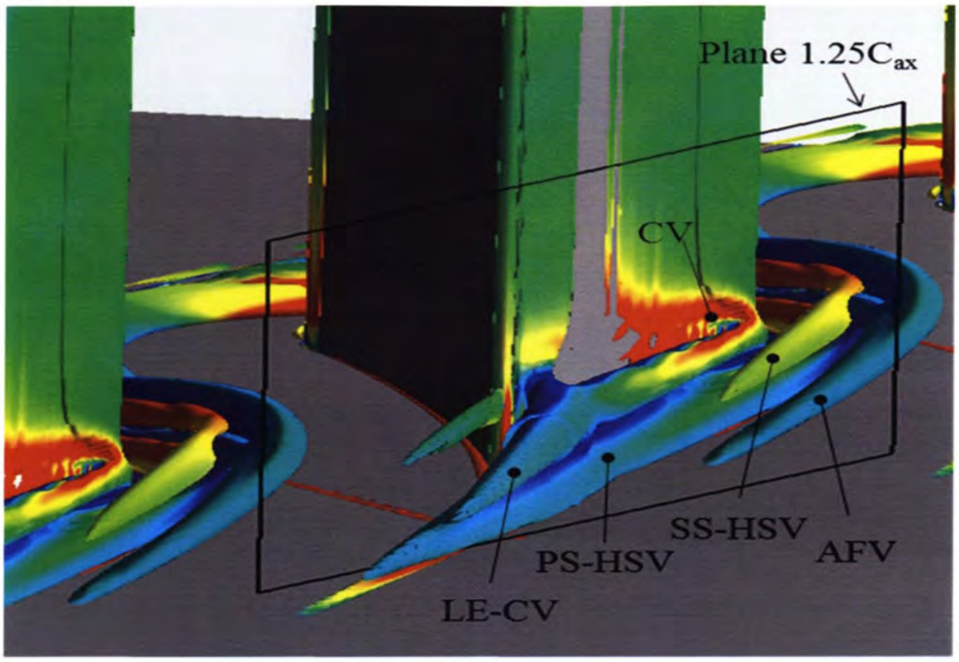

(a) Vortex core

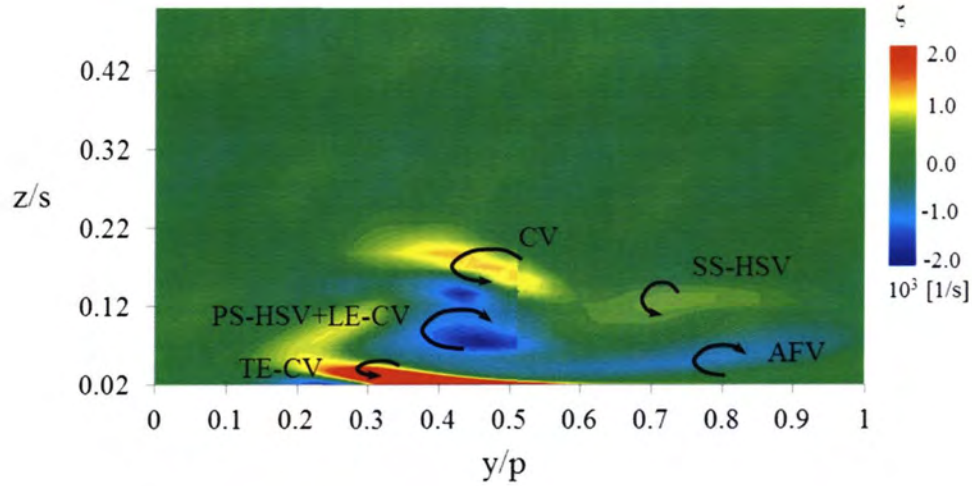

(b) Vorticity at Plane 1.25C$_{ax}$

Figure 102 Predicted flow structures near blade TE at MFR=1.25% by l=-0.36

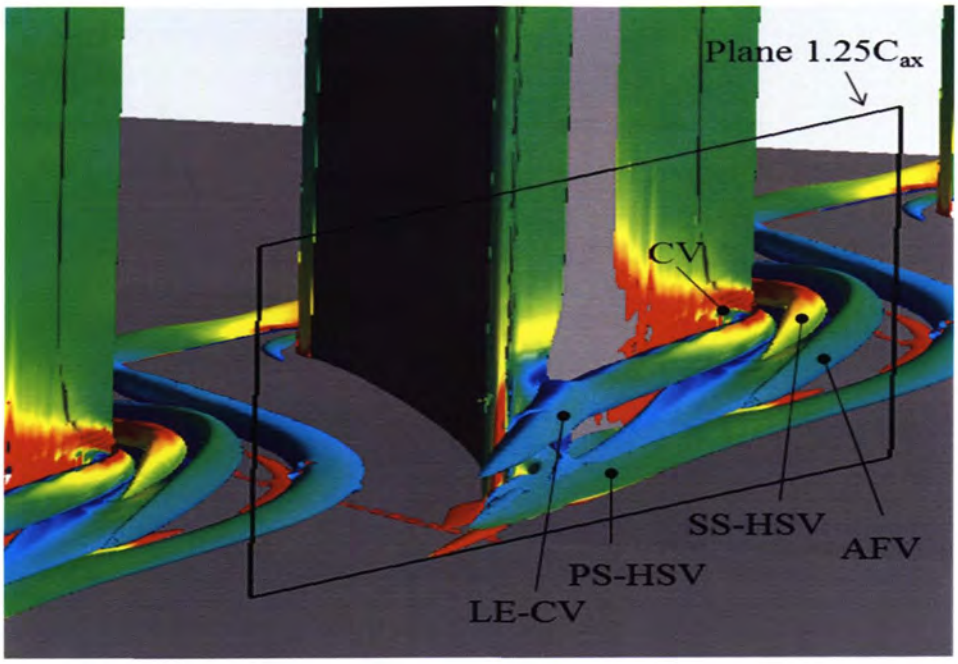

(a) Vortex core

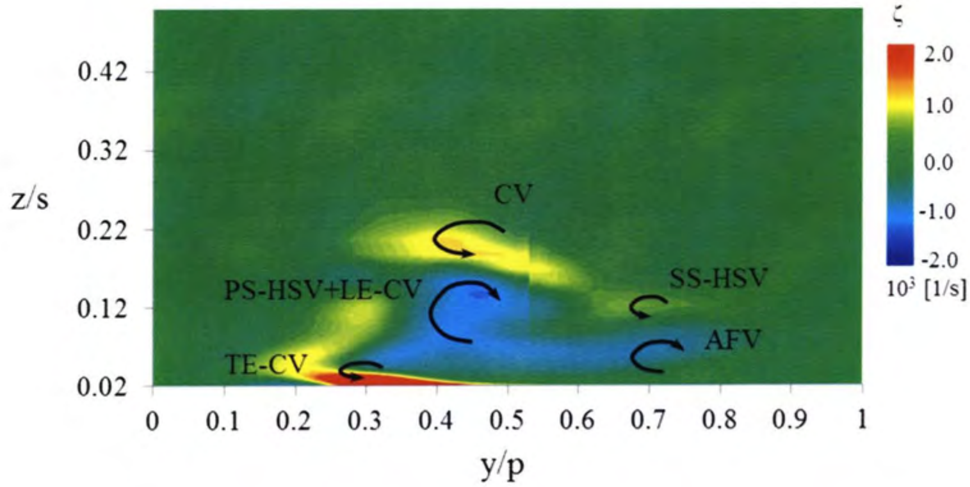

(b) Vorticity at Plane 1.25C$_{ax}$

Figure 103 Predicted flow structures near blade TE at MFR=1.25% by l=-0.10

4.3.2 Thermal performances

Figure 104 presents the performance of η at MFR = 1.25% by each slot position, l which is illustrated by the black horizontal line. The change on η contour can clearly be observed. At l=-0.36, η shows slightly lower performance compared to -0.63 where the yellow regions indicates the higher η slightly reduced. Different phenomenon shown by the case of l=-0.10 where the red region indicates a higher level of η became wider near the blade SS. However, the region near to the blade LE almost not be protected by the leakage flow due to the higher blockage caused by the higher pressure in stagnation region. This phenomenon has been shown in Figure 99 where the leakage flow tend to swirl inside the slot instead of the endwall surface resulting unprotected area near this region. This means the leakage flow tends to migrate towards passage center and might be the reason for the higher level of η is observed. In contrast, the level of η clearly increased for the case of, l= -0.90 in comparison with the baseline case. Since the slot located far away from the blade LE compared to other cases, the widest protection region was obtained and the red region which indicates higher η also increases. Moved the slot away from the blade LE allows the coolant to be laterally penetrated and provided much better protection layer. Regardless the position of slot, the region close to the blade PS is remains unprotected even the slot was moved closer. Noted that the higher level of η is presented at the same region where the AFV is generated.

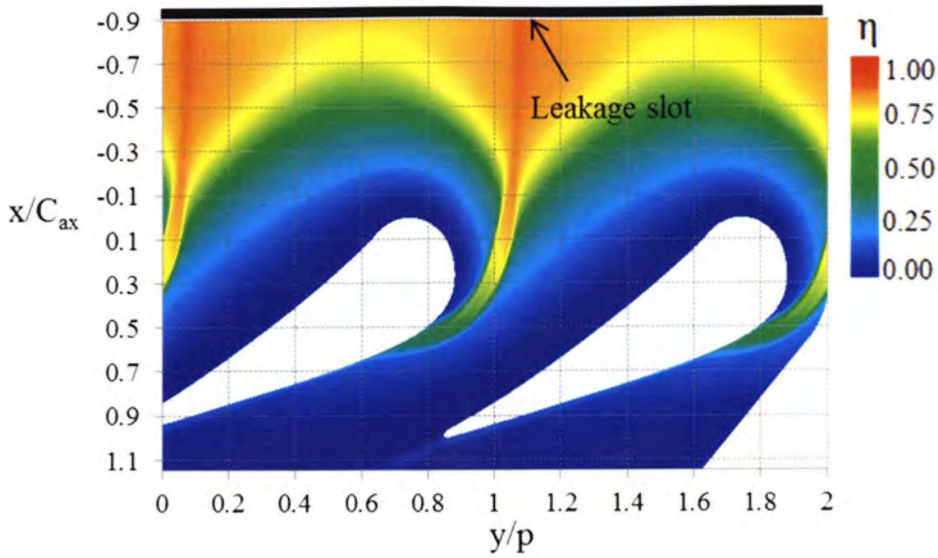

η
1.00
0.75
0.50
0.25
0.00
Leakage slot
x/C_ax
y/p
-0.9
-0.7
-0.5
-0.3
-0.1
0.1
0.3
0.5
0.7
0.9
1.1
0
0.2
0.4
0.6
0.8
1
1.2
1.4
1.6
1.8
2

(a) l = -0.90

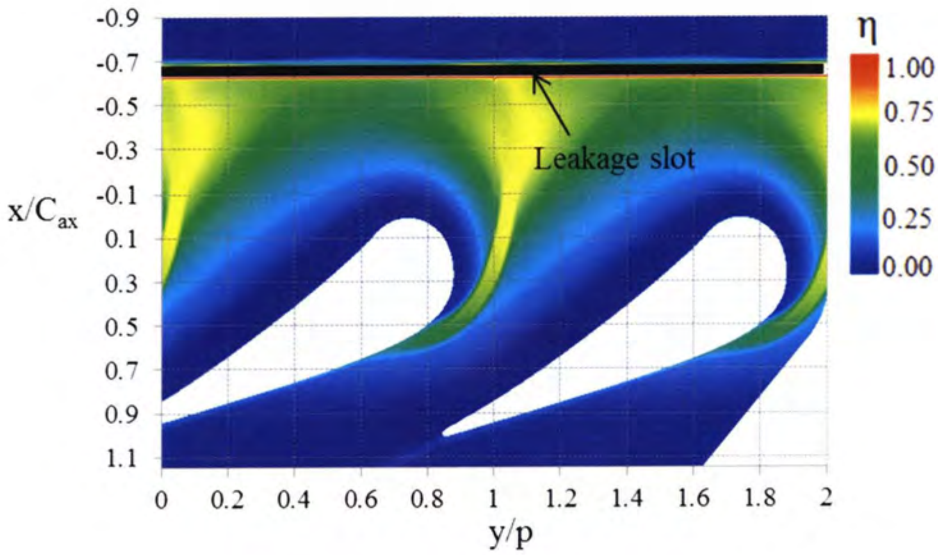

η
1.00
0.75
0.50
0.25
0.00
Leakage slot
x/C_ax
y/p
-0.9
-0.7
-0.5
-0.3
-0.1
0.1
0.3
0.5
0.7
0.9
1.1
0
0.2
0.4
0.6
0.8
1
1.2
1.4
1.6
1.8
2

(b) l = -0.63

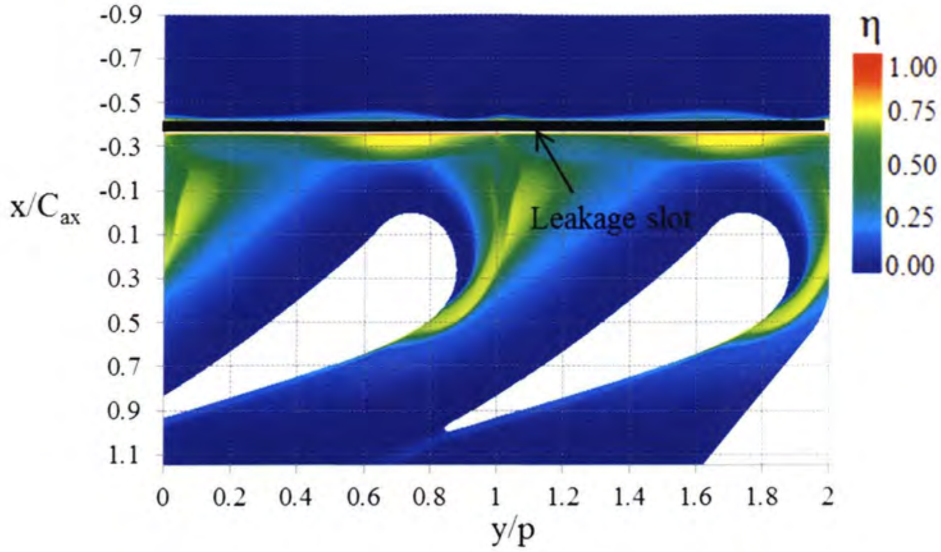

(c) l = -0.36

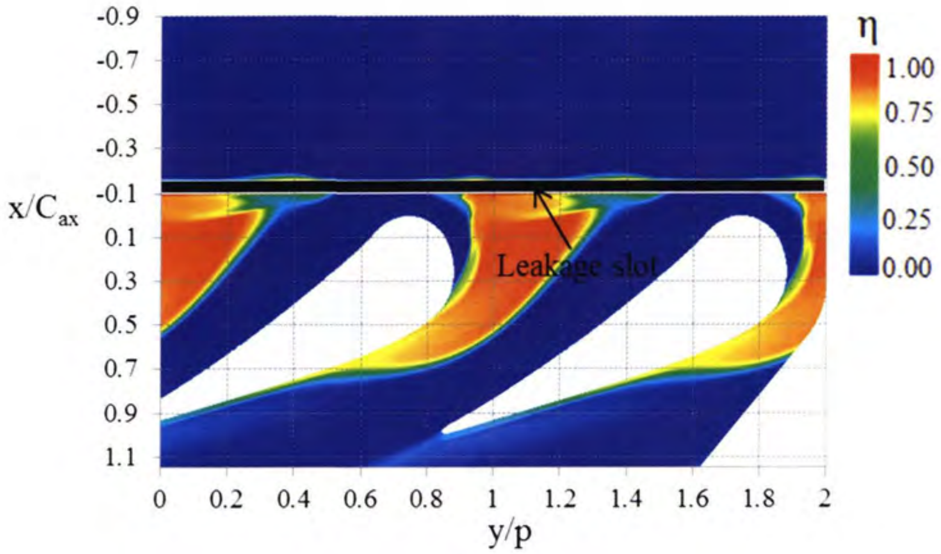

(d) l = -0.10

Figure 104 Predicted film cooling effectiveness contours by slot position effect

4.4 Laterally averaged η by slot modification

The laterally averaged film cooling effectiveness are plotted in Figure 105 by the effect of the slot orientation (β =90° 60°, 45°and 30°) while Figure 106 illustrates the effects of slot position (l=-0.90, -0.63, -0.36 and -0.10). By the effect of β, laterally averaged η significantly increase by the shallower angle. It relatively increases approximately 30% when β is changed to 60°in comparison with normal injection followed by another 20% for β=45°. However, the differences seem to be reduced at further downstream of the passage especially just downstream of blade throat at x/C_{ax}=0.6 where for β =90°, 60°and 45° are almost the same level. Different performance by β =30° where it always higher than others along the passage. At x/C_{ax}=0.6, the performance slightly raised for the whole cases might be due to the vortex core which was mixed out with the leakage flow was deflected towards endwall surface by the LE-CV near the blade throat thus higher η is obtained.

Since the positions of slot are differing in Figure 106, the starting point of the curve is different. If the comparison is made starting from x/C_{ax}=-0.30, the performance illustrated by the case of l=-0.9, -0.63 and -0.36 are almost the same where η is approximately 0.5. Positioned the slot further away from this point continuously increased the performance as shown by the case of l=-0.90 and -0.63. By l=-0.10, relatively higher performance has been shown compared to others. The leakage flow coming from this slot location could provide higher temperature different compared with others which were already mixed out with the mainstream. The mixed out flow would have relatively lower temperature than the leakage flow. Based on the thermal performance show by whole cases, to change the slot injection angle is considered as the most effective way to improve the cooling compared to the slot position. Furthermore, there are very limited space between the combustor and high-pressure turbine endwall if the position of slot is considered

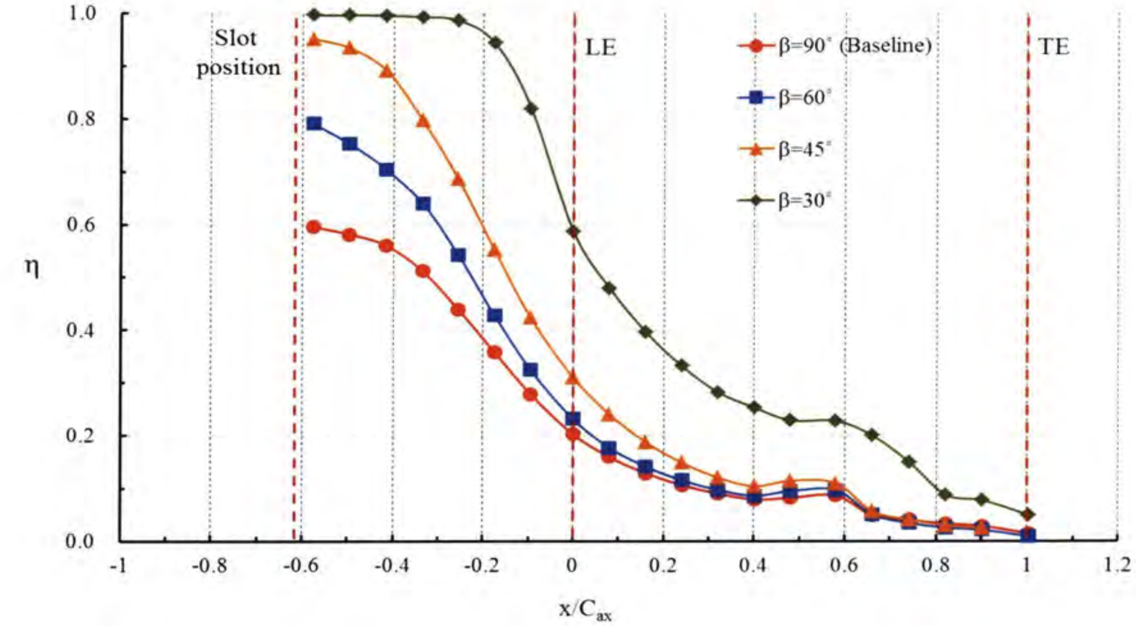

Figure 105 Laterally averaged film cooling effectiveness at MFR=1.25% by slot orientation, β effect

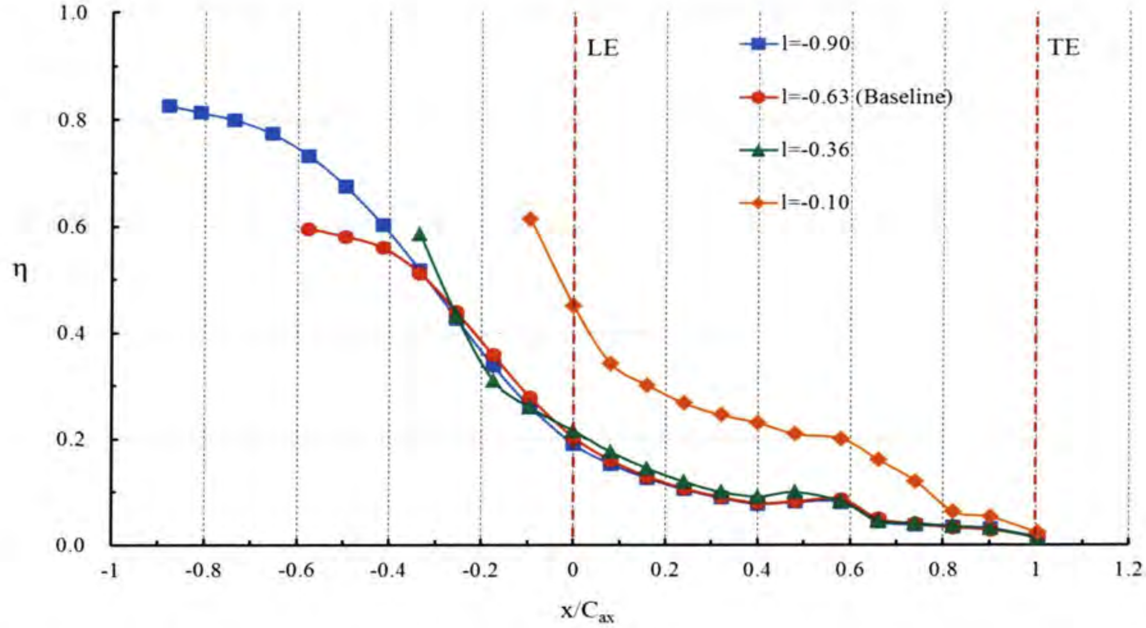

Figure 106 Laterally averaged film cooling effectiveness at MFR=1.25% by slot position, *l* effect

Chapter 5

Conclusions

The potential of leakage flows through a baseline slot configuration (90° injection at l= -0.63) to work as a cooling in order to protect the endwall surfaces in high pressure turbine cascade has been investigated. The measurement by 5-holes Pitot tube enables the clarification of three-dimensional flow behavior with the C_{pt} and ζ contours plotted. As for the thermal investigation, the TLC layer coating on the endwall surfaces allowed the detecting of temperature different and the transient method was applied to determine h and η. The capability of numerical simulation was also investigated by the validation with the experimental results. Authors also have taken the advantage of numerical simulation to predict the effects on aero-thermal performance by changing the slot configuration in terms of positions and orientations. Based on the results obtained, the following conclusions can be drawn:

- Both EFD and CFD represent almost similar trend of performance and enable authors to take advantage of numerical simulation to accurately predict the interaction of ejected leakage flow with the main stream. Leakage flow has significantly affected the secondary flow fields. Based on tested MFR, this loss region expanded approximately 40%-50% of area. MFR=2.25% was contributed to the highest loss among others. The newly generated vortical structures have been captured by the CFD with a higher swirling strength travel along the blade SS, which consequently contributed to the additional losses
- The loss core which was indicated in the baseline case was also affected by the leakage injection. Injecting the leakage flow from the blade upstream was predicted to amplify the strength of PS HSV so that it lifted-off adjacent blade SS with slightly higher position resulting higher loss core position in spanwise direction The mass-averaged

total pressure loss was proportional to the MFR and the graph plotted enable the authors to estimate the loss providing with another case of MFR. CFD over predicted the loss approximately 3% to 5% compared to the measurement.

- The discrepancy between CFD and EFD in terms of shape and position of the loss core was predicted associated by the flow behavior inside the plenum chamber. It was predicted to provide a significant effect of the formation of AFV on the endwall which consequently presented a difference loss contour.
- Film cooling effectiveness increases as to MFR, at the rate of at least 50% of the region for every 0.5% increase of MFR. Area averaged film cooling effectiveness increases approximately 7% whereas CFD predicted about 12% for 1% increase of MFR. This was due to the smaller temperature measurement range and the heat loss phenomenon during the temperature measurement. The thermal performance on the endwall region was also highly influenced the secondary flows behavior in providing the cooling protection area. SST turbulence model captured the presence of flow separation caused a lower HTC region on endwall surface which was also captured by the experimental especially for the MFR = 1.75% case.
- The injection of leakage flow at higher MFR of 2.25% through the inclined slot angle was predicted to reduce the strength of the secondary flow vortices near endwall. As a result, at fixed MFR=2.25%, injection with $\beta=30^{\circ}$ contributed the lowest averaged loss among cases. The performance of leakage flow through a shallow injection angle not only reduce the loss, but also was predicted to provide the wider cooling layer with higher η on the endwall surfaces. Blade PS and SS near the endwall corner were also protected by the slot configuration of $\beta=30^{\circ}$ and 45°
- Positioned the slot at l=-0.90 could provide a better cooling performance with a less secondary loss effects. At MFR=1.25%, the loss was predicted to reduce approximately 1.0% after changing the position of slot from l=-0.63 to -0.90. However, it was increased approximately 2.0% and 4.0% after shifted the slot closer towards blade LE at l=-0.36 and l=-0.10, respectively. Predicted film cooling effectiveness also indicates a positive trend of contour at l=-0.90. The wider protection area has been provided after moved the slot away from blade LE.
- The prediction presented that to change the slot orientation was the most effective way in order to increase both aero and thermal performance of in high-pressure turbine.

References

[1] Denton, J.D. "Loss mechanisms in turbomachines". ASME Paper No. 93-GT-435, 1993

[2] Hawthorne, W.R. "Some formulae for the calculation of secondary flows in cascades." Aero. Research Council, Report No. 17519, 1955.

[3] Sieverding, C. H.; 1984 "Recent Progress in the Understanding of Basic Aspects of Secondary Flows in Turbine Blade Passages", ASME Paper No. 84-GT-78, ASME Journal of Engineering for Gas Turbines and Power, Vol. 107, pp. 248-257

[4] Klein, A. Unterschungen uber den Einfluss der Zustromgrenzschicht auf die Sekundarstromung in den Beschaufelungen von Axialturbinen. Forsch. Ing., Bd 32, Nr 6, 1966; English translation: "Investigation of the entry boundary layer on the secondary flows in the blading of axial turbines. BHRA T 1004, 1966.

[5] Langston, L.S., Nice, M.L. and Hooper, R.M. "Three-dimensional flow within a turbine passage", Journal of Engineering for Power, Vol. 99, pp. 21-28, 1977.

[6] Georgiou, D.P., Papavasilopoulos, V.A. and Alevisos, M. "Experimental contribution on the significance and the control by transverse injection of the horseshoe vortex", ASME Paper No. 96-GT255,1996

[7] Sharma, O.P. and Butler, T.L. "Predictions of endwall losses and secondary flows in axial flow turbine cascades", ASME Paper No. 86-GT-228, 1986.

[8] Goldstein, R.J. and Spores, R.A. "Turbulent transport on the endwall in the region between adjacent turbine blades", Transactions of the ASME, Journal of Heat Transfer, Vol. 110, pp. 862-869, 1988

[9] Sharma, O. P. and Butler, T. L.; 1986 "Prediction of Endwall Losses and Secondary Flows in Axial Flow Turbine Cascades", ASME Paper No. 86-GT-228, Dusseldorf, West Germany.

[10] Wang, H. P., Olson, S. J., Goldstein, R. J. and Eckert, E. R. G.; 1995 "Flow Visualisation in a Linear Turbine Cascade of High Performance Turbine Blades", ASME Paper No. 95-GT-7, Houston, Texas

[11] Gregory-Smith, G.G. and Graves, C.P. "Secondary flows and losses in a turbine cascade", AGARD Paper CP351 No. 17, 1983.

[12] Abdulla-Altaii, A.K. and Raj, R.S. "Secondary flow development downstream of a blade endwall corner", ASME Paper No. 94-GT-459, 1994.

[13] Yamamoto, A., Kaba, K. and Matsunuma, T. "Measurement and visualisation of three-dimensional flows in a linear turbine cascade", ASME Paper No. 95-GT-341, 1995.

[14] Moore, J. and Adhye, R.Y. "Secondary flows and losses downstream of a turbine cascade", ASME Paper No. 85-GT-64, 1985.

[15] Gregory-Smith, D.G. "Secondary flows and losses in axial flow turbines", ASME Paper No. 82-GT19, 1982.

[16] Kang, M. B. and Thole, K.A., 1999 "Flowfield Measurements in theEndwall Region of a Stator Vane", ASME Paper No. 99-GT-188, ASME Journal of Turbomachinery, Vol. 122, pp. 255-262

[17] Radomsky, R. W. and Thole, K. A., 2000, "High Freestream Turbulence Effects on Endwall Heat Transfer for a Gas Turbine Stator Vane ", 122, pp. 699-708.

[18] Sundaram, N. and Thole, K. A., 2009, "Film-Cooling Flow fields with Trenched Holes on an Endwall", Journal of Turbomachinery, 131, pp.

[19] H.J.Rehder, A.Dannhauer, "Experimental Investigation of Turbine Leakage Flows on the Three-Dimensional Flow Field and Endwall Heat Transfer", Journal of Tur bomach, Vol.129, 2007, pp. 608-618

[20] A.A. Thrift,K.A.Thole, S. Hada, 2011,"Effects of Orientation and Position of the Combustor-Turbine Interface on the Cooling of a Vane Endwall", ASME 2011, GT2011-455

[21] Blair, M.F., 1974, "An Experimental Study of Heat Transer and Film Cooling on Large-Scale Turbine Endwalls", ASME Journal of Heat Transfer, Vol. 96, pp. 524-529.

[22] Takeishi, K., Matsuura, M., Aoki, S. and Sato, T.; 1990 "An Experimental Study of Heat Transfer and Film Cooling on Low Aspect Ratio Turbine Nozzles", ASME Paper No. 89-GT-187, ASME Journal of Turbomachinery, Vol. 112, pp. 488-496.

[23] Blair, M. F.; 1992 "An Experimental Study of Heat Transfer in a Large-Scale Turbine Rotor Passage", ASME Paper No. 92-GT-195, Cologne, Germany

[24] Kost, F., and Nicklas, M., 2001. "Film-Cooled Turbine Endwall in a Transonic Flow Field: Part I - Aerodynamic Measurements," ASME J Turbomach 123, pp. 709–719

[25] Kost, F., and Mullaert, A., 2006. "Migration of Film-Coolant from Slot and Hole Ejection at a Turbine Vane Endwall", GT2006-90355

[26] S.P.Lynch,K.A.Thole, "The Effect of Combustor-Turbine Interface Gap Leakage on the Endwall Heat Transfer for a Nozzle Guide Vane", Journal of Turbomachinery,

Vol.130, 2008, pp041019-1-041019-10

[27] Kang, M. B., Kohli, A., and Thole, K. A., 1999, "Heat Transfer and Flowfield Measurements in the Leading Edge Region of a Stator Vane Endwall", Journal of Turbomachinery, 121, pp. 558-568.

[28] J.D.Piggush,T.W.Simon, "Heat Transfer Measurements in a First-Stage Nozzle Cascade Having Endwall Contouring Misalignment and Leakage Studies", Transaction of ASME Vol.129,2007, pp. 782-790

[29] W.G. Aizon, K. Funazaki, 2012, "Aero-Thermal Performance of Purge Flow in Turbine Cascade Endwall Cooling", Applied Mechanics and Material, Vol.229-231,pp.737-741

[30] Funazaki, K., 2000, "Discussion on Accuracy of Transient Heat Transfer Measurement by Use of Thermochromic Liquid Crystal," Journal of the Gas Turbine Society of Japan, Vol. 28, pp. 397-404.

[31] Kline, S.J. (1985a), "The purposes of uncertainty analysis. Journal of Fluids Engineering", Transactions of the ASME, June 1985

[32] Coleman, H.W., and Steele, W.G. (1999). "Experimentation and Uncertainty Analysis for Engineers", 2nd Ed., John Wiley & Sons, New York, pp. 275

[33] Moffat, R.J. (1985)."Using uncertainty analysis in the planning of an experiment", Journal of Fluids Engineering, Vol. 107, No. 6, pp. 173-178.

[34] Alok, D., "Film cooling from a row of holes supplemented with anti-vortex holes", 2007.

[35] http://gehonda.com/products/hf120/explore.html
Last access: September 12, 2013

[36] Genrup, M.; 2005, "On Degradation and Monitoring Tools for Gas and Steam Turbines", Department of Heat and Power Engineering, Lund Institute of Technology, Lund, Sweden, ISRN LUTMDN/TMHP--05/1027--SE.

[37] Han, J.C., Dutta, S., and Ekkad, S. V., 2000, Gas Turbine Heat Transfer and Cooling Technology,

[38] Taylor & Francis, New York. Frank G. R, 2006, "Numerical and Experimental Investigations of Design Parameters Defining Gas Turbine Nozzle Guide Vane Endwall Heat Transfer", pg. 53, Doctoral thesis, Royal Institute of Technology, Stockholm.